UNIVERSITAT DE VALÈNCIA

FACULTAT DE FÍSICA

DEPARTAMENT DE FÍSICA TEÒRICA

PROGRAMA DE DOCTORAT EN FÍSICA

Nuclear effects in neutrino-nucleus interactions: the role of spectral functions

---

DOCTORAL THESIS

Author:
Joanna E. SOBCZYK

Supervisor:
Dr. Juan M. NIEVES PAMPLONA

October 2019

Dr. Juan Miguel Nieves Pamplona, Investigador Científico del Consejo Superior de Investigaciones Científicas

CERTIFICA: Que la presente Memoria *"Nuclear effects in neutrino-nucleus interactions: the role of spectral functions"* ha sido realizada bajo mi dirección en el Departamento de Física Teórica de la Universidad de Valencia por Joanna E. Sobczyk como Tesis para obtener el grado de Doctor en Física.

Y para que así conste, en cumplimiento con la legislación vigente, presenta ante el Departamento de Física Teórica, la referida memoria, firmando el presente certificado en Burjassot (Valencia) a 21 de Octubre de 2019.

Fdo: Juan Miguel Nieves Pamplona

"*The marquis stared at Richard, openly amused. "What a refreshing mind you have, young man," he said. "There really is nothing quite like total ignorance, is there?"*

Neil Gaiman, Neverwhere

UNIVERSITAT DE VALÈNCIA

Abstract

Nuclear effects in neutrino-nucleus interactions: the role of spectral functions

by Joanna E. SOBCZYK

In this Thesis we present a wide analysis of nuclear effects which are crucial for a proper description of neutrino-nucleus scattering. We use a well-established many-body framework, successful in modelling a great variety of nuclear processes. In particular, we analyze the role of the spectral functions accounting for the modifications of the dispersion relation of nucleons embedded in the nuclear medium. We concentrate on processes mostly governed by one-body mechanisms, studying possible approximations to evaluate the particle-hole propagator using spectral functions and performing a series of analyses and comparisons with other approaches for the quasielastic mechanism.

We also investigate how to include together spectral functions and long-range random-phase approximation (RPA) correlations in the evaluation of nuclear responses, discussing the existing interplay between both types of nuclear effects. At low energy transfers (≤ 50 MeV), we compare our predictions for inclusive muon and radiative pion captures in nuclei, and charge-current (CC) neutrino-nucleus cross sections with experimental results. We also present an analysis of intermediate energy quasielastic neutrino scattering for various targets and both neutrino and antineutrino CC driven processes. Moreover, we briefly compare our spectral function and RPA results to predictions obtained within other representative approaches. Since there is no precise data available for CC neutrino-nucleus cross section, we perform a comparison of our spectral function model (and other approaches) with the electron scattering inclusive data on ^{12}C, in the energy region relevant for the T2K experiment.

Further, we pay attention to the scaling properties of our model. Scaling features of the nuclear electromagnetic response functions unveil aspects of nuclear dynamics that are crucial for interpreting neutrino- and electron-scattering data. Obtained scaling functions are characterized by an asymmetric shape, although less pronounced than that exhibited by the experimental one, derived from the longitudinal electromagnetic response function. We also show that this asymmetry, only mildly affected by final state interactions, is mostly due to nucleon-nucleon correlations, encoded in the continuum component of the hole spectral function.

Next, we present results for the quasielastic weak production of Λ and Σ hyperons induced by $\bar{\nu}$ scattering off nuclei. We employ hole spectral functions and we describe the propagation of the hyperons in the nuclear medium by means of a Monte Carlo cascade. The latter strongly modifies the kinematics and the relative production rates of the hyperons, leading to a non-vanishing Σ^+ cross section, to a sizable enhancement of the Λ production and to drastic reductions of the Σ^0 and Σ^- distributions. We also compute the quasielastic weak Λ_c production cross section, paying special attention to estimate the uncertainties induced by the model dependence of the $n \to \Lambda_c$ weak matrix element in the free space.

Lastly, we study the τ polarization in CC quasielastic (anti)neutrino-nucleus scattering. We show that the spectral functions, while playing an important role in the prediction of the differential cross sections, produce much less visible effects on the polarization components of the outgoing τ.

Acknowledgements

"There are only two ways to live your live.
One is as though nothing is a miracle.
The other as is though everything is a miracle."
Albert Einstein

My work in neutrino physics at IFIC has been a great adventure, which I will always keep in my memory as one of the most enjoyable and fruitful periods of my life. It is, therefore, a great joy to mention here those who were the closest and the most important people to me during this time and who accompanied me on this path.

First of all, I would like to thank my supervisor, Juan Nieves, for the opportunity to work with him. I will never forget the long discussions and explanations he was willing to give me every time I needed it. He taught me not only theoretical physics but also transmitted courage to ask challenging questions, pay attention to details, and regard highly scientific honesty. His constant help, support and encouragement have made the last two years a truly enjoyable time.

I will also remember the friendly and familiar atmosphere which I could always experience in our group from the first moment I entered it. Thanks to the openness of Eulogio Oset, Manuel Vicente-Vacas and Luis Alvarez-Ruso, I immediately felt I was a part of the group. Coffee-breaks, lunches and simple chats have become an indispensable part of each day. These short breaks quite often served as moments to "recharge batteries" and cheered me up a lot.

There is nothing more encouraging than having by one's side people who follow the same road. And we were lucky to be many PhD students at the same time in our group. Many special thanks to Eduardo and Rafael for their company while sharing the same office and everything inside it, including tea-bags, coffee and even a small fan which saved our lives during hot Valencia summers. Pedro, Vinicius and Gustavo, our next-door companions are not less present in my memory. I could always count on their sense of humor and help: in physics, as computer experts and in many small everyday-life problems. Thank you for these numerous moments when we laughed, chatted, and supported each other!

On my scientific path I was very lucky to meet and collaborate with people who were both outstanding physicists and great persons. Among them, I would like to express my gratitude in a special way to Noemi Rocco and Alessandro Lovato, who were my first and closest collaborators and also friends. I am not able to list here all the things I would like to thank them for. I will keep in my memory the days spent together in Valencia, Chicago, and on various workshops and conferences. Also, I would like to give my warmest thanks to Eliecer Hernández and Federico Sánchez. It has been an honor to discuss physics and work together with such experienced and brilliant physicists.

In this place I also want to express my gratefulness for Stefan Pokorski who many years ago transmitted me his love for physics and – despite a different road I chose – supported me. I regard as a special gift the time that was given me to work with him.

Last but not least, I would like to thank my parents and the rest of my family, who have always been there when I needed their help, even when I was not aware of it. This warm company and closeness – sometimes in spite of the long distance which separated us – has been crucial in many situations. In a special way I want to thank my dad who introduced me to the world of neutrino physics and always encouraged me with his unfailing sense of humor.

At this moment I have in my mind many people whom I met in the last few years and who left many bright memories. Although I am not able to mention each of them by name, I would like to repeat after Marcel Proust: "Let us be grateful to people who make us happy; they are the charming gardeners who make our souls blossom."

Contents

List of Abbreviations

SF	**S**pectral **F**unction
QE	**Q**uasi-**E**lastic
DIS	**D**eep **I**nelastic **S**cattering
NN	**N**ucleon-**N**ucleon
MF	**M**ean-**F**ield
RMF	**R**elativistic **M**ean-**F**ield
CC	**C**harge **C**urrent
NC	**N**eutral **C**urrent
EM	**E**lectro **M**agnetic
MC	**M**onte **C**arlo
MCC	**M**onte **C**arlo **C**ascade
FSI	**F**inal **S**tate **I**nteraction
FG	**F**ermi **G**as
GFG	**G**lobal **F**ermi **G**as
LFG	**L**ocal **F**ermi **G**as
LDA	**L**ocal **D**ensity **A**pproximation
RPA	**R**andom **P**hase **A**pproximation
CRPA	**C**ontinuum **R**andom **P**hase **A**pproximation
CBF	**C**orrelated **B**asis **F**unctions
IA	**I**mpulse **A**pproximation
PWIA	**P**lane **W**ave **I**mpulse **A**pproximation
CQM	**C**onstituent **Q**uark **M**odel
GFMC	**G**reen's **F**unction **M**onte **C**arlo

When we use nonrelativistic kinematics for nucleons, we choose the origin of energy in their mass.

To my family scattered around the world

Resumen

En esta tesis hemos estudiado la interacción neutrino-núcleo, en el régimen cuasielástico, haciendo un especial énfasis en la importancia de las correcciones nucleares.

Motivación

En el estudio de la física de oscilaciones de neutrinos, los desafíos más importantes que se presentan en la actualidad son (i) medir el valor de la fase de la violación de la simetría CP y (ii) discernir entre jerarquía normal o invertida en el respeto de masas de los neutrinos. Los futuros experimentos diseñados para resolver estas (y otras) cuestiones, incluyendo posibles descubrimientos de Física más allá del Modelo Estándar, sobre todo DUNE y T2HK, contarán con una estadística muy alta, así que las incertidumbres sistemáticas van a jugar un papel principal. Los errores sistemáticos que vienen de las secciones eficaces (anti)neutrino-núcleo están entre las fuentes más importantes de incertidumbres, y tienen que ser reducidas al nivel de $1-3\,\%$, para cumplir las expectativas experimentales.

La teoría de interacciones de neutrinos con núcleos entra en el análisis de los parámetros de oscilaciones de manera no trivial, influyendo en varias etapas de los estudios. Además, el flujo de neutrinos nunca es mono-energético, y su distribución tiene incertidumbres del orden del $5\,\%$ (el número exacto depende del experimento). Como la probabilidad de oscilación es función de la energía del neutrino, hay que reconstruir esta última, con suficiente precisión, en función de la energía. Siguiendo la discusión presentada en la Ref. [1], la información sobre las interacciones neutrino-núcleo influye en el análisis de oscilaciones de varios modos

- El método para la reconstrucción de la energía del neutrino depende del tipo de detector. En general, sus limitaciones (por ejemplo el hecho de que se detectan sólo partículas a partir de un cierto umbral energético o que no se observan las partículas neutras, etc.), requieren la utilización de generadores Monte Carlo que se basan, a su vez, en modelos nucleares.

- Aceptación de los eventos de una cierta topología (los detalles del análisis en cada experimento son distintos). También es importante controlar los procesos que contribuyen al fondo, y pueden imitar a otros, induciendo identificaciones erróneas. Por ejemplo, los piones producidos en interacciones de corrientes neutras pueden ser malinterpretados como electrones producidos por procesos de corrientes cargadas debidos a un ν_e incidente. La manera de distinguir entre los dos depende básicamente de los modelos teóricos implementados en los generadores Monte Carlo.

- La eficiencia de los detectores también depende de los modelos nucleares, porque está en gran medida basada en las predicciones de las distribuciones de partículas salientes, obtenidas a partir de distribuciones Monte Carlo.

Las incertidumbres sistemáticas en el detector lejano (que mide el espectro de neutrinos después de la posible oscilación) se pueden reducir parcialmente usando información del detector cercano. Su papel consiste en medir el flujo de neutrinos y las secciones eficaces, y a partir de ahí corregir y correlacionar las observaciones de ambos detectores. Aunque gracias a esto

se pueden disminuir los errores, no se cancelan totalmente (la eficacia de los detectores, el tipo de núcleo y el flujo de neutrinos son distintos en ambos casos), y los modelos de interacciones neutrino-núcleo siguen jugando un papel importante en el análisis de datos del detector lejano.

Formalismo

En el Capítulo 2 hemos introducido el formalismo empleado en esta Tesis. Hemos empezado por el Modelo Estándar que describe las interacciones fundamentales. En particular, hemos discutido en cierto detalle las interacciones de neutrinos con el sector de los quarks. En la teoría efectiva nuclear que describe la física de bajas energías, los grados de libertad relevantes son bariones y mesones, estados compuestos de quarks. Los mecanismos que exploramos en la Tesis involucran nucleones e hiperones. Su interacción cuasielástica (QE) con una prueba electrodébil se puede parametrizar en términos de seis factores de forma. Los factores de forma que aparecen en las transiciones $N \to N$ y $N \to Y$ se relacionan bajo el supuesto de simetría de sabor SU(3). Más adelante, cuando se consideran interacciones con núcleos, es necesario incluir efectos nucleares. El problema es difícil de resolver, con diversos mecanismos, cuya importancia cambia con el momento transferido al núcleo. El enfoque más básico, discutido en la Sec. 2.3.1, consiste en incluir sólo correlaciones estadísticas. En un sistema de fermiones a temperatura cero, de acuerdo con el principio de exclusión de Pauli, las partículas ocupan todos niveles energéticos hasta el nivel de Fermi. Además, utilizando la LDA (aproximación de densidad local), el nivel de Fermi se relaciona con el perfil de densidad, y se llega así al modelo LFG (*local Fermi gas*). Es un punto de partida para profundizar en los detalles del modelo teórico presentado en la Tesis.

En primer lugar hemos introducido algunas nociones básicas para describir la dinámica del nucleón en el medio nuclear. En particular, sus funciones de Green (y su modificación cuando se incluye la autoenergía en el medio) y su relación con las funciones espectrales (SF). A continuación se discute como la respuesta del sistema nuclear frente a una sonda electrodébil, para momentos transferidos suficientemente altos, se puede expresar en términos de funciones espectrales. En la última parte del Capítulo 2 introducimos otros efectos nucleares, como la resumación RPA (*Random Phase Approximation*) o la implementación del balance energético correcto, relevantes a bajas energías.

En el Capítulo 3 se estudia más en detalle las funciones espectrales. Siguiendo el mismo esquema que en el Capítulo 2, hemos tomado como punto de partida el modelo del gas de Fermi. Las funciones espectrales en este caso tienen simplemente forma de funciones paso, que representan una distribución plana para el momento de nucleón (el caso de LFG es un poco distinto porque el nivel de Fermi depende de la densidad del núcleo). En la Sec. 3.2 se discuten rasgos dinámicos fundamentales del modelo semi-fenomenológico desarrollado en la Ref. [2] para calcular la autoenergía del nucleón en el medio nuclear. Este método utiliza los datos experimentales de dispersión nucleón-nucleón (NN) para definir una interacción efectiva NN en el medio, que incluye correlaciones de corto y largo alcance (RPA). Como ha sido demostrado en las Refs. [3, 4, 5, 6, 7, 8, 9, 10], el modelo describe satisfactoriamente diversos procesos nucleares. Una de sus ventajas reside en el hecho de que se puede tratar dentro del mismo esquema, tanto a los nucleones iniciales como a los finales, y se puede aplicar para cualquier núcleo simétrico de isospín. A pesar de que el cálculo de la Ref. [2] se realizó utilizando aproximaciones no relativistas, después fue extendido al caso relativista en la Ref. [5]. Esta extensión se puede realizar gracias a que el elemento principal del modelo, la sección eficaz NN experimental, obviamente es consistente con un tratamiento relativista. También, hemos considerado la posibilidad de no incluir efectos nucleares en la función espectral de partícula para grandes transferencias de momento. A tal efecto es necesario fijar el origen absoluto de energías, incluyendo un término fenomenológico adicional, ajustando el valor experimental de la energía

de extracción (*removal energy*), utilizando las reglas de suma de D. Koltun discutidas en la Ref. [11].

El estudio de la interacción neutrino-núcleo, en el régimen cuasielástico, ha sido abordado desde distintos modelos teóricos. En la Sec. 3.3 hemos hecho un resumen de los más utilizados en el análisis de datos experimentales de dispersión de neutrinos, y en los generadores Monte Carlo. Así, en la Subsec. 3.3.1 nos hemos concentrado en el formalismo CBF [12, 13] basado en la aproximación de impulso (*Impulse Approximation*), que describe con éxito varias reacciones electrodébiles nucleares [14, 15, 16, 17, 18, 19]. En los Capítulos 5-7 hemos realizado diversas comparaciones utilizando este modelo y el derivado en la Ref. [2]. La función espectral de agujero en el modelo CBF está compuesta de dos partes. La dominante viene dada por cálculos obtenidos utilizando el modelo de capas, corregidos incluyendo factores espectroscópicos experimentales. Esta descripción de campo medio (*mean-field*, MF) no es adecuada para describir la parte de altas energías y momentos de la función de onda del nucleón. Esta contribución se considera utilizando un formalismo *ab initio* tipo *Correlated Basis Function* para materia nuclear simétrica, y se añade a la parte MF utilizando la LDA. Para incluir las interacciones de estados finales, se emplea otra estrategia, basada en la teoría general de Glauber que usa datos de transparencias nucleares y la parte real del potencial óptico NN, obtenido del ajuste de un potencial fenomenológico tipo Dirac a los datos experimentales.

Hemos considerado otros cuatro esquemas teóricos. El modelo GiBUU [20] está basado también en la LDA y utiliza un potencial fenomenológico (que depende de la densidad del medio y del momento de nucleón) obtenido de los estudios sobre reacciones de iones pesados. Este formalismo es relativista, permitiendo así una descripción consistente del estado inicial y final. El modelo SuSA (*Superscaling Approach*) [21] sigue otra idea. Empezando por las propiedades de escala (*scaling*) de la sección eficaz electrón-núcleo, es posible extraer una función universal de *scaling* de los datos experimentales, que no depende de forma separada de q^0, $|\vec{q}|$ (energía y momento transferidos al núcleo) sino que lo hace de una única variable construida a partir de ambas, y usarla para predecir reacciones neutrino-núcleo en el régimen QE. El grupo de Ghent ha desarrollado un formalismo MF usando un potencial Skyrme con parámetros ajustados a las excitaciones de bajas energías en núcleos esféricos [22]. El efecto de las correlaciones de largo alcance (RPA) está incluido usando la misma interacción residual. Por último, el modelo MECM [23], desarrollado inicialmente por el grupo de Lyon, también considera estas últimas correcciones utilizando una interacción efectiva residual tipo Landau-Migdal, similar a la discutida en la Sec. 2.5.2.

En el Capítulo 4 hemos empezado estudiando dos procesos inclusivos, descritos por el mecanismo de reacción QE, la captura muonica y la captura radioactiva de piones en núcleos. Estas reacciones involucran transferencias de energía-momento al núcleo muy pequeñas, y constituyen por tanto tests muy exigentes de la aplicabilidad del modelo de la Ref. [3] utilizado en esta tesis. Se observa que las SFs son responsables de la reducción del pico QE, extienden la magnitud de las funciones de respuesta hasta energías transferidas más altas y mueven la posición del pico en la misma dirección. El resultado general es una disminución de las anchuras integradas y cambios considerables de las distribuciones diferenciales. Los efectos tipo RPA en los observables integrados son significativamente más pequeños cuando las correcciones debidas al uso de SFs realistas están incluidas. Este patrón es muy diferente a lo que ocurre en el modelo del LFG, donde las correcciones inducidas por la resumación tipo RPA son muy importantes, de hasta un 40 %. Este interesante resultado fue mencionado ya en [3], y es debido al cambio de las relaciones de dispersión del nucleón en el medio nuclear. Además, este efecto está de acuerdo con los resultados de las Refs. [22, 24], donde se concluye que los efectos RPA en cálculos de MF son moderados para valores de Q^2 suficientemente grandes, fuera del régimen de excitación de las resonancias gigantes.

En líneas generales, los resultados obtenidos para procesos de energías bajas (incluyendo correcciones debidas a RPA y SF), presentados en el Capítulo 4, aunque sujetos a ciertos errores

teóricos (debido a las incertidumbres de los parámetros RPA y a posibles contribuciones de estados discretos), describen los datos experimentales con buena precisión, y proporcionan una mejora sobre la descripción que se obtiene en modelos donde sólo se considera el bloqueo de Pauli y el balance energético correcto de la reacción.

En la captura radiativa de piones hemos observado que el uso de SF realistas coloca el pico QE en una posición razonable y modifica de forma apreciable la distribución diferencial de la anchura de desintegración. Estos resultados son mucho más robustos que las predicciones obtenidas sólo con LFG o RPA. No obstante, la descripción está sujeta a incertidumbres inducidos por el espectro discreto de estados nucleares que no se incluye en el modelo. Para la captura muonica sólo disponemos de los datos de anchuras integradas. Nuestro modelo describe estos datos muy bien para varios núcleos simétricos de isospín. Estos resultados junto con los de las secciones eficaces inclusivas medidas por los detectores LSND, KARMEN y LAMPF en carbono cerca del umbral energético de la reacción, y que también están de acuerdo con las predicciones obtenidas incluyendo efectos nucleares del tipo SF+RPA, confirman la fiabilidad del marco teórico principal analizado en este trabajo.

La discusión anterior también proporciona una mayor veracidad para las predicciones obtenidas en esta tesis para energías intermedias de neutrinos, interesantes desde el punto de vista de los experimentos de oscilaciones y que se presentan a continuación. Calculamos en función de la energía los efectos nucleares tipo RPA y debido a SF para reacciones nucleares inclusivas inducidas por neutrinos y antineutrinos. Mostramos resultados para secciones eficaces totales y diferenciales y se presenta un análisis detallado de los incertidumbres teóricos de las predicciones. A continuación discutimos diferentes predicciones de los otros esquemas teóricos detallados en el Cápitulo 3 con los obtenidos con el modelo teórico utilizado previamente. Se analiza el origen de las diferencias y similitudes de los resultados, correlacionándoles con los elementos dinámicos que incluye cada modelo. También discutimos las razones σ_μ / σ_e en diversos núcleos y mostramos que las incertidumbres teóricas en las mismas están por debajo del 5 %.

Por último en este cápitulo, hemos realizado también una comparación exhaustiva de diversos modelos teóricos con los datos inclusivos de dispersión electrón-núcleo, en la región de momento-energía transferidos importantes para el experimento T2K. Todos los esquemas teóricos que hemos considerado LDA, CBF, GiBUU, proporcionan una descripción muy razonable de los datos. No obstante, para hacer una comparación más significativa, sería imprescindible incluir otros mecanismos que dan contribuciones a la sección eficaz en esta región cinemática, como por ejemplo la excitación de la resonancia $\Delta(1232)$ o contribuciones debidas a la excitación de dos partículas y dos agujeros (2p2h).

Propiedades de *scaling*

El Capítulo 5 está dedicado a estudiar las propiedades de *scaling* de la respuesta nuclear que se infiere de la densidad de nucleones, una magnitud muy importante para entender el *scaling* de las funciones de respuesta electromagnética longitudinal y transversal [25]. Hemos estudiado la respuesta asociada a la densidad de nucleones en ^{12}C en una región cinemática con grandes transferencias de momento y energía, donde se pueden ignorar modos colectivos de excitación nuclear. En el estudio hemos utilizado SF realistas obtenidas dentro de los esquemas CBF y LDA SF.

Hemos visto que los dos modelos producen funciones de *scaling* (de la densidad de nucleones) similares en ^{12}C, que se caracterizan por una forma asimétrica, aunque menos pronunciada que la obtenida de los datos experimentales. La CBF SF incluye una descripción más exacta del estado fundamental de ^{12}C, pero puede ser sólo utilizada para núcleos con capas cerradas

(*closed-shell*). Por otra parte, dentro del modelo LDA se puede ampliar a la descripción al núcleo de ^{40}Ar, que se va a emplear en el futuro detector del experimento DUNE [26].

Hemos también discutido un modelo simplificado para la dinámica nuclear, que retiene los aspectos principales del problema de muchos cuerpos, para analizar el origen dinámico del *scaling* de primer tipo exhibido por la función de respuesta de la densidad de nucleones. Hemos argumentado que su forma asimétrica se debe principalmente a la dinámica asociada con la excitación del tipo $2p1h$ incorporada en la componente del continuo de la SF de agujero derivada en la Ref. [27], que a su vez está íntimamente relacionada con las correlaciones NN de corto alcance. En el modelo semi-fenomenológico de la Ref. [2], este efecto se incluye a través de la parte imaginaria de la autoenergía del agujero, ImΣ. En este último modelo se encuentra también una apreciable reducción de ImΣ, debida a los efectos de polarización, en la región de bajos momentos y energías del nucleón. Sin embargo, las correcciones de RPA producen pequeñas modificaciones en las componentes de alto momento, responsables de la asimetría. Por otra parte, la asimetría se ve solo suavemente aumentada por los efectos de interacción de estados finales (FSI). Estas correcciones, relevantes sobre todo en la región de bajos momentos transferidos, producen un desplazamiento del pico hacia valores más bajos de ψ'^{nr} (una función de q^0 y $|\vec{q}|$) y una redistribución del espectro hacia valores mayores de ψ'^{nr}. De acuerdo con los estudios de *relativistic mean-field* (RMF) llevados a cabo en la Ref. [28], la asimetría de la función de *scaling* se atribuye a un aumento dinámico de las componentes pequeñas de los espinores de Dirac, que no están presentes en la función de respuesta no relativista. Sin embargo, en este estudio y de forma análoga a los resultados de GFMC (*Green Function MC*) de la Ref. [25], observamos la asimetría usando un modelo no relativista para las funciones espectrales de partícula y agujero. Nuestros resultados no están en contradicción con la visión de *scaling* en RMF. La hipótesis es que algunas correlaciones pueden tener su origen en la reducción no relativista realizada a nivel de MF. La corroboración de esta hipótesis requiere un estudio más detallado.

En el ámbito del formalismo de SF, encontramos que, una vez se divide por los prefactores que describen los vértices de interacción con un nucleón, las respuestas electromagnéticas longitudinal y transversal dan lugar a la misma función, que está íntimamente conectada con la respuesta asociada a la densidad de nucleones. Las pequeñas diferencias existentes se deben a las discrepancias entre los prefactores calculados para un gas de Fermi o con SF realistas. Por lo tanto, además de corrientes de dos cuerpos y efectos colectivos, la ruptura del *scaling* de tipos cero y uno hay que atribuirla a las deficiencias del modelo nuclear usado para estimar los elementos de transición del nucleón inmerso en el medio nuclear.

Producción de hiperones

En el Capítulo 6 hemos estudiado la producción débil de hiperones Λ y Σ en la dispersión de $\bar{\nu}_\mu$ por núcleos. Hemos prestado especial atención a los efectos nucleares resultantes del uso de SFs de agujero realistas. Como en otras partes de esta tesis, para describir las correlaciones del estado inicial, hemos empleado dos modelos de la función espectral de agujero. Por otra parte la propagación de hiperones en el medio nuclear ha sido aproximada por una cascada Monte Carlo (MCC), que trata al movimiento de los hiperones de manera clásica. La MCC no cambia la sección eficaz inclusiva ($\bar{\nu}_l, l^{\pm}Y$), si se considera la suma de canales $Y = \Lambda$, Σ^0, Σ^- y Σ^+. Sin embargo los efectos producidos por la MCC son claramente visibles en procesos exclusivos, como el espectro energético o las distribuciones angulares de los hiperones salientes. Por ejemplo, a pesar de que el Σ^+ no se produce en el vértice de interacción débil, las colisiones secundarias son responsables de su producción. Por supuesto, cuando se suman todos los posibles canales, se recupera la sección eficaz inclusiva, como ya hemos mencionado

Los resultados obtenidos con el modelo semi-fenomenológico LDA SF [2] y el esquema CBF SF [29, 27] coinciden bastante bien, y así proporcionan una estimación robusta de la importancia de correlaciones dinámicas del estado nuclear inicial, que no se consideraron en el trabajo de Ref. [30], basado en el modelo LFG. En este cápitulo discutimos también cómo las secciones eficaces inclusivas doble diferenciales $d^2\sigma/(d\cos\theta dq^0)$, [$\theta$ es el ángulo de dispersión del leptón cargado saliente] están afectadas por las correlaciones presentes en la función espectral de agujero, que causan una reducción del pico QE y una redistribución hacia la región de energías transferidas más altas. En el caso de la distribución $d\sigma/dq^2$ y la sección eficaz total, los efectos de utilizar una SF realista no son tan importantes como para el caso de $d^2\sigma/(d\cos\theta dq^0)$, y menores que los producidos por la FSI del hiperón en su camino de salida del núcleo. La MCC modifica de forma significativa los resultados obtenidos con la aproximación de impulso para procesos exclusivos, dando lugar a una sección eficaz no nula para Σ^+, a un aumento de la producción de hiperones Λ y a una reducción drástica de Σ^- y Σ^0 en el estado final.

Hay que mencionar que los efectos de la MCC obtenidos en nuestro cálculo son mucho más visibles que los reflejados en la Ref. [30]. Esto se debe a una implementación imprecisa, en este último trabajo, del bloqueo de Pauli para los nucleones salientes producidos en interacciones secundarias, que llevaron a una reducción importante del número de colisiones experimentadas por los hiperones durante su trayectoria por el núcleo.

Motivados por las recientes mediciones de la colaboración BESIII de las anchuras parciales de la desintegración $\Lambda_c \to \Lambda\ell^\pm\nu_\ell$ ($\ell = e, \nu$), y por los resultados de CHORUS para la razón de la sección eficaz de producción de Λ_c en la dispersión CC neutrino-núcleo, hemos calculado también en este cápitulo la producción débil de Λ_c en ^{16}O. Hemos estimado cuidadosamente las incertidumbres teóricas que afectan al elemento de matriz $n \to \Lambda_c$. Para tal fin, hemos utilizado factores de forma calculados en diversos esquemas teóricos, empezando por los resultados de QCD en el retículo (LQCD) de la Ref. [31], hasta usar los modelos quark relativista y no relativista de las Refs. [32, 33, 34, 35]. Hay que señalar que mientras que para las transiciones $N \to \Lambda$, Σ^0, Σ^- las predicciones teóricas son consistentes con los datos experimentales a nivel de nucleón, en el caso de la producción de Λ_c la incertidumbre más relevante está relacionada con diferentes parametrizaciones de los factores de forma. Por eso no hemos tenido en cuenta efectos nucleares más allá de los incluidos en modelo de gas de Fermi, porque su inclusión introduciría errores teóricos adicionales (el comportamiento de Λ_c en el medio nuclear no es bien conocido). También es probable que las correcciones provenientes de estos efectos nucleares sean más pequeñas que las discrepancias producidas por el uso de los diversos conjuntos de factores de forma. Encontramos una variación significativa entre las predicciones obtenidas con los diferentes modelos, a pesar de que todos estén constreñidos por el valor experimental de la anchura de desintegración $\Lambda_c \to \Lambda e^+\nu_e$. Es una consecuencia directa de la ambigüedad inevitable inducida por la extrapolación de los factores de forma desde la región de q^2 relevante para la desintegración del barión encantado Λ_c hasta la cinemática que gobierna su producción en reacciones inducidas por neutrinos. Hemos estimado no obstante, que las incertidumbres teóricas están por debajo del 30 % para $E_\nu \lesssim 3{,}5$ GeV. Para las energías de neutrino correspondientes a los flujos de MINERvA y DUNE, predecimos secciones eficaces – normalizadas al número de neutrones – de $\sigma(E_\nu = 3\,\text{GeV})/N = (0{,}9^{+0{,}2}_{-0{,}1}) \times 10^{-40}\text{cm}^2$ y $\sigma(E_\nu = 5\,\text{GeV})/N = (4{,}5^{+2{,}0}_{-0{,}9}) \times 10^{-40}\text{cm}^2$, respectivamente. Como hemos mencionado, por simplicidad en este análisis preliminar, no hemos incluido correlaciones dinámicas del estado inicial, ni efectos de FSI.

Observables de polarización en producción de lepton τ

En la última parte de la tesis hemos estudiado la polarización del leptón τ saliente en el proceso de corrientes cargadas inducido por (anti)neutrinos en núcleos (el análisis está hecho para ^{16}O y considerando sólo el mecanismo cuasielástico). Desde el punto de vista teórico, la dispersión de $\nu_\tau/\bar{\nu}_\tau$ por núcleos posibilita un estudio más amplio del papel que juegan las correlaciones nucleares del estado fundamental en la descripción de la interacción neutrino-núcleo. La masa de los leptones de $\tau^\pm$, mucho más pesada que la de los leptones $\mu^\pm$ y $e^\pm$, permite acceder a detalles de la respuesta nuclear no explorados con la interacción electrón-núcleo o $\nu_{e,\mu}$-núcleo. Hay en total cinco funciones de estructura necesarias para la descripción del tensor hadrónico en la dispersión neutrino-núcleo. Las reacciones inducidas por ν_μ y ν_e son principalmente sensibles sólo a tres de ellas, mientras que las contribuciones de las otras dos están suprimidas por las masas pequeñas de $\mu^\pm$ y $e^\pm$.

Los componentes de polarización longitudinal y transversal del τ saliente son observables interesantes desde el punto de vista experimental y teórico. Como ya hemos mencionado, ofrecen una visión más profunda de las propiedades del tensor hadrónico, ya que son sensibles a varias combinaciones de funciones de estructura. Para obtener una descripción realista de la dinámica nuclear, incluyendo correlaciones NN, hemos utilizado también en este contexto las funciones espectrales LDA y CBF, derivadas en las Refs. [2] y [29, 27]. Estas SF son realistas y como ya hemos puesto de manifiesto predicen respuestas nucleares inclusivas, en la región del pico QE, en buen acuerdo con medidas experimentales para reacciones inducidas por neutrinos y electrones. Debemos mencionar en este contexto, que el uso de funciones espectrales de agujero es considerablemente más realista que la utilización de masas efectivas para el nucleón en la descripción del estado inicial, como se hizo en el estudio previo de la Ref. [36]. Utilizar una masa efectiva constante, es sólo una aproximación a los efectos producidos por el cambio de la relación de dispersión del nucleón en el medio nuclear.

Para cada uno de los modelos, CBF y LDA, hemos usado una prescripción ligeramente distinta en el cálculo del elemento de matriz de la corriente entre nucleones en el medio nuclear. La ambigüedad viene del hecho de que el nucleón que sufre la interacción con el bosón de gauge $W^\pm$ está fuera de la capa de masas, con una distribución de energía-momento determinada por la SF. En el caso del modelo CBF, el nucleón inicial se asume que está en la capa de masas pero con la distribución de momentos de la SF. La distribución de energía de la SF se utiliza para corregir la energía transferida. El modelo LDA trata al nucleón inicial fuera de la capa de masas con energía y momento determinado por la función espectral de agujero. No obstante, sigue existiendo una ambigüedad porque el elemento de matriz a nivel de nucleón (incluyendo la suma sobre espines) está calculado asumiendo nucleones en capa de masas. Los resultados para los ángulos hacia delante dependen mucho de la prescripción, que afecta a las secciones eficaces y a las componentes de polarización. Sin embargo, las discrepancias se hacen muy pequeñas ya para ángulos de 4°. Hemos mostrado que los efectos nucleares presentes en las funciones espectrales son considerables en el caso de distribuciones diferenciales, produciendo una reducción del pico QE y un desplazamiento hacia las energías transferidas más altas, como en casos anteriores. Los efectos nucleares son menos importantes para las componentes de polarización, porque estas se obtienen como un cociente de términos proporcionales al tensor hadrónico, y se producen cancelaciones importantes de los efectos nucleares.

Chapter 1

Introduction

Neutrinos play a crucial role in the history of particle physics. Their existence and physical properties were proposed and discussed by theoretical physicists; confirmed or rejected by a series of experiments, which have become increasingly complex and nowadays are conducted by extended international collaborations. The evidence of this turbulent, though fruitful history, are four Nobel Prizes received in the span of the last 50 years.

The prehistory of neutrino physics began over a century ago, with the discovery of radioactivity. In 1914, J. Chadwick observed that the β-decay with one outgoing electron (as the process was understood at that time) has a continuous energy spectrum while the final state with just two particles should restrict the electron energy to a single well-defined value. In 1927, Ellis and Wooster repeated the experiment measuring the energy loss in Radium to Polonium decay and confirmed the previous results.

A quest of explaining this queer observation began, leading Niels Bohr as far as to propose that the energy is conserved in a statistical way, but not in every process. W. Pauli was looking for another solution to this puzzle, such that the fundamental law of energy conservation was saved. In 1930, (rather timidly) he suggested that an unknown, neutral, spin 1/2 and very light particle was produced in the process, leaving the scene undetected. He called this particle a neutron, which a few years later was renamed by E. Fermi to "neutrino" - after Chadwick discovered a particle we call neutron nowadays.

This hypothesis was at first received rather reluctantly, since it could not be experimentally confirmed. Nevertheless, Pauli's ideas had strong supporters and few years later (1933) E. Fermi developed a theory of four-fermion Hamiltonian to describe β-decay process:

$$\mathscr{H} = G_F \, \bar{p} \gamma^{\mu} n \, \bar{e} \gamma_{\mu} \nu + \text{ h.c.} \tag{1.1}$$

with G_F known nowadays as the Fermi constant. This theory was universal, since it described all the processes for which four fermions interact (proton, neutron, electron, neutrino and/or their antiparticles). The coupling G_F governs the strength of all these processes, among them $\bar{\nu} + p \to n + e^+$ interaction. It seemed that the cross section for antineutrino interaction with proton was so small that it would be technically impossible ever to measure it [37]. This conclusion, driven by H. Bethe and R. Peierls from Fermi's theory, was challenged almost 10 years later by B. Pontecorvo. In 1946 he proposed an experiment of inverse β-process with a powerful source of neutrinos, like the Sun or a nuclear reactor. Ten years later, this idea served for the first neutrino detection in the experiment by C. Cowan and F. Reines (who received a Nobel Prize in 1995).

These first steps both in experimental and theoretical neutrino physics were just the beginning of a long history. They opened doors to further investigations, which have expanded greatly in the 20th and 21st century, along with other developments in various branches of particle physics. Neutrinos were found to be left-handed particles (and therefore they do not conserve parity, one of the three fundamental discrete symmetries together with time reversal

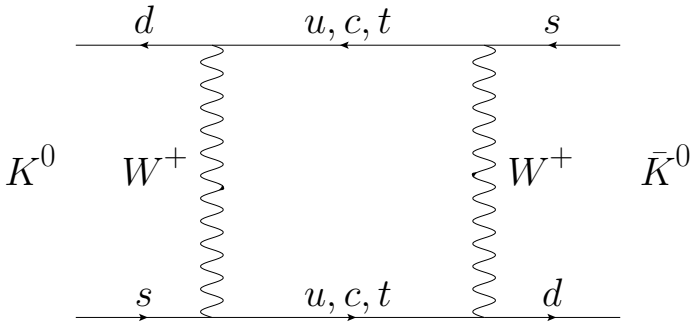

FIGURE 1.1: $K^0 \rightleftharpoons \bar{K}^0$ mixing through W^+ boson exchange. Weak interactions do not conserve strangeness.

and charge conjugation). The distinction between electron and muon neutrinos was experimentally confirmed in 1962. In the 1960s Glashow, Weinberg and Salam proposed the Standard Model (SM) to unify electromagnetic and weak interactions through the symmetry breaking of the pattern $\mathrm{SU(2)_L \times U(1)_Y \to U(1)_{EM}}$. This theory was a milestone for particle physics. Neutrinos were included into the SM, along with other known fermions: charged leptons and quarks. Their properties are unique, in comparison to the latter mentioned particles, since they appear only as the left-handed helicity states. According to the SM, neutrinos are massless. This theoretical assumption, however, was experimentally rejected in 1998 by the SuperKamiokande experiment. It is the only strong hint about physics beyond the SM that we are aware of nowadays. This observation belongs to a separate chapter of neutrino's history - their peculiar feature which nowadays we know as neutrino oscillations.

1.1 Neutrino oscillations

The idea of neutrino oscillations was proposed by B. Pontecorvo already in the late 1950s, taking inspiration from the work of Gell-Mann and Pais [38] on $K^0 \rightleftharpoons \bar{K}^0$ oscillations. Neutral kaons K^0 and $\bar{K}^0$ have opposite strangeness number (± 1) and are produced in strong interaction processes: $\pi^- + p \to K^0 + \Lambda$ and $\pi^+ + p \to K^+ + \bar{K}^0 + p$. The strong force conserves strangeness, so both kaons are indistinguishable if the weak interactions are turned off. However, while propagating, neutral kaons can change their identity through the weak processes which do not conserve strangeness. We understand this process nowadays as shown in the Feynman diagram depicted in Fig. 1.1.

Pontecorvo considered a similar mixing mechanism between ν and $\bar{\nu}$ states. Let us recall, that at that time only one neutrino flavour was known. Ten years later, an experiment in Brookhaven [39] confirmed that (at least) two types of neutrino exist in Nature, ν_e and ν_μ. Pontecorvo explored the possibilities of various transitions between them (and their antiparticles). In the same paper [40] he pointed out that the Sun is an excellent source of neutrinos.

Theory of neutrino oscillations is based on the assumption that flavour states are not mass eigenstates. In the following we will assume that only three flavours of neutrinos exist. [1] The two bases can be related by a complex rotation, represented by a unitary 3×3 matrix U:

$$|\nu_\alpha\rangle = \sum_i U^*_{\alpha i} |\nu_i\rangle\,, \quad i = 1,2,3\,, \quad \alpha = e,\mu,\tau\,. \tag{1.2}$$

It is called the Pontecorvo–Maki–Nakagawa–Sakata (PMNS) matrix, and is an analog to the Cabibbo–Kobayashi–Maskawa (CKM) matrix which describes quark mixing in the SM. The

[1] We do not consider sterile neutrinos or any other extension to the SM. Their existence would change the exposed analysis of neutrino mixing, introducing some additional parameters.

matrix is conventionally parametrized by three angles (θ_{12}, θ_{13}, θ_{23}) and one phase δ (there are additional two phases if neutrinos are Majorana particles which are not included below since they do not influence the oscillation analyses):

$$U = \begin{pmatrix} 1 & 0 & 0 \\ 0 & c_{23} & s_{23} \\ 0 & -s_{23} & c_{23} \end{pmatrix} \begin{pmatrix} c_{13} & 0 & s_{13}e^{-i\delta} \\ 0 & 1 & 0 \\ -s_{13}e^{i\delta} & 0 & c_{13} \end{pmatrix} \begin{pmatrix} c_{12} & s_{12} & 0 \\ -s_{12} & c_{12} & 0 \\ 0 & 0 & 1 \end{pmatrix}$$
$$= \begin{pmatrix} c_{12}c_{13} & s_{12}c_{13} & s_{13}e^{-i\delta} \\ -s_{12}c_{23} - c_{12}s_{23}s_{13}e^{i\delta} & c_{12}c_{23} - s_{12}s_{23}s_{13}e^{i\delta} & s_{23}c_{13} \\ s_{12}s_{23} - c_{12}c_{23}s_{13}e^{i\delta} & -c_{12}s_{23} - s_{12}c_{23}s_{13}e^{i\delta} & c_{23}c_{13} \end{pmatrix} \tag{1.3}$$

with $s_{ij} \equiv \sin\theta_{ij}$ and $c_{ij} \equiv \cos\theta_{ij}$. The goal of oscillation experiments is to determine the parameters of the PMNS matrix by measuring probabilities of (dis)appearance of neutrinos of a given flavour. Let us consider the propagation of free neutrinos:

$$|\nu_i(t)\rangle = e^{-i(E_i t - \vec{p}_i\vec{x})}|\nu_i(0)\rangle\,. \tag{1.4}$$

Neutrinos, nearly massless, can be safely treated as ultrarelativistic particles: $E_i = \sqrt{p^2 + m_i^2} \approx E + \frac{m_i^2}{2E}$ with $E = p$. Since their velocity $v \approx c$, we have also $t \approx L$, with L – the distance they travel in time t ($c = 1$). With all of this, we get

$$|\nu_i(L)\rangle = e^{-im_i^2 L/2E}|\nu_i(0)\rangle \tag{1.5}$$

Neutrinos are produced and detected in electroweak processes, in which they have a determined weak lepton flavour. Between the source and the detector, they propagate as free particles according to Eq. (1.5). Each mass eigenstate propagates differently (due to the mass splitting) leading to a non-zero probability of finding a distinct neutrino flavour after travelling a distance L:

$$\mathscr{P}(\alpha \to \beta) = |\langle \nu_\beta(L)|\nu_\alpha(0)\rangle|^2 = \Big|\sum_i U_{\alpha i}^* U_{\beta i} e^{-im_i^2 L/2E}\Big|^2 \tag{1.6}$$

Therefore, oscillations can only occur if the mass splitting is different from 0, so at least one of neutrinos has to be massive.

In a simple case of two flavour mixing, $U_{2\times2}$ is a rotation matrix with just one parameter, the angle θ:

$$U_{2\times2} = \begin{pmatrix} \cos\theta & \sin\theta \\ -\sin\theta & \cos\theta \end{pmatrix} \tag{1.7}$$

The probability of detecting neutrino flavour β if the source produces ν_α (with $\alpha \neq \beta$) is given by

$$\mathscr{P}_{\alpha\to\beta} = \sin^2(2\theta)\sin^2\big(\frac{\Delta m^2 L}{4E}\big)\,. \tag{1.8}$$

Since the aim of experiments is the determination of the unknown parameters of the model (in this simplified situation there are only two: θ and Δm^2), one needs to measure the probability $\mathscr{P}_{\alpha\to\beta}$, for different values of E or/and L.

A huge effort has been devoted to determine the unknown parameters of Eq. (1.3). They are fitted using global analysis of the results obtained from various oscillation experiments sensitive to different combinations of the PMNS matrix parameters and mass splittings. The sensitivity depends on the interplay between neutrino energies, source-detector distances, and neutrino flavours (both produced and detected).

The recent discussion in Ref. [1] indicates that there are three main challenges in this field. The most demanding one is to determine whether (and to what extent) the lepton sector breaks

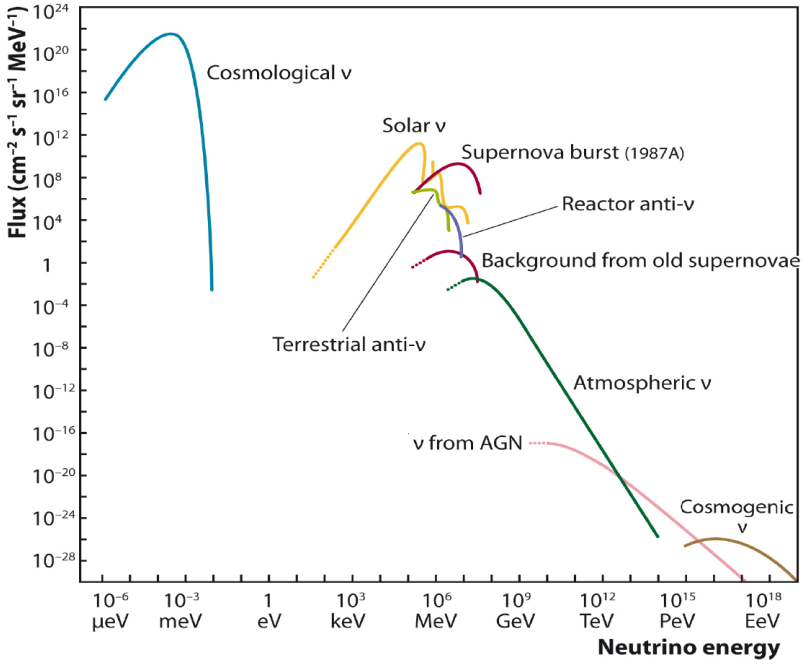

FIGURE 1.2: Flux of neutrinos from various sources as a function of their energy [41].

CP (charge conjugation and parity symmetry). The strength of the CP violation is driven by the phase δ in Eq. (1.6). The other two challenges are to improve our knowledge of the value of θ_{23} and establish the neutrino mass ordering (normal or inverted, *i.e.* what is the order of the eigenstates $m_3 > m_2 > m_1$ or $m_2 > m_1 > m_3$). The latter information can be determined in oscillation experiments when the matter effects in Earth are taken into account.

One of the fundamental reasons why neutrino oscillation experiments are so demanding, is the fact that neutrinos interact weakly. The cross-sections are many orders of magnitudes smaller than the ones obtained in electromagnetic processes. Since neutrinos cannot be directly detected, their properties can be inferred only through analyses of their interactions with the nuclei that form the detectors.

1.2 Neutrino experiments

Since the time of the first experiment of neutrino detection in 1956 by Cowan and Reines, a lot has been explored about neutrino properties. Our current knowledge about the natural sources of neutrinos observed on Earth is shown in Fig. 1.2. Neutrinos, along with photons, are the most abundant particles in the Universe. The cosmic neutrino background is a reminiscence of the Big-Bang, a fingerprint of the very beginning of the Universe. Cosmic neutrinos being far the most abundant source, are also the lowest energetic ones (with the mean energy ~ 0.1 MeV), making their detection extremely demanding and not yet achieved. However, the study of the cosmic microwave background has given an upper limit on the sum of neutrino masses (an information which cannot be inferred from oscillation analyses which are sensitive to squared neutrino mass differences).

Further, in Fig. 1.2 we see that the Sun is the next leading source of (electron) neutrinos measured on Earth. In 1968, the Homestake experiment [42] observed for the first time a deficit of solar neutrinos with respect to the predictions of solar models (it could detect only ν_e, while ν_μ flew through undetected). This puzzle, called the solar neutrino problem, was later confirmed by the Kamiokande detector [43], and the GALLEX [44, 45] and SAGE [46] experiments which – to corroborate the result – used different detection methods. Finally, the Sudbury Neutrino

Observatory (SNO) in 2001 measured the total flux of incoming neutrinos which agreed with the predictions of solar models, and confirmed the electron neutrino disappearance [47]. Solar neutrino experiments are sensitive to the θ_{12} angle. Together with KamLand [48] (which detected antineutrinos from reactor sources of a similar energy range to the solar neutrinos), these experiments were able to give estimates for θ_{12} and Δm^2_{12}.

Few years before SNO results, in 1998, SuperKamiokande finally confirmed the theory of neutrino oscillations, measuring the appearance of electron neutrinos, $\nu_\mu \to \nu_e$, produced in the atmosphere [49]. When cosmic-rays (mostly protons) interact with nuclei in the high altitude atmosphere, they produce π and K mesons. Subsequently they decay, producing neutrinos. In particular, π^+ decays predominantly to μ^+ and ν_μ. Since μ^+ is also unstable, it decays further $\mu^+ \to e^+ + \nu_e + \bar{\nu}_\mu$. For neutrino energies < 1 GeV, the ratio of muon to electron (anti)neutrinos is to good approximation known to be equal to two. The neutrino oscillation experiment at Kamioka measured neutrinos coming from all directions, which means that they travelled different distances until reaching the detector. This zenith-angular dependence gave a clear signal of neutrino oscillations (a change of the ν_μ / ν_e ratio) and put constraints on the θ_{23} and Δm^2_{23} parameters. Later, this result has been confirmed by other experiments with higher precision (MINOS [50], T2K [51]). The next generation of atmospheric neutrino experiments (PINGU [52], ORCA [53], Hyper-Kamiokande [54]) will focus its effort on determining the mass ordering.

The two mixing angles measured for solar and atmospheric neutrinos appeared to be large (which is opposite to the situation in the quark sector where the mixing angles of the CKM matrix are small). The third angle θ_{13} was determined by the reactor experiments Daya Bay [55], Double Chooz [56] and RENO [57].

Apart from natural sources of neutrinos, an effective way to produce an intense neutrino beam is to use proton accelerators. This is done in J-PARC (Japan), CERN (Switzerland) and Fermi National Lab (USA). These three facilities produce neutrinos which are then detected in short-baseline (the distance from the source is of the order of few hundred meters) and long-baseline (distances are now of the order of hundreds of kilometers) experiments, and their energy is in the range of hundreds of MeV or few GeV. These neutrino beams are used to perform precise measurements of the PMNS matrix and neutrino mass differences. In the near future, the scientific program of the long-baseline experiments will be focused especially on the determination of the CP violating phase. It is an observable very difficult to measure, which requires not only a highly precision experiments, but also a detailed knowledge of other oscillation parameters. DUNE [58, 26] and T2HK [59] experiments, which both will start operating in 2026, are designed to perform this measurement by observing both $\nu_\mu \to \nu_e$ and $\bar{\nu}_\mu \to \bar{\nu}_e$ disappearance processes. They follow two complementary approaches. T2HK will use a water Cherenkov detector placed at 295 km from the source which corresponds to the position of the first oscillation maximum for the neutrino energy beam peaking at ~ 0.5 GeV. DUNE, with a much longer baseline of 1300 km, has a broader and higher energetic flux to cover the first and the second oscillation maxima. One of the challenges of this measurement is the fact that both CP violation and the matter effects inside the Earth affect the shape of the $\mathscr{P}_{\alpha\to\beta}$ probability distribution. Moreover, their strengths are of comparable size. Depending on the mass hierarchy, the combined effect is either very strong, or it partially cancels. DUNE is designed to discern both the mass ordering and estimate the CP violating phase, since it will have access to two oscillation maxima.

As a final remark, we would like to mention that the neutrino studies do not concentrate only on the oscillation analysis (which comprises also searches of physics beyond the three-flavour scenario). Neutrino, thanks to its weak interactions, can travel cosmic distances with practically no distortion. This feature opens many opportunities of observing physical phenomena or studying astrophysical objects which could not be explored with other elementary particles. In supernovae explosions, 99% of the gravitational energy is released through an outburst of

neutrinos, which escape faster than any other particles. From the last detected supernova explosion 1987A, over 30 years ago in the Large Magellanic Cloud, 25 neutrino events were detected by three experiments on Earth. This information was used to constrain our knowledge on both neutrino properties and astrophysical processes (like the mechanisms responsible for the explosion of massive stars) [60]. Quite recently we have entered the era of multi-messenger astrophysics, in which combined information from gravitational waves, neutrinos and gamma rays is available.

1.3 Challenges in neutrino detection

The greatest challenge of the experiments which plan to measure the CP violating phase, is the control of uncertainties. They should not exceed few percent to obtain the required precision. T2HK and DUNE are designed to keep the statistical error at the level of $\sim 3\%$. This precision is unprecedented in the neutrino long baseline experiments which – especially for the antineutrino mode – usually exceeded 10%. Therefore, the control of systematic uncertainties will become a major issue since they should not be larger than a few percent. At the current running experiments, T2K and NOvA, the reported values are in the range of $3-10\%$. There are various sources of systematic errors. Among them, there are uncertainties which arise due to the imperfect flux determination, not fully understood detector response or imprecise modeling of neutrino-nucleus interactions. In the following we will focus on the latter problem, being the main motivation for our studies. The theory of neutrino-nucleus interactions enters the analysis of oscillation parameters in a non trivial way. It affects the experimental studies on various stages and the fact that the neutrino beams are not monochromatic poses further difficulties. In order to mark the most important issues, let us start with a general expression for the event rate for oscillation $\nu_\alpha \to \nu_\beta$ (for a given event topology). Following the discussion of Ref. [1], one can express it as:

$$N_{\alpha\to\beta}(p_{\text{reco}}) = \sum_i \phi_\alpha(E_{\text{real}}) \times \mathscr{P}_{\alpha\to\beta}(E_{\text{real}}) \times \sigma_\beta^i(p_{\text{real}}) \times \varepsilon_\alpha(p_{\text{real}}) \times R_i(p_{\text{real}}; p_{\text{reco}}) \quad (1.9)$$

with p_{reco} and p_{real} being neutrino reconstructed and real momenta, respectively. The sum is done over i - all the possible interactions, which can lead to an observed event topology. Besides, $\phi_\alpha(E_{\text{real}})$ is a flux of incoming neutrinos of a flavour α, $\mathscr{P}_{\alpha\to\beta}(E_{\text{real}})$ is the probability of oscillation, $\sigma_\beta^i(p_{\text{real}})$ is the total cross section for interaction channel i, $\varepsilon_\alpha(p_{\text{real}})$ is the detector efficiency and $R_i(p_{\text{real}}; p_{\text{reco}})$ is the probability of reconstruction of p_{real} as p_{reco} in the case of reaction mechanism i.

As can be noted, the functions on the right hand side of Eq. (1.9) depend on the real neutrino energy-momentum, while the event rate $N_{\alpha\to\beta}$ is a function of reconstructed energy. The energy of the neutrino for a particular event is not known, since the accelerator neutrinos are produced in a flux with a width of the order of a few hundred MeV or even GeV. It could be precisely reconstructed if the detector was able to measure all the outgoing particles. However, this is far from being true. Detection of every event has its limitations: it is insensitive to the particles below a certain threshold, or neutral particles, or those which are not contained in the fiducial volume of the detector. The details of the reconstruction analysis depend on the specific experimental technique which is used. Water Cherenkov detectors (*e.g.* HyperKamiokande) are sensitive only to the radiation of particles above a certain threshold. In the case of the T2K experiment (and this will be also inherited by T2HK) the energy is reconstructed assuming knowledge about the interaction that took place (*i.e.* the presumption about the initial and final hadrons), using as an input the measured outgoing lepton energy-momentum. This so-called kinematical method has a clear shortcoming. In the case when there are many possible interaction channels leading to the same observed topology, the method does not discern between them

and might reconstruct the energy wrongly assuming a process different from the one which actually took place. Another approach is used in liquid argon detectors (*e.g.* DUNE), in which the energy deposition of the outgoing particles is measured, and therefore they are sensitive to the hadrons produced in each interaction. Using this knowledge and energy conservation, the energy of the incoming neutrino can be estimated. However, this procedure, known as calorimetric method, also has its deficiencies. It requires a precise identification of the produced hadrons, which is not always possible; especially for neutral particles which may leave the detector without being observed. This poses a serious threat since the undetected low energetic neutrons or pions drastically influence the result of the analysis. In both kinematical and calorimetric methods, it is therefore indispensable to support the analysis with a precise knowledge about neutrino-nucleus interactions (not only providing the total cross sections but also exclusive observables, like outgoing particles distributions).

Furthermore, the sum over i in Eq. (1.9) should be done over all the interactions which lead to the same observed topology. Let us notice, that the success of the correct prediction depends strongly on whether all the physical processes are taken into account. An omission of any mechanism (which gives a substantial contribution) can bias the analysis. Usually, there are several possible contributions. A strategy for their acceptance depends on every experiment. For instance, T2K selects CC0π events (no pion in the final state and any number of nucleons). This, however, does not mean that pions have not been produced in the primary vertex, since they can be reabsorbed on their way through the nucleus. It should be noted that measurements are additionally distorted by the presence of backgrounds. As mentioned, some processes can mimic others: *e.g.* in large Cherenkov tanks, photons from π^0s produced in neutral current interactions can be misinterpreted as electrons produced in charge current processes. In these cases our ability to discern between the two situations depends on our knowledge of the neutrino-nucleus interactions encoded into the Monte Carlo event generators. In some cases the background gives a substantial contribution and should be kept well under control.

Lastly, the determination of the detectors efficiency is also affected by uncertainties coming from the modeling of the neutrino-nucleus interactions, since it is based on the Monte Carlo predictions of the distribution of outgoing particles in the detector.

Systematic uncertainties partially cancel if both near and far detectors are used. In the near detector no oscillation $\alpha \to \beta$ takes place, and therefore the expression for the event rate in Eq. (1.9) has a simpler form. One might expect that some systematic errors of measurements done in the two detectors are correlated and therefore data taken from the near detector can be used to obtain higher precision in the far detector. To a large extent this is true. Nevertheless, the errors do not cancel exactly (*e.g.* if the material of the detectors is different) and the analysis is very challenging.

The theoretical input from neutrino-nucleus interactions enters the analysis of experimental data through the Monte Carlo (MC) event generators. They should contain reliable models for neutrino-nucleus interactions, and thus be able to simulate the "real" events, which – statistically – coincide with the experimental observations. A great majority of neutrino-nucleus scattering studies is focused on serving oscillation experiments to better understand the nuclear responses. Some of them are directly implemented in the MC generators.

1.4 Outline

Apart from a strong motivation coming from the experimental studies, neutrino-nucleus scattering is also an interesting topic for nuclear physics. Neutrino cross sections incorporate richer information than electron-scattering ones, providing an excellent testing ground for nuclear structure, many-body mechanisms and reaction models. In addition, neutrino cross section measurements allow to investigate the axial structure of the nucleon and baryon resonances,

enlarging the views of hadron structure beyond what is presently known from experiments with hadronic and electromagnetic probes. Thus, and besides the large activity in the last 15 years, a new wave of neutrino-nucleus theoretical works and detailed analysis have recently become available [14, 61, 62, 63, 64, 65, 66, 67, 68, 19].

In this Thesis we will focus our investigation on neutrino and antineutrino scattering on nuclei without pions produced in the primary vertex of the interaction. When in this first step the gauge boson interacts with only one nucleon, it is the so-called quasielastic mechanism (QE). It is a fundamental detection channel for long-baseline neutrino experiments, such as T2K, MINOS, NOvA and the future DUNE and T2HK. At intermediate energies, a microscopical description of the interaction of neutrinos with nuclei (which form part of the detectors), should at least account for three distinctive nuclear corrections, in addition to the well-established Pauli-blocking effects. These are in-medium nucleon dispersion relation, long-range collective RPA[2] effects, and gauge boson multinucleon absorption modes.

We will focus on the first one (also investigating its interplay with RPA), since we will study processes mostly governed by one-body mechanisms when a single nucleon is produced. We shall also investigate the case when the final state is a strange or charm baryon, however these processes are much suppressed and play a lesser role in the experimental analysis. There exists an abundant literature addressing multinucleon contributions to the pionless QE cross section in the context of the so-called MiniBooNE axial mass puzzle and the problem of the neutrino energy reconstruction [69, 70, 71, 72, 23, 73, 74, 75, 76, 77, 78, 79, 80, 81, 82, 83], and we refer the reader to these works for details. We would only like to mention that this topic has become quite relevant in neutrino reactions since the neutrino beams are not monochromatic but wide-band [84, 85] (in particular, DUNE will use much wider neutrino flux than HyperKamiokande and therefore the energy reconstruction will depend stronger on the understanding of the nuclear effects).

In Chpt. 2 we introduce fundamental theoretical concepts which form a basis for further studies. We will start with a general description of neutrinos and the other fermions in the SM, and their interactions. This very elegant theory in the strong sector (QCD) works properly in the high-energy regime, while perturbative QCD is not able to describe physical processes at lower energies. Quarks confinement brings in new degrees of freedom: mesons and baryons. The interactions of these composed particles with leptons are described by a complicated dynamics. In Subsec. 2.2.2, we present in general processes in which neutrinos scatter off a nucleon, producing a single baryon state: either a nucleon or a strange hyperon. A good understanding of these reactions in the free space is not enough from the point of view of oscillation experiments, since detectors are build of nuclei rather than of free nucleons. Therefore, in Sec. 2.3 we introduce some notions that serve for a description of nucleons inside of a nuclear medium (nucleon self-energy and propagator, spectral functions, etc.). Next, the formalism for the QE process is developed with a particular emphasis put on the Lindhard function, which will be used in further analyses. Finally, Sec.2.5 presents an overview of various nuclear effects: Coulomb distortion of outgoing lepton, considerations about a correct energy balance, RPA effects and final state interactions.

Spectral functions account for the modifications of the dispersion relation of nucleons embedded in the nuclear medium. Their role in the description of electroweak interactions with nuclei is the main topic of this Thesis. We begin Chpt. 3 with the simplest model for spectral functions which takes into account only statistical correlations between fermions (the Fermi gas model). Afterwards, in Sec. 3.2 we introduce a semi-phenomenological model, developed

[2]RPA stands for the random phase approximation to compute the effects of long-range nucleon-nucleon correlations.

in [2], which we will extensively use in further studies in Chpts. 4-7. Within this model, the nucleon properties in the nuclear matter are derived starting from the experimental elastic NN scattering cross section, incorporating, consistently with the low density theorems, some medium polarization (RPA) corrections. The approach is nonrelativistic and it is derived for isospin symmetric nuclear matter. The resulting nucleon self-energies stay in good agreement with microscopic calculations, and provide effective masses, nucleon momentum distributions, etc. which also coincide with sophisticated many-body results. There are many other approaches that are used to describe the QE process. They account for nuclear effects in various ways. A short survey is given in Sec. 3.3.

Due to many challenges in the detection of neutrinos, there is very scarce (and rather low-quality) data available which could serve as a benchmark to check models of neutrino-nucleus interaction. In Chpt. 4 we present a comparison of the predictions of the model of Sec. 3.2 in the case of various physical processes not only induced by neutrinos. Firstly, we consider muon and radiative pion captures in nuclei. These low-energy processes serve as an excellent test for nuclear effects, since their role for this kinematics is increasingly important. Next, we show a detailed comparison of various models and an analysis of inclusive neutrino induced charge-current processes in the intermediate and low energy regimes. Lastly, we perform a detailed comparison of various models for the case of electron scattering on ^{12}C in the energy-momentum range particularly important for the T2K experiment. Using electrons instead of neutrinos as a probing particle changes the interaction from vector-axial to pure vector. However, the spectral functions to be used are the same both in weak and electromagnetic processes.

Electron scattering experiments performed in the 1970s revealed an interesting property in the region of low energy transfer and high momentum (corresponding to the QE region). The inclusive electron-nucleus cross section, or response functions, divided by a factor which encompasses physics of electron-nucleon scattering, exhibit the scaling property. Scaling functions obtained from the data can serve as a benchmark for theoretical models. Also, a universal scaling function has become a starting point for a phenomenological SuperScaling Approach (see Subsec. 3.3.3). In Chpt. 5 we define the scaling function from the nucleon-density response function and analyze the scaling properties for the two models of spectral functions, introduced in Secs. 3.2 and 3.3.1, also identifying the sources of scaling breaking.

The production of strange and charm ground-state baryons in weak processes is the topic of Chpt. 6. The obtained cross sections are much lower than these of the dominating QE scattering because of the small value of the Cabibbo angle. Still, the decaying hyperons produce pions which give contributions to the background and therefore are important in the field of oscillation studies. For the case of strange hyperons, we investigate how the inclusion of spectral functions changes their final distributions. Also, hyperons suffer final state interactions due to rescattering processes on their way through the nucleus. These effects modelled by means of a Monte Carlo cascade turn out to play a major role. Next, we focus on weak Λ_c production. In this case SU(3) flavour symmetry that can be used to relate $c \to d$ with $c \to s$ processes, is strongly broken. We analyze the model dependence of the form factors proposed by various theoretical calculations, and find the uncertainties that are induced in the nuclear cross section.

A great majority of oscillation experiments measure appearance or disappearance of electron and muon neutrinos. The physics of τ neutrinos is more challenging to be explored since much higher energies are needed to produce $\tau^{\pm}$, which on top of that decays very rapidly. In Chpt. 7 the spectral function formalism is used to compute the differential cross section and the polarization components for several kinematical setups, relevant for neutrino-oscillation experiments. The effects of the nuclear corrections in these observables are investigated by comparing the results obtained using realistic spectral functions previously introduced (Secs. 3.2 and 3.3.1), with those deduced within the global Fermi gas model, where only statistical correlations are accounted for.

Lastly, the main conclusions and an outlook are presented in Chpt. 8. The notation, normalizations and conventions used in this Thesis are gathered and exposed in Appendix A.

Chapter 2

Theoretical concepts

The complex nature of neutrino-nucleus interactions demands a careful analysis of both initial and final nuclear states. As mentioned, it combines various physical reaction mechanisms at different energy scales, ranging from low-energetic processes in which collective phenomena play a crucial role, up to energies in which neutrinos probe the structure of nucleons.

A nucleus is a system of nucleons with nontrivial interactions which requires the inclusion of two- and many-body forces acting between them to describe some properties, like the binding energy in light nuclei. Already at this "fundamental" level of defining the nucleon-nucleon (NN) potential, the problem suffers from theoretical uncertainties. Interaction between two nucleons inside of the nuclear medium is even more intricate and it is governed by a complicated dynamics.

In the span of the last 70 years a lot of effort has been devoted to describe nuclear forces. There are potentials proposed by various theoretical groups (for a topical review see Ref. [86]). In the 1960s models based on one-boson-exchange were introduced and developed. The NN potential was modelled by an exchange of bosons, most importantly π, ρ, ω and σ. Each of these mesons was introduced to describe a different property of the nuclear force, since they dominate at various energy ranges and isospin channels of the NN potential. Together they recover some basic properties of the nuclear force: a strong repulsive core at short distances and a long tail produced by the one pion exchange (see Fig. 2.1). Still, the obtained agreement with the NN scattering data was qualitative rather than quantitative. Afterwards, a two-pion-exchange contribution was added to the potentials in order to improve their performance (*e.g.* the Bonn meson exchange model of Ref. [87]). In the 1990s with abundant NN scattering data sets available, a different phenomenological approach was developed. The proposed potentials (*e.g.* Nijmegen group [88], CD-Bonn [89] or v_{18} potential by Argonne group [90]) were constructed by introducing a large set of possible nonrelativistic operators and fixing the coupling constants to successfully describe the large samples of experimental phase shifts. More recently, the potentials calculated within the Chiral Perturbation Theory (χPT) have gained on popularity [91]. The idea of χPT consists in constructing the most general Lagrangian respecting chiral symmetry, ordering the terms in number of derivatives (since the small parameter of the theory is the pion momentum). The χPT calculations are more difficult when applied to nuclear physics since in the chiral limit ($q \to 0, m_u, m_d, m_\pi \to 0$), the nuclear interactions do not vanish. The foundation for this approach was suggested by S. Weinberg in a series of works [92, 93, 94]. He proposed to use the Lippman-Schwinger equation to iterate the NN potential calculated perturbatively within χPT.

A description of the nucleus requires solving the many-body problem using some free-space NN potential. In the era of advanced numerical calculations, the task can be approached within the so-called ab-initio methods, which provide a description of the nuclear system with a great precision. Nevertheless, the accurateness of these approaches has a high price: a huge computational time and memory consumption. In many practical applications there is a need for simpler, more phenomenological models, which would still reproduce the bulk of physical

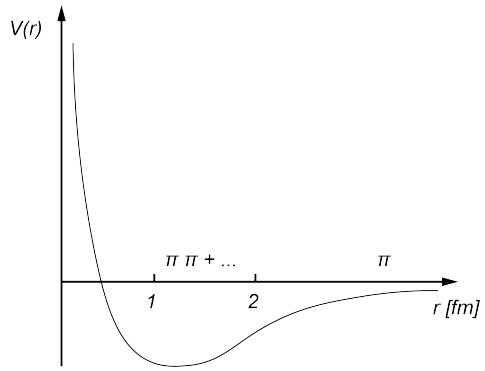

FIGURE 2.1: A schematic picture of the central part of the NN potential. One pion exchange is responsible of the long-range part of the interaction. At intermediate distances, the dynamics is governed by two-pion exchange (and other contributions). At short-distances the potential becomes strongly repulsive.

properties, failing, however, to recover some details of the system. A family of mean-field (MF) methods follows this approach.

Lepton scattering

When a lepton scatters off a nucleus, the interaction depends on the transferred energy-momentum. Already at this level, we should be aware that one makes an approximation, assuming one-boson (γ, Z^0, $W^{\pm}$) exchange with the nuclear target. The assumption, however, is well grounded since this first-order contribution is much larger than further corrections coming from two- (and many-) gauge boson exchanges.

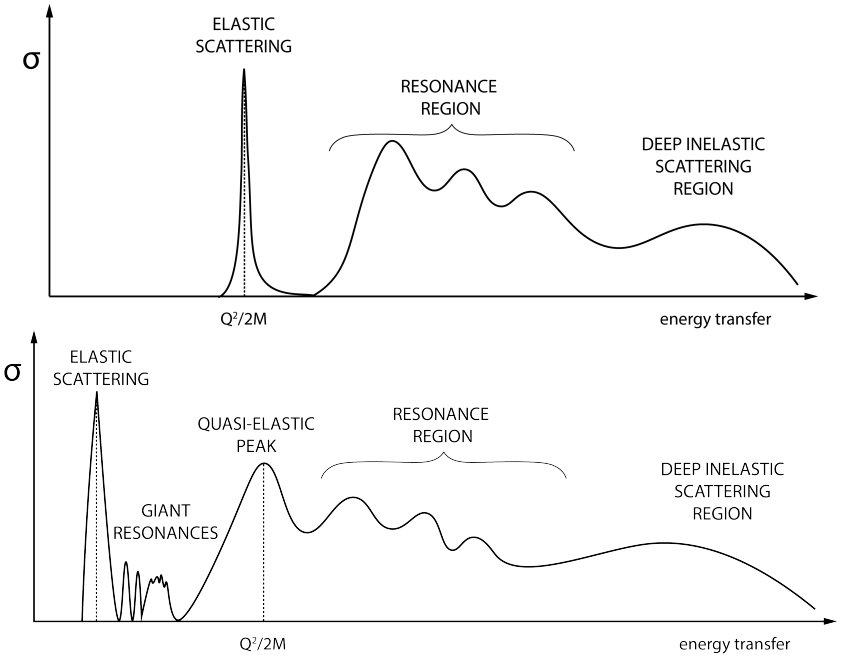

FIGURE 2.2: Spectra of lepton-nucleon (upper panel) and lepton-nucleus (lower panel) scattering.

In Fig. 2.2 we show a schematic shape of the differential cross section $d\sigma/dq^0$ of a lepton scattering off a nucleon (top panel) and off a nucleus (bottom panel), where q^0 is the energy

transfer in the laboratory system. One can observe that various physical mechanisms dominate the cross section, depending on the energy-momentum transferred to the hadronic system.

In the case of scattering on a single nucleon, three regions can be distinguished. Starting from low q^0 values, the first peak corresponds to the QE scattering (it is an elastic process when no charge is exchanged) for which the relation between the transferred energy and momentum $\vec{q}$ is fixed by the conservation law: $(M+q^0)^2 - \vec{q}^2 = M^2$ (where we use an average nucleon mass M). Next, for higher q^0 we observe a region of resonance excitations. The lightest one, $\Delta(1232)$, gives the biggest contribution to the cross section. At higher energy transfers, the deep inelastic scattering (DIS) starts dominating. In this region we have scattering with quarks and gluons instead of individual nucleons.

An analogous situation occurs when the interaction takes place on a nucleus. In this case, however, the underlying dynamics of the constituent nucleons makes the description more demanding. We additionally observe new low-energy mechanisms: elastic scattering and the region of excitation of giant resonances (collective nuclear modes). The QE peak becomes broader because of the motion of the nucleons. At intermediate energies the scattering can be described fairly well as taking place on a single nucleon bound in the nucleus (so-called Impulse Approximation, IA). This assumption is correct when the resolution of the electroweak probe is high enough and the wavelength of the interacting gauge boson is smaller than the typical range of the inter-nucleon distances in a nucleus ~ 1 fm ≈ 200 MeV^{-1}. The QE scattering observed as a delta-like peak for a single nucleon, here gives rise to a peak which is much wider and shifted due to the NN interactions inside the nucleus. Similarly, the produced resonances above the QE peak should also be properly treated inside the nuclear medium, with different properties from those exhibited in the vacuum. One can also observe that the tails of distributions of the QE and Δ excitation overlap. In fact, there is an additional contribution in this so-called dip region, not visible in the spectrum as a separate peak, coming from the scattering on two (or more) nucleons leading to multi-nucleon knockout processes. This mechanism is essential to describe correctly the experimental data, although its strength is significantly smaller than the contribution coming from the scattering on a single in-medium bound nucleon.

This Thesis will be mainly devoted to the description of the role played by nuclear effects (especially concentrating on the SFs) in lepton-nucleus scattering. In the energy regime in which the IA is applicable, it becomes increasingly important to model properly the nucleons' behaviour inside the nucleus in terms of SFs. The QE mechanism is particularly well suited to perform such analysis. Firstly, the vertex of interaction $\nu_\ell + N \to \ell + N'$ has a simple and well established structure[1] and, thus, the theoretical uncertainties are dominated by the nuclear model. Secondly, one can study how both initial and outgoing nucleons are affected by the nuclear medium. The SFs provide a coherent picture in which the particle and the hole states can, in principle, be described in the same formalism. Lastly, the QE scattering is a dominating channel for many neutrino oscillation experiments. Therefore, it is crucial to understand the physics which governs this process to be able to reconstruct the incoming neutrino energy.

Outline

We will start this chapter with a short overview of the electroweak interactions in the SM. In particular, we will focus on how neutrinos couple to quarks via intermediating gauge bosons. This description is applicable only in the high-energy regime (for high values of $Q^2 = -q^2 = \vec{q}^2 - (q^0)^2$), where a meaningful perturbative expansion in terms of quark fields can be performed. At lower Q^2, the theory becomes nonperturbative. An effective description has to

[1] This is certainly true for the vector part of interaction which is known from electron scattering experiments. The axial part is not so well constrained.

be introduced to model the dynamics of the new emerging degrees of freedom: mesons and baryons.

In Sec. 2.2, we introduce the lepton-nucleon interactions. Let us notice that for some dynamical mechanisms already at this level, various theoretical models have considerable problems to describe the experimental data (an important example from the point of view of neutrino experiments is the pion production reaction). Therefore, it is important to establish their reliability before considering the scattering off nucleus (*i.e.* embedding the interaction into the nuclear medium). In Subsec. 2.2.2 we focus our attention on the QE scattering expressing the hadronic current in terms of form factors. In the limit of unbroken SU(3) flavour symmetry of three light quarks, the form factors of the $N \to N'$ processes can be related to the ones which describe the production of strange hyperons. This is a topic explored with some details in Subsec. 2.2.3.

In Sec. 2.3 we introduce basic notions used in nuclear physics to describe the behaviour of nucleons inside the nuclear medium: they gain a self-energy which modifies their dispersion relations with respect to their properties in the vacuum. Next, the Green's function (propagator) will enable us to define the spectral functions. We will start the discussion from a simple model of noninteracting particles in Subsec. 2.3.1. In the language of thermodynamics, the system is an ideal gas of fermions at zero temperature. Even though the Fermi gas (FG) model seems to be too simplistic to give any meaningful physical results, it works surprisingly well in some cases. Still, in general it should not be treated as a trustworthy approach. In Subsec. 2.3.2 we will introduce the Local Density Approximation (LDA) according to which a nucleus can be locally treated as nuclear matter of constant density. This allows to introduce the local Fermi Gas (LFG) model, which we will adopt as a starting point for our approach, further improved with some additional nuclear effects.

Having introduced all the preliminaries, we will proceed in Sec. 2.4 to the description of the neutrino interaction with nuclei. Assuming the LDA in Subsec. 2.4.1, we develop a general formalism to relate the cross section of the neutrino-nucleus interaction with the self-energy of the $W^{\pm}$ boson in the nuclear medium. The main dynamical mechanism we will explore is the QE scattering (although we will also consider strange and charmed hyperon production in Chpt. 6). During the discussion, the notion of the Lindhard function will naturally emerge. We will pay special attention to it, showing in Subsec. 2.4.4 how it can be expressed in terms of the spectral functions.

In Sec. 2.5 we will introduce some further nuclear effects: Coulomb corrections which affect charged leptons, the correct energy balance and the Random Phase Approximation (RPA). Lastly, we will devote few words on the Final State Interactions (FSI). In general terms the latter effect is related to the description of the outgoing hadron particles which interact with the residual nucleus (in this Thesis we will focus on nucleons and hyperons).

2.1 Neutrinos in the Standard Model

The SM of fundamental interactions was proposed by Salam, Weinberg and Glashow in 1967 [95, 96, 97]. The theory describes the dynamics of elemental particles: leptons and quarks, introducing gauge fields (four mediating bosons of the electroweak sector and eight gluons), and one scalar particle: the Higgs boson, which realizes the Higgs mechanism of spontaneous symmetry breaking in the electroweak sector. The SM is based on an assumption that $\mathrm{SU}(3) \times \mathrm{SU}(2)_{\mathrm{L}} \times \mathrm{U}(1)_{\mathrm{Y}}$ is an internal local gauge symmetry of the system, where $\mathrm{SU}(3)$ describes quantum chromodynamics (QCD), while $\mathrm{SU}(2)_{\mathrm{L}} \times \mathrm{U}(1)_{\mathrm{Y}}$ are gauge groups of the electroweak sector, called respectively *weak isospin* and *hypercharge*. In the following we will concentrate on the electromagnetic and weak interactions parts of the SM, leaving aside the dynamics of the QCD sector. The structure of the SM is based on a formalism developed by Yang and Mills

[98] who, inspired by electromagnetism, considered gauge theories of the nonabelian SU(N) group.

The abelian $\mathrm{U}(1)_Y$ group has one generator, while $\mathrm{SU}(2)_\mathrm{L}$ has three generators T_a which obey the commutation relation:

$$[T_a, T_b] = i\varepsilon_{abc} T_c \tag{2.1}$$

with ε_{abc} the three dimensional fully antisymmetric Levi-Civita tensor. Particularly, we are interested in representations of the Lie algebras of the $\mathrm{SU}(2)_\mathrm{L}$ and $\mathrm{U}(1)$ groups acting on the physical fields of our theory. The generators T_a and $\frac{Y}{2}$ of the fundamental representation act on the fermion fields ψ of the SM. In analogy to spin, T_a are weak isospin generators defined in terms of Pauli matrices $T_a = \frac{1}{2}\sigma_a$. The general transformation under a local rotation is given by

$$\psi(x) \xrightarrow{\mathrm{U}(1)_Y} e^{-iY\alpha(x)/2}\psi(x) \qquad\qquad \psi(x) \xrightarrow{\mathrm{SU}(2)_Y} e^{-iT_j\alpha_j(x)}\psi(x) \tag{2.2}$$

with $\alpha(x)$ being the local parameter of the rotation. According to the SM, neutrinos are massless particles, grouped into three families. They exist only as left-handed particles, forming three doublets with the corresponding charged leptons, which appear in both chirality states[2]:

$$\psi_L = \begin{pmatrix} \nu_e \\ e^-_L \end{pmatrix}, \quad \begin{pmatrix} \nu_\mu \\ \mu^-_L \end{pmatrix}, \quad \begin{pmatrix} \nu_\tau \\ \tau^-_L \end{pmatrix}, \quad e^-_R, \quad \mu^-_R, \quad \tau^-_R. \tag{2.3}$$

with $e^-_{L,R} = (1 \mp \gamma_5)e^-$, and similarly for the other fermion fields.

Quarks, similarly to charged leptons, exist in both chirality states, and are grouped into three doublets for left-handed quarks, and six right-handed singlets:

$$q_L = \begin{pmatrix} u_L \\ d_L \end{pmatrix}, \quad \begin{pmatrix} s_L \\ c_L \end{pmatrix}, \quad \begin{pmatrix} t_L \\ b_L \end{pmatrix}, \quad u_R, \quad d_R, \quad s_R, \quad c_R, \quad b_R, \quad t_R. \tag{2.4}$$

In what follows we will consider only the first generation of leptons and quarks. The description of the other two families runs in parallel with the only difference due to the mass of the particles.

Left-handed and right-handed particles transform differently under rotations of $\mathrm{SU}(2)_\mathrm{L} \times \mathrm{U}(1)_\mathrm{Y}$ groups. The right-handed fermions are singlets under $\mathrm{SU}(2)_\mathrm{L}$. Each particle should be assigned the proper quantum numbers: the third component of the weak isospin T_3 and the hypercharge $\frac{Y}{2}$. They should obey a relation which determines the electric charge (as a consequence of the symmetry breaking $\mathrm{SU}(2)_\mathrm{L} \times \mathrm{U}(1)_\mathrm{Y} \to \mathrm{U}(1)_\mathrm{EM}$):

$$Q = T_3 + \frac{Y}{2}. \tag{2.5}$$

The values of T_3 and $Y/2$ for the first generation of leptons and quarks are shown in Table 2.1. Let us stress that $Y/2$ depends on the chosen convention (here we will fix the scale setting the electromagnetic charge to -1 for electrons). The weak isospin is known from the commutation relations of the generators of the $\mathrm{SU}(2)$ Lie algebra. This puts constraints on the hypercharge Y.

In order to make the Lagrangian invariant under local symmetry transformations, one has to redefine the derivatives acting on the fermion fields in such a way that new spin-1 fields are introduced, which are used to define the covariant derivative. This set of "gauge bosons" with their own transformation laws, will make the kinetic terms of the Lagrangian transform in a proper way. Each gauge boson, which will be denoted as W^a_μ and B_μ, corresponds to generators of the adjoint representation of the $\mathrm{SU}(2)_\mathrm{L}$ and $U(1)$ groups, respectively. Covariant derivatives

[2] In principle, one can extend the SM to include right-handed neutrinos which would be sterile, *i.e.* they will not interact with other particles. Here, however, we will not consider this scenario.

	e_L	ν_e	e_R	u_L	d_L	u_R	d_R
T_3	$-1/2$	$1/2$	0	$1/2$	$-1/2$	0	0
$Y/2$	$-1/2$	$-1/2$	-1	$1/6$	$1/6$	$2/3$	$-1/3$

TABLE 2.1: Assignment of quantum numbers of the $\mathrm{SU(2)_L \times U(1)_Y}$ group.

operate differently on left-handed and right-handed fermions:

$$\begin{aligned} D_\mu \psi_R &= \left(\partial_\mu + ig'\frac{Y}{2}B_\mu\right)\psi_R \\ D_\mu \psi_L &= \left(\partial_\mu + ig'\frac{Y}{2}B_\mu + ig\vec{T}\vec{W}_\mu\right)\psi_L \end{aligned} \tag{2.6}$$

For the theory to be consistent, the gauge bosons transform under infinitesimal rotations as

$$\begin{aligned} B_\mu &\xrightarrow{U(1)_Y} B_\mu - \frac{1}{g'}\frac{Y}{2}\partial_\mu \alpha(x) \\ W^a_\mu T_a &\xrightarrow{SU(2)_L} W^a_\mu T_a - \frac{1}{g}\partial_\mu \alpha_a(x) T_a + W^a_\mu \varepsilon_{abc}\alpha_a(x) T_c \end{aligned} \tag{2.7}$$

The Lagrangian for the (first generation of) fermions before spontaneous symmetry breaking can be then expressed in a compact form as [99]:

$$\mathscr{L}_{\mathrm{EW}} = \bar{\psi}_L i\not{D}\psi_L + \bar{e}_R i\not{D} e_R + \bar{q}_L i\not{D} q_L + \bar{u}_R i\not{D} u_R + \bar{d}_R i\not{D} d_R \tag{2.8}$$

This theory, however, does not describe the physical world, since both fermions and gauge bosons remain massless particles. One has to spontaneously violate the symmetry to generate the massive terms which – if introduced explicitly – would break the symmetry. As has been already mentioned, this is done in the SM with the Higgs mechanism. Although it can be realized in various ways, the standard solution consists in introducing a Higgs doublet of scalar charged and neutral fields, which are coupled to the gauge bosons through the covariant derivative; and also interact with the fermionic fields through the so-called Yukawa couplings, since these terms are allowed by the local gauge symmetry. The Higgs sector is introduced to the SM by means of a self-interacting term (potential) which is essential since it leads to the spontaneous breaking of the symmetry: the vacuum state does not preserve $\mathrm{SU(2)_L \times U(1)_Y}$. After the symmetry violation, the vacuum expectation value of the Higgs gives rise to the masses of the remaining fields of the theory. In addition, gauge bosons W^3_μ and B_μ should be rotated to obtain mass-definite neutral particles, while combinations of W^1_μ and W^2_μ lead to the physical $W^\pm_\mu$ states:

$$\begin{aligned} A_\mu &= \sin\theta_W W^3_\mu + \cos\theta_W B_\mu \\ Z^0_\mu &= \cos\theta_W W^3_\mu - \sin\theta_W B_\mu \\ W^\pm_\mu &= \frac{1}{\sqrt{2}}(W^1_\mu \mp i W^2_\mu) \end{aligned} \tag{2.9}$$

where the Weinberg angle θ_W can be related to the coupling constants g, g' and the electric charge e:

$$e = g'\cos\theta_W = g\sin\theta_W\,, \qquad \tan\theta_W = \frac{g'}{g} \tag{2.10}$$

In terms of these newly defined physical gauge bosons we can rewrite the covariant derivative as

$$D_\mu = \partial_\mu + ieQA_\mu + i\frac{g}{\sqrt{2}}\left(T^+W_\mu^+ + T^-W_\mu^-\right) + i\frac{g}{\cos\theta_W}(T_3 - Q\sin^2\theta_W)Z_\mu^0 \tag{2.11}$$

with $T^\pm = T_1 \pm iT_2$. Now one can rewrite the Lagrangian of Eq. (2.8) as a sum of the so-called electromagnetic (EM), charged-current (CC) and neutral-current (NC) parts [99]:

$$\begin{aligned}\mathscr{L}_{\rm EW} &= \mathscr{L}_{\rm EM} + \mathscr{L}_{\rm CC} + \mathscr{L}_{\rm NC} \\ &= -eA_\mu J^\mu_{\rm EM} - \frac{g}{2\sqrt{2}}\left(W_\mu^+ J^\mu_{\rm CC} + W_\mu^- J^{\mu\dagger}_{\rm CC}\right) - \frac{g}{2\cos\theta_W} Z_\mu J^\mu_{\rm NC}\end{aligned} \tag{2.12}$$

When the quark mixing is ignored (considering only the first generation of fermions), the currents J_μ are given by:

$$\begin{aligned}J^\mu_{\rm EM} =& -\bar{e}\gamma^\mu e + \frac{2}{3}\bar{u}\gamma^\mu u - \frac{1}{3}\bar{d}\gamma^\mu d \\ J^\mu_{\rm CC} =& \bar{\nu}_e\gamma^\mu(1-\gamma_5)e + \bar{u}\gamma^\mu(1-\gamma_5)d \\ J^\mu_{\rm NC} =& \frac{1}{2}\bar{\nu}_e\gamma^\mu(1-\gamma_5)\nu_e - \frac{1}{2}\bar{e}\gamma^\mu(1-\gamma_5)e + \sin^2\theta_W\,\bar{e}\gamma^\mu e \\ &+ \frac{1}{2}\bar{u}\gamma^\mu(1-\gamma_5)u - \frac{1}{2}\bar{d}\gamma^\mu(1-\gamma_5)d + \sin^2\theta_W\,(-\frac{2}{3})\bar{u}\gamma^\mu u + \sin^2\theta_W\,\frac{1}{3}\bar{d}\gamma^\mu d\end{aligned} \tag{2.13}$$

When the quark mixing is turned on, we take into account the fact that quarks which couple to gauge bosons are not the mass eigenstates. The Higgs mechanism allows mixing between different generations in such a way that:

$$\begin{aligned}&\Psi_u = (u,c,t)\,, \quad \Psi_d = (d,s,b) \quad - \text{ vectors of quarks in the mass basis} \\ &\Psi'_{u_{(L,R)}} = U_{u_{(L,R)}}\Psi_{u_{(L,R)}}\,, \quad \Psi'_{d_{(L,R)}} = U_{d_{(L,R)}}\Psi_{d_{(L,R)}} \quad - \text{ rotation to the flavour basis}\end{aligned} \tag{2.14}$$

where the matrices $U_{u,d}$ are unitary. The transformation between these two bases (of definite flavour and mass) is described by the Cabibbo-Kobayashi-Maskawa matrix $V_{\rm CKM}$. It will affect the quark content of the CC, which in the case of more than one generation reads

$$\bar{\Psi}'_{u_L}\gamma^\mu\Psi'_{d_L} = \bar{\Psi}_{u_L}\gamma^\mu U^\dagger_{u_L}U_{d_L}\Psi_{d_L} \equiv \bar{\Psi}_{u_L}\gamma^\mu V_{\rm CKM}\Psi_{d_L} \tag{2.15}$$

For two generations $V_{\rm CKM}$ is defined just by the Cabbibo angle θ_C:

$$V_{\rm CKM} = \begin{pmatrix}\cos\theta_C & \sin\theta_C \\ -\sin\theta_C & \cos\theta_C\end{pmatrix} \tag{2.16}$$

and therefore the quark CC in this case is given by:

$$j^\mu_{\rm cc} = \bar{u}\gamma^\mu(1-\gamma_5)(d\cos\theta_C + s\sin\theta_C) \tag{2.17}$$

with u, d, s being quark mass eigenstates.

2.2 Neutrino scattering off a single nucleon

Let us consider the $\nu_\ell/\bar{\nu}_\ell(k) + N \to \ell^\mp(k') + X$ reaction where k is the four-momentum of the incoming (anti)neutrino ν_ℓ. The outgoing lepton ℓ has momentum k' and may be of any

flavour: e (electron), μ (muon) or τ (tau). For the conventions used in this Thesis we refer to the Appendix A. The scattering takes place on a nucleon N of momentum p and mass M, producing a hadronic final state X (which in general is a multiparticle state). This CC reaction is mediated via a $W^{\pm}$ boson of momentum $q = k' - k$. From the experimental point of view, the CC reactions are the most important processes for neutrino detection, since the outgoing charged lepton can be observed. On the other hand, in the NC processes – where the Z^0 boson instead of the $W^{\pm}$ is interchanged – the final lepton is a neutrino which is not seen in the detectors. Still, the NC processes play an important role as a background in many experiments and their treatment is therefore crucial for precise measurements. The cross section for the CC reaction is given by

$$\frac{d\sigma}{dE_{k'}d\Omega_{k'}} = \frac{G_F^2}{4\pi^2}\frac{|\vec{k}'|}{|\vec{k}|}L_{\mu\sigma}(k,k')W_N^{\mu\sigma}(p,q)\,. \tag{2.18}$$

where G_F is the Fermi constant related to the gauge coupling g and the $W^{\pm}$ mass M_W as $G_F/\sqrt{2} = g^2/8M_W^2$ and $L_{\mu\nu}$ and $W_N^{\mu\nu}$ are the lepton and nucleon hadron tensors respectively. The lepton tensor, which describes the interaction vertex of the neutrino, the gauge boson and the outgoing lepton, reads

$$\begin{aligned} L_{\mu\sigma}(k,k') &= \frac{1}{8}\mathrm{Tr}[\not{k}\gamma_\mu(1\mp\gamma_5)(\not{k}'+m_\ell)\gamma_\sigma(1\mp\gamma_5)] \\ &= k_\mu k'_\sigma + k'_\mu k_\sigma - g_{\mu\sigma}k\cdot k' \pm i\varepsilon_{\mu\sigma\alpha\beta}k'^{\alpha}k^{\beta} \end{aligned} \tag{2.19}$$

Some more details on the normalization conventions can be found in Appendix A, and a most general discussion is included in Appendix D. The antisymmetric part of the tensor comes with opposite sign for neutrinos and antineutrinos. The antisymmetric part of interaction is absent in the electromagnetic case when both incoming and outgoing leptons are unpolarized. This richer structure of the lepton tensor (comparing to the EM case) will consequently affect the result of the contraction with the nucleon hadron tensor, which encodes the physics of the strong interactions:

$$\begin{aligned} W_N^{\mu\sigma}(p,q) =& \frac{1}{2M}\overline{\sum}\prod_i\left(\int\frac{dp_{x_i}^3}{(2\pi)^3 2E_{x_i}}\right)(2\pi)^3\delta(\sum_i p_{x_i} - p - q) \\ & \langle X,p_x|j_{cc}^{\mu}(0)|N,p\rangle\langle X,p_x|j_{cc}^{\sigma}(0)|N,p\rangle^*, \end{aligned} \tag{2.20}$$

where we sum final and average over initial particle spins. As already mentioned, the final state $|X,p_x\rangle$ is in general a multi-particle state $|X,p_x\rangle = \prod_i |X_i,p_{x_i}\rangle$. The CC for quarks j_{cc}^{μ} is given by Eq. (2.17). The fact that $\cos\theta_C$ is much larger than $\sin\theta_C$ reduces the cross section for the production of strange particles. Consequently, we will see in Chpt. 6, that strange hyperon production cross sections are one order of magnitude lower than those found for nucleon QE scattering. We split the hadron tensor into symmetric and antisymmetric parts:

$$W_N^{\mu\sigma} = W_{N\,(s)}^{\mu\sigma} + iW_{N\,(a)}^{\mu\sigma} \tag{2.21}$$

where the antisymmetric tensor is only probed when the antisymmetric part of the lepton tensor is present. Therefore, (in the case of an unpolarized beam of leptons) we are sensitive to the contribution coming from $W_{N\,(a)}^{\mu\sigma}$ only for neutrino induced reactions. Moreover, the difference between neutrino and antineutrino cross sections is driven by this term. This fact is of particular importance for future experiments measuring the CP violating phase.

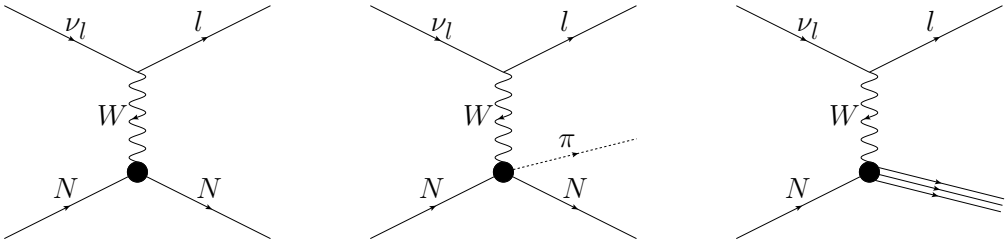

FIGURE 2.3: Three main mechanisms for neutrino-nucleon scattering: QE (left), pion production (center) and DIS (right).

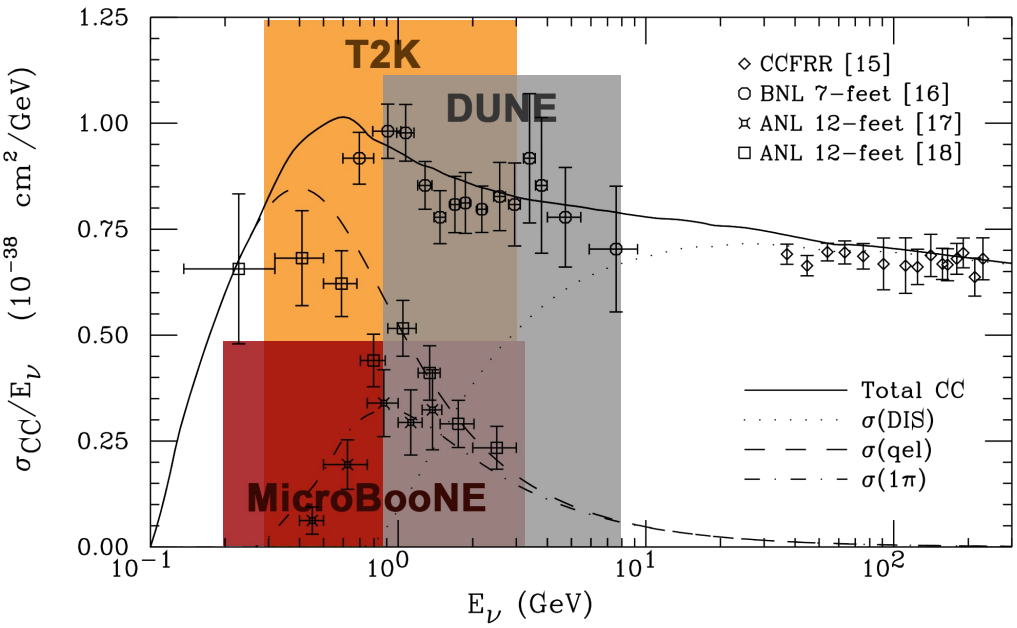

FIGURE 2.4: Neutrino-nucleus cross section as a function of the neutrino energy (plot taken from Ref. [100]). On top of it we marked the energy range of fluxes used in T2K, DUNE and MicroBooNE. Other long baseline experiments cover a similar energy spectrum.

2.2.1 Dynamical mechanisms

The general final state $|X, p_x\rangle$ introduced in Eq. (2.20) describes any possible outgoing particles produced by the j^{μ}_{cc} current of Eq. (2.17). In fact, one can consider mechanisms going beyond the $u \to d,s$ transition but they are much suppressed. For example charmed hyperon production will be studied in Chpt. 6. The contribution of each particular mechanism to the total cross section depends on the value of the energy-momentum transfer to the nucleon. The main mechanisms (important in the neutrino oscillation experiments) are: QE scattering, pion production (through resonance excitations) and DIS, which are depicted schematically in Fig. 2.3. The range of energies between the resonance region and DIS, so-called SIS (Shallow Inelastic Scattering) region, is challenging to model since there is no clear distinction between both mechanisms. The approximate contributions of the different mechanisms to the total cross section are shown in Fig. 2.4. The typical energy-fluxes of accelerator neutrinos in the long baseline experiments may vary from tens of MeV to few GeV (with long tails up to tens of GeV). Particularly in Fig. 2.4, we can see the energy range of three experiments: T2K, DUNE and MicroBooNE. We clearly observe that the QE mechanism dominates for $0.1 - 1$ GeV, which overlaps mostly with the flux energy of the T2K and MicroBooNE experiments. Still, even for DUNE the QE scattering gives a large contribution.

In addition to these three main mechanisms, there are others, suppressed either by phase-space (when more particles are produced in the final state, *e.g.* two or more pion production) or because of other dynamical reasons. Let us notice that, as mentioned, the processes driven by the $u \to s$ transition are smaller by a factor $\tan^2\theta_C \approx 1/18$. In the following Subsection, we will focus more on the QE mechanism.

2.2.2 Quasielastic scattering

QE scattering is the simplest mechanism among the ones enumerated in the previous Subsection. The outgoing particle is just a single nucleon $|X, p_x\rangle = |N', p'\rangle$. We will use relativistic descriptions of both incoming and outgoing nucleons. The structure of the general CC operator of Eq. (2.17) in this case leads to four terms. We refer to Appendix B for details. The vertex can be written as

$$\langle N', p'|j^{\mu}_{cc}|N, p\rangle = \bar{u}(p')\Gamma^{\mu}u(p) = \bar{u}(p')(V^{\mu} - A^{\mu})u(p) \tag{2.22}$$

with the vector and axial contributions given in terms of Lorentz invariant form factors:

$$\begin{aligned} V^{\mu} &= \cos\theta_C\left(F_1^V(q^2)\gamma^{\mu} + i\mu_V F_2^V(q^2)/(2M)\sigma^{\mu\nu}q_{\nu}\right) \\ A^{\mu} &= \cos\theta_C\left(G_A(q^2)\gamma^{\mu}\gamma_5 + G_P(q^2)q^{\mu}/M\gamma_5\right) \end{aligned} \tag{2.23}$$

Isospin invariance allows to relate the vector form factors to the electromagnetic ones. The explicit expressions for the form factors, with $\tau = -q^2/4M^2$, are:

$$\begin{aligned} F_1^V &= F_1^p - F_1^n & \mu_V F_2^V &= \mu_p F_2^p - \mu_n F_2^n \\ F_1^{p,n} &= \frac{G_E^{p,n} + \tau G_M^{p,n}}{1+\tau} & \mu_{p,n}F_2^{p,n} &= \frac{G_M^{p,n} - G_E^{p,n}}{1+\tau} \end{aligned} \tag{2.24}$$

For the proton- and neutron-electric and magnetic form factors, there are many parametrizations available. We adopted in this work the Galster parametrization [101] where

$$G_E^p = \frac{1}{(1-q^2/M_V^2)^2}\,, \quad G_M^p = \mu_p G_E^p\,, \quad G_E^n = -\frac{\mu_n\tau}{(1+\lambda_n\tau)}G_E^p\,, \quad G_M^n = \mu_n G_E^p \tag{2.25}$$

with $M_V = 0.843$ GeV, $\mu_p = 2.7928$, $\mu_n = -1.9113$, and $\lambda_n = -5.6$.

For the axial form factor G_A, we assume the standard dipole parametrization

$$G_A = \frac{g_A}{(1-q^2/M_A^2)^2}\,, \tag{2.26}$$

where the nucleon axial-vector coupling constant is taken to be $g_A = 1.257$ and the axial mass $M_A = 1.049$ GeV. The Partially Conserved Axial Current (PCAC) theorems allow us to write the pseudo-scalar form factor in terms of the axial one as (see Appendix B)

$$G_P = \frac{2M^2}{(m_\pi^2 - q^2)}G_A \tag{2.27}$$

with m_π being the pion mass. Let us notice that the $G_P(q^2)$ form factor plays a negligible role if the mass of outgoing lepton is small. This is because all the terms of the hadron tensor $W_N^{\mu\nu}$ that depend on G_P will be proportional to q^{μ}, q^{ν} or $q^{\mu}q^{\nu}$ but q^{μ} contracted with the lepton tensor vanishes in the massless lepton limit. This form factor will be more important in the case of τ

production, as discussed in Chpt. 7. It can been measured in muon and radiative muon capture processes from the muonic hydrogen ground state [102].

2.2.3 $N \to \Lambda, \Sigma^0, \Sigma^-$ form factors

The same discussion of the elastic mechanism can be applied to describe the weak production of strange hyperons. They are baryons, three-quark bound states, which contain one strange quark s.

In the limit of equal masses of quarks u, d and s, the dynamics of the system is invariant under $\mathrm{SU}(3)$ rotations in the flavour space. The symmetry is not as exact as isospin $\mathrm{SU}(2)$ acting in the space of u and d quarks because of the mass splitting: $m_u \approx 2.2$ MeV, $m_d \approx 4.7$ MeV and $m_s \approx 95$ MeV. Nevertheless, it is still relatively good, taking into account that the mass of next-heavy charm quark is $m_c \approx 1275$ MeV.

In the limit of unbroken $\mathrm{SU}(3)$ symmetry, baryons are grouped into four multiplets: $3 \otimes 3 \otimes 3 = 1 \oplus 8 \oplus 8 \oplus 10$. The hyperons we will consider: Λ, Σ^0, Σ^- enter into an octet:

$$B = \begin{pmatrix} \frac{1}{\sqrt{2}}\Sigma^0 + \frac{1}{\sqrt{6}}\Lambda & \Sigma^+ & p \\ \Sigma^- & -\frac{1}{\sqrt{2}}\Sigma^0 + \frac{1}{\sqrt{6}}\Lambda & n \\ \Xi^- & \Xi^0 & -\frac{2}{\sqrt{6}}\Lambda \end{pmatrix} \tag{2.28}$$

We want to consider an interaction with an external source j^μ_{cc} which accounts for both $u \to d$ and $u \to s$ transitions (see Eq. (2.17)). These transitions are related by $\mathrm{SU}(3)$ rotations, which thus can be written in terms of the Gell-Mann matrices λ_i (see Appendix A). The CC can be expressed as

$$j^\mu_{cc} = \begin{pmatrix} \bar{\Psi}_u & \bar{\Psi}_d & \bar{\Psi}_s \end{pmatrix} \gamma^\mu (1-\gamma_5) \begin{pmatrix} 0 & \cos\theta_C & \sin\theta_C \\ 0 & 0 & 0 \\ 0 & 0 & 0 \end{pmatrix} \begin{pmatrix} \Psi_u \\ \Psi_d \\ \Psi_s \end{pmatrix} \tag{2.29}$$

Let us introduce

$$T_{cc} = \begin{pmatrix} 0 & \cos\theta_C & \sin\theta_C \\ 0 & 0 & 0 \\ 0 & 0 & 0 \end{pmatrix} = \frac{\cos\theta_C}{2}(\lambda_1 + i\lambda_2) + \frac{\sin\theta_C}{2}(\lambda_4 + i\lambda_5) \tag{2.30}$$

acting in the flavour space. For the electromagnetic case we would have

$$T_{em} = \begin{pmatrix} 2/3 & 0 & 0 \\ 0 & -1/3 & 0 \\ 0 & 0 & -1/3 \end{pmatrix} = \frac{1}{2}\left(\lambda_3 + \frac{1}{\sqrt{3}}\lambda_8\right) \tag{2.31}$$

The $\mathrm{SU}(3)$ invariant matrix element of the CC transition between octet baryon states. It contains two possible terms:

$$\langle B', p' | j^\mu_{cc} | B, p \rangle = \bar{u}(p')\Gamma^\mu u(p) \left(D\mathrm{Tr}\left(T_{cc}\{B, \bar{B}'\}_+\right) + F\mathrm{Tr}\left(T_{cc}[B, \bar{B}']\right) \right) \tag{2.32}$$

In the above equation B and $\bar{B}'$ are understood as matrices in flavour space, with no momentum or spin dependence and the trace is taken in the $\mathrm{SU}(3)$ flavour space. D and F are low energy constants fitted to data (semileptonic decays of nucleons and hyperons): $F + D = 1.267 \pm 0.003$ and $F - D = -0.341 \pm 0.016$. We also introduced a reduced matrix element $\bar{u}(p')\Gamma^\mu u(p)$ with Γ^μ being a general vertex of the interaction. Using the analog expression to Eq. (2.32) for the electromagnetic current, we recover the relationship between the vector part of the weak

	$f_1(q^2)$	$f_2(q^2)$	$g_1(q^2)$
$p \to \Lambda$	$-\sqrt{\frac{3}{2}}F_1^p(q^2)$	$-\sqrt{\frac{3}{2}}\frac{M_Y}{M+M_Y}\mu_p F_2^p(q^2)$	$-\sqrt{\frac{3}{2}}\frac{1+2x}{3}G_A(q^2)$
$n \to \Sigma^-$	$-\left(F_1^p(q^2)+2F_1^n(q^2)\right)$	$-\frac{M_Y}{M+M_Y}(\mu_p F_2^p(q^2)+2\mu_n F_2^n(q^2))$	$(1-2x)G_A(q^2)$
$p \to \Sigma^0$	$-\frac{1}{\sqrt{2}}\left(F_1^p(q^2)+2F_1^n(q^2)\right)$	$-\frac{M_Y}{M+M_Y}\frac{1}{\sqrt{2}}\left(\mu_p F_2^p(q^2)+2\mu_n F_2^n(q^2)\right)$	$\frac{1-2x}{\sqrt{2}}G_A(q^2)$

TABLE 2.2: Form factors for $u \to s$ transitions (see Eq. (2.33)), with $x = \frac{F}{F+D} \approx 0.73$.

interaction and the electromagnetic interaction $\langle p|j^\mu_{em}|p\rangle - \langle n|j^\mu_{em}|n\rangle = \langle p|j^\mu_{cc(V)}|n\rangle$. Further, the $N \to N'$ form factors can be related to the ones appearing in the $N \to Y$ transitions, where $Y = \Lambda, \Sigma^0, \Sigma^-$. The general structure of interaction vertex $W^\pm NY$ can be then expressed as

$$\Gamma^\mu_Y = \left[\gamma^\mu f_1(q^2) + i\sigma^{\mu\nu}\frac{q_\nu}{M_Y}f_2(q^2) + \frac{q^\mu}{M_Y}f_3(q^2)\right] - \left[\gamma^\mu g_1(q^2) + i\sigma^{\mu\nu}\frac{q_\nu}{M_Y}g_2(q^2) + \frac{q^\mu}{M_Y}g_3(q^2)\right]\gamma_5 \tag{2.33}$$

with M_Y, the hyperon mass. Let us notice a difference of a $2M/M_Y$ (M/M_Y) multiplicative factor with respect to the previous vertex definition in Eq. (2.23), in the case of the f_2 (g_2) form factor. This change of notation has been introduced to make a connection with the usual conventions employed for the $\Lambda_c \to N$ transition, discussed in Chpt. 6. We will neglect the f_3 and g_3 form factors when working only with light leptons (see the discussion below Eq. (2.27)). From G-parity invariance we also get that for $N \to N'$ process $g_2 = 0$ and $f_3 = 0$ [30]. Assuming SU(3) the same applies to processes driven by the $u \to s$ transition. The remaining f_1, f_2 and g_1 form factors can be related with the form factors defined in the previous Subsection as detailed in Table 2.2.

2.3 Nucleons in the nuclear medium

The relatively simple process of neutrino-nucleon scattering becomes a nontrivial problem when the interaction does not take place on a free nucleon, but on a particle bound in the nucleus. Previously, all the unknown dynamics has been encoded into the form factors. For the vector part, its q^2-dependence (in the energy regime relevant for the QE mechanism) is well constrained by various experiments. The only poorly known piece of information is the axial form factor [103]. In the near future, lattice QCD techniques will be able to provide a reliable q^2 dependence of G_A [104].

In the case of the neutrino-nucleus cross section, the complicated many-body dynamics of the nuclear system dramatically changes the situation, and introduces new theoretical uncertainties. One of the fundamental challenges that we encounter is the fact that the majority of nuclear calculations are done using nonrelativistic formalisms. They break down when the energy-momentum transfer to the nucleus is high enough (already at $|\vec{q}| \approx 600$ MeV). This is a serious obstacle, which puts some strict limitations on the models. *E.g.* the results of ab-initio approaches (which aspire to be a benchmark for other less sophisticated models) are

reliable only for a limited kinematics. There are various ways to proceed in this situation – prescriptions how to promote nonrelativistic calculations to the relativistic regime – proposed by different theoretical groups. We will discuss some of them in the following chapters.

In addition to the already mentioned ab-initio calculations, a usual method to deal with the many-body problem is the MF approach. It consists in reducing the many-body dynamics to a situation in which a single nucleon is submerged in a MF potential. In this simple picture, each constituent particle feels the same potential generated by the other particles of the system. Nucleons being fermions occupy different quantum states. Solving the potential problem, one obtains approximate energy levels and wave functions of the nuclear system. Although this reduction of the many-body problem does not capture all the details and nuclear properties of the system, it has proved to work well in many applications. The proposed potential itself should be chosen in such a way, that the residual interaction between nucleons can be regarded as a small correction.

In the following subsections we will introduce some fundamental notions used in nuclear physics. Particularly we will focus on those which form the theoretical basis for the approach developed by the Valencia group (see for instance Ref. [3]), which is predominantly employed in this Thesis.

2.3.1 Noninteracting system

The simplest model, which will be our starting point for more advanced considerations, is the so-called Fermi gas model, in which fermions do not interact with each other, *i.e.* the Hamiltonian has the simple form

$$\mathscr{H}_0 = \sum_{i=1}^{\mathscr{N}} \frac{p_i^2}{2M}\,. \tag{2.34}$$

The ground state of the system is comprised of $\mathscr{N}$ particles which occupy all the available energy levels up to the Fermi level E_F with the corresponding momentum $p_F = \sqrt{2ME_F}$. Let us notice that in the case of infinite systems (nuclear matter) modelled as ideal Fermi gases at zero temperature $T = 0$, the Fermi level coincides with the chemical potential of the system μ, and it is equal for both adding or removing a particle from the system (for a review of statistical and thermodynamical properties of ideal gases see Ref. [105]).

Using thermodynamical properties of the system we can relate its density ρ with the Fermi level. The standard approach to this problem is to assume that we have $\mathscr{N}$ particles in a box of volume $V = L^3$. Particles are described as plane waves with periodic boundary conditions. We will use the second quantization formalism with creation and annihilation operators normalized as:

$$a_\alpha^\dagger|0\rangle = |\alpha\rangle\,, \qquad \{a_\alpha, a_{\alpha'}^\dagger\} = \delta_{\alpha\alpha'} \tag{2.35}$$

where $|0\rangle$ is the ground state and we denote by α all quantum numbers that characterize the state. In addition to spin and isospin (which we will not write explicitly), three integers n_x, n_y, n_z label each state, which define the momentum components, $p_i = n_i \frac{2\pi}{L}$ (we assume $\hbar = 1$).

$$\psi_\alpha(\vec{r}) = \frac{1}{\sqrt{V}} e^{in_x \frac{2\pi}{L} r_x} e^{in_y \frac{2\pi}{L} r_y} e^{in_z \frac{2\pi}{L} r_z} a_\alpha^\dagger = \frac{1}{\sqrt{V}} e^{i\vec{p}\vec{r}} a_\alpha^\dagger \tag{2.36}$$

With this normalization, we may interpret $\psi_\alpha(\vec{r})$ as the probability density of finding a particle in a state characterized by the quantum numbers α within the volume V:

$$\int_V d^3r |\psi_\alpha(\vec{r})|^2 = 1 \tag{2.37}$$

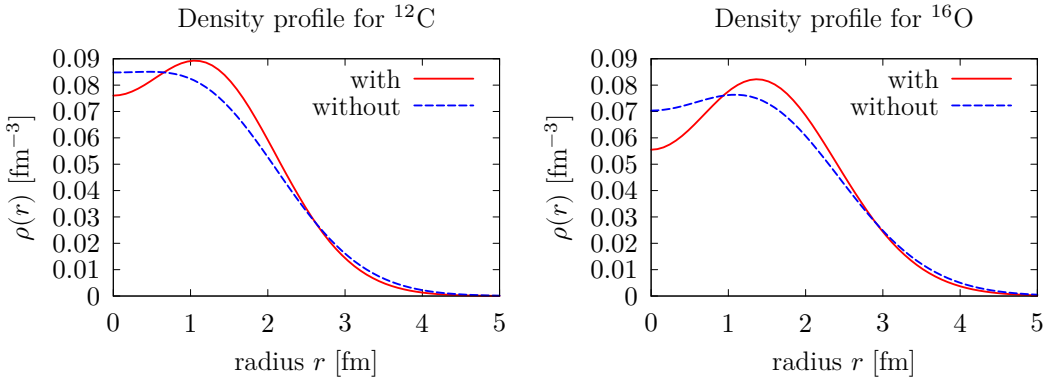

FIGURE 2.5: Comparison of the density profiles for light nuclei with and without taking into account that nucleons are not pointlike (the density is equal for protons and neutrons).

In the limit of infinite number of particles, the sum over $\{n_x, n_y, n_z\}$ is replaced with an integration

$$\sum_{n_x,n_y,n_z} \to \frac{V}{(2\pi)^3} \int d^3p \tag{2.38}$$

On top of this, we have to sum over other degrees of freedom (spin, isospin) which will give an additional ν factor. The number of particles $\mathscr{N}$ in the system is then given by:

$$\mathscr{N} = \int_V d^3r \sum_\alpha \langle 0|\psi_\alpha^\dagger \psi_\alpha|0\rangle = \frac{\nu V}{(2\pi)^3} \int d^3p\, \theta(p_F - p) = \frac{\nu V}{6\pi^2} p_F^3 \tag{2.39}$$

In the thermodynamical limit $\mathscr{N} \to \infty$, $V \to \infty$ with constant density $\mathscr{N}/V = \rho$, we find

$$\rho = \nu \frac{p_F^3}{6\pi^2}\,. \tag{2.40}$$

In order to model a nucleus as a Fermi gas of noninteracting particles, one can either consider it as a system of a constant density ρ (global Fermi gas, GFG) or that it has an r-dependent density with the density profile determined from experiments (local Fermi gas, LFG). The LFG is based on the Local Density Approximation (LDA), introduced in the next subsection. For isospin asymmetric nuclei, one should deal with different densities of neutrons and protons, and therefore, distinct Fermi levels.

2.3.2 Local Density Approximation (LDA)

The primary nuclear systems of our interest will be nuclei which serve as targets in the detectors of neutrino oscillation experiments. In many of them, the neutrino scattering takes place on carbon ^{12}C or oxygen ^{16}O (with other elements also present in smaller proportion: calcium, iron, lead...). Liquid argon detectors, among which DUNE focuses a lot of attention recently, need a special comment in this regard. Argon is difficult to model since it is an open-shell and isospin asymmetric nucleus. In the determination of the CP violating phase, one is required to measure both neutrino and antineutrino oscillations. If the interaction takes place on asymmetric nucleus, the nuclear effects affect differently the ν and $\bar{\nu}$ modes. It is therefore essential to understand the peculiarity of this nuclear system in detail. In the results presented in this Thesis, we will focus our attention mainly on carbon and oxygen targets, since the SFs we will employ are designed to describe symmetric nuclear matter (the notion of spectral function will be introduced in the next Subsec. 2.3.3). Nevertheless, in some cases we also provide predictions for argon, assuming

	Nucleus	R_p (fm)	R_n (fm)	a
MHO	^{12}C	1.692	1.692	1.082
MHO	^{16}O	1.833	1.833	1.544
MHO	^{18}O	1.881	1.975	1.544
Fermi	^{23}Na	2.773	2.810	0.540
Fermi	^{40}Ca	3.51	3.43	0.563
Fermi	^{44}Ca	3.573	3.714	0.563

TABLE 2.3: Parameters for the charge and neutron matter density profiles given in Eq. (2.41) for different nuclei used in this work. The parameter a is either dimensionless for MHO or is given in [fm] for the two-parameter Fermi distributions.

that it is almost isospin symmetric, therefore in this regard similar to carbon and oxygen; and neglecting the fact of its much more complicated nuclear structure.

The LDA assumes that each point of nucleus locally looks like infinite nuclear matter of a given constant density. In this approximation, a nucleus is a system characterized by the density profiles of protons and neutrons. This description certainly oversimplifies the physical situation, in comparison to *e.g.* shell-models which give a much more detailed picture of the nuclei. Nevertheless, in some applications, the LDA might be a good enough approximation, depending on the particular observable we are interested in. It proved to be quite accurate for the study of inclusive responses to weak probes, which explore the whole nuclear volume. In particular, it was successfully used when considering real photon scattering off nuclei in Ref. [106] and for the description of lepton DIS in Ref. [10]. In this Thesis we perform a series of comparisons between the predictions obtained from a SF based on the LDA with those derived from the SF calculated in Ref. [27]. The latter consists of two parts: a shell-model one and a high energy-momentum component (obtained within ab-initio calculations using the LDA).

Assuming the LDA, firstly, one performs the calculation in a nuclear medium of constant density. Then, the result is folded with the density profile of a particular nucleus. We also should mention that the LDA is especially well-suited to use in the MC event generators since for each event a point of interaction can be generated according to the profile $d\sigma/dr$, where r is the distance from the center of a nucleus.

In this Thesis, we use nucleus density profiles from [107, 108, 109]. Lighter nuclei are described by the modified harmonic oscillator model (MHO), while heavier (beyond oxygen) by a Fermi distribution function:

$$\begin{aligned} \text{MHO}: \quad & \rho(r) = \rho_0 \left(1 + a\left(\frac{r}{R}\right)^2\right) \exp\left(-\left(\frac{r}{R}\right)^2\right) \\ \text{Fermi}: \quad & \rho(r) = \frac{\rho_0}{1+\exp((r-R)/a)} \end{aligned} \tag{2.41}$$

The parameters for various nuclei are compiled in Table 2.3. Additionally, we take into account that nucleons are not point-like particles, by means of the prescription described in Sec. II of Ref. [110] [see Eqs. (12-14) of this reference].

In Figs. 2.5 and 2.6 we show the difference between the density distribution with and without this latter effect. As can be seen for heavier nuclei, described by the Fermi distribution function, the effect is quite small.

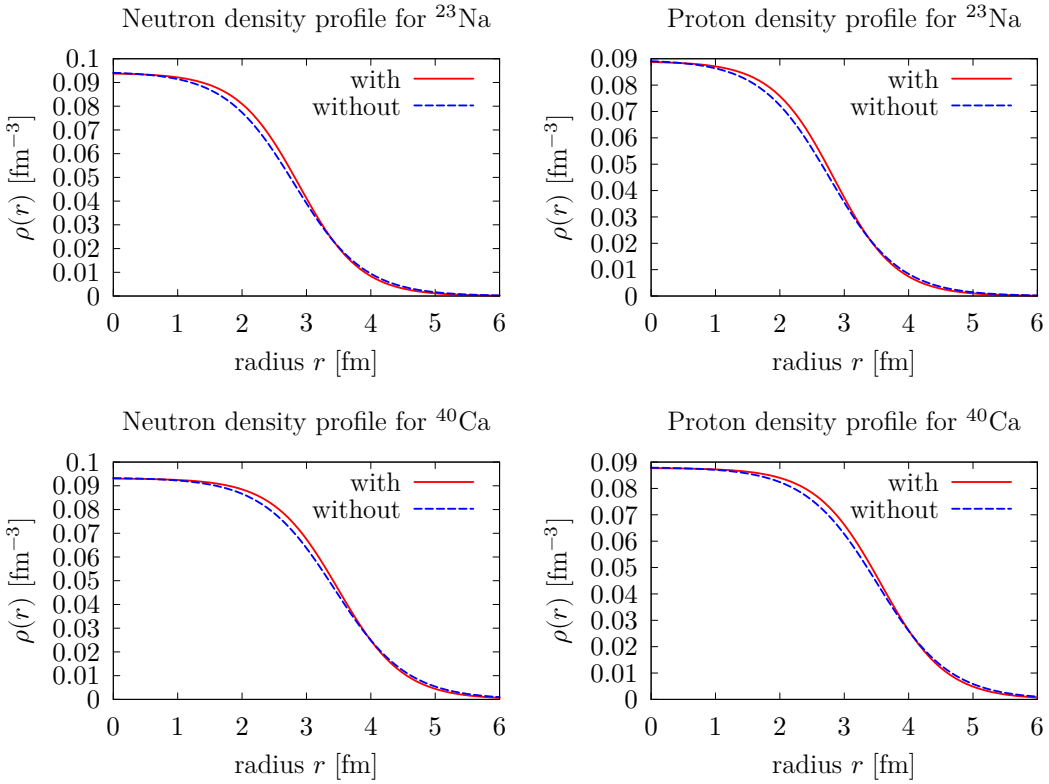

FIGURE 2.6: Comparison of the density profiles for sodium and calcium nuclei with and without taking into account that nucleons are not pointlike. On the left panels – neutron density, on the right ones – proton density.

2.3.3 Nucleon propagator in the nuclear medium. Spectral functions.

Let us consider a many-body system described by a Hamiltonian $\mathscr{H}$ which apart from the kinetic energy (see Eq. (2.34)) has also two-body (and in general many-body) interaction terms. The ground state of the system in the Heisenberg picture obeys a time-independent Schrödinger equation:

$$\mathscr{H}|\Psi_0\rangle = E_0|\Psi_0\rangle \tag{2.42}$$

with E_0, the energy of the ground system, and $|\Psi_0\rangle$ normalized $\langle\Psi_0|\Psi_0\rangle = 1$. Solving Eq. (2.42) (and in general finding excited states, eigenvectors and eigenvalues of the Hamiltonian) is not an easy task, since the system is comprised of strongly interacting particles and it is very difficult to identify convergent perturbative approximations. Some properties of the many-body system, however, can be described in terms of the in-medium fermion propagator (Green's function). This approach, discussed in detail in Ref. [111] simplifies the calculation of higher order corrections in perturbation theory. Also, it can be used to obtain some fundamental observables of the system: the excitation energies and the ground state of the system; or the expectation value of a single particle operator in the ground state (*e.g.* nucleon density operator which will be the topic of Chpt. 5) [105, 111].

Let us start these considerations from the case of a single particle propagation in the free space. The propagator of a particle with quantum numbers α' and energy E from the state α' to the state α is given by

$$G_{\rm sp}(\alpha,\alpha',E) = \langle 0|a_\alpha \frac{1}{E-\mathscr{H}+i\varepsilon} a^\dagger_{\alpha'}|0\rangle \tag{2.43}$$

where $|0\rangle$ represents the vacuum state. If we decompose the Hamiltonian into the kinetic and potential parts

$$\mathscr{H} = \mathscr{H}_0 + U \tag{2.44}$$

and use the operator identity

$$\frac{1}{A-B} = \frac{1}{A} + \frac{1}{A}B\frac{1}{A-B} \tag{2.45}$$

to rewrite the Green's function in terms of $A \equiv E - \mathscr{H}_0$ and $B = U$:

$$\begin{aligned} G_{\rm sp}(\alpha,\alpha',E) =& \langle 0|a_\alpha \frac{1}{E-\mathscr{H}_0+i\varepsilon} + \frac{1}{E-\mathscr{H}_0+i\varepsilon}U\frac{1}{E-\mathscr{H}_0-U+i\varepsilon}a^\dagger_{\alpha'}|0\rangle \\ =& \langle 0|a_\alpha \frac{1}{E-\mathscr{H}_0+i\varepsilon}a^\dagger_{\alpha'}|0\rangle \\ &+ \sum_{\beta,\beta'}\langle 0|a_\alpha \frac{1}{E-\mathscr{H}_0+i\varepsilon}a^\dagger_\beta|0\rangle\langle 0|a_\beta U a^\dagger_{\beta'}|0\rangle\langle 0|a_{\beta'}\frac{1}{E-\mathscr{H}_0-U+i\varepsilon}a^\dagger_{\alpha'}|0\rangle \\ =& G^0_{\rm sp}(\alpha,\alpha',E) + \sum_{\beta,\beta'} G^0_{\rm sp}(\alpha,\beta,E)U(\beta,\beta')G_{\rm sp}(\beta',\alpha',E)\,. \end{aligned} \tag{2.46}$$

where we have introduced a complete set of states and the unperturbed propagator $G^0_{\rm sp}$.

Propagation in the many-body system is defined by either adding or removing a particle from the ground state of $\mathscr{N}$ correlated particles $|\Psi_0\rangle$. A fundamental difference with respect to the vacuum case given by Eq. (2.43), is the fact that we should also consider the propagation of "hole states", which accounts for the fact that a particle can be removed from the system. Let us start from the time representation (we will Fourier transform it to the energy one). Therefore, the one-body Green's function in the nuclear environment is defined as the annihilation of a particle α' at time t' and the creation of a particle α at time t:

$$G(\alpha,t;\alpha',t') = -i\langle\Psi_0|\mathscr{T}[a_\alpha(t)a^\dagger_{\alpha'}(t')]|\Psi_0\rangle \tag{2.47}$$

where $\mathscr{T}$ is the time-ordering operator. The time dependence of the removal and addition operators $a_\alpha(t)$, $a_{\alpha'}(t)^\dagger$ is given by:

$$a_\alpha(t) = e^{i\mathscr{H}t}a_\alpha e^{-i\mathscr{H}t}\,. \tag{2.48}$$

When we insert Eq. (2.48) into Eq. (2.47) we get that the Green's function just depends on the time difference $\Delta t = t - t'$,

$$\begin{aligned} G(\alpha,\alpha';\Delta t) = -i\Big\{ &\theta(\Delta t)\sum_n e^{i(E_0-E_n)\Delta t}\langle\Psi_0|a_\alpha|\Psi_n\rangle\langle\Psi_n|a^\dagger_{\alpha'}|\Psi_0\rangle \\ &- \theta(-\Delta t)\sum_m e^{i(E_0-E_m)\Delta t}\langle\Psi_0|a^\dagger_\alpha|\Psi_m\rangle\langle\Psi_m|a_{\alpha'}|\Psi_0\rangle\Big\} \end{aligned} \tag{2.49}$$

where we have inserted a complete set of intermediate states $|\Psi_n\rangle$, $|\Psi_m\rangle$ with one more and one less particles, respectively. For both cases they are eigenstates of the Hamiltonian $\mathscr{H}|\Psi_{n,m}\rangle = E_{n,m}|\Psi_{n,m}\rangle$. The Fourier transformation from the time to the energy space reads:

$$G(\alpha,\alpha',E) = \int d(\Delta t)\, e^{iE\Delta t}G(\alpha,\alpha',\Delta t) \tag{2.50}$$

Using the representation of the step function in Eq. (2.49):

$$\theta(t-t') = -\int \frac{dE}{2\pi i} \frac{e^{-iE(t-t')}}{E+i\varepsilon} \tag{2.51}$$

and after some further calculation one can obtain $G(\alpha,\alpha',E)$. Taking $\alpha=\alpha'$ in the momentum basis $\alpha \equiv \vec{p}$ (for simplicity we omit spin and isospin dependence):

$$\begin{aligned} G(\vec{p},E) &= \langle\Psi_0|a_p^\dagger \frac{1}{E+(\mathscr{H}-E_0)-i\varepsilon} a_p|\Psi_0\rangle + \langle\Psi_0|a_p \frac{1}{E-(\mathscr{H}-E_0)+i\varepsilon} a_p^\dagger|\Psi_0\rangle \\ &\equiv G_h(\vec{p},E) + G_p(\vec{p},E)\,. \end{aligned} \tag{2.52}$$

We have separated the Green's function into two parts. The particle Green's function G_p describes the propagation of a particle state and therefore it is defined for $E>\mu$, μ being the chemical potential[3], because all the states up to μ are occupied. Whereas G_h is defined for $E\leq\mu$. Eq. (2.52) is the analogue to Eq. (2.43) except for the hole term [105, 111].

The physical interpretation of Eq. (2.52) is the following. If we insert a complete set of eigenstates with either one more or less particles, like in Eq. (2.49), we will get that the poles, which correspond to eigenvalues of the Hamiltonian $\mathscr{H}$, are placed either in E_n-E_0 or E_0-E_m. They signal the position of the excited states of the system with either one additional $|\Psi_n\rangle$ or one removed particle $|\Psi_m\rangle$ (with respect to the ground state). Therefore, it is useful to introduce an object called *spectral function* (SF) which is defined as the probability density of adding or removing a particle of a given momentum $\vec{p}$ and energy E from the ground state. The hole and particle SFs are related to the imaginary-part of the corresponding Green's functions through

$$\begin{aligned} S_h(\vec{p},E) &= +\frac{1}{\pi}\mathrm{Im}G_h(\vec{p},E), \quad E\leq\mu \\ S_p(\vec{p},E) &= -\frac{1}{\pi}\mathrm{Im}G_p(\vec{p},E), \quad E>\mu\,, \end{aligned} \tag{2.53}$$

There is yet another notion worth introducing: the occupation number. It is defined as the momentum distribution of the hole state,

$$n(\vec{p}) = \int_{-\infty}^{\mu} dE S_h(\vec{p},E) \tag{2.54}$$

We will use the occupation number in Chpt. 6, when analyzing the source of scaling breaking in QE processes.

For the GFG introduced in Subsec. 2.3.1, the Green's function takes a simple form

$$G^0_{NR}(\vec{p},E) = \frac{\theta(|\vec{p}|-p_F)}{E-\vec{p}^{\,2}/2M+i\varepsilon} + \frac{\theta(p_F-|\vec{p}|)}{E-\vec{p}^{\,2}/2M-i\varepsilon}\,. \tag{2.55}$$

As has been said before, this treatment of the nuclear physics is nonrelativistic. The starting point of our consideration was the Schrödinger equation Eq. (2.42). However, for a noninteracting system the relativistic expressions of the Green's function are straightforward to obtain (in the case of interacting systems, the problem is much more complex). Using the relativistic dispersion relations $E_p^2 = M^2+\vec{p}^{\,2}$, and introducing the four-vector $p^\mu=(p^0,\vec{p})$, one easily finds

$$G^0(p) = \frac{\theta(|\vec{p}|-p_F)}{p^2-M^2+i\varepsilon} + \frac{\theta(p_F-|\vec{p}|)}{p^2-M^2-i\varepsilon}\,. \tag{2.56}$$

[3]Note that the definition of the thermodynamic limit ($\mathscr{N}\to\infty, V\to\infty$ but $\mathscr{N}/V$ constant) implies $\mu(\mathscr{N}+1) = \mu(\mathscr{N})+\mathscr{O}(\mathscr{N}^{-1})$.

In further applications we will use predominantly relativistic kinematics. Let us notice that by doing the nonrelativistic reduction we obtain

$$G^0(p) = \frac{1}{p^0 + E_p + i\varepsilon}\frac{\theta(p_F - |\vec{p}|)}{p^0 - E_p - i\varepsilon} + \frac{\theta(|\vec{p}| - p_F)}{p^0 - E_p + i\varepsilon}\frac{1}{p^0 + E_p - i\varepsilon}$$

$$\underset{non-rel}{\approx} \frac{1}{2M}\left[\frac{\theta(p_F - |\vec{p}|)}{p^0 - M - \vec{p}^{\,2}/2M - i\varepsilon} + \frac{\theta(|\vec{p}| - p_F)}{p^0 - M - \vec{p}^{\,2}/2M + i\varepsilon}\right], \tag{2.57}$$

where an additional factor $1/2M$ with respect to Eq. (2.55) has appeared.

2.3.4 Nucleon self-energy

In Eq. (2.46) we expressed in general terms a recursive relation to obtain the full propagator in the case of a single particle affected by a potential U. In analogy to this situation, one can consider a many-body system, which Hamiltonian contains two-body (and three-body) interactions between constituent particles. The modification with respect to the noninteracting Green's function is accounted for an irreducible self-energy $\Sigma(\alpha,\alpha;E)$, which depends on the quantum numbers α, α' and in general is a complex quantity. The recursive Dyson equation which relates the Green's function of the interacting system with the noninteracting propagator would read [111]:

$$G(\alpha,\alpha',E) = G^0_{NR}(\alpha,\alpha',E) + \sum_{\beta,\beta'} G(\alpha,\beta,E)\Sigma(\beta,\beta',E)G^0_{NR}(\beta',\alpha',E)\,, \tag{2.58}$$

where G^0_{NR} is a free particle propagator. Eq. (2.58) is diagrammatically depicted in Fig. 2.7. In an infinite nuclear matter, the propagators are diagonal in momentum $\beta = \beta' \equiv \vec{p}$ (for simplicity we neglect spin, isospin, and any other quantum numbers), and we get

$$G(\vec{p},E) = G^0_{NR}(\vec{p},E) + G(\vec{p},E)\Sigma(E,\vec{p})G^0_{NR}(\vec{p},E)\,. \tag{2.59}$$

The solution has the form:

$$G(\vec{p},E) = \frac{1}{E - \vec{p}^{\,2}/2M - \Sigma(E,\vec{p})} \tag{2.60}$$

When the calculation is performed in nuclear matter, we implicitly assume the ρ dependence of Σ and G. In this approximation we can clearly see that the self-energy $\Sigma(E,\vec{p})$ changes the dispersion relations of the fermion and the imaginary part of Σ induces its width in the medium.

From the definition of the spectral functions in Eq. (2.53), we find

$$S_{p,h}(\vec{p},E) = \mp\frac{1}{\pi}\frac{\mathrm{Im}\Sigma(E,\vec{p})}{\left(E - \vec{p}^{\,2}/2M - \mathrm{Re}\Sigma(E,\vec{p})\right)^2 + \mathrm{Im}\Sigma(E,\vec{p})^2} \tag{2.61}$$

with $E \leq \mu$ or $E \geq \mu$ for S_h and S_p respectively. The chemical potential μ in this case does not coincide with the Fermi level of noninteracting particles system. It should be corrected to take into account the fermion self-energy:

$$\mu(p_F) = \frac{p_F^2}{2M} + \mathrm{Re}\Sigma(\mu(p_F),p_F) \tag{2.62}$$

At the Fermi surface we have $\mathrm{Im}\Sigma(\mu(p_F),p_F) = 0$ and it changes sign when crossing energies from $E < \mu$ to $E > \mu$. As before, we have omitted the ρ dependence in the SFs to shorten the

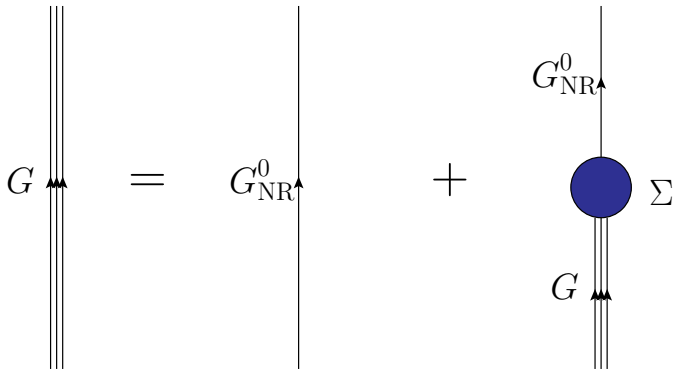

FIGURE 2.7: Dyson equation for the full propagator G, expressed in terms of the noninteracting Green's function G^0_{NR} and the irreducible self-energy Σ.

notation (they depend on the density through the nucleon self-energy).

2.4 Neutrino-nucleus interaction

In analogy to Eq. (2.18), the CC inclusive cross section for scattering of a neutrino on a nucleus can be written as

$$\frac{d^2\sigma}{d\Omega_{k'}dE_{k'}} = \left(\frac{G_F}{2\pi}\right)^2 \frac{|\vec{k}'|}{|\vec{k}|} L_{\mu\nu} W^{\mu\nu} \tag{2.63}$$

The lepton tensor is still given by Eq. (2.19), while the hadron tensor $W^{\mu\nu}$ describes a process which takes place on a nucleus:

$$W^{\mu\nu} = \frac{1}{2M_i}\overline{\sum}_f (2\pi)^3 \delta^4(P_f - P - q) \langle f|j^\mu_{cc}(0)|i\rangle \langle f|j^\nu_{cc}(0)|i\rangle^* \tag{2.64}$$

where M_i is the mass of the initial nucleus and $|i\rangle$, $|f\rangle$ are initial and final nuclear states with momenta P and P_f, respectively. In this context there are other possible dynamical mechanisms contributing to the cross section, apart from those mentioned in Sec. 2.2.1. One that has focused a lot of attention in the neutrino community is the multinucleon knockout, where the scattering takes place on two (or more) nucleons producing two (or more) outgoing nucleons.

The Lorentz structure of the hadron tensor should be built using just the two available vectors, P^μ and q^μ. Starting from the Lorentz invariance of the system, the most general form of the hadron tensor is given in terms of six structure functions,

$$\begin{aligned}\frac{W^{\mu\nu}}{2M_i} =& -g^{\mu\nu}W_1 + \frac{P^\mu P^\nu}{M_i^2}W_2 + i\frac{\varepsilon^{\mu\nu\delta\sigma}P_\delta q_\sigma}{2M_i^2}W_3 + \frac{q^\mu q^\nu}{M_i^2}W_4 \\ &+ \frac{P^\mu q^\nu + P^\nu q^\mu}{2M_i^2}W_5 + i\frac{P^\mu q^\nu - P^\nu q^\mu}{2M_i^2}W_6\,,\end{aligned} \tag{2.65}$$

The structure function W_6 does not contribute to the cross section because its contraction with the lepton tensor vanishes. Thus the W_3 term is the only antisymmetric term that contributes to the cross sections, and induces the differences between neutrino and antineutrino processes. When choosing the reference frame of the static initial nucleus with the momentum transfer in the z direction, $\vec{q} = |\vec{q}|\hat{z}$, the structure functions can be expressed in terms of the hadron tensor

elements:

$$W_1 = \frac{W^{xx}}{2M_i}, \quad W_2 = \frac{1}{2M_i}\left(W^{00} + W^{xx} + \frac{(q^0)^2}{|\vec{q}|^2}(W^{zz} - W^{xx}) - 2\frac{q^0}{|\vec{q}|}\mathrm{Re}W^{0z}\right),$$

$$W_3 = -i\frac{W^{xy}}{|\vec{q}|}, \quad W_4 = \frac{M_i}{2|\vec{q}|^2}(W^{zz} - W^{xx}),$$

$$W_5 = \frac{1}{|\vec{q}|}\left(\mathrm{Re}W^{0z} - \frac{q^0}{|\vec{q}|^2}(W^{zz} - W^{xx})\right), \quad W_6 = \frac{\mathrm{Im}W^{0z}}{|\vec{q}|}. \tag{2.66}$$

In this way we have reformulated our problem, which now conveniently summarizes in calculating W^{xx}, W^{xy}, W^{00}, W^{zz}, W^{0z}. Because of rotational symmetry we also have that $W^{xx} = W^{yy}$. Let us notice that W^{xy} contracts with L_{xy} which is non-zero only for neutrinos (or polarized charged leptons).

The differential CC cross section can be written as [3]:

$$\begin{aligned}\frac{d^2\sigma}{dE_{k'}d\Omega_{k'}} =& \frac{|\vec{k}'|E_{k'}M_iG^2}{\pi^2}\left\{2W_1\sin^2\frac{\theta}{2} + W_2\cos^2\frac{\theta}{2} - W_3\frac{E_k + E_{k'}}{M_i}\sin^2\frac{\theta}{2}\right.\\ &+ \frac{m_\ell^2}{E_{k'}(E_{k'} + |\vec{k}'|)}\left(W_1\cos\theta - \frac{W_2}{2}\cos\theta + \frac{W_3}{2}\left(\frac{E_{k'} + |\vec{k}'|}{M_i} - \frac{E_k + E_{k'}}{M_i}\cos\theta\right)\right.\\ &\left.\left.+ \frac{W_4}{2}\left(\frac{m_\ell^2}{M_i^2}\cos\theta + \frac{2E_{k'}(E_{k'} + |\vec{k}'|)}{M_i^2}\sin^2\frac{\theta}{2}\right) - W_5\frac{E_{k'} + |\vec{k}'|}{2M_i}\right)\right\}.\end{aligned} \tag{2.67}$$

The second part of the above equation depends linearly on the squared mass of the outgoing lepton. For electrons (and even muons) it can be safely neglected, leaving just the first three terms which depend on W_1, W_2 and W_3. The latter one, proportional to W^{xy} does not contribute in the case of charge lepton scattering driven by photon exchange. This way we get the well-known result that the electron scattering can be described in terms of just two structure functions (longitudinal and transverse). Certainly, the prefactor is different in that case, since the intermediate boson is a photon instead of W^+ boson.

2.4.1 Hadron tensor

The expression for the hadron tensor of Eq. (2.64) has a compact form which encompasses many nuclear configurations. Therefore, in general its evaluation is a nontrivial task. To simplify this problem, in our formalism we will adopt the LDA (see Subsec. 2.3.2).

In the following, we will relate the hadron tensor with the self-energy of the gauge boson which travels through the nuclear medium (in the case of neutrino charge-current interaction it will be $W^\pm$). This discussion has been recapitulated in Refs. [6, 3, 4] for EM and CC reactions. It follows the steps:

1. Calculating the self-energy of the incoming lepton in the nuclear medium. It depends on the self-energy of the gauge boson, denoted as $\Pi_W^{\mu\eta}$.

   The self-energy $\Sigma_\nu^r(k;\rho)$ of a neutrino of helicity r and momentum k in nuclear matter of density ρ, at leading order in the Fermi constant, is diagrammatically shown in Fig. 2.8.

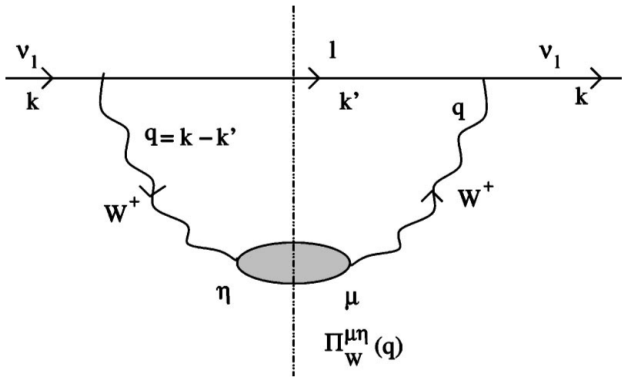

FIGURE 2.8: Neutrino (ν_ℓ) self-energy in the nuclear medium: in first approximation (one boson exchange), the neutrino interacts via a W^+ boson, producing an intermediate lepton state ℓ.

This loop diagram is given by

$$-i\Sigma_\nu^r(k;\rho) = \int \frac{d^4q}{(2\pi)^4}\bar{u}_r(k)\Big[-i\frac{g}{2\sqrt{2}}\gamma_L^\mu iD_{\mu\alpha}(q)(-i)\Pi_W^{\alpha\beta}(q;\rho)$$
$$iD_{\beta\sigma}(q)i\frac{\not{k}'+m_\ell}{k'^2-m_\ell^2+i\varepsilon}(-i\frac{g}{2\sqrt{2}})\gamma_L^\sigma\Big]u_r(k) \qquad (2.68)$$

where we have Dirac spinors $u_r(k)$ projected only to left-handed neutrinos by $\gamma_L^\mu = \gamma^\mu(1-\gamma_5)$, and the $W^\pm$ propagator, which for a low energy transfer becomes $D_{\mu\nu}(q) = -g_{\mu\nu}/M_W^2$ leading to a contact interaction. The sum over lepton spins produces a trace which results in the lepton tensor $L_{\mu\nu}$,

$$\Sigma_\nu(k;\rho) = \frac{8iG_F}{\sqrt{2}M_W^2}\int\frac{d^4q}{(2\pi)^4}\frac{L_{\mu\nu}\Pi_W^{\nu\mu}(q;\rho)}{k'^2-m_\ell^2+i\varepsilon} \qquad (2.69)$$

2. Relating the lepton scattering cross section with the imaginary part of its self-energy, which is computed by means of the Cutkosky cutting rules.
The first step is to relate the imaginary part of the self-energy with the decay width of the particle in the medium,
$$\Gamma(k;\rho) = -\frac{1}{k^0}\mathrm{Im}\Sigma_\nu(k;\rho) \qquad (2.70)$$
To obtain $\mathrm{Im}\Sigma_\nu$ we cut the loops of the Feynman diagram as shown in Fig. 2.8 by a vertical line putting on-shell the intermediate lepton (ℓ) and the particles that are exchanged in the loops of the W self-energy (we have still not shown them explicitly). This allows to perform the integration over the energy, and thus we get for $k^0 > 0$
$$\mathrm{Im}\Sigma_\nu(k;\rho) = \frac{8G_F}{\sqrt{2}M_W^2}\int\frac{d^3k'}{(2\pi)^3}\frac{\theta(q^0)}{2E_{k'}}\mathrm{Im}(L_{\nu\mu}\Pi_W^{\mu\nu}(q;\rho)) \qquad (2.71)$$
Having this result, we next relate the cross section with the decay width of the particle. The probability of decay (interaction) is given by Γdt. The cross section measures the probability of interaction per unit of area, $\sigma = \Gamma dtdS$, and since the integration over time may be related to an integration over space, $dt = vdx$ (where v is the velocity of the particle), we obtain
$$d\sigma = \Gamma dtdS = \Gamma vdxdS = \Gamma vd^3r \qquad (2.72)$$

which leads to

$$\sigma = -\frac{1}{|\vec{k}|}\int \mathrm{Im}\Sigma_\nu(k;\rho)d^3r \tag{2.73}$$

The above derivation has been performed for nuclear matter of a constant density ρ. By means of the LDA, we can obtain results for finite nuclei. At each point of the space, we calculate $\Sigma_\nu(k;\rho(r))$ in infinite nuclear matter of constant-density $\rho(r)$. Then we integrate over the volume (nucleus) taking into account that the density changes with the radius.

Thus, the relation between the inclusive cross section and the gauge boson self-energy reads

$$\sigma = -\frac{1}{|\vec{k}|}\int \mathrm{Im}\Sigma(k;\rho)d^3r = -\frac{1}{|\vec{k}|}\frac{8G_F}{\sqrt{2}M_W^2}\int d^3r\int\frac{d^3k'}{(2\pi)^3}\frac{\theta(q^0)}{2E_{k'}}\mathrm{Im}(L_{\mu\nu}\Pi_W^{\nu\mu}(q;\rho)) \tag{2.74}$$

3. Finally, the comparison of equations (2.63) and (2.74) allows to relate the hadron tensor to the gauge boson self-energy. Decomposing the contraction[4] $L_{\nu\mu}\Pi_W^{\mu\nu}$ we get:

$$\sigma = -\frac{1}{|\vec{k}|}\frac{4G_F}{\sqrt{2}M_W^2}\int d^3r\int\frac{d^3k'}{(2\pi)^3}\frac{\theta(q^0)}{2E_{k'}}\Big(L^s_{\mu\nu}\mathrm{Im}(\Pi_W^{\mu\nu}(q;\rho)+\Pi_W^{\nu\mu}(q;\rho)) - L^a_{\mu\nu}\mathrm{Re}(\Pi_W^{\mu\nu}(q;\rho)-\Pi_W^{\nu\mu}(q;\rho))\Big) \tag{2.75}$$

from where we obtain

$$W_s^{\mu\nu} = -\theta(q^0)\left(\frac{2\sqrt{2}}{g}\right)^2\int\frac{d^3r}{2\pi}\mathrm{Im}(\Pi_W^{\mu\nu}(q;\rho)+\Pi_W^{\nu\mu}(q;\rho))$$

$$W_a^{\mu\nu} = -\theta(q^0)\left(\frac{2\sqrt{2}}{g}\right)^2\int\frac{d^3r}{2\pi}\mathrm{Re}(\Pi_W^{\mu\nu}(q;\rho)-\Pi_W^{\nu\mu}(q;\rho)) \tag{2.76}$$

The self-energy of the gauge boson contains all possible modes of nuclear excitations: $1p1h$, $1p1h1\pi$, $2p2h$, Δh, etc. which are shown in Fig. 2.9, where ph (Δh) stands for the nuclear excitation of a particle–hole ($\Delta(1232)$–hole)) pair [105, 112]. All these contributions were studied in a series of publications [106, 6, 3, 73, 113] for real and virtual photons and CC and NC neutrino inclusive reactions.

2.4.2 The quasielastic mechanism

The QE mechanism has the simplest dynamics of all listed processes in the previous section (first diagram in Fig. 2.9). It corresponds to the situation in which the whole four momentum q is transferred to one nucleon producing a single nucleon in the final state.

The $W^\pm NN$ interaction vertex has already been discussed in Subsec. 2.2.2 in the case of free nucleons. To build the 1p1h loop diagram we also need the nucleon propagator in the nuclear matter introduced in Subsec. 2.3.3.

Let us start with the case of the LFG. Then, the only difference with the situation in the vacuum, are the Pauli blocking factors. For the relativistic case we define

$$S(p;\rho) \quad = (\not{p}+M)G^0(p;\rho) \tag{2.77}$$

[4]Note that lepton tensor splits also into a symmetric and antisymmetric part, i.e., $L_{\mu\nu} = L^s_{\mu\nu} + iL^a_{\mu\nu}$.

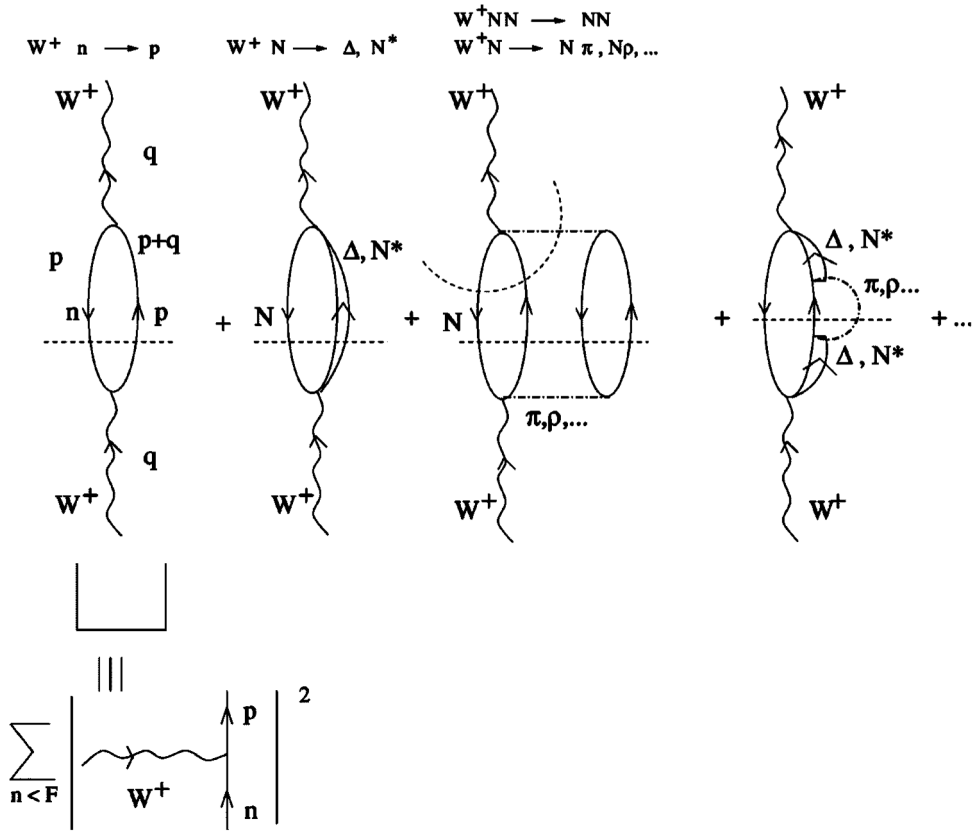

FIGURE 2.9: Different contributions to the W^+ self-energy in nuclear matter.

where $G^0(p;\rho)$ was given in Eq. (2.57). With all these ingredients we can calculate the 1p1h contribution to the W^+ self-energy that reads [4]:

$$-i\Pi_W^{\mu\nu}(q;\rho) = -\left(\frac{g}{2\sqrt{2}}\right)^2 \int \frac{d^4p}{(2\pi)^4} \mathrm{Tr}[\Gamma^\nu(q) S(p;\rho) \bar{\Gamma}^\mu(q) S(p+q;\rho)]$$

$$= -\cos^2\theta_C \left(\frac{g}{2\sqrt{2}}\right)^2 \int \frac{d^4p}{(2\pi)^4} A^{\mu\nu}(p,q) G^0(p;\rho) G^0(p+q;\rho) \qquad (2.78)$$

where $\bar{\Gamma}^\mu = \gamma^0 (\Gamma^\mu)^\dagger \gamma^0$, with the vertex Γ^μ defined as in Eq. (2.22), and the hadron tensor for a single nucleon

$$A^{\mu\nu}(p,q) = \frac{1}{\cos^2\theta_C} \mathrm{Tr}[\bar{\Gamma}^\mu(q)(\not{p}+\not{q}+M)\Gamma^\nu(q)(\not{p}+M)] \qquad (2.79)$$

After integration over p^0 using Cauchy's theorem, we obtain (for isospin symmetric nuclear matter)

$$W^{\mu\nu}(q) = -\frac{\cos^2\theta_C}{2M^2} \int_0^\infty dr r^2 \left\{ -\theta(q^0) \int \frac{d^3p}{(2\pi)^2} \frac{M}{E_p} \frac{M}{E_{p+q}} \delta(q^0 + E_p - E_{p+q}) \right.$$

$$\left. \times\, \theta(p_F(r) - |\vec{p}|)\theta(|\vec{p}+\vec{q}| - p_F(r)) A^{\nu\mu}(p,q)\Big|_{p^0=E_p} \right\} \qquad (2.80)$$

In the above equation we have put both the hole and particle states on-shell by cutting the propagators with the Cutkosky rule. We can see how the hadron tensor (neglecting the interaction vertices in $A^{\nu\mu}(p,q)$) is determined by the imaginary part of the 1p1h propagator, which is also called the Lindhard function [105, 112] or polarization propagator. In Chpt. 5 we will discuss in detail its scaling properties.

Eq. (2.80) can be generalized for the case of asymmetric nuclear matter in a straightforward way, introducing proton and neutron densities $\rho_p \neq \rho_n$. For the CC process, the hole and particle states have different charge, so $\theta(p_F - |\vec{p}|)\theta(|\vec{p}+\vec{q}| - p_F) \to \theta(p_{F\text{hole}} - |\vec{p}|)\theta(|\vec{p}+\vec{q}| - p_{F\text{particle}})$ with Fermi levels obtained using ρ_p or ρ_n.

Finally, we would like to discuss the structure of the hadron tensor from Eq. (2.80). In addition to the Pauli blocking factors, let us notice that the energy conservation function has a simple form $\delta(q^0 + E_p - E_{p+q})$ and it points at the position of the free space QE peak, in the limit of $|\vec{p}| = 0$. In this case we would have $\delta(q^0 + M - E_q)$, which leads to a solution $q^0 = -q^2/2M$. This is exactly the condition which has to be fulfilled in the case of scattering on free nucleons, and it can be understood as a fixed relation between the energy and angle of outgoing lepton. In the FG model we allow the initial nucleons to have momentum below p_F. This provides a spread of a width for the QE peak which becomes larger for growing values of p_F.

In the following chapters we will see how this simple relation for noninteracting nucleons changes when nuclear effects are accounted for, and consequently how it affects the shape of the QE peak.

2.4.3 The Lindhard function for a Fermi gas

The hadron tensor for the QE process is determined by the imaginary part of the $1p1h$ propagator. In the limit of large momentum transfer (where the effect of collective excitation modes can be safely neglected) the polarization propagator in nuclear matter for free Fermi gas reads:

$$\bar{U}(q;\rho) = -2i \int \frac{d^4p}{(2\pi)^4} 2MG^0(p;\rho) 2MG^0(p+q;\rho) \tag{2.81}$$

which is known as the Lindhard function. The factor 2 comes from summing over spins. We do not sum over isospin (which would give another factor 2). In Subsec. 2.5.2 we will introduce $U_N = 2\bar{U}$ which is the nucleon Lindhard function summed over isospin. As we will see, it is used in the denominator of the RPA response function, whose evaluation requires the sum over all possible intermediate ph excitations. Integrating over p^0 we find

$$\bar{U}(q;\rho) = 2 \int \frac{d^3p}{(2\pi)^3} \frac{M}{E_p} \frac{M}{E_{p+q}} \frac{\theta(p_F - |\vec{p}|)\theta(|\vec{p}+\vec{q}| - p_F)}{q^0 + E_p - E_{p+q} + i\varepsilon} + \cdots (q \to -q) \tag{2.82}$$

where some real terms for $q^2 < 4M^2$, and suppressed in the nonrelativistic limit, have been neglected. The contribution of the free space loop function is also included in the definition of Eq. (2.81). For $q^2 \geq 4M^2$, the free space loop gets an imaginary part due to the creation of a nucleon-antinucleon pair (ph excitation of the Dirac instead of the Fermi sea, using the terminology of Ref. [112]), while its logarithmically divergent real part renormalizes the properties (mass and couplings) of the nucleon in the free space. Note that non-zero imaginary parts for $q^2 < 0$ are only produced by ph excitations around the Fermi level.

The imaginary part of $\bar{U}(q;\rho)$ is easily obtained using the distribution identity

$$\frac{1}{\omega \pm i\varepsilon} = \mathscr{P}\left(\frac{1}{\omega}\right) \mp i\pi\delta(\omega) \tag{2.83}$$

where $\mathscr{P}$ stands for the principal value. The second term ($q \to -q$) in Eq. (2.82) describes a crossed term which does not contribute to the imaginary part when $q^0 > 0$, and thus we find

$$\mathrm{Im}\bar{U}(q;\rho) = -\theta(q^0)\int \frac{d^3p}{(2\pi)^2}\frac{M}{E_p}\frac{M}{E_{p+q}}\delta(q^0+E_p-E_{p+q}) \times \theta(p_F-|\vec{p}|)\theta(|\vec{p}+\vec{q}|-p_F) \tag{2.84}$$

which appears between the curly brackets of the expression for the hadron tensor in Eq. (2.80). The integral above may be analytically calculated, even after introducing $A^{\mu\nu}$ as required to find the hadronic tensor for a noninteracting LFG. Expressions can be found in Appendix B of Ref. [3].

The nonrelativistic reduction ($\mathrm{Im}\bar{U}_{\mathrm{NR}}$) of $\mathrm{Im}\bar{U}(q;\rho)$ is found by setting to one the factors M/E_p and M/E_{p+q} and using nonrelativistic nucleon dispersion relations to solve the energy-conserving delta function,

$$\mathrm{Im}\bar{U}_{\mathrm{NR}}(q;\rho) = -\theta(q^0)\int \frac{d^3p}{(2\pi)^2}\delta\left(q^0+\vec{p}^{\,2}/2M-(\vec{p}+\vec{q})^2/2M\right) \times \theta(p_F-|\vec{p}|)\,\theta(|\vec{p}+\vec{q}|-p_F)\,. \tag{2.85}$$

All the integrations involving the tensor $A^{\mu\nu}$ can also be done analytically and are compiled in the Appendix C of Ref. [3] for the nonrelativistic case.

2.4.4 The Lindhard function for interacting systems

In this subsection we will investigate the situation when the nucleons are not free particles. The nuclear effects are accounted for by introducing the self-energy into the nucleon propagator, as it has been discussed in Subsec. 2.3.4.

The Lehmann representation of the dressed nucleon propagator in the nuclear medium can be expressed in terms of the spectral functions [105]:

$$G(E,p;\rho) = \int_{\mu}^{\infty}\frac{S_p(E',p)}{E-E'+i\varepsilon}dE' + \int_{-\infty}^{\mu}\frac{S_h(E',p)}{E-E'-i\varepsilon}dE'\,. \tag{2.86}$$

These modified propagators enter now the definition of the Lindhard function. Since we are interested in the imaginary part of the Lindhard function, we may use Cauchy's residue theorem to obtain

$$\mathrm{Im}\bar{U}_{\mathrm{SF}}(q,\rho) = -\frac{\theta(q^0)}{4\pi^2}\int d^3p\int_{\mu-q^0}^{\mu} dE S_h(E,\vec{p})S_p(q^0+E,\vec{p}+\vec{q})\,. \tag{2.87}$$

It means that for CCQE scattering, one can account for the nucleon self-energy effects in an isospin symmetric nuclear medium of density ρ by modifying Eq. (2.80) accordingly:

$$W^{\mu\nu}(q) = \frac{\cos^2\theta_C}{2M^2}\frac{\theta(q^0)}{4\pi^2}\int_0^{\infty}drr^2\int d^3p\int_{\mu-q^0}^{\mu}dE S_h(E,\vec{p}) \times S_p(q^0+E,\vec{p}+\vec{q})A^{\nu\mu}(p,q)\Big|_{p^0=E_p} \tag{2.88}$$

2.5 Other nuclear effects

Apart from the nuclear effects which are taken into account by means of the spectral functions, we should also consider some further modifications.

Nucleus	Q [MeV]	$\bar{Q}$ [MeV]
^{12}C	16.827	13.88
^{16}O	14.906	10.931
^{18}O	1.144	14.413
^{23}Na	3.546	4.887
^{40}Ca	13.809	1.822
^{44}Ca	3.142	6.170

TABLE 2.4: Parameters Q and $\bar{Q}$ for different nuclei used in this work.

2.5.1 Correct energy balance and Coulomb distortion effects

These corrections are relevant at low energies. When a particle scatters off a nucleus and deposits energy, in the $1p1h$ approximation, it is not fully transferred into the ejected nucleon's energy, but some part goes to compensate the binding energy of the hit bound nucleon. This is taken into account in the $1p1h$ contribution to the self-energy by considering that (we will discuss the situation for CC processes; the modifications for NC or EM ones are straightforward):

1. The initial and final nuclear configurations have different number of neutrons and protons. In that case, some energy Q has to compensate the transition between the initial and final ground states.

2. In an isospin asymmetric nuclear-matter, there is a gap between neutron and proton Fermi levels, so in the calculation of the hadron tensor (Eq. (2.80)) we get already a non-zero energy $Q_{gap}(r)$ which is the minimal energy needed for the process to occur within a LFG. It should be subtracted from the experimental Q value to enforce the correct (experimental) energy balance in the reaction.

This means that in the calculation of the hadronic tensor, we use a shifted value of q^0 (see Ref. [3] for more details),

$$q^0 \to q^0 - (Q - Q_{gap}(r)) \tag{2.89}$$

The Q and $Q_{gap}(r)$ values will be different for neutrino and antineutrino driven processes and in the latter case we will denote them as $\bar{Q}$ and $\bar{Q}_{gap}(r)$. The $Q/\bar{Q}$ values used in this work are collected in Table 2.4.

On the other hand, the charged lepton gets distorted by its electromagnetic interaction with the nucleus which produces a change of its propagation in the nuclear medium. We will implement this effect using the semi-classical approach proposed in Refs. [114, 115, 116], where the self-energy acquired by the charged lepton is taken into account. In a good approximation, this self-energy is proportional to the Coulomb potential created by the nucleus:

$$\Sigma = 2k'^0 V(r) \tag{2.90}$$

where $V(r)$ depends on the charge distribution of the nucleus, $\rho_{\rm ch}(r)$,

$$V(r) = -4\pi\alpha \left[\frac{1}{r} \int_0^r r'^2 \rho_{\rm ch}(r') dr' + \int_r^\infty r' \rho_{\rm ch}(r') dr' \right] \tag{2.91}$$

and α is the fine structure constant. This self-energy will affect both energy and momentum of the lepton, making them local functions depending on r, $E_{k'}(r)$ and $k'(r)$. Asymptotically for $r \to \infty$ we have $E_{k'}(r) \to E_{k'}$ and $k'(r) \to k'$, so that the energy and momentum are conserved in the reaction. From the conservation of energy we have

$$V(r) + E_{k'}(r) = E_{k'} \tag{2.92}$$

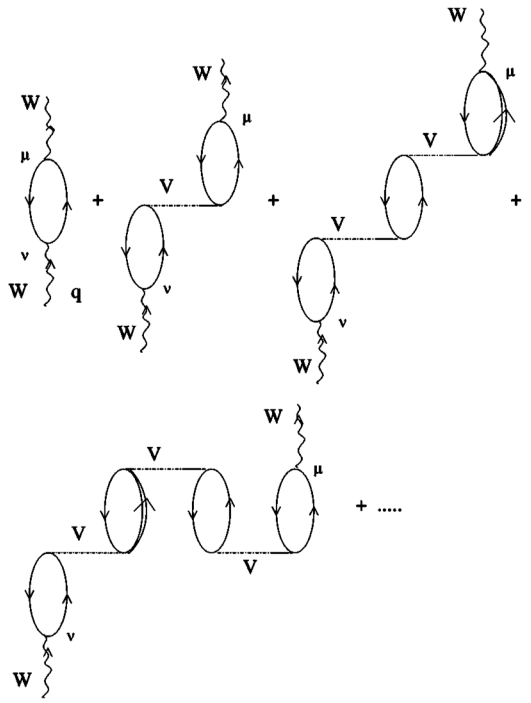

FIGURE 2.10: RPA series of ph and Δh excitations.

and then $|\vec{k}'(r)| = \sqrt{(E_{k'} - V(r))^2 - m_\ell^2}$. This also affects the momentum transfer $\vec{q}(r) = \vec{k} - \vec{k}'(r)$ and should be taken into account in the integration over d^3k' in Eq. (2.71).

Including these effects we get a modified CCQE hadron tensor that now reads

$$W^{\mu\nu}(q) = -\frac{\cos^2\theta_C}{2M^2}\int_0^\infty dr r^2 \frac{|\vec{k}'(r)|E_{k'}(r)}{|\vec{k}'|E_{k'}}\theta(E_{k'}(r) - m_\ell)\left(-\theta(q'^0)\right)$$
$$\int \frac{d^3p}{(2\pi)^2}\frac{M}{E_p}\frac{M}{E_{p+q'}}\delta(q'^0 + E_p - E_{p+q'})$$
$$\times \theta(p_F - |\vec{p}\,|)\theta(|\vec{p} + \vec{q}'| - p_F)A^{\nu\mu}(p,q')\Big|_{p^0=E_p} \tag{2.93}$$

where $q'^0 = q^0 - (Q - Q_{gap}(r))$ and $\vec{q}' = \vec{k} - \vec{k}'(r)$.

Coulomb distortion is rather a small effect for light nuclei, getting only sizable for heavier ones and low energy outgoing charged leptons, when $V(r)$ is of the same order as $E_{k'}$.

2.5.2 RPA

RPA correlations account for some nuclear medium polarization effects sensitive to the collective degrees of freedom of the nucleus. These corrections bear some resemblance with the polarization experienced by a probe charge inside of an electron gas [112]. Within the model employed in [6, 3, 113], a series of ph and Δh excitations (Fig. 2.10), which interact via an effective spin-isospin nonrelativistic potential, is summed up [112].(Also here we are limited to moderate energy and momentum transfers because of the use of nonrelativistic approximations.)

This effective interaction includes a contact Landau-Migdal potential,

$$V = c_0\Big\{ f_0(\rho) + f_0'(\rho)\vec{\tau}_1\cdot\vec{\tau}_2 + g_0(\rho)\vec{\sigma}_1\cdot\vec{\sigma}_2 + g_0'(\rho)\,(\vec{\sigma}_1\cdot\vec{\sigma}_2)\,(\vec{\tau}_1\cdot\vec{\tau}_2)\Big\} \tag{2.94}$$

The constants in Eq. (2.94) were determined from (low energy) calculations of nuclear electric and magnetic moments, transition probabilities, and giant electric and magnetic multipole resonances [117, 118],

$$f_i(\rho(r)) = \frac{\rho(r)}{\rho(0)} f_i^{(in)} + \left(1 - \frac{\rho(r)}{\rho(0)}\right) f_i^{(ex)} \tag{2.95}$$

with

$$f_0^{(in)} = 0.07 \quad f_0^{(ex)} = -2.15 \quad f'^{(in)}_0 = 0.33 \quad f'^{(ex)}_0 = 0.45$$

and $c_0 = 380$ MeV fm^3, $g_0 = 0.575$ and $g'_0 = 0.725$.

In the $S = T = 1$ sector, we improve the interaction and include explicitly pion and ρ meson exchanges, which separate the nonrelativistic potential into transverse and longitudinal channels,

$$c_0 g'_0 (\vec{\sigma}_1\cdot\vec{\sigma}_2)(\vec{\tau}_1\cdot\vec{\tau}_2) \to \vec{\tau}_1\cdot\vec{\tau}_2 \sum_{i,j} \sigma^i \sigma^j V_{ij}^{\sigma\tau} \tag{2.96}$$

$$V_{ij}^{\sigma\tau} = \hat{q}_i\hat{q}_j V_l(q) + (\delta_{ij} - \hat{q}_i\hat{q}_j) V_t(q) \tag{2.97}$$

with $\hat{q} = \vec{q}/|\vec{q}|$ and the longitudinal and transverse potentials given by,

$$V_l(q) = \frac{f^2}{m_\pi^2}\left\{ \left(\frac{\Lambda_\pi^2 - m_\pi^2}{\Lambda_\pi^2 - q^2}\right)^2 \frac{\vec{q}^{\,2}}{q^2 - m_\pi^2} + g' \right\}, \quad f^2/4\pi = 0.08, \quad \Lambda_\pi = 1200\,\text{MeV}$$

$$V_t(q) = \frac{f^2}{m_\pi^2}\left\{ C_\rho \left(\frac{\Lambda_\rho^2 - m_\rho^2}{\Lambda_\rho^2 - q^2}\right)^2 \frac{\vec{q}^{\,2}}{q^2 - m_\rho^2} + g' \right\}, \quad C_\rho = 2, \quad \Lambda_\rho = 2500\,\text{MeV} \tag{2.98}$$

and $g' = 0.63$, as used in [6, 3, 113]. Moreover $\Delta(1232)$ degrees of freedom in the nuclear medium are also considered, which opens the possibility of taking into account Δh excitations in the RPA series, as mentioned above. It affects only the $S = T = 1$ sector and the interaction ph-Δh and Δh-Δh is taken from [119] (see also [112] for details). The RPA sum leads to substitutions in some terms of the hadron tensor obtained within the $1p1h$ approximation (see Appendix A of Ref. [3]). For instance, the $(S = T = 1)-$RPA sum produces, in a schematic way and for a free LFG model, a replacement of the type

$$\begin{aligned} &\text{Im}\bar{U}(q;\rho)\,[a\hat{q}_i\hat{q}_j + b\,(\delta_{ij} - \hat{q}_i\hat{q}_j)] \\ &\quad\to\ \text{Im}\bar{U}(q;\rho)\left[a\frac{\hat{q}_i\hat{q}_j}{|1 - U(q;\rho)V_l(q)|^2} + b\frac{\delta_{ij} - \hat{q}_i\hat{q}_j}{|1 - U(q;\rho)V_t(q)|^2}\right] \end{aligned} \tag{2.99}$$

where $U(q;\rho) = U_N + U_\Delta$ takes into account the ph and the Δh excitations, with $U_N = 2\bar{U}$ (the factor of 2 accounts for a sum over isospin, not explicitly carried out in the definition given in Eq. (2.82)) in a symmetric medium. For positive values of q^0, the backward propagating ph excitation has no imaginary part, and for QE kinematics the $\Delta(1232)$ Lindhard function U_Δ is also real[5]. Nevertheless, we refer the reader to [3] for a detailed description of the RPA resummation within this formalism.

[5] Analytical expressions for U_Δ can be found for example in Ref. [112], while expressions for the real part of the relativistic Lindhard function U_N can be found in Ref. [120]. The corresponding nonrelativistic counterparts, obtained by setting to one the factors M/E_p and M/E_{p+q} and using nonrelativistic nucleon dispersion relations in Eq. (2.82), can be found in Refs. [105, 112].

In this Thesis we would like to focus on the situation when RPA and SF effects are included together. As sketched above, polarization effects are computed by summing up an infinite series of ph and Δh excitations. In principle to be fully consistent, one should include also the nucleon self-energy into all of them, which means that in the denominator of each RPA correction we should have $\bar{U}_{SF}$ instead of $\bar{U}$ (both imaginary and real parts). Moreover one should consider the Δ spectral function in the nuclear medium. All these refinements would introduce further corrections in the density expansion implicitly assumed in the model. However, one should be cautious. The RPA coefficients that appear in the $ph(\Delta\text{h})$–$ph(\Delta\text{h})$ effective interaction were long time ago fitted to data, using a model of noninteracting nucleons [117, 118, 119, 121], and since then, they have been successfully used in several nuclear calculations at intermediate energies, as mentioned. Note that the imaginary part of the $ph-$propagator (the Lindhard function) appears both in the numerators and denominators of Eq. (2.99). Its contribution to the latter ones is in general small because in most of the available phase space, the denominators of the RPA series are being dominated by the real parts, which start by 1 in addition to the $(\mathrm{Re}\,U\,V_{l,t})$ contribution. However, the role of the imaginary part of the $ph-$propagator in the numerators is essential, because it determines the allowed $(q^0,|\vec{q}\,|)$ regions, together with their relative weight into the final response. These allowed regions are obviously different when an interacting LFG or a free LFG of nucleons is being considered. Even in this latter case and for moderate energy and momentum transfers, allowed $(q^0,|\vec{q}\,|)$ regions depend on whether relativistic or nonrelativistic nucleon kinematics is being used. Because our treatment of the RPA and the SF effects is nonrelativistic, this will be an important source of systematic uncertainties affecting our predictions. Later we will come back to this point in more detail.

Thus, we consider $\mathrm{Im}\bar{U}_{SF}$ in the numerators of the RPA series, and to avoid having to retune the RPA parameters which affect the real part of the denominators, we have adopted the following strategy. We leave the real part of the Lindhard function in the RPA denominators unchanged, which for consistency with the $ph(\Delta h)-ph(\Delta h)$ force is computed in the nonrelativistic limit, while we also use SFs to compute the imaginary parts in the denominators. In this manner we remove nonphysical peaks, that would be generated when in the denominator $\mathrm{Im}\bar{U}=0$ and in the numerator $\mathrm{Im}\bar{U}_{SF}\neq 0$. Next and to estimate the theoretical uncertainties, we follow the work of Ref. [122] and we take uncorrelated Gaussian distributions with relative errors of 10%, for all the parameters that enter into the effective interaction employed in the construction of the RPA series. In the case of CC-driven processes, these are $f_0^{\prime(in)}$, $f_0^{\prime(ex)}$, f, f^*, Λ_π, C_ρ, Λ_ρ and g', since the isoscalar terms of the effective interaction do not contribute to CC induced reactions. Finally, by means of a Monte Carlo (MC) simulation, we find for any observable predicted by the model its probability distribution. Theoretical errors and uncertainty bands on the derived quantities will be always obtained by discarding the highest and lowest 16% of the sample values, to leave a 68% confidence level (CL) interval.

Finally, the CC hadron tensor with inclusion of Coulomb distortion, binding energy, RPA and SF effects takes the form:

$$W^{\mu\nu}(q) = \frac{\cos^2\theta_C}{2M^2}\int_0^\infty dr r^2 \frac{|\vec{k}'(r)|E_{k'}(r)}{|\vec{k}'|E_{k'}}\theta(E_{k'}(r)-m_\ell)\theta(q'^0) \times \int \frac{d^3p}{(2\pi)^2}\int_{\mu-q'^0}^{\mu} dE S_h(E,\vec{p})S_p(q'^0+E,\vec{p}+\vec{q}\,')A^{\nu\mu}_{RPA}(p,q')\Big|_{p^0=E_p} \tag{2.100}$$

with $q'^0 = q^0-(Q-Q_{gap}(r))$ and $\vec{q}\,' = \vec{k}-\vec{k}\,'(r)$, as discussed above and $A^{\nu\mu}_{RPA}$ given in Appendix A of Ref. [3], with the real part of the RPA denominators computed using the nonrelativistic reduction of $\bar{U}(q;\rho)$. We recall here that the SFs depend on r through the dependence of the particle and hole self-energies on the local density.

2.5.3 Final state interactions

Final state interactions (FSI) denominate the effects which the nuclear medium exerts on the outgoing hadrons produced in the primary vertex. In the inclusive processes they can be described in terms of the particle spectral functions. They encompass both elastic and inelastic channels which affect a particle on its way through the nuclear medium. However, since the spectral functions are calculated using nonrelativistic theoretical models, usually one ought to account for these effects using a more phenomenological approach.

An important issue from the point of view of neutrino experiments are distributions of outgoing hadrons. In this case, it is not enough to employ the particle SF since it incorporates different channels of interaction, and therefore sums over all possible outgoing states. *E.g.* a produced nucleon in the primary vertex on its way can change trajectory or excite a pion which might be then detected. All these final states observed in the experiment correspond to just one primary mechanism, the QE process.

The MC event generators used in neutrino experiments model lepton-nucleus scattering processes generally splitting them into two stages: (1) calculation of the initial interaction (primary vertex) and (2) the inter-nuclear cascade (which is sometimes also denoted as "final state interactions", although here we will not follow this convention). The cascade is a semi-classical approach to describe the possible interactions that the outgoing particles suffer inside the nucleus before getting outside. What is important to notice is that the cascade does not modify the kinematics of the outgoing lepton (*i.e.* the differential cross section), while the FSI effects which are accounted for by the particle SF do influence the cross section. In order to perform a correct simulation, one has to be careful not to double count the same effect in the FSI and inter-nuclear cascade. Still, this problem is somehow inherent to the procedure, which treats a quantum-mechanical processes using a classical approach.

In this Thesis we will distinguish between the FSI effects which we will be modelled by the particle SF and used to calculate the inclusive cross sections, and those described by the inter-nuclear cascade. The latter ones will be further discussed in Chpt. 6, where we will study the production of strange hyperons.

Chapter 3

Models of spectral functions and other nuclear effects

In the previous chapter we introduced some basic notions used in many-body quantum theory. Among them we defined the one-body Green's functions, the spectral and the Lindhard functions. We have also shown in Subsec. 2.4.2 that the Lindhard function appears as the integration kernel when the hadron tensor of the $1p1h$ process is calculated, and therefore it encompasses the nuclear effects that are included by means of the in-medium modification of the Green's functions. This will be investigated more thoroughly in Chpt. 5 by means of the scaling properties of the response functions.

In this chapter we will focus our attention on the spectral functions. They are a convenient tool widely used by various theoretical groups to account for nuclear effects in the neutrino-nucleus interactions. As already mentioned in the previous chapter, the relativistic regime (which we will mostly consider) might force us to neglect or only approximately take into account nuclear corrections in the particle SF, which − calculated in nuclear models − is usually obtained within nonrelativistic schemes. Nevertheless, the hole SF still can be safely used, because it describes the dynamics of nucleons whose momenta are of the order of few hundred MeV (and typically lie below the Fermi level ~ 250 MeV).

In this respect an important concern arises: since in certain cases we are not able to treat nucleons (both holes and particles) within the same formalism, under what assumptions we are allowed to describe them in terms of different approaches. And consequently, how to account for the particle SF. These questions have been answered differently by various theoretical groups. Before making a survey of the diverse approaches, however, as an introduction, we will briefly discuss the FG model, which is still widely used for experimental studies in the MC event generators. Afterwards, in Sec. 3.2, we will focus on a model for the SFs which is extensively used in this Thesis. It was originally proposed by the Valencia group in Ref. [2]. Here, we will sketch the main assumptions and demonstrate how the calculation is performed. We also show how the SFs obtained within this model differ from those obtained in the FG picture of the nucleus. To that end we will compare the imaginary part of the Lindhard function calculated within both approaches. This discussion is based on the findings of Ref. [4].

Next, we analyze certain approximations to use the particle SF in the relativistic regime. There are two possible solutions which were proposed in the past: either neglecting any interaction between the struck nucleon and the nucleus (*i.e.* using the FG model for the particle SF), or implementing a procedure which would account for some relativistic corrections in the calculation of the nucleon self-energy.

The last section of this chapter is devoted to the description of other theoretical approaches proposed by various groups working on neutrino-nucleus interactions. We will start with and focus mainly on the SF approach of Ref. [27] which assumes the IA and uses the factorization scheme. In further chapters we will perform various comparisons with results obtained in this formalism. In addition to this model, in Subsec. 3.3.2 we will briefly describe how the GiBUU framework treats nucleons in the nuclear medium. The SuperScaling Approach, introduced in

Subsec. 3.3.3, will be interesting from the point of view of the scaling analysis of our response function in Chpt. 5. Next, in Subsec. 3.3.4, we will present a model which is being developed by the Ghent group based on a MF approach incorporating continuum RPA effects. Finally, in Subsec. 3.3.5, we will introduce another RPA scheme which is used by M. Martini and collaborators. The last two approaches include long range correlations (RPA) effects. Although they account for different nuclear dynamics, which go beyond the description in terms of the spectral function formalism, we will perform some comparisons of the predictions of these approaches with the results obtained within the model including RPA effects discussed and outlined in Subsec. 2.5.2.

3.1 Statistical correlations - Fermi gas model

We start our considerations with the most basic model, already introduced in Subsec. 2.3.1. Here we will additionally include a binding energy $B > 0$, understood as a "constant mean-field", which affects the hole states and accounts for the binding of nucleons in the nucleus.

From Eq. (2.55) and the definition of SFs of Eq. (2.53) we obtain for the global Fermi gas of protons or neutrons:

$$\begin{aligned} \bar{S}_h^{\mathrm{GFG}}(\vec{p},E) =& \frac{6\pi^2}{p_F^3}\theta(p_F-|\vec{p}|)\delta(E-\vec{p}^{\,2}/2M+B) \\ S_p^{\mathrm{GFG}}(\vec{p},E) =& \theta(|\vec{p}|-p_F)\delta(E-\vec{p}^{\,2}/2M)\,, \end{aligned} \tag{3.1}$$

where $\bar{S}_h(\vec{p},E) = 2VS_h(\vec{p},E)/\mathscr{N}$ is normalized as

$$\int \frac{d^3p}{(2\pi)^3} dE\, \bar{S}_h(\vec{p},E) = 1\,. \tag{3.2}$$

In the case of the local Fermi gas, the SFs depend on the density because p_F is a function of ρ:[1]

$$\begin{aligned} S_h^{\mathrm{LFG}}(\vec{p},E) =& \theta(p_F-|\vec{p}|)\delta(E-\vec{p}^{\,2}/2M+B)\,, \\ S_p^{\mathrm{LFG}}(\vec{p},E) =& \theta(|\vec{p}|-p_F)\delta(E-\vec{p}^{\,2}/2M)\,. \end{aligned} \tag{3.3}$$

As we can appreciate, the LFG model has just one parameter - the binding energy B. Its value was fixed using data from various experiments on electron scattering off nuclei. In the case of the GFG, there is also the Fermi momentum to be adjusted.

Let us notice that the binding energy enters the energy conserving function in the Lindhard function of the FG model (see Eq. (2.87)):

$$\begin{aligned} \delta(E-(\vec{p}^{\,2}/2M-B))\delta(E+q^0-(\vec{p}+\vec{q})^2/2M) = \\ \delta(q^0+\vec{p}^{\,2}/2M-B-(\vec{p}+\vec{q})^2/2M)\,. \end{aligned} \tag{3.4}$$

It shifts the position of the QE peak towards higher energy transfers $q^0 := q^0 + B$. Actually, B more than an absolute binding energy should be understood as a difference between the MF energy felt by the hole and the particle nucleons.

[1] Let us notice that when we define the Lindhard function in terms of spectral functions, in the case of the LFG we get a result which is ρ-dependent and then should be integrated over the nucleus density profile. This is not the case of the GFG for which we do not perform the latter integration.

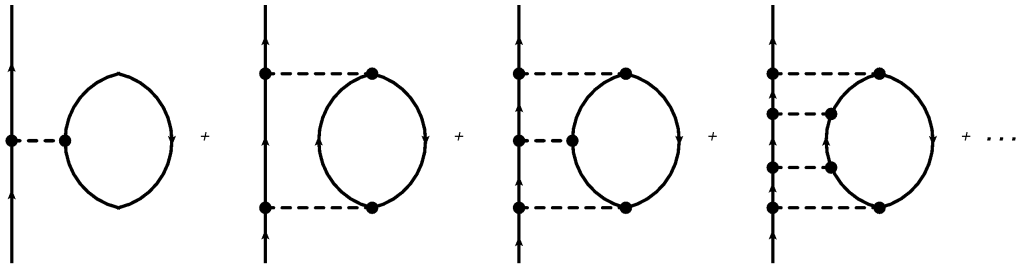

FIGURE 3.1: Series of diagrams which summed up give rise to the nucleon self-energy.

In this simple case, the relativistic expressions are obtained by replacing

$$E - \vec{p}^{\,2}/2M \rightarrow E + M - \sqrt{\vec{p}^{\,2} + M^2} \tag{3.5}$$

in the energy conserving delta functions of Eqs. (3.1) and (3.3).

3.2 LDA SF model

In this Section, we will describe the nucleon SF derived in the semi-phenomenological model of Ref. [2]. In spite of its simplicity, the approach has been successfully used to describe a number of inclusive nuclear reactions [3, 4, 5, 123, 124, 6, 7, 8, 9, 10]. As has been already mentioned, the nuclear calculations are typically performed in a nonrelativistic framework. Besides, the derivation assumes an isospin symmetric nuclear matter. When referring to the SFs obtained within this model we will denote them by “LDA SF", since they are obtained in Ref. [2] using the LDA approximation. In a first step, the nucleon self-energy Σ is obtained, which will determine the Green's function, according to Eq. (2.60).

3.2.1 Nucleon's self-energy

The main idea standing behind this approach, which implements the low-density theorems, is to obtain an effective NN potential in the medium from the experimental NN elastic scattering cross sections. In this way, some short-range correlations are also included, since they affect the input data. In-medium effects are incorporated through polarization corrections (*i.e.* the RPA sum). It has been shown that the resulting SFs obtained within this model stay in good agreement with some of the microscopic calculations of Ref. [125, 126, 127, 128, 129]. For the hole state, the nonrelativistic kinematics is sufficiently accurate, but this is not the case for the nucleon ejected from the nucleus. It usually has a high momentum, that corresponds to the energy-momentum transfer to the nucleus.

To account for the in-medium modifications, the authors of Ref. [2] perform a ladder sum of diagrams as depicted in Fig. 3.1. The dashed lines correspond to the effective in-medium NN potential, obtained from experimental data as has been mentioned above.

Besides performing the sum of Fig. 3.1, there are some further approximations and nuclear effects implemented which are essential to describe properly the behaviour of the nucleons in the nuclear medium. One of them is a prescription of how to extrapolate data, parametrized by the on-shell nucleon momentum in the laboratory frame, to the case of off-shell nucleons. Another one, which plays an important role, is the RPA sum of the series of diagrams depicted in Fig. 3.2. The effective interaction between two $1p1h$ or Δh excitations can be split into longitudinal and transverse parts, originating from pion and ρ meson exchange as we already mentioned in Sec. 2.5.2. Here, the authors of Ref. [2] approximate the potential as being driven by the transverse channel $[\tau_i\tau_j\,\sigma_i\sigma_j(|\vec{q}|^2\delta_{ij} - q_iq_j)]$, neglecting the longitudinal part, which is largely suppressed.

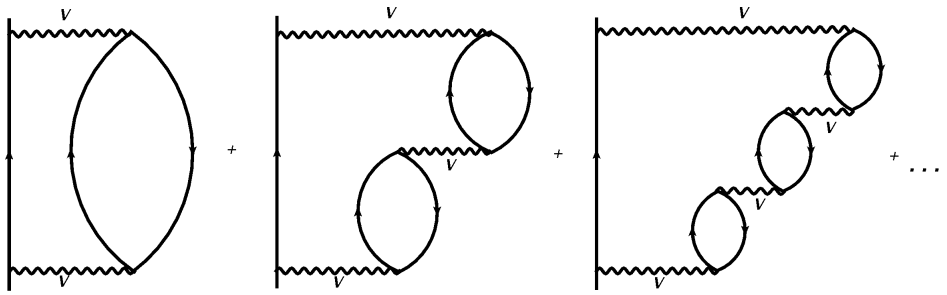

FIGURE 3.2: Series of Feynman diagrams which contribute to the polarization of the NN interaction in the medium.

In the first step of calculation the imaginary part of the self-energy, ImΣ, is evaluated. Its magnitude and behaviour was found to be similar to the results of Refs. [125, 126] obtained in much more elaborated microscopic models. The imaginary part of Σ accounts for the collisional broadening: in the nuclear medium new channels of a particle's "decay" are possible, and even particles which are stable in vacuum (*e.g.* proton) through NN collisions gain some width.

By means of a dispersion relation, the imaginary part of the self-energy can be used to calculate the real part:

$$\mathrm{Re}\Sigma(E,\vec{p}) = -\frac{1}{\pi}\mathscr{P}\int_{\mu}^{\infty}\frac{\mathrm{Im}\Sigma(E',\vec{p})}{E-E'}dE' + \frac{1}{\pi}\mathscr{P}\int_{-\infty}^{\mu}\frac{\mathrm{Im}\Sigma(E',\vec{p})}{E-E'}dE'\,. \tag{3.6}$$

An additional Fock term, depicted as the first diagram in Fig. 3.1, has to be added. It does not contribute to ImΣ, since it is purely real. On top of that, there are some Hartree type diagrams (giving real contributions) not included in the calculations. By definition, they do not depend on the momentum of the nucleon. Therefore, the self-energy in this approach is calculated up to some terms which are not momentum-dependent.

There are many properties of the nucleon in the nuclear medium which can be obtained within this model without further knowledge of the Hartree terms. Among them, there are nucleon momentum distributions or effective masses. These have also been compared with some more advanced calculations of Ref. [127, 129] and proved to give comparable results. It should be clear now that the real part of the self-energy obtained within this model cannot be treated as an absolute value. Nevertheless, in view of further applications in principle it should not pose a problem. We want to use the self-energy as an input to calculate the spectral functions, which subsequently are used in the polarization propagators (Lindhard functions). Therefore, eventually we will deal with $1p1h$ excitations, in which the difference between two nucleon self-energies appear. If both the hole and the particle states contain a part which is constant (momentum independent) they will cancel when the imaginary part of $1p1h$ propagator is being computed.

Since the difference between the real parts of the self-energies is important, in Fig. 3.3 we show them for two different nucleon momenta $(E,\vec{p}\,)$ and $(E+q^0,\vec{p}+\vec{q}\,)$, respectively, as a function of q^0 and $|\vec{q}\,|$. The plots have been done for three different nuclear densities. This difference $\mathrm{Re}\Sigma(E,\vec{p};\rho) - \mathrm{Re}\Sigma(E+q^0,\vec{p}+\vec{q};\rho)$ has a direct impact on the position of the QE peak. We see that the it shifts towards larger energy transfers when the particle-hole state is being "dressed", with respect to the naive approximate position of $q^0 = \vec{q}^{\,2}/2M$. This is because the difference of the real parts of hole and particle self-energies is negative in the vicinity of the naive (free) position of the QE peak.

Concerning the interest in the $2p2h$ excitations [72, 23, 73, 74, 75, 76, 77, 78, 79, 80, 81, 82, 83, 130, 131, 132, 133] we want to stress that there is one contribution of this type taken into account in the nucleon self-energy (although it is only a part of the $2p2h$ calculation performed

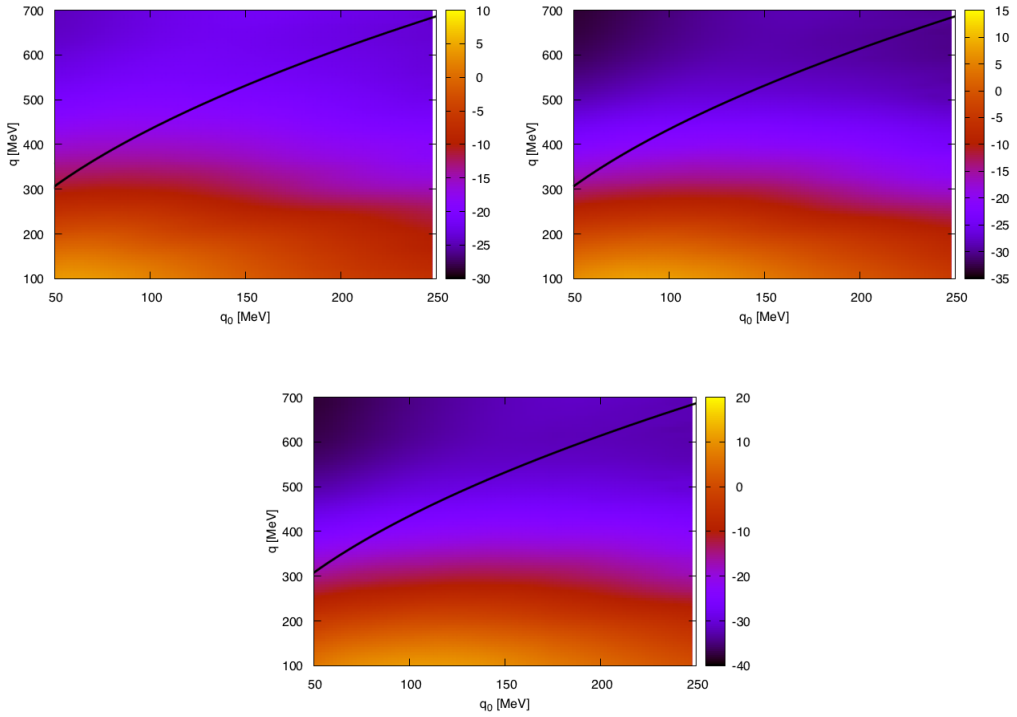

FIGURE 3.3: Difference between the real parts of hole and particle self-energies, *i.e.*, $\mathrm{Re}\Sigma(E,|\vec{p}|;\rho) - \mathrm{Re}\Sigma(E+q^0,|\vec{p}+\vec{q}|;\rho)$, with $(E,p) = (\frac{3}{5}\frac{p_F^2}{2M}, \sqrt{\frac{3}{5}}p_F)$ and $\vec{p}\perp\vec{q}$. Panels correspond to three different densities: $\rho = 0.05\,\mathrm{fm}^{-3}$ (top left), $\rho = 0.1\,\mathrm{fm}^{-3}$ (top right) and $\rho = 0.15\,\mathrm{fm}^{-3}$ (center). Results are displayed in [MeV] units. The contour shows the approximate position of the QE peak, $q^0 = \vec{q}^{\,2}/2M$, for noninteracting nucleons.

in [73]). This is depicted in Fig. 3.4, where the nucleon particle propagator is dressed up by a $1p1h$ excitation. The real part of the total nucleon self-energy, obtained from the imaginary part, also contains information about this $2p2h$ excitation. Even in the approximation where the imaginary part of the nucleon self-energy is neglected in the calculation of the SFs, this $2p2h$ contribution would be partially taken into account.

3.2.2 Lindhard function within the LDA SF approach

Nucleon self-energies directly enter the definition of spectral functions, see Eq. (2.61). They change dispersion relations of nucleons in the nuclear medium, *i.e.* the density response of the system which is proportional to the Lindhard function introduced in Eq. (2.87) of Subsec. 2.4.4.

A word of caution should be added at this point. The result in Eq. (2.87) has a simple form, however it is not easy from a computational point of view. Looking at Eq. (2.61) we may infer that the spectral functions have forms of narrow peaks (see Figs. 10,14,16 of Ref. [2]), especially for energies close to the Fermi level (where $\mathrm{Im}\Sigma(q^0,\vec{q}\,) \to 0$). Moreover, in the case of the LDA SF, $\mathrm{Re}\Sigma(q^0,\vec{q}\,)$ is obtained from the dispersion relation of Eq. (3.6). Therefore, it is result of yet another integration, which is also quite time consuming. Because of the large computational time needed to evaluate the imaginary part of the non-free Lindhard function, it is advisable to introduce approximations that work well in some situations. For energy transfers q^0 high enough, the width of the particle SF is much larger than that of the hole SF (see analysis in Sec. 3.2.5). In this region, one could explore the validity of approximating S_h^{LDA} by a delta

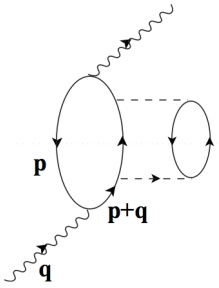

FIGURE 3.4: The 2p2h contribution included in the nucleon self-energy. By cutting the diagram with a horizontal line (Cutkosky cut) we put two hole and two particle states on-shell.

function:

$$S_h^{\rm LDA}(E,\vec{p}\,) = \delta\left(E-\bar{E}(\vec{p}\,)\right)\theta\left(\mu-\bar{E}(\vec{p}\,)\right) \tag{3.7}$$

with $\bar{E}$ being a self-consistent solution of

$$\bar{E}(\vec{p}\,) = \frac{\vec{p}^{\,2}}{2M} + {\rm Re}\Sigma(\bar{E}(\vec{p}\,),\vec{p};\rho) \tag{3.8}$$

This simplification, used in Ref. [3], saves one integration and then we are left with:

$${\rm Im}\bar{U}^{\rm LDA}_{\rm SF\ approx}(q,\rho) = -\frac{\theta(q^0)}{4\pi^2}\int d^3p\, S_p^{\rm LDA}\left(q^0+\bar{E}(\vec{p}\,),\vec{p}+\vec{q}\,\right)\theta(\mu-\bar{E}(\vec{p}\,)) \tag{3.9}$$

The reliability of this approximation will be discussed in detail in Sect. 3.2.5. There, we will see that it is reasonable at intermediate energies, where it leads to cross sections around 5-10% larger than those obtained with the full expression for ${\rm Im}\bar{U}_{\rm SF}(q,\rho)$. Nevertheless, in this Thesis we will not adopt this approximation, and we will present results from the many body model derived in Ref. [3] using either full SFs for both particle and hole nucleon lines, or leaving the particle state free.

3.2.3 Lindhard function with a noninteracting particle SF

As has been mentioned, in the case of relativistic energies, we are interested in using just the hole spectral function, without "dressing" the propagator of the particle state. This amounts to take a hadron tensor of the form:

$$W^{\mu\nu}_{\rm LDA\ IA}(q) = \frac{\cos^2\theta_C}{2M^2}\theta(q^0)\int d^3r\int\frac{d^3p}{(2\pi)^3}\int_{\mu-q^0}^{\mu} dE\, S_h^{\rm LDA}(E,\vec{p}\,)\frac{M^2}{E_p E_{p+q}} \times\theta(|\vec{p}+\vec{q}|-p_F)\delta(q^0+E+M-E_{p+q})A^{\nu\mu}(p,q)\Big|_{p^0=E_p} \tag{3.10}$$

and the corresponding Lindhard function would now read

$${\rm Im}\bar{U}^{\rm LDA\ IA}_{\rm SF}(q,\rho) = -\frac{\theta(q^0)}{4\pi^2}\int d^3p\int_{\mu-q^0}^{\mu} dE\, S_h^{\rm LDA}(E,\vec{p}\,)\frac{M^2}{E_p E_{p+q}} \times\theta(|\vec{p}+\vec{q}|-p_F)\delta(q^0+E+M-E_{p+q})\,. \tag{3.11}$$

This cannot be directly done in the approach outlined in the previous subsection. The model of Ref. [2] does not give a prescription of how to calculate the constant, density dependent, contribution to the real part of the nucleon self-energy generated by Hartree-type diagrams. Nevertheless, one can estimate appropriate (absolute) values for the real part of the nucleon-hole

self-energy by looking at the binding energy per nucleon. We follow here Ref. [5], where the EMC effect was studied using the nucleon self-energy derived in [2], and include phenomenologically a constant term $C\rho$ in ReΣ requiring the binding energy per nucleon, $|\varepsilon_A|$, to be the experimental one. When the constant term $C\rho$ is added, the chemical potential becomes:

$$\mu = \frac{p_F^2}{2M} + \widehat{\mathscr{C}}, \quad \widehat{\mathscr{C}} = \mathrm{Re}\Sigma(p_F^2/2M, p_F) + C\rho \tag{3.12}$$

and the SFs are now

$$S_{p,h}^{\mathrm{LDA}}(\vec{p},E) = \mp\frac{1}{\pi}\frac{\mathrm{Im}\Sigma(\widehat{E},\vec{p})}{\left(E - \vec{p}^2/2M - \mathrm{Re}\Sigma(\widehat{E},\vec{p}) - C\rho\right)^2 + \mathrm{Im}\Sigma(\widehat{E},\vec{p})^2} \tag{3.13}$$

where we have used a notation $\widehat{E} \equiv E - \widehat{\mathscr{C}}$.

The binding energy per nucleon is then given by the sum rule [11]

$$|\varepsilon_A| = -\frac{1}{2}\left(\langle E\rangle + \frac{A-1}{A-2}\langle T\rangle\right) \tag{3.14}$$

where T and E are average kinetic and removal energies, respectively, expressed in terms of the hole SF [5]:

$$\begin{aligned}\langle T\rangle &= \frac{4}{A}\int d^3r \int \frac{d^3p}{(2\pi)^3}\frac{\vec{p}^{\,2}}{2M}\int_{-\infty}^{\mu} S_h(\vec{p},E)dE\,,\\ \langle E\rangle &= \frac{4}{A}\int d^3r \int \frac{d^3p}{(2\pi)^3}\int_{-\infty}^{\mu} S_h(\vec{p},E)EdE\,,\end{aligned} \tag{3.15}$$

where A is the number of nucleons in the system.

The parameter C in carbon (which we will mainly use in our further calculations) turns out to be around 0.8 fm^2. This leads to $|\varepsilon_A| = 7.8$ MeV (see Table I of Ref. [5]) and provides around 25-30 MeV repulsion at density $\rho = 0.17$ fm^{-3}.

It has to be noted that the results of Ref. [2] are not affected by the momentum-independent term added to the self-energy, as they only depend upon energy differences. Analogously, the Lindhard function given in Eq. (2.87) does not depend on $C\rho$, as this term can be removed by the change of integration variable $E \to \widehat{E}$. Indeed, this change of variable leads to an expression like that of Eq. (2.87), with particle and hole spectral functions and chemical potential given in Eqs. (2.61) and (2.62), but with Re$\Sigma(E,\vec{p})$ replaced by Re$\Sigma(E,\vec{p}) -$ Re$\Sigma(p_F^2/2M, p_F)$. Note also that the new integration limits become $p_F^2/2M$ and $p_F^2/2M - q^0$. This is precisely the result that one would obtain within the semi-phenomenological model of Ref. [2], where the calculations of the self-energy were performed assuming only kinetic energies for the nucleon and the self-energies were always referred to the value at the Fermi surface. If $C\rho$ is neglected in Eqs. (3.12) and (3.13), one obtains exactly the same expression for the response function.

Knowing the absolute values of ReΣ, we can perform some comparisons with other calculations and approaches. The first check will be done with energy-dependent Dirac optical model potentials for several nuclei which were given in [134]. They were obtained by fitting proton-nucleus elastic scattering data for the energies of the range 20-1040 MeV. This approach has been widely employed in analyses of electron-induced proton knockout [135]. It uses scalar (S) and vector (V) complex potentials in the Dirac equation, and the dependencies of these potentials on the kinetic energy, t_{kin}, and radial coordinate, r, are found by fitting the scattering solutions to the measured elastic cross section, analyzing power, and spin rotation function. Schrödinger equivalent (SE) potentials, constructed out of the scalar and vector potentials, are also given in [134].

In the left panel of Fig. 3.5, we compare the SE ^{208}Pb central potentials displayed in the top panel of Fig. 6 of Ref. [134] for $t_{\rm kin} = 20$ MeV and 100 MeV with $\mathrm{Re}\Sigma(M + t_{\rm kin} = M + \vec{q}^{\,2}/2M, \vec{q}; \rho)$, as a function of r. We reproduce quite well the Wood-Saxon form of the potentials, which is not surprising since the model of Ref. [2] satisfies the low densities theorems, and describe simultaneously the results for both kinetic energies.

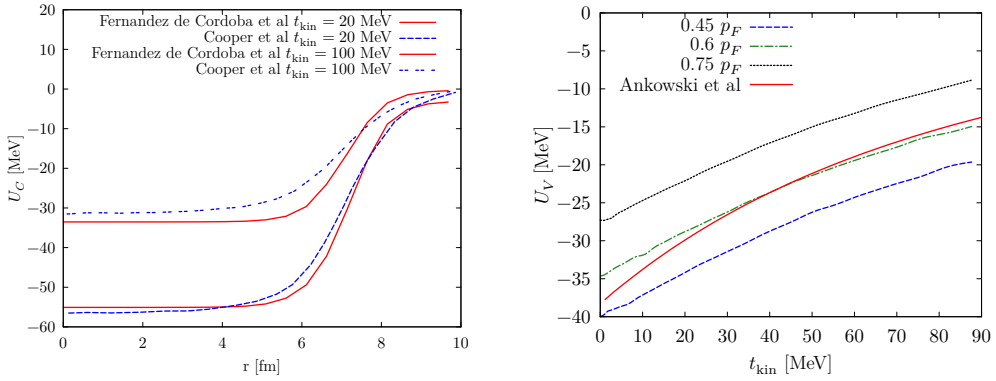

FIGURE 3.5: Left: The dashed lines stand for the Schrödinger equivalent central potentials, taken from the top panel of Fig. 6 of Ref. [134], for $t_{\rm kin} = 20$ MeV and 100 MeV in ^{208}Pb. The solid lines show $\mathrm{Re}\Sigma(M + t_{\rm kin}, \vec{q}; \rho)$ obtained with the model of Ref. [2], with $t_{\rm kin} = \vec{q}^{\,2}/2M$. Right: The solid line (red) shows the real part of the carbon optical potential for proton, obtained from the Dirac phenomenological fit of Ref. [134] and taken from the Fig. 1 of Ankowski et al., [14], as a function of the nucleon kinetic energy. Also in the right panel, the dashed, dashed-dotted and dotted lines show the results obtained from Eq. (3.19) for three different values of the modulus of the hole (local) momentum. In all cases we take $\vec{p} \perp \vec{q}$. Both in the left and right panels, we add a constant term $C\rho$, with $C = 0.8$ fm^2, to the real part of the nucleon self-energy,

Another comparison which can be done, is to check further the energy-dependence of the real part of the self-energy. Using the scalar and vector potentials as defined in Ref. [134], we can write the total proton energy $E'_{\rm tot}$ as

$$E'_{\rm tot} = \sqrt{(M+S)^2 + \vec{p}^{\,\prime 2}} + V\,. \tag{3.16}$$

In Ref. [14], the authors defined a kinetic-energy dependent potential (when only the real parts are taken, and for in-medium energy $E'_{\rm tot}$) as

$$U_V(t_{\rm kin}) = \int d^3r \rho(r) \mathrm{Re}(E'_{\rm tot}) - \sqrt{M^2 + \vec{p}^{\,\prime 2}}, \qquad t_{\rm kin} = \sqrt{M^2 + \vec{p}^{\,\prime 2}} - M\,. \tag{3.17}$$

Its behaviour is shown in Fig. 1 of Ref. [14] for carbon. The potential U_V is used in this reference to modify the energy spectrum of the outgoing nucleon (thus, playing the role of the particle spectral function):

$$t_{\rm kin} = \frac{|\vec{k}|^2(1-\cos\theta')}{M + |\vec{k}|(1-\cos\theta')}, \tag{3.18}$$

with $|\vec{k}|$ and θ' denoting the energy of the beam of (massless) particles and the angle of the outgoing lepton, respectively. The region of low $t_{\rm kin}$, which is especially important for the QE scattering, is strongly modified by the interactions between the outgoing proton and the spectator system [14].

It means that we assume $t_{\rm kin} = q^0$ and $q^0 = -q^2/2M$. The outgoing nucleon has a momentum $\vec{p} + \vec{q}$ (with $\vec{p}$ being the hole state momentum). Thus the potential U_V can be estimated as

$$U_V(t_{\rm kin}) \sim \frac{1}{A}\int d^3r \rho(r) \bar{E}(\vec{p}+\vec{q}) - \frac{\vec{q}^{\,2}}{2M}, \quad t_{\rm kin} = \frac{\vec{q}^{\,2}}{2M} \tag{3.19}$$

with $\bar{E}(\vec{p})$ being a self-consistent solution of Eq. (3.8). In the right panel of Fig. 3.5, we show results obtained with the model of Ref. [2] for ReΣ, supplemented with the constant term $C\rho$, for three different values of the hole (local) momentum ($p \propto p_F(r)$) and compare with the potential obtained from the fits carried out in Ref. [134]. We find a reasonable agreement with similar dependencies on $t_{\rm kin}$ and differences in the magnitude of the potential of the order of $5-10$ MeV at most, which could be partially re-absorbed either by modifying the parameter C or using an appropriate average momentum. The comparisons in Fig. 3.5 are sensitive to the absolute values of ReΣ.

3.2.4 Relativistic approximation

In the calculations presented in the previous subsections, we have assumed nonrelativistic kinematics. In order to account for the relativistic effects in the calculation of the self-energies, the M/E_p factors can be included in the phase space. Also the nucleon's energy, E_p, is calculated including some relativistic corrections.

Following Ref. [5, 123], the relativistic version of the SFs reads now

$$S^{\rm LDA\ rel}_{p,h}(\vec{p},E) = \mp\frac{1}{\pi}\frac{\frac{M}{E_p}{\rm Im}\Sigma(E,\vec{p})}{\left(E+M-E_p-\frac{M}{E_p}{\rm Re}\Sigma(E,\vec{p})\right)^2+\left(\frac{M}{E_p}{\rm Im}\Sigma(E,\vec{p})\right)^2}, \tag{3.20}$$

This equation has been derived noting that the self-energy operator is diagonal in the spin space if we consider nucleons submerged into spin and isospin symmetric nuclear matter. Also, Σ is a short-notation for $\bar{u}\Sigma u$ with spinors $\bar{u}$ and u being dimensionless normalized to unity.

3.2.5 Analysis of spectral function effects

As we have shown in Eq. (2.100) for the inclusive neutrino-nucleus and will show in Eqs. (4.11) and (4.15) for the muon and radiative pion captures in nuclei, the cross sections of these processes depend on the imaginary part of the Lindhard function[2] Im$\bar{U}_{SF}$. In the case of pion capture this dependence is direct, while for a CC process the situation is more complicated because the interaction vertex gives rise to the $L_{\mu\nu}W^{\mu\nu}$ contraction, inducing a dependence of the $A^{\mu\nu}(p,q)$ tensor on the hole momentum p. Thus, we will present first a short analysis of the SF effects on the imaginary part of Lindhard function for two different energy regimes. Both, real and imaginary parts of the particle and hole self-energies enter into the evaluation of Im$\bar{U}_{SF}$. As mentioned above, the real part modifies the dispersion relation of the nucleon embedded in the nuclear medium, while the imaginary part accounts for some many-body decay channels.

In Ref. [3], the imaginary part of the hole self-energy was neglected (see Eq. (3.7)) to save computational time. We will discuss below that, though this approximation could be reasonable for intermediate neutrino energies, it is not appropriate for low nuclear excitation energies. Moreover, for intermediate energies, we will show that the approximation of Eq. (3.7) overestimates the cross sections by around 5-10%. Given that highly accurate theoretical predictions are essential to conduct the analysis of neutrino properties, here we will improve on this and in Subsec. 4.2.2, neutrino and antineutrino cross sections for argon, carbon and oxygen targets will be obtained using the full particle and hole SFs.

Low energy transfers

For low energy transfers, q^0, we should take into account the width of the hole state (imaginary part of the nucleon self-energy) going beyond the approximation of Eq. (3.7). The reason can

[2]For the sake of clarity, in this section we will omit the arguments of the Lindhard function when possible.

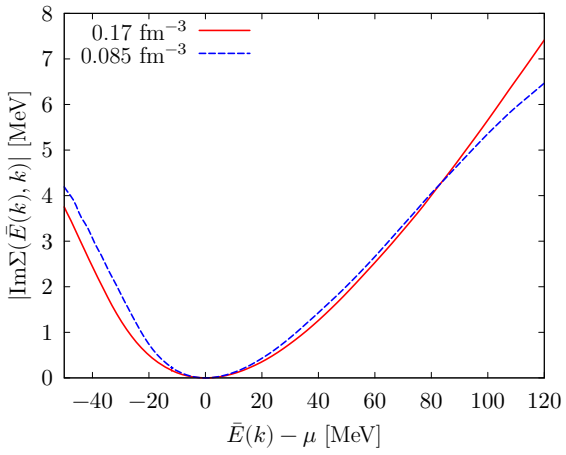

FIGURE 3.6: $\mathrm{Im}\Sigma(\bar{E}(k),k)$ as a function of $\bar{E}(k)$ (self-consistent solution of Eq. (3.8)) calculated for two different nuclear matter densities using the model of Ref. [2].

be understood from the results of Fig. 3.6. There, we show the imaginary part of the self-energy $\mathrm{Im}\Sigma(\bar{E}(k),\vec{k};\rho)$ as a function of the energy $\bar{E}(k)$, with $\bar{E}$ being the solution of Eq. (3.8), and two different nuclear matter densities. We have adopted the model derived in Ref. [2]. Naturally, there is a lower limit for $\bar{E}$, when the momentum is equal to 0, and an upper limit to be consistent with the nonrelativistic approximations. There exists a minimum at the Fermi surface ($\bar{E}(p_F)=\mu$), and in its vicinity, both the hole and particle state widths are of the same magnitude, while for higher energies the imaginary part of the particle self-energy grows and it becomes in modulus significantly larger than the typical values taken by that of the hole state. Hence, it is not justified to neglect the hole width in the low excitation-energy regime, while for higher energy transfers keeping it is much less important.

In Fig. 3.7 we show both $\mathrm{Im}\bar{U}_{\mathrm{SF}}^{\mathrm{LDA}}$ (using Eq. (2.87) with the SFs obtained with the LDA model of Ref. [2]) and the approximated $\mathrm{Im}\bar{U}_{\mathrm{SF\,approx}}^{\mathrm{LDA}}$ (see Eq. (3.9)), obtained from Eq. (3.7) when S_h is replaced by a delta function. The full calculation leads to smaller values (in modulus), which can be even better appreciated if we compare a profile of this 3D plot. For this, we use the energy-momentum dependence from muon and pion capture kinematics, *i.e.*, $\mathrm{Im}\Sigma(q^0,|\vec{q}|;\rho)=\mathrm{Im}\Sigma(q^0=m_{\mu/\pi}-|\vec{q}|-Q_{\mu/\pi},|\vec{q}|;\rho)$, for $\rho=0.074$ fm^{-3} in ^{12}C ($Q_{\mu/\pi}$ accounts for the binding energy effects and the existing difference between the experimental Q values and those deduced from the isospin-asymmetric LFG picture of the nucleus). Results are shown in Fig. 3.8, where we can see that the difference induced by keeping the imaginary part of the nucleon self-energy in the hole state could reach 30% at the peak. Let us remind here that the integration over a function which contains two delta-like peaks is highly demanding from a computational point of view. Fig. 3.6 shows that as the excitation energy approaches the Fermi surface, the widths of both, particle and hole, SFs are getting smaller, making both SFs similar to delta functions. This is why for very low energy transfers, of the order of few MeV, the calculation may show some numerical instabilities, as can be appreciated in Fig. 3.8.

Finally, in Fig. 3.9 we show the ratio $\mathrm{Im}\bar{U}_{\mathrm{SF}}^{\mathrm{LDA}}/\mathrm{Im}\bar{U}_{\mathrm{SF\,approx}}^{\mathrm{LDA}}$ for low energy and momentum transfers, where the error induced by neglecting the hole width can be better appreciated.

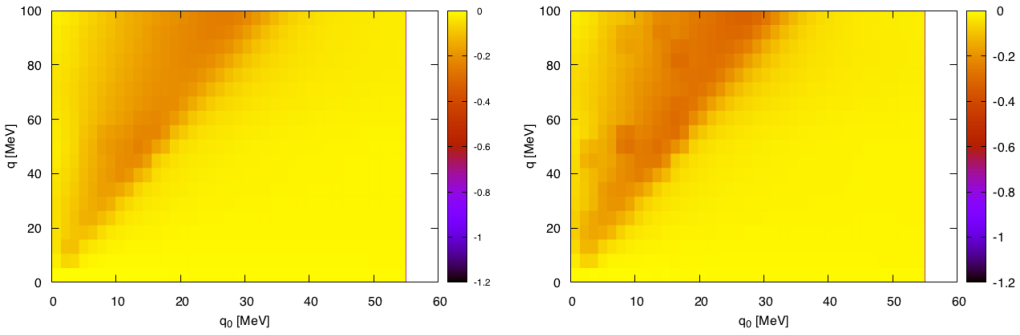

FIGURE 3.7: Comparison of $\mathrm{Im}\bar{U}^{\mathrm{LDA}}_{\mathrm{SF}}(q^0,q;\rho)$ computed from Eq. (2.87) keeping the width of both particle and hole lines (left) and the approximated $\mathrm{Im}\bar{U}^{\mathrm{LDA}}_{\mathrm{SFapprox}}$ (Eq. (3.9)) obtained by neglecting the imaginary part of the hole self-energy (right). The density employed is $\rho = 0.09$ fm^{-3} and the Lindhard functions are displayed in [fm^{-2}] units.

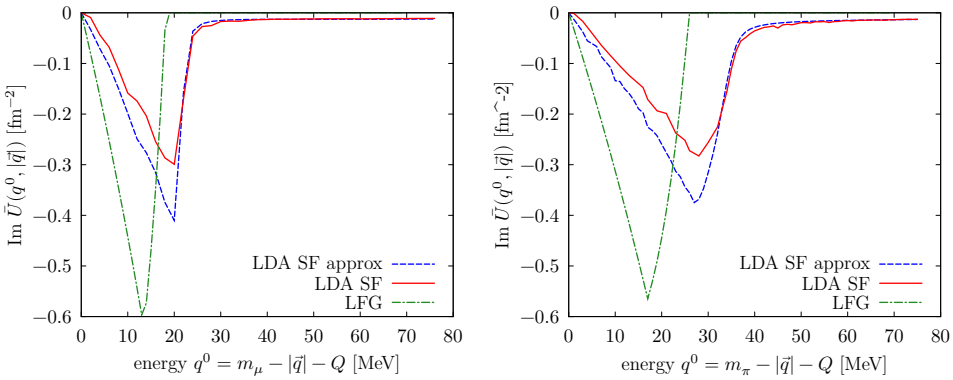

FIGURE 3.8: Comparison of different approaches to $\mathrm{Im}\bar{U}(q^0,|\vec{q}|;\rho)$ as a function of q^0 in ^{12}C and $\rho = 0.074$ fm^{-3}. Inclusive muon/pion capture kinematics is used and hence $|\vec{q}| = m_\mu - q^0 - Q_\mu$ (left) and $|\vec{q}| = m_\pi - q^0 - Q_\pi$ (right). The dashed-double dotted green curves stand for the imaginary part of the Lindhard function computed in a free LFG using nonrelativistic kinematics.

Intermediate energy transfers

In Fig. 3.10, we show $\mathrm{Im}\bar{U}^{\mathrm{LDA}}_{\mathrm{SF}}$ and the imaginary part of the free LFG nonrelativistic Lindhard function, $\mathrm{Im}\bar{U}_{\mathrm{NR}}$ (Eq. (2.85)), in a wider energy region. We clearly observe[3] that $\mathrm{Im}\bar{U}^{\mathrm{LDA}}_{\mathrm{SF}}$ (on the left) takes non-zero values in a much wider part of the $(q^0,|\vec{q}|)$ available phase-space. In the case of $\mathrm{Im}\bar{U}_{\mathrm{NR}}$ (on the right), there is a very well marked band of nonzero values. On the other hand, $\mathrm{Im}\bar{U}_{\mathrm{NR}}$ takes values generally lower (larger in absolute value) than $\mathrm{Im}\bar{U}^{\mathrm{LDA}}_{\mathrm{SF}}$. These effects are clearly visible in Fig. 3.11, where $\mathrm{Im}\bar{U}^{\mathrm{LDA}}_{\mathrm{SF}}$ and $\mathrm{Im}\bar{U}_{\mathrm{NR}}$ for $|\vec{q}| = 300$ MeV and density $\rho = 0.09$ fm^{-3} are displayed. Although this plot cannot be directly compared with the cross section for neutrino scattering, one may expect that the SF corrections would move the position of the QE peak (the dispersion relation of a nucleon embedded in the nuclear medium is different because the effects of $\mathrm{Re}\Sigma(q^0,|\vec{q}|;\rho)$; see also Fig. 3.3) and this peak would be generally lower, with a partial, but sizable, spreading of its strength.

In Fig. 3.11, we also show results for $\mathrm{Im}\bar{U}^{\mathrm{LDA}}_{\mathrm{SF\ approx}}$, as a function of the energy transfer. We see that though the approximation of Eq. (3.7) used in Eq. (3.9) works better than for low energies, it produces values of $\mathrm{Im}\bar{U}^{\mathrm{LDA}}_{\mathrm{SF}}$ (in modulus) around the QE peak systematically larger ($\sim 7\%$) than those obtained when the width of the hole state is maintained. The largest part

[3] Note that in the high energy and momentum transfer region, there will be relativistic effects not considered in the plots of Fig. 3.10.

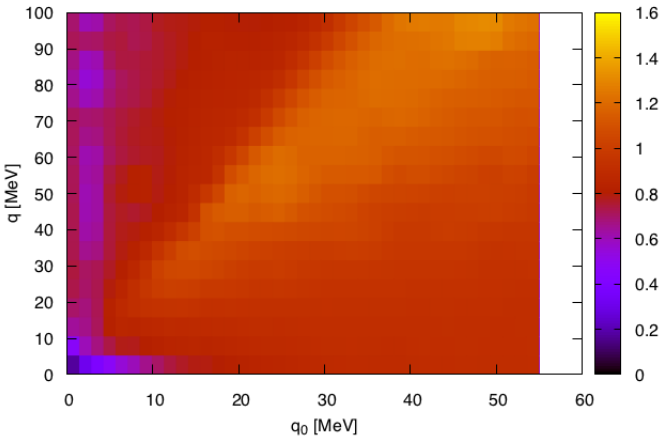

FIGURE 3.9: Ratio of $\mathrm{Im}\bar{U}^{\mathrm{LDA}}_{\mathrm{SF}}/\mathrm{Im}\bar{U}^{\mathrm{LDA}}_{\mathrm{SF\ approx}}$ for $\rho = 0.09$ fm^{-3}.

of this enhancement is produced for having neglected in Eq. (3.7) the inverse of the Jacobian determinant

$$\left|1-\frac{\partial \mathrm{Re}\Sigma(E,\vec{p})}{\partial E}\right|^{-1}_{E=\bar{E}(\vec{p})}, \tag{3.21}$$

that appears in the reduction of $S_h^{\mathrm{LDA}}(E,\vec{p})$ to $\delta\left(E-\bar{E}(\vec{p})\right)$, when the $\mathrm{Im}\Sigma(E,\vec{p})\to 0$ limit is taken. The above factor is the quasiparticle strength and it is related to the inverse of the effective mass [129].

Computing the partial derivative of $\mathrm{Re}\Sigma(E,\vec{p})$ is also numerically involved, and since accurate theoretical cross sections are important to conduct neutrino oscillation analyses, here we improve the predictions presented in Ref. [3], by considering full SF effects also at intermediate energies. Thus in Subsec. 4.2.2, we will show results obtained using fully dressed particle and hole propagators, maintaining both real and imaginary parts of the in-medium nucleon self-energies.

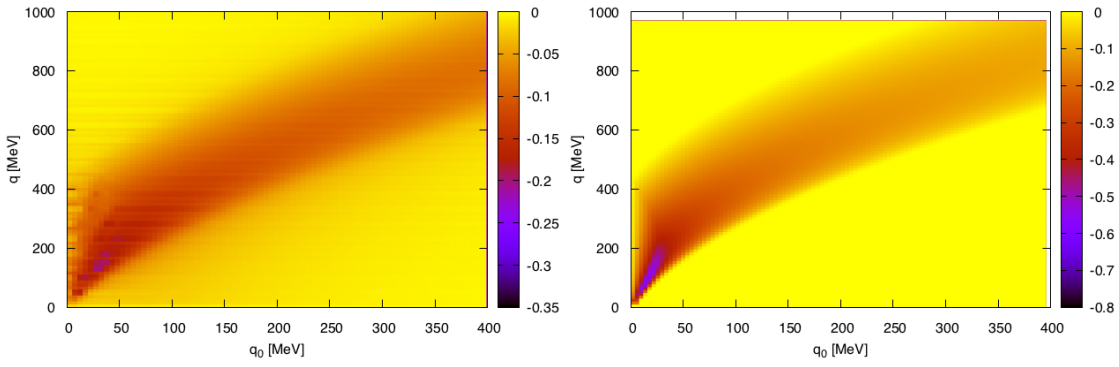

FIGURE 3.10: Imaginary parts of the full LDA SF and the free LFG Lindhard functions in fm^{-2} units and for density $\rho = 0.09$ fm^{-3}. On the left, we show results for $\mathrm{Im}\bar{U}^{\mathrm{LDA}}_{\mathrm{SF}}$, while on the right panel the noninteracting LFG $\mathrm{Im}\bar{U}_{\mathrm{NR}}$ is depicted.

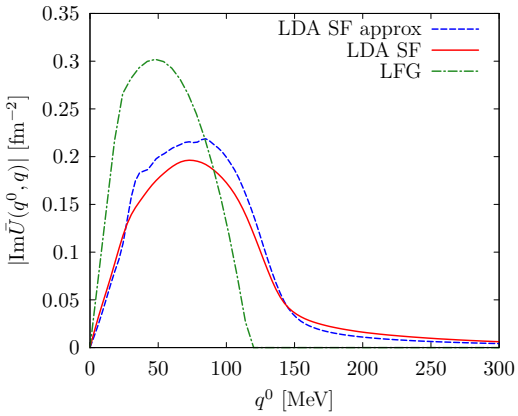

FIGURE 3.11: $|\mathrm{Im}\bar{U}^{\mathrm{LDA}}_{\mathrm{SF}}|$ (solid), $|\mathrm{Im}\bar{U}^{\mathrm{LDA}}_{\mathrm{SFapprox}}|$ (dashed) and $|\mathrm{Im}\bar{U}_{\mathrm{NR}}(q)|$ (dashed-dotted) for $|\vec{q}|$ =300 MeV and density $\rho = 0.09$ fm^{-3}, as a function of the energy transfer.

3.3 Other theoretical approaches

There are several frameworks which are currently used to describe neutrino-nucleus interaction processes in the QE regime. They range from purely phenomenological approaches, like in the case of SuSA model, to more computationally involved MF calculations. Some of them (GiBUU [20], MEMC [72] models) are based on the LDA, and therefore substantially simplify calculations which can be conducted in the plane wave basis. Since we focus our considerations in the QE region, we also mention models which describe long-range correlations through the resummation of RPA-type series. In this section we will briefly resume the building blocks of these approaches. In the next chapters we will show some comparisons.

3.3.1 CBF spectral function approach

The formalism developed in Refs. [12, 13] based on the factorization scheme has been very successful in describing many reaction mechanisms for neutrino-nucleus interaction. In the following, we will sketch how the spectral function appears in the hadron tensor when the IA is employed. The SFs discussed in Refs. [12, 13] are comprised of a MF part and a high momentum-energy one calculated within the Correlated Basis Functions (CBF) formalism [136]. They were calculated for ^{12}C and ^{16}O nuclei. In the subsequent chapters, we will denominate this model as "CBF", to distinguish it from other calculations of the hole SF.

Impulse Approximation

Let us recall that in Eq. (2.64) we defined initial and final nuclear states $|i\rangle$, $|f\rangle$ and a CC operator which describes a transition between them. Within the IA scheme the final nuclear state factorizes as

$$|f\rangle \longrightarrow |l\rangle \otimes |f\rangle_{A-1}\,. \tag{3.22}$$

and the electroweak current of Eq. (2.64) is written as a sum of one-body contributions $j^{\mu}_{cc} = \sum_i j^{i\,\mu}_{cc}$. This approximation can be safely applied under the assumption that the struck nucleon is decoupled from the spectator $(A-1)$ particles (*i.e.* at relatively large momentum transfer, $|\vec{q}| \gtrsim 500$ MeV).

In the Eq. (3.22) we introduced $|l\rangle$, the single-nucleon state produced at the electroweak vertex with momentum $\vec{l}$, energy E_l, and spin-isospin state η_l. The state $|f\rangle_{A-1}$ describes the residual $(A-1)$ system, its energy and recoiling momentum are fixed by energy and momentum

conservation

$$E_f^{A-1} = q^0 - E_l + E_0\,, \quad \vec{P}_f^{A-1} = \vec{q} - \vec{l}\,. \tag{3.23}$$

with the initial state energy E_0. Exploiting the single-nucleon completeness relation

$$\sum_p |p\rangle\langle p| = \sum_{\eta_p} \int \frac{d^3p}{(2\pi)^3} |\vec{p},\eta_p\rangle\langle\vec{p},\eta_p| = 1\,, \tag{3.24}$$

and the factorization of the final state of Eq. (3.22), the matrix element of the current can be written as

$$\langle i|\, j^\mu_{cc}|f\rangle \to \sum_p \langle i|[|p\rangle \otimes |f\rangle_{A-1}]\langle p|\sum_i j^{i\,\mu}_{cc}|l\rangle\,. \tag{3.25}$$

Substituting the last equation in Eq. (2.64), the incoherent contribution to the hadron tensor is given by

$$\begin{aligned} W^{\mu\nu}(q) = A \sum_{l,p,p'} \sum_f & \langle p|\left(j^{1\,\mu}_{cc}\right)^\dagger |l\rangle\langle l| j^{1\,\nu}_{cc}|p'\rangle \\ & \times \langle 0|[|f\rangle_{A-1} \otimes |p\rangle][{}_{A-1}\langle f| \otimes \langle p'|]|0\rangle \delta(q^0 - E_l - E_f^{A-1} + E_0)\, \theta(|\vec{l}| - p_F)\,. \end{aligned} \tag{3.26}$$

Momentum conservation in the single-nucleon vertex implies $\vec{p} = \vec{p}\,' = \vec{l} - \vec{q}$. Charge conservation and the assumption that the nuclear ground state is a zero-spin state imply $\eta_p = \eta_{p'}$. Therefore, using the identity

$$\delta(q^0 - E_l - E_f^{A-1} + E_0) = \int dE\, \delta(q^0 + E + M - E_l)\delta(E + M + E_f^{A-1} - E_0)\,, \tag{3.27}$$

the hadron tensor can be expressed as

$$\begin{aligned} W^{\mu\nu}(q) = A \sum_{\eta_p\eta_l} \int \frac{d^3p}{(2\pi)^3} dE\, \bar{S}_h^{\rm CBF}(\vec{p},\eta_p,E) & \times \langle \vec{p},\eta_p| j^{1\,\mu}_{cc}|\vec{p}+\vec{q},\eta_l\rangle^\dagger \\ & \times \langle \vec{p},\eta_p| j^{1\,\nu}_{cc}|\vec{p}+\vec{q},\eta_l\rangle \delta(q^0 + E + M - E_{p+q})\,. \end{aligned} \tag{3.28}$$

The hole SF

$$\bar{S}_h^{\rm CBF}(\vec{p},\eta_p,E) = \sum_f |\langle 0|[|\vec{p},\eta_p\rangle \otimes |f\rangle_{A-1}]|^2 \times \delta(E + M + E_f^{A-1} - E_0) \tag{3.29}$$

gives the probability distribution of removing a nucleon with momentum $\vec{p}$ and spin-isospin η_p from the target nucleus, leaving the residual $(A-1)$ system with an energy $E_0 - E - M$. It is normalized according to Eq. (3.2).

For closed-shell nuclei and isospin-symmetric nuclear nuclear matter, the SFs of spin-up and spin-down nucleons coincide. In addition, neglecting the Coulomb interactions and the other (small) isospin-breaking terms, the proton and neutron SFs turn out to be identical, yielding

$$\bar{S}_h^{\rm CBF}(\vec{p},\eta_p,E) \simeq \frac{1}{4}\bar{S}_h^{\rm CBF}(\vec{p},E) = \sum_f |\langle 0|[|\vec{p}\rangle \otimes |f\rangle_{A-1}]|^2 \times \delta(E + M + E_f^{A-1} - E_0) \tag{3.30}$$

In the relativistic regimes, the factors M/E_p and M/E_{p+q} have to be included to account for the implicit covariant normalization of the four-spinors of the initial and final nucleons in

the matrix elements of the relativistic current j^{μ}_{cc}, hence

$$W^{\mu\nu}(q) = \frac{A}{4}\sum_{\eta_p\eta_l}\int \frac{d^3p}{(2\pi)^3}dE\bar{S}_h^{\rm CBF}(\vec{p},E)\frac{M}{E_p}\frac{M}{E_{p+q}}\theta(|\vec{p}+\vec{q}|-p_F)$$

$$\times\langle\vec{p},\eta_p|\left(j^{1}_{cc}{}^{\mu}\right)^{\dagger}|\vec{p}+\vec{q},\eta_l\rangle\langle\vec{p}+\vec{q},\eta_l|j^{1}_{cc}{}^{\nu}|\vec{p},\eta_p\rangle\delta(q^0+E+M-E_{p+q})\,. \qquad (3.31)$$

Note that, within the IA the ejected nucleon is treated as a plane wave and the particle SF coincides with the one of the GFG model given in Eq. (3.1) with the relativistic expression of Eq. (3.5) for the energy of the particle state.

CBF spectral function

The hole SF presented below has been computed following Ref. [27] and it is comprised of two contributions

$$\bar{S}_h^{\rm CBF}(\vec{p},E) = \bar{S}_h^{1h}(\vec{p},E) + \bar{S}_h^{\rm corr}(\vec{p},E)\,. \qquad (3.32)$$

The $1h$ contribution is obtained from a modified mean-field scheme

$$\bar{S}_h^{1h}(\vec{p},E) = \sum_{\alpha\in\{\rm F\}} Z_\alpha|\phi_\alpha(\vec{p})|^2F_\alpha(E-E_\alpha)\,, \qquad (3.33)$$

where the sum includes all occupied single-particle states, labeled by the index α, and $\phi_\alpha(\vec{p})$ is the Fourier transform of the shell-model orbital with energy E_α. Note that $|\phi_\alpha(\vec{p})|^2$ yields the probability of finding a nucleon with momentum $\vec{p}$ in the state α. The *spectroscopic* factor $Z_\alpha < 1$ and the function $F_\alpha(E-E_\alpha)$, describing the energy width of the state α, account for the effects of residual interactions that are not included in the MF picture. In the absence of residual interactions, $Z_\alpha \to 1$ and $F_\alpha(E-E_\alpha) \to \delta_\alpha(E-E_\alpha)$. The spectroscopic factors and the widths of the s and p states of ^{12}C have been taken from the analysis of $(e,e'p)$ data carried out in Refs. [137, 138].

As for the correlated part, at first CBF calculations in isospin-symmetric nuclear matter of the hole SF are carried out for several values of the density, identifying the MF and correlated contributions. The correlated part for finite nuclei is then obtained through an LDA procedure

$$\bar{S}_h^{\rm corr}(\vec{p},E) = \int d^3r\,\rho(\vec{r})\bar{S}_{h,NM}^{\rm corr}(\vec{p},E;\rho(\vec{r}))\,, \qquad (3.34)$$

where $\rho(\vec{r})$ is the nuclear density distribution of a given nucleus and $\bar{S}_{h,NM}^{\rm corr}(\vec{p},E;\rho)$ is the correlation component of the SF of isospin-symmetric nuclear matter at density ρ. The use of the LDA to account for $\bar{S}_h^{\rm corr}(\vec{p},E)$ is based on the premise that short-range nuclear dynamics are unaffected by surface and shell effects. The energy-dependence exhibited by $\bar{S}_h^{\rm corr}(\vec{p},E)$, showing a widespread background extending up to large values of both $\vec{p}$ and E, is completely different from that of $\bar{S}_h^{1h}(\vec{p},E)$. For $|\vec{p}| > p_F$, $\bar{S}_h^{\rm corr}(\vec{p},E)$ coincides with $\bar{S}_h^{\rm CBF}(\vec{p},E)$ and its integral over the energy gives the so-called continuous part of the momentum distribution.

Correlated Basis Function

The hole SF does not depend on the momentum transfer, hence it can be safely computed within nonrelativistic many-body theory, where nuclear dynamics is described by the Hamiltonian

$$H = \sum_i \frac{\vec{p}_i{}^2}{2M} + \sum_{j>i} v_{ij} + \sum_{k>j>i} V_{ijk}\,. \qquad (3.35)$$

In the above equation $\vec{p}_i$ is the momentum of the i-th nucleon, while the potentials v_{ij} and V_{ijk} describe two- and three-nucleon interactions, respectively. Realistic two-body potentials are obtained from accurate fits to the available data on the deuteron and NN scattering, and reduce to the Yukawa one-pion-exchange interaction at large distances. The state-of-the-art phenomenological parametrization of v_{ij}, referred to as Argonne v_{18} potential [90], is written in the form

$$v_{ij} = \sum_{n=1}^{18} v^n(r_{ij}) O_{ij}^n, \tag{3.36}$$

with $r_{ij} = |\vec{r}_i - \vec{r}_j|$ and

$$O_{ij}^{n\leq 6} = [1, (\vec{\sigma}_i \cdot \vec{\sigma}_j), S_{ij}] \otimes [1, (\vec{\tau}_i \cdot \vec{\tau}_j)] \,, \tag{3.37}$$

where $\vec{\sigma}_i$ and $\vec{\tau}_i$ are Pauli matrices acting in the spin and isospin space, respectively, and S_{ij} is the tensor operator given by

$$S_{ij} = \frac{3}{r_{ij}^2}(\vec{\sigma}_i \cdot \vec{r}_{ij})(\vec{\sigma}_j \cdot \vec{r}_{ij}) - (\vec{\sigma}_i \cdot \vec{\sigma}_j) \,. \tag{3.38}$$

The operators corresponding to $n = 7-14$ are associated to non-static components of the NN interaction, while those corresponding to $n = 15-18$ account for small violations of charge symmetry. The inclusion of V_{ijk} is needed to explain the binding energies of the three-nucleon systems and nuclear matter saturation properties [139, 140].

In Refs. [29, 27], the nuclear overlaps, $\langle 0|[|\vec{k}\rangle \otimes |f\rangle_{A-1}]$, involving the ground-state and a nonrelativistic $1h$ and $2h1p$ states were evaluated using the CBF theory. Within this formalism, a set of correlated states (CB) is introduced

$$|n\rangle_{\rm CB} = \frac{\mathscr{F}|n\rangle}{\langle n|\mathscr{F}^\dagger \mathscr{F}|n\rangle^{1/2}} \,, \tag{3.39}$$

where $|n\rangle$ is an n independent particle state, generic eigenstate of the free Fermi gas (FG) Hamiltonian, and the many-body correlation operator $\mathscr{F}$ is given by

$$\mathscr{F} = S\Big[\prod_{j>i=1}^{A} F_{ij}\Big] \,. \tag{3.40}$$

The form of the two-body correlation operator F_{ij}, reflects the complexity of the NN potential

$$F_{ij} = \sum_{n=1}^{6} f^n(r_{ij}) O_{ij}^n \,, \tag{3.41}$$

with $O_{ij}^{n\leq 6}$ given in Eq. (3.37). The CB states are first orthogonalized (OCB) [141] preserving, in the thermodynamical limit, the diagonal matrix elements between CB states. Then, standard perturbation theory is used to express the eigenstates of the many-body Hamiltonian of Eq. (3.35) in terms of the OCB. Any eigenstate has a large overlap with the $n-$hole-$m-$particle OCB and hence perturbation theory in this basis is rapidly converging.

The nuclear-matter SF can be conveniently split into two components, displaying distinctly different energy dependencies [12, 13, 142, 27]. The single-particle one, associated to one-hole ($1h$) states in $|f\rangle_{A-1}$ of Eq. (3.29), exhibits a collection of peaks corresponding to the energies of the single-particle states belonging to the Fermi sea. The continuum, or correlation, component corresponds to states involving at least two-hole–one-particle ($2h-1p$) contributions in $|f\rangle_{A-1}$. Its behavior as a function of E is smooth and it extends to large values of removal energy and momentum [29]. It has to be noted that the correlated part would be strictly zero if nuclear correlations were not accounted for.

Inclusion of FSI through a convolution scheme

In the kinematical region in which the interactions between the struck particle and the spectator system can not be neglected, the CBF SF results have to be modified to include the effect of FSI. Following Ref. [14], the real part of the optical potential U is considered. It is derived from the Dirac phenomenological fit of Ref. [134] to describe the propagation of the knocked-out particle in the MF generated by the spectator system. This potential, given as a function of the kinetic energy of the nucleon $t_{kin}(\vec{p}) = \sqrt{\vec{p}^{\,2} + M^2} - M$, modifies the energy spectrum of the struck nucleon

$$\tilde{E}_{p+q} = E_{p+q} + U\left(t_{\rm kin}(\vec{p}+\vec{q})\right). \tag{3.42}$$

The multiple scatterings that the struck particle undergoes during its propagation through the nuclear medium are taken into account using a convolution scheme [14]. The CBF SF responses are folded with the function $f_{\vec{p}+\vec{q}}$, normalized as

$$\int_{-\infty}^{+\infty} d\omega f_{\vec{p}+\vec{q}}(\omega) = 1\,. \tag{3.43}$$

The hadron tensor is then given by

$$W^{\mu\nu}(q) = \frac{A}{4}\sum_{\eta_p\eta_l}\int\frac{d^3p}{(2\pi)^3}dE\int d\omega' \bar{S}_h^{\rm CBF}(\vec{p},E)\frac{M}{E_p}\frac{M}{E_{p+q}}\theta(|\vec{p}+\vec{q}|-p_F)\,f_{\vec{p}+\vec{q}}(q^0-\omega')$$

$$\times\langle\vec{p},\eta_p|\left(j_{cc}^{1\,\mu}\right)^\dagger|\vec{p}+\vec{q},\eta_l\rangle\langle\vec{p}+\vec{q},\eta_l|j_{cc}^{1\,\nu}|\vec{p},\eta_p\rangle\delta(\omega'+E+M-\tilde{E}_{p+q})\,. \tag{3.44}$$

Within the convolution scheme, correlations in both the hole and particle SFs are accounted for. As for the latter, comparing the above result with Eq. (5.26) yields

$$S_p(\vec{p}+\vec{q},q^0+E) = \theta(|\vec{p}+\vec{q}|-p_F)\int d\omega' f_{\vec{p}+\vec{q}}(q^0-\omega')\delta(\omega'+E+M-\tilde{E}_{\vec{p}+\vec{q}})\,. \tag{3.45}$$

At moderate momentum transfers, the hole and particle SFs can be consistently obtained using nonrelativistic many-body theory. However, in the kinematical region of large momentum transfer the dynamics of the struck nucleon in the final state can no longer be described using the nonrelativistic formalism. The FSI folding function is estimated employing a generalization of the Glauber theory, devised to describe high energy proton-nucleus scattering [143]

$$f_{\vec{p}}(\omega) = \delta(\omega)\sqrt{T_{\vec{p}}} + \int\frac{dt}{2\pi}e^{i\omega t}\left[\bar{U}_{\vec{p}}^{FSI}(t) - \sqrt{T_{\vec{p}}}\right] = \delta(\omega)\sqrt{T_{\vec{p}}} + (1-\sqrt{T_{\vec{p}}})F_{\vec{p}}(\omega)\,, \tag{3.46}$$

where the strength of the FSI is given by the nuclear transparency $T_{\vec{p}}$ and the finite width function $F_{\vec{p}}(\omega)$. The Glauber factor $\bar{U}_{\vec{p}}^{FSI}(t)$, a detailed discussion of which can be found in Ref. [12], is given in terms of the NN scattering amplitudes. The relation between $\sqrt{T_{\vec{p}}}$ and $\bar{U}_{\vec{p}}^{FSI}(t)$ can be best understood noting that [12]

$$T_{\vec{p}} = \lim_{t\to\infty} P_{\vec{p}}(t) = \lim_{t\to\infty}|\bar{U}_{\vec{p}}^{FSI}(t)|^2\,, \tag{3.47}$$

where $P_{\vec{p}}(t)$ is the probability that the struck nucleon does not undergo re-scattering processes during a time t after the electromagnetic interaction. In absence of FSI $\bar{U}_{\vec{p}}^{FSI}(t) = 1$, implying in turn $T_{\vec{p}} = 1$ and $f_{\vec{p}}(\omega) \to \delta(\omega)$.

In Ref. [14] the convolution scheme was further approximated, assuming that for large momentum transfer $t_{kin}(|\vec{p}+\vec{q}|) \simeq t_{kin}(|\vec{q}|)$. As a consequence, the real part of the optical potential

only produces a shift of the response to lower energy transfer. In the results presented in Chpts. 5-7, we retain the full dependence on $|\vec{p}+\vec{q}|$, which brings about a Jacobian when solving the angular integral of the initial momentum of the nucleon. This Jacobian, not negligible in the kinematical regime where FSI are important, quenches the quasielastic peak of the response, enhancing its tails.

In order to make contact with the LDA SF formalism of Sec. 3.2, we rewrite the particle SF as

$$S_p(\vec{p},E) = \theta(|\vec{p}|-p_F)\left[\sqrt{T_{\vec{p}}}\delta(E+M-\tilde{E}_p)+(1-\sqrt{T_{\vec{p}}})F_{\vec{p}}(E+M-\tilde{E}_p)\right]. \tag{3.48}$$

In the simple case of a zero-range NN interaction and neglecting correlation effects in the eikonal factor [144]

$$F_{\vec{p}}(E+M-E_p) = -\frac{1}{\pi}\frac{\mathrm{Im}V(\vec{p})}{(E+M-\tilde{E}_p)^2+\mathrm{Im}V(\vec{p})^2}, \tag{3.49}$$

where

$$\mathrm{Im}V(\vec{p}) = -\frac{1}{2}\rho v_p \sigma_p. \tag{3.50}$$

In the above equation, $v_p = |\vec{p}|/M$ is the velocity of the struck particle, which in the eikonal approximation is assumed to be constant, ρ is the average nuclear density, and σ_p is the total NN cross section.

Under these assumptions, Eq. (3.48) can be rewritten as

$$S_p(\vec{p},E) \simeq \theta(|\vec{p}|-p_F)\Big[-\frac{1}{\pi}\frac{\mathrm{Im}V(\vec{p})}{(E+M-\tilde{E}_p)^2+\mathrm{Im}V(\vec{p})^2}+\delta P_p^{FSI}\Big], \tag{3.51}$$

where

$$\delta P_p^{FSI} = \sqrt{T_{\vec{q}}}\Big[\delta(E+M-\tilde{E}_p)+\frac{1}{\pi}\frac{\mathrm{Im}V(\vec{p})}{(E+M-\tilde{E}_p)^2+\mathrm{Im}V(\vec{p})^2}\Big]. \tag{3.52}$$

The term δP_p^{FSI} is expected to be small in large nuclei since $T_{\vec{p}} = 0$ in infinite nuclear matter. In addition, it vanishes for $\mathrm{Im}V \to 0$, as in this limit the Lorentzian distribution cancels the δ-function. Neglecting δP_p^{FSI}, the expression reported in Eq. (3.51) is reminiscent of the definition of the SF in terms of the nucleon self-energy given in Eq. (3.20). Therefore, the approaches discussed in Secs. 3.2 and 3.3.1 can be approximately connected through the following identifications

$$\theta(|\vec{p}|-p_F)\mathrm{Im}V(\vec{p}) \to \frac{M}{E_p}\mathrm{Im}\Sigma(\vec{p},\widehat{E})\Big|_{\mathrm{avg}}, \quad E>\mu \tag{3.53}$$

$$U\left(t_{kin}(\vec{p})\right) \to \frac{M}{E_p}\mathrm{Re}\Sigma(\vec{p},\widehat{E})+C\rho\Big|_{\mathrm{avg}}, \quad E>\mu \tag{3.54}$$

for some average density. The step function in Eq. (3.53), which accounts for Pauli-blocking effects as in the FG model, implies that the particle SF vanishes when $|\vec{p}+\vec{q}| < p_F$. We should stress that the LDA SF approach employs a dynamical particle self-energy that separately depends on both the energy and momentum.

3.3.2 GiBUU

GiBUU (Giessen-Boltzmann-Uehling-Uhlenbeck) is an elaborated framework that provides a description of a great variety of nuclear processes [20], among them the lepton-nucleus interaction [145]. It is based on the quantum-kinetic transport theory, and allows to explore both inclusive and exclusive processes. In this approach the key approximation is the LDA. For the description of the nucleus ground state, nucleons' momenta are distributed according to the LFG model and submerged into the momentum and position dependent potential $U(\vec{p},\vec{r})$. It was obtained from an energy-density functional that reproduces the saturation for nuclear matter and was firstly used for the description of heavy-ion reactions:

$$U(\vec{p},\vec{r}) = A\frac{\rho(\vec{r})}{\rho_0} + B\left(\frac{\rho(\vec{r})}{\rho_0}\right)^{\tau} + \frac{2C}{\rho_0} g \int \frac{d^3p'}{(2\pi)^3} \frac{\Theta(p_F - |\vec{p}|)}{1 + (\frac{\vec{p}-\vec{p}'}{\Lambda})^2}, \tag{3.55}$$

where $\rho_0 = 0.168$ fm^{-3} and $g = 4$. GiBUU offers few possible parametrizations. The standard one uses $A = -29.3$ MeV, $B = 57.2$ MeV, $C = -63.6$ MeV, $\tau = 1.76$ and $\Lambda = 2.13$ fm^{-1}. This translates into an effective mass of the nucleons bound in a nucleus:

$$M^*(\vec{p},\vec{r}) = M + U(\vec{p},\vec{r}) \tag{3.56}$$

or equivalently can be expressed in terms of spectral functions for the nuclear matter:

$$\begin{aligned} S_h^{\text{GiBUU}}(E,|\vec{p}|;\rho) &= \theta\big(p_F(\rho) - p\big)\,\delta\big(E - M^* + \sqrt{M^{*2} + p^2}\big), \\ S_p^{\text{GiBUU}}(E,|\vec{p}|;\rho) &= \theta\big(p - p_F(\rho)\big)\,\delta\big(\sqrt{M^{*2} + p^2} - M^* - E\big). \end{aligned} \tag{3.57}$$

In the above equations, E is the removal energy for the hole spectral function (here we follow the notation of [64]) and for the particle spectral function E is the nucleon's kinetic energy. Even though the difference in the notation of S_p^{GiBUU} and S_h^{GiBUU} may be at first sight misleading, it was chosen in this way to correspond to the notation of Eq. (8) of Ref. [14]. The r-dependence of the argument of the δ function in Eq. (3.57) changes the dispersion relation in comparison to the Fermi gas model. After integrating it over volume in S_h^{GiBUU}, it does not have any more the form of $E(p) = \sqrt{M^2 + \vec{p}^2} - M$, but it becomes smeared out.

The hadron tensor reads:

$$\begin{aligned} W^{\mu\nu}(q) = \frac{\cos^2\theta_C}{2M^2} \int d^3r \int \frac{d^3p}{(2\pi)^3} \int dE \frac{M}{E_p} \frac{M}{E_{p+q}} S_h^{\text{GiBUU}}(E,\vec{p};\rho) \\ \times S_p^{\text{GiBUU}}(q^0 - E, \vec{p} + \vec{q};\rho) A^{\nu\mu}(p,q). \end{aligned} \tag{3.58}$$

In principle GiBUU uses spectral functions that take into account collisional broadening - the fact that nucleons interact with the nuclear medium [146]. This effect, however, is turned-off in the standard GiBUU simulation as it yields similar results for the inclusive cross section. Not only does the collisional broadening have to be included in the hole state, but also for the final state interactions in order to involve off-shell nucleons. The latter effect requires a more time-consuming computation (and it has to be taken into account when studying exclusive processes). It is worth noticing that the phenomenological potential U is used consistently to describe the hole and particle states. The particle state thus "feels" the same MF potential as the hole state.

3.3.3 SuperScaling Approach (SuSA)

The SuperScaling Approach of Ref. [21] is a phenomenological model which starting point is the scaling and superscaling properties of the electromagnetic interactions with nuclei. The

main assumption of this approach is the existence of a universal scaling function which can be obtained analyzing the scattering data of electrons on nuclei, and that can be used also to study the neutrino-nucleus interaction.

The procedure to obtain the scaling function consists of two steps. First, the experimental differential cross section is divided by the cross section of lepton-nucleon scattering. The resulting "reduced cross section" is in principle function of two variables: energy q^0 and momentum $|\vec{q}|$ transfers. In the second step, the reduced cross section is considered as a function of a new scaling variable $\psi'(q_0, |\vec{q}|)$. It happens that below the QE peak, the separate energy-momentum transfer dependencies and nuclear target dependence disappear. This property was called superscaling. Above the QE, the situation becomes more complex since there are other processes playing an increasing role and they break the scaling properties of the system.

It has been studied that the longitudinal response of the system scales well in all the kinematical region of the QE peak while the transverse one breaks down for energy transfer above the peak. This is because some non-elastic processes contribute largely to the latter response. Therefore, the authors of Ref. [147] introduced the "experimental longitudinal scaling function", f_L^{exp} extracting it from the data. This function was then used as the universal scaling function to study the nuclear response to a weak probe.

A lot of effort has been devoted to explore how the scaling properties of electron-nucleus process can be used to predict the neutrino scattering cross sections, for which – as we have already explained – the nuclear response of the system is more complex than for electrons. SuSA assumes that both processes (electromagnetic and charge-current) scale in the same way. This hypothesis has been found to be reasonable, since most of the models based on the Impulse Approximation also retain this feature [148]. Different nuclear responses are build multiplying f_L^{exp} by a corresponding responses on a single nucleon.

As a final remark, we want to say that in 2014 a new version of the SuperScaling model has been proposed [148], denoted as SuSAv2. It combines the scaling properties of the nuclear system with results computed for isovector and isoscalar response functions within the relativistic mean field (RMF) in the region of medium and high energy transfers.

3.3.4 Ghent model

The theoretical approach developed in Ghent [22] is based on a mean field approximation. Single particle bound states are calculated using an effective Skyrme interaction. The parameters of this NN potential (SkE2) were fixed against the low-energy excitations of spherical nuclei.

On top of this, some long-range correlation effects are implemented. They are included as a modification of the particle-hole Green's function, by resolving the self-consistent equation:

$$\Pi_{\mathrm{RPA}}(x_1,x_2;E) = \Pi_0(x_1,x_2;E) + \frac{1}{\hbar}\int dx dx' \Pi_0(x_1,x;E)\tilde{V}(x,x')\Pi_{\mathrm{RPA}}(x',x_2;E) \qquad (3.59)$$

where $\tilde{V}$ is a Skyrme residual interaction between the ph excitations (Δh excitations are not considered). The same potential is employed to obtain the Hartree-Fock wave functions with the inclusion of a form factor, and thus the NN interaction is treated in a consistent way.

In the model, both the hole and the particle states are calculated within the same, nonrelativistic Skyrme potential. On the one hand, in this way the outgoing nucleon's description includes the effects of final state interactions. On the other, this approach has problems in the relativistic regime and should not be used at high energies. Nevertheless, it provides an excellent description of low-lying giant resonances which cannot be recovered by any other approaches presented in this section. They are particularly well visible for forward angles of scattered lepton (*i.e.* at low energy transfer).

The influence of Coulomb forces between the outgoing charged lepton and the nucleus has been addressed for intermediate energies by implementing a modified effective momentum

approach (MEMA), while for low energies it was accounted for using a Fermi function. This correction is important at low momentum transfers, as has been explained in Sec. 2.5.

The model has been validated for the inclusive double-differential cross sections of electron-nucleus scattering in the energy region of the QE peak (and below). In order to be able to use the model approximately for higher energy-momentum transfers, a procedure of how to include relativistic corrections to the kinematics has been introduced.

3.3.5 MECM model

Martini, Ericson, Chanfray, Marteau (MECM) model of Ref. [72, 149] has many features in common with the approach described here in Sec. 2.5.2. The calculations are also conducted for nuclear matter, using the LDA. One of the virtues of this approach is a consistent incorporation of various dynamical mechanisms, in particular a series of *ph* and Δh excitations, as a sum of inclusions to the polarization propagator. Each response function, which contributes to the cross section, is obtained from the imaginary part of the polarization propagator:

$$R(q) = -\frac{1}{\pi}\mathrm{Im}\Pi^0(q) \tag{3.60}$$

In a first step, a propagator without nuclear corrections is calculated $\Pi^0(q)$, *i.e.* FG, obtained for infinite nuclear matter. Next, the RPA summation is performed by solving

$$\Pi = \Pi^0 + \Pi^0 V \Pi \tag{3.61}$$

which has the same structure as Eq. (3.59), but is calculated in the momentum basis (this can be done since one assumes infinite nuclear matter).

Interactions between *ph* and Δh excitations are parametrized as:

$$\begin{aligned}
V_{NN} &= (f' + V_\pi + V_\rho + V_{g'})\vec{\tau}_1 \cdot \vec{\tau}_2 \\
V_{N\Delta} &= (V_\pi + V_\rho + V_{g'})\vec{\tau}_1 \cdot \vec{T}_2^\dagger \\
V_{\Delta N} &= (V_\pi + V_\rho + V_{g'})\vec{T}_1 \cdot \vec{\tau}_2 \\
V_{\Delta\Delta} &= (V_\pi + V_\rho + V_{g'})\vec{T}_1 \cdot \vec{T}_2^\dagger
\end{aligned} \tag{3.62}$$

with

$$\begin{aligned}
V_\pi &= F_\pi^2(q)\frac{\vec{q}^{\,2}}{q^2 - m_\pi^2}\vec{\sigma}_1 \cdot \hat{q}\,\vec{\sigma}_2 \cdot \hat{q} \\
V_\rho &= F_\rho^2(q)\frac{\vec{q}^{\,2}}{q^2 - m_\rho^2}\vec{\sigma}_1 \times \hat{q}\,\vec{\sigma}_2 \times \hat{q} \\
V_{g'} &= F_\pi^2(q) g' \vec{\sigma}_1 \cdot \vec{\sigma}_2
\end{aligned} \tag{3.63}$$

This effective interaction has an analogous structure as the one in Eq. (2.98). It has longitudinal and transverse parts, described in terms of π and ρ meson exchange. All the parameters can be found in Ref. [72] below Eq. (9). In particular, the effective Landau-Migdal parameter is taken to be $g'_{NN} = 0.7$ and $g'_{N\Delta} = 0.5$, as compared to $g' = 0.63$ used in our case.

The solution of Eq. (3.61) has a form:

$$\mathrm{Im}\Pi = |\Pi|^2 \mathrm{Im}V + |1 + \Pi V|^2 \mathrm{Im}\Pi^0 \tag{3.64}$$

The first term represents pion production. The second one is a correction to bare polarization propagator Π^0 where the factor $|1 + \Pi V|^2$ accounts for collective effects.

As a last remark, we want to add that the presented formalism is only valid for limited kinematics. To push its applicability to higher energy transfers, the responses are divided by $r^2 = (1 + q^0/M)^2$, a factor which corrects for relativistic corrections [72]. Still, the collective modes play an important role only for low energy transfers.

Chapter 4

How to validate and compare models?

Neutrino oscillation experiments are the main motivation for the studies of neutrino-nucleus interactions. The uncertainty of nuclear models is an important source of systematic error. The latter should be at the level of $1-3\%$ for the next generation experiments, in particular in ratios of nuclear cross sections.

Questions appear regarding the size of the theoretical uncertainty in the MC simulations and the limit of this uncertainty below which one cannot reach with the existing models. It is difficult to properly address these questions in a straightforward way because no verification of the model predictions against the data can be done in the case of neutrinos. Not only do they interact weakly, but also the neutrino beams are not monoenergetic, which blurs the final analysis.

Validation of the models for neutrino-nucleus scattering is an urgent need and at the same time a nontrivial task. Experimental difficulties to detect neutrinos require from models a good predictivity in a wide range of energies (see Fig. 2.4). They should incorporate all dynamical mechanisms that give (substantial) contribution to the cross section. Neutrino experiments depend on the MC generators which themselves make use of theoretical models developed by various groups. It is therefore equally important – for models which aim to be used in the MCs – that they were reliable and capable of fast computation.

In this chapter we will present different ways to test the validity of our model that includes full SF [2] and RPA [3] effects. The chapter is based on the findings of Refs. [4, 150]. We will begin with an analysis of two low-energy processes: inclusive nuclear muon and pion radiative captures. The dynamics of the first one is the same as in antineutrino scattering off nuclei, while the latter one has a simpler interaction structure. Both of them will serve us to investigate how the spectral functions (*e.i.* their influence on the Lindhard function) and the RPA effects describe experimental data. In the kinematics probed in these processes the nuclear effects tend to play a very important role. Therefore, they will provide us with a valuable piece of information.

There is some low-energy neutrino scattering data available from LSND, KARMEN and LAMPF experiments [151, 152, 153]. Usually, the measurements are affected by considerable uncertainties. We will also show the predictions of our model with these cross sections. For the CC neutrino-nucleus interaction at intermediate energies we will perform a wide analysis of the nuclear effects included in our model, focusing our attention mainly on the interplay between SFs and RPA corrections. In addition, we present a broad comparison with other theoretical approaches introduced and shortly described in the previous chapter.

A different idea of how to perform a comparison between the models, is to use electron scattering data. There are plenty of measurements done, for a wide energy spectrum and various nuclei. The measurements done on ^{12}C are especially convenient from our perspective (carbon is used in many neutrino detectors) and the abundant data covers a wide range of energy-momentum transfers. The electron interaction with nucleons has a vector structure (there is no antisymmetric part of the lepton tensor), while for neutrinos it has a vector-axial character. Therefore, electrons can give us just partial information about the reliability of the different theoretical models. Still, this comparison might be treated as an indispensable test of the models.

4.1 Muon capture and radiative pion capture

In this section we will shortly describe the capture of a bound pion or muon by the nucleus. In particular, we will study

$$(A_Z - \mu^-)^{1s}_{\text{bound}} \to \nu_\mu + X \tag{4.1}$$

$$(A_Z - \pi^-)_{\text{bound}} \to \gamma + X \tag{4.2}$$

Both μ^- and π^- are electromagnetically bound to the nucleus, but since their masses are of the order of 200-300 heavier than that of the electron, their wave functions significantly overlap with the density distribution of the nucleus. This is the reason why they do not form stable atoms and the strong interaction produces (complex) corrections to the electromagnetic energy levels in the case of pionic atoms. We analyze these low energetic[1] processes because in this energy range, the nuclear effects are essential and clearly visible, while they play a lesser role at intermediate energies. Muon capture dynamics is governed by CC interactions and hence the formalism presented in Subsec. 2.4.1 can be employed. Radiative pion capture is on the other hand governed by a different dynamics, which will be shortly presented in the next subsection. The general argumentation from Subsec. 2.4.1 holds, but the self-energies of the pion and the muon in the nuclear medium are strongly dominated, because of kinematical reasons, by the QE reaction mechanism (*i.e.*, $1p1h$ excitation).
The decay width is computed (schematically) in the following way within the LDA:

1. We calculate the width $\hat{\Gamma}(q, \rho_n(r), \rho_p(r))$ for proton and neutron nuclear matter densities.

2. For the considered nucleus, we obtain the μ^- or π^- wave functions, $\phi(r)$, and the energy levels by solving the Schrödinger or Klein-Gordon equations, respectively. In this latter case (pionic atoms), besides the electromagnetic potential[2] , a pion-nucleus optical (strong) potential is additionally taken into account. This potential has been developed microscopically and it is exposed in detail in Ref. [121].

3. Finally, we evaluate
$$\Gamma = \int d^3r |\phi(r)|^2 \hat{\Gamma}(q, \rho_n(r), \rho_p(r)) \tag{4.3}$$
to obtain the decay width in finite nuclei.

The idea behind the above approximation is the following: At every point of the nuclear matter, there is "a piece" of μ^- (π^-) given by $|\phi(r)|^2 d^3r$, which has a decay width $\hat{\Gamma}(q, \rho_n(r), \rho_p(r))$. The integration over the whole volume leads to the total width. We make the additional kinematical assumption that the bound μ^- or π^- is at rest.

4.1.1 Pion radiative capture

In the case of radiative pion capture, following the formalism derived in Ref. [154], its $1p1h$ self-energy (see Fig. 4.1) is given by

$$-i\Pi(q;\rho) = -\sum_{s,\lambda} \int \frac{d^4k}{(2\pi)^4} \int \frac{d^4p}{(2\pi)^4} iG(p;\rho) iG(q-k+p;\rho) \times iD_0(k)(-i)T_\lambda(-i)T_\lambda^\dagger \tag{4.4}$$

[1] Note that the energy transferred to the nuclear system is at most the mass (m) of the muon or the pion, and in practice, it is significantly smaller since the QE peak is located in the vicinity of $m^2/2M$.

[2] Both for the muon and pion cases, finite size and vacuum polarization corrections are taken into account in the derivation of this part of the potential.

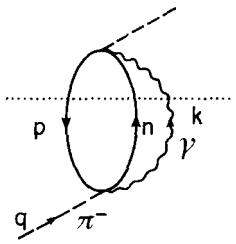

FIGURE 4.1: Pion self-energy related to the $\pi N \to \gamma N$ process.

where a sum over the spin s of the nucleons and the photon polarization λ is performed. On the other hand, $D_0(k) = 1/((k^0)^2 - \vec{k}^2 + i\varepsilon)$ is the photon propagator and T is the amplitude for the process $\pi^- p \to n\gamma$. For low π momentum (the pion is bound), the contact (Kroll-Ruderman) term gives by far the largest contribution, which with recoil corrections reads

$$T_\lambda = i2Me\sqrt{2}\frac{f}{m_\pi}(1+\frac{m_\pi}{2M})\vec{\sigma}\vec{\varepsilon}(\lambda) \tag{4.5}$$

where e is the proton charge ($e^2/4\pi = \alpha \sim 1/137$) and $\vec{\varepsilon}$ is the photon polarization vector. Let us notice that there is no dependence on momenta in the vertex, so the integration over p gives us directly the Lindhard function $\bar{U}(q-k)$. After summing over spins and polarizations we get

$$\Pi(q;\rho) = i\int \frac{d^4k}{(2\pi)^4}\bar{U}(q-k;\rho)D_0(k)16\pi\alpha\frac{f^2}{m_\pi^2}\left(1+\frac{m_\pi}{2M}\right)^2 \tag{4.6}$$

Next we use the Cutkosky rules to calculate the imaginary part of this self-energy diagram (putting the particles cut by the dotted line in Fig. 4.1 on-shell), and assuming a static pion $q^0 = m_\pi$, $\vec{q} = 0$, justified to study the capture from bound states, and thus we find

$$\mathrm{Im}\Pi(q;\rho) = \int_0^{m_\pi}\frac{d|\vec{k}||\vec{k}|}{(2\pi)^2}\mathrm{Im}\bar{U}(m_\pi - |\vec{k}|,\vec{k};\rho)16\pi\alpha\frac{f^2}{m_\pi^2}\left(1+\frac{m_\pi}{2M}\right)^2 \tag{4.7}$$

Recalling Eq. (2.70), we find

$$\frac{d\hat{\Gamma}(\rho)}{d|\vec{k}|} = -\frac{\theta(m_\pi - |\vec{k}|)}{m_\pi}\frac{4\alpha|\vec{k}|}{\pi}\mathrm{Im}\bar{U}(m_\pi - |\vec{k}|,\vec{k};\rho)\frac{f^2}{m_\pi^2}\left(1+\frac{m_\pi}{2M}\right)^2 \tag{4.8}$$

The final result in finite nuclei is obtained by folding the above expression with the pion bound wave function as indicated in Eq. (4.3). We will also enforce the correct energy balance in the decay, which changes the argument of the Lindhard function (energy that is transferred into the final nuclear system).

$$\mathrm{Im}\bar{U}(m_\pi - |\vec{k}|,\vec{k};\rho) \to \mathrm{Im}\bar{U}\left(m_\pi - |\vec{k}| - (Q - Q_{gap}(r)),\vec{k};\rho\right) \tag{4.9}$$

Taking into account the RPA effects is also much less complicated in this decay than in the case of lepton scattering because of the simplicity of the vertex. We have only one RPA series to sum up (driven by the transverse effective interaction in the medium), where we include both the *ph* and the Δh excitations [154]:

$$\mathrm{Im}\bar{U} \to \frac{\mathrm{Im}\bar{U}}{|1-(U_N+U_\Delta)V_t|^2} \tag{4.10}$$

Nucleus	^{12}C		^{40}Ca	
nl	1s	2p	2p	3d
w_{nl}	0.1	0.9	0.7	0.3
Γ_{nl}^{abs} [keV]	3.14 ± 0.14	0.00136 ± 0.00020	1.59 ± 0.02	0.0007 ± 0.0003
Pauli [eV]	88.9	18.3×10^{-3}	41.5	20.9×10^{-3}
RPA [eV]	48.3 ± 2.1	$(11.1 \pm 0.4) \times 10^{-3}$	24.3 ± 0.9	$(13.8 \pm 0.4) \times 10^{-3}$
LDA SF [eV]	58.6	12.2×10^{-3}	23.9	11.7×10^{-3}
LDA SF+RPA [eV]	50.6 ± 1.3	$(11.1 \pm 0.2) \times 10^{-3}$	21.5 ± 0.5	$(11.1 \pm 0.1) \times 10^{-3}$

TABLE 4.1: Inclusive radiative pion capture widths from the $1s$ and $2p$ and the $2p$ and $3d$ levels in ^{12}C and ^{40}Ca, respectively. Theoretical errors in the RPA predictions show MC 68% CL intervals derived from the uncertainties on the $ph(\Delta h)$–$ph(\Delta h)$ effective interaction as discussed in Sec. 2.5.2. Within the LDA SF+RPA scheme, we obtain ratios $R^{(\gamma)}$ of $(0.9 \pm 0.1)\%$ and $(1.4 \pm 0.2)\%$ for carbon and calcium, respectively. The experimental values reported in Ref. [155] for these ratios are $(1.92 \pm 0.20)\%$ for ^{12}C and $(1.94 \pm 0.18)\%$ for ^{40}Ca. In this latter reference, in the case of carbon, the contributions of transitions to the ^{12}B ground and excited states turned out to be around 20-25% of the total ratio. Thus, the continuum contribution for ^{12}C was estimated to be $(1.50 \pm 0.15)\%$ [155].

In addition, the consideration of the particle and hole SFs affects only the imaginary part of the Lindhard function, and including all effects together,

$$\frac{d\hat{\Gamma}(\rho)}{d|\vec{k}|} = -\frac{4\alpha}{\pi}\frac{f^2}{m_\pi^2}\left(1+\frac{m_\pi}{2M}\right)^2 \theta\left(\widehat{m}_\pi(r)-|\vec{k}|\right)|\vec{k}|\,\frac{\mathrm{Im}\bar{U}_{\mathrm{SF}}^{\mathrm{LDA}}\left(\widehat{m}_\pi(r)-|\vec{k}|,\vec{k};\rho\right)}{|1-(U_N'+U_\Delta)V_t|^2} \tag{4.11}$$

with $\widehat{m}_\pi(r) = m_\pi - (Q - Q_{gap}(r))$, and we use the notation U_N' to recall that its imaginary part is computed using LDA SFs to avoid fictitious singularities.

Comparison with data

Let us analyze how the total decay width changes when we include additional nuclear effects to Pauli blocking, implemented through the imaginary part of the Lindhard function calculated for a noninteracting LFG of nucleons. Neither SF effects, nor the correct energy balance in the reaction were considered in the previous work of Ref. [154], where this formalism (LFG+RPA) was used for the first time. Experimentally, it is rather difficult to distinguish between radiative pion capture processes from different pionic atom orbits. Indeed, only the weighted ratio

$$\frac{dR^{(\gamma)}}{d|\vec{k}|} = \sum_{nl}\frac{w_{nl}}{\Gamma_{nl}^{abs}}\frac{d\Gamma_{nl}^{(\gamma)}}{d|\vec{k}|} \tag{4.12}$$

can be measured. In the above equation $|\vec{k}|$ is the outgoing photon energy, w_{nl} (normalized to unity) gives the absorption probability from each nl pionic level, taking into account the electromagnetic transitions and the strong absorption. Γ_{nl}^{abs} is the total pion absorption width from the orbit nl and $\Gamma_{nl}^{(\gamma)}$ is the width due to the radiative capture of the pion from the orbit nl. We will present results for carbon and calcium, and we use the same values for w_{nl} and Γ_{nl}^{abs} as in Ref. [154], which are collected in Table 4.1. Our predictions are also given in the same table, while the differential decay branching ratios are displayed in Fig. 4.2.

Let us first notice that also here the use of interacting LDA SFs produces a quenching of the QE peak. Actually, the in-medium dispersion relations shift the position of the peak about 10 MeV towards lower outgoing photon energies (higher transferred energies to the nucleus), and generate a tail which goes into the low photon energy region. The width of the particle-nucleon (see diagram of Fig. 3.4 in Chpt. 3) also contributes to this tail. This 10 MeV difference between

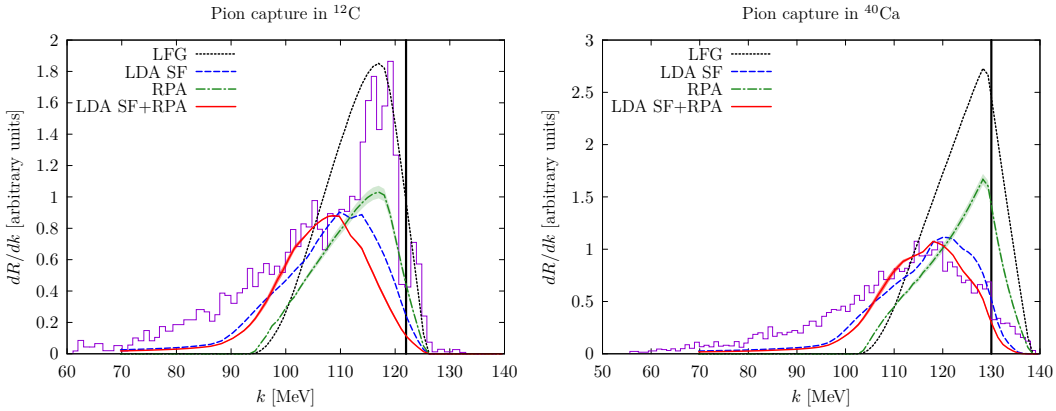

FIGURE 4.2: Photon energy distributions (arbitrary units) from pion capture in ^{12}C (left) and ^{40}Ca (right). Experimental spectra are taken from Ref. [155]. Theoretical LDA SF+RPA curves were adjusted to data in the peak, other curves (LFG, RPA, LDA SF) were scaled by the same factor. Error bands on the RPA predictions show MC 68% CL intervals derived from the uncertainties in the $ph(\Delta h)$–$ph(\Delta h)$ effective interaction as discussed in Sec. 2.5.2. The vertical lines show the maximum photon energy for the continuum contribution, $(A_Z - \pi^-)_{\text{bound}} \to \gamma + n + (A-1)_{Z-1}$, where the final nucleus is left in its ground state.

the position of the peaks, which was almost unnoticed for intermediate energies, here plays an important role.

In the case of ^{40}Ca we see that the position of the QE peak for the LDA SF+RPA stays in very good agreement with the data. However, and despite the improvement due to the use of realistic SFs, we observe a clear discrepancy with experiment at photon energies below 100 MeV. In our microscopic description, the origin of the distribution comes from the motion of the nucleons in the nucleus. Mechanisms where two nucleons are simultaneously excited with the γ creation would give rise to photons with less energy[3] (these are different mechanisms than final state interaction of the struck nucleon in one body processes because the photon has already been created and does not modify its energy). It was argued in Ref. [154] that such contributions could explain the observed discrepancies at low photon energies. This was confirmed in [156], where two-body mechanisms were taken into account using a semi-phenomenological approach. The LDA SF+RPA decay width distribution also underestimates the data for photon energies above 130 MeV (marked with a vertical line in Fig. 4.2), this is to say above the $^{39}\text{K} + n$ threshold. This region cannot be properly described with the present formalism, because it can only be filled in by discrete transitions (delta-like peaks convoluted with the experimental photon energy resolution, which is around 2 MeV [155]) of the type,

$$(^{40}\text{Ca} - \pi^-)_{\text{bound}} \to \gamma + ^{40}\text{K}^* \tag{4.13}$$

where the final ^{40}K nucleus is left either in the ground or in an excited state. These contributions are not properly included in the present approach, and their evaluation requires certainly a good description of the nuclear states of the initial and final nuclei. The contribution above 130 MeV is moderately small, but together with the deficiencies discussed above at low energies explain why the current model underestimates by around a 30% of the measured ratio $R^{(\gamma)}$ (see caption of Table 4.1).

For ^{12}C the situation is somehow different and discrete transitions play a more important role and they are clearly visible in the spectrum. In this case, the $^{11}\text{B} + n$ threshold is located

[3] As mentioned, the particle-nucleon width included in the particle SF contributes to the tail. Note however, there exist other 2p2h mechanisms, involving meson-exchange-currents or the excitation of the $\Delta(1232)$ (see the discussion of Sect. 8 of Ref. [154]).

at $|\vec{k}| \sim 122$ MeV, and peaks above a continuum are observed at 117, 120, and 125 MeV. The peak at 125 MeV can be associated with the production of the ^{12}B ground state, while the other two peaks are related to transitions to excited states of ^{12}B* [155]. Except for the high photon energy region, clearly dominated by these peaks, and the low energy tail, where two-nucleon mechanisms need to be included, the LDA SF+RPA distribution provides also in carbon a reasonable description of the spectrum. It is remarkably better than that obtained when these nuclear effects are not taken into account. With respect to integrated ratios, and for meaningful comparison of our predictions with data, it is necessary to subtract the discrete contributions. The integrated ratio accounting for the one neutron knock-out contribution is estimated to be $R^{(\gamma)}_{\rm exp;cont} \sim (1.50 \pm 0.15)\%$ in [155], that is around a 40% higher than our prediction. The difference should be partially attributed to the low energy tail, but other source of the deviations comes from the experimental absorption widths used in the present calculation and those in which the experimental set–up was based on. The deviations may also be due to the uncertainty of the values of w_{nl}. It would be interesting to disentangle experimentally the capture from different atomic states to allow a direct comparison with the theory, free of the assumptions made on the values of w_{nl}.

4.1.2 Muon capture

Muon capture is studied in full analogy to pion capture. A major difference is that the outgoing particle is a neutrino ν_μ instead of a γ, which implies that this process is driven by CC interactions. We have shown in Subsec. 2.4.1 that the neutrino self-energy is determined by the W^+ spectral properties. The inclusive decay width of a bound muon absorbed by the nucleus is obtained from the imaginary part of its self-energy (spin-averaged) in the nuclear medium, which in turn is determined by the W^- self-energy, $\bar{\Pi}^{\mu\nu}_W(q;\rho_p,\rho_n) = \Pi^{\mu\nu}_W(q;\rho_n,\rho_p)$, in this case. The latter quantity is computed following the steps outlined in Subsec. 2.4.1 for the W^+ case. Thus one easily gets [3]

$$\begin{aligned}\hat{\Gamma}(\rho_p,\rho_n) &= -\frac{1}{m_\mu}\frac{4G_F}{\sqrt{2}M_W^2}\int\frac{d^3k}{(2\pi)^3}\frac{\theta(q^0)}{2|\vec{k}|}\mathrm{Im}\left[L_{\mu\nu}\bar{\Pi}^{\mu\nu}_W(q;\rho_p,\rho_n)\right] \\ &= \frac{G_F^2\cos^2\theta_C}{m_\mu}\int\frac{d^3k}{(2\pi)^3}\frac{1}{2|\vec{k}|}L_{\mu\nu}T^{\mu\nu}(q;\rho_p,\rho_n) \qquad (4.14)\end{aligned}$$

where we have assumed that the muon is at rest, which simplifies the kinematics and the computation of the hadronic tensor ($T^{\mu\nu}$) that is clearly dominated by the excitation of a *ph* nuclear component (QE mechanism). The muon binding energy, B^{1s}_μ, is also taken into account, however its value for the considered (light) nuclei is at most 1 MeV – see Table 4.2. We have also enforced the correct energy balance: $q^0 \to q^0 - [\bar{Q} - \bar{Q}_{gap}] = m_\mu - B^{1s}_\mu - |\bar{k}| - [\bar{Q} - \bar{Q}_{gap}]$, considering that the muon is captured from the $1s$ orbit. The $1p1h$ hadron tensor, after including LDA SF and RPA corrections reads

$$\begin{aligned}T^{\mu\nu}(q;\rho_p,\rho_n) = \frac{\theta(q^0)}{4M^2}\int\frac{d^3p}{(2\pi)^2}\int_{\mu_n-q^0}^{\mu_p} dE S_h^{\rm LDA}(E,\vec{p}) \\ \times S_p^{\rm LDA}(E+q^0,\vec{p}+\vec{q})A^{\mu\nu}_{RPA}(p,q)\Big|_{p^0=E_p} \qquad (4.15)\end{aligned}$$

As in the case of radiative pion capture, the final result in finite nuclei is obtained by folding with the muon bound wave function as indicated in Eq. (4.3).

	^{12}C	^{16}O	^{18}O	^{23}Na	^{40}Ca
B_μ^{1s}	0.100	0.178	0.178	0.336	1.064

TABLE 4.2: The B_μ^{1s} value used to enforce the correct energy balance in muon capture processes.

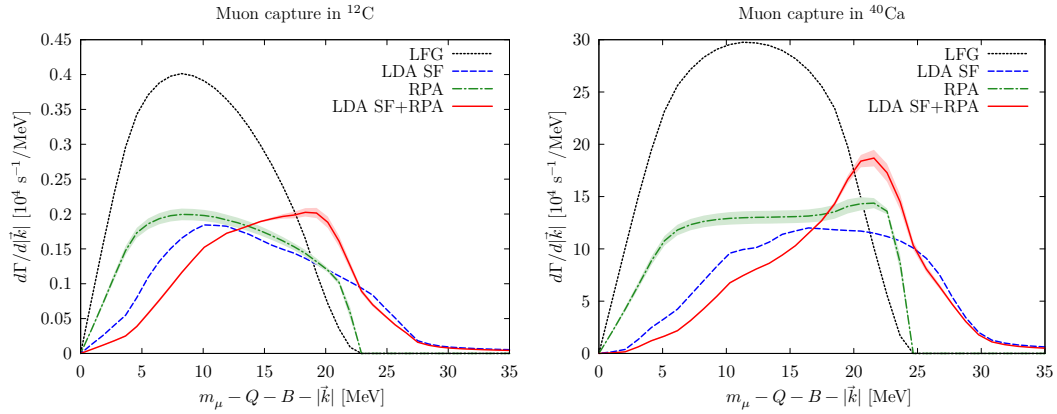

FIGURE 4.3: Inclusive muon capture differential widths for ^{12}C (left) and ^{40}Ca (right), as a function of the energy transfer. Error bands on the RPA predictions show MC 68% CL intervals derived from the uncertainties in the *ph*(Δh)–*ph*(Δh) effective interaction as discussed in Sec. 2.5.2.

Comparison with data

The analysis of the inclusive muon capture results is similar to that presented in the previous subsection for the radiative pion capture. The most important difference is that obviously the outgoing neutrino distributions have not been measured. In addition, the interaction vertex is also different, and the transferred energy to the nucleus, and thus the maximum momentum transfer, is around 35 MeV (mass difference between the pion and the muon) smaller than in the case of pion capture. This different kinematics influences the effects produced by the non-free SFs, as shown in Fig. 3.8.

The results for muon capture are shown in Table 4.3. We do not study heavy nuclei, like ^{208}Pb, because LDA SFs were evaluated for symmetric nuclear matter. Our predictions stay in a very good agreement with the data, however the actual description could be likely poorer since, in principle, discrete contributions have not been properly taken into account, as we discussed for the case of pion capture. Nevertheless, the results of Table 4.3 clearly show that RPA and LDA SF effects provide a much better description of the data. RPA correlations induce modifications on the LDA SF integrated decay rates significantly less important than those appreciated in the free LFG results. However, the RPA collective effects significantly modify the shape of the decay width distributions, as can be seen in Fig. 4.3, producing a shift of the maximum position, which is moved towards (higher) energies transferred to the nucleus of around 20 MeV. Indeed the RPA produces an enhancement of the distribution in this region of excitation energies, which can be related to the nuclear giant resonances (see for instance Refs. [117, 118, 157, 158]). A similar situation could be also seen in Fig. 4.2 for the case of pion capture, where we also see that the RPA correlations increase the LDA SF results for photon energies of around 100 (110) MeV in carbon (calcium). Note however, the individual giant resonances would show up as narrow peaks in the decay width distributions, while in the present approach, the RPA correlations provide only an enhanced signature, which likely will give a reasonable description of the integrated distributions.

Nucleus	Pauli (10^4 s^{-1})	RPA (10^4 s^{-1})	LDA SF (10^4 s^{-1})	LDA SF+RPA (10^4 s^{-1})	Exp. (10^4 s^{-1})
^{12}C	5.76	3.37 ± 0.16	3.22	3.19 ± 0.06	3.79 ± 0.03
^{16}O	18.7	10.9 ± 0.4	10.6	10.3 ± 0.2	10.24 ± 0.06
^{18}O	13.8	8.2 ± 0.4	7.0	8.7 ± 0.1	8.80 ± 0.15
^{23}Na	64.5	37.0 ± 1.5	30.9	34.3 ± 0.4	37.73 ± 0.14
^{40}Ca	498	272 ± 11	242	242 ± 6	252.5 ± 0.6

TABLE 4.3: Experimental and theoretical total muon capture widths for different nuclei. Data are taken from Ref. [159], and when more than one measurement is quoted in [159], we use a weighted average: $\overline{\Gamma}/\sigma^2 = \sum_i \Gamma_i/\sigma_i^2$, with $1/\sigma^2 = \sum_i 1/\sigma_i^2$. Theoretical errors in the RPA predictions show MC 68% CL intervals derived from the uncertainties on the $ph(\Delta h)$–$ph(\Delta h)$ effective interaction as discussed in Sec. 2.5.2.

4.2 Neutrino scattering

4.2.1 The inclusive $^{12}\mathrm{C}(\nu_\mu, \mu^-)X$ and $^{12}\mathrm{C}(\nu_e, e^-)X$ reactions near threshold

The low energy pion and muon capture decay rates discussed in the Sec. 4.1 were measured with a good precision and certainly provide an important test for our model. Here we will compare our results with other existing experimental neutrino low energy data. One of the characteristics of neutrino experiments is that the beams are not monochromatic and thus the nuclear cross section should be folded with the neutrino energy-flux $F(E_\nu)$,

$$\sigma = \frac{1}{N}\int_{E_\nu^{min}}^{E_\nu^{max}} dE_\nu \sigma(E_\nu) F(E_\nu), \quad N = \int_{E_\nu^{min}}^{E_\nu^{max}} dE_\nu F(E_\nu). \tag{4.16}$$

The flux depends on the neutrino source and for the experiments (LAMPF, KARMEN, LSND) that we will consider in this subsection, electron neutrinos were produced from the muon decay at rest ($\mu^+ \to \nu_e + \bar{\nu}_\mu + e^-$), and in this case the flux is approximately described by the Michel distribution,

$$F(E_\nu) \propto E_\nu^2 (E_\nu^{max} - E_\nu), \quad E_\nu^{max} = \frac{m_\mu^2 - m_e^2}{2m_\mu} \approx 53\,\mathrm{MeV}, \quad E_\nu^{min} = 0. \tag{4.17}$$

In the LSND experiment at Los Alamos, the inclusive $^{12}C(\nu_\mu, \mu^-)X$ cross section was measured using a pion decay in flight ν_μ beam, with energies ranging from zero[4] to 300 MeV (distribution is given in [160]). The electron neutrino flux distribution has a maximum around 35 MeV, while for the muon neutrino beam, over 80% of the flux has an energy below 180 MeV. Thus, these processes involve very low energy transfers, as can be seen in Fig. 4.4, especially in the electron neutrino case where the excitation energies are only of few MeV, and hence we are facing the limit of applicability of the model. Nevertheless, the results compiled in Table 4.4 (flux-weighted distributions shown in Fig. 4.5) stay in surprisingly good agreement with the data from LSND, KARMEN and LAMPF experiments. Nuclear effects (LDA SF+RPA) turn out to be essential and clearly improve the results obtained by only imposing Pauli blocking and the correct energy balance in the reactions (results denoted as LFG in Fig. 4.5 and Table 4.4). In the table, a few selected theoretical calculations [large basis shell model (SM) results of Refs. [161, 162] and the CRPA ones from Ref. [163]] are also compiled. Our approach might look simplified with respect to the ones just mentioned, but it incorporates both RPA and LDA

[4]The neutrino laboratory threshold energy E_ν^{min} is around 123 MeV.

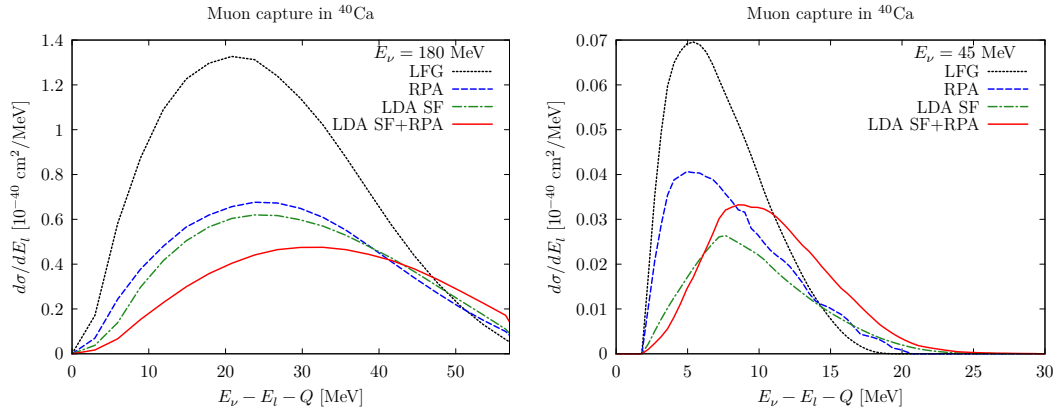

FIGURE 4.4: Left (right) panel: Differential cross section for inclusive CC muon (electron) neutrino scattering from ^{12}C at 180 (45) MeV. The calculations have been done using nonrelativistic kinematics and with/without LDA SF and RPA effects.

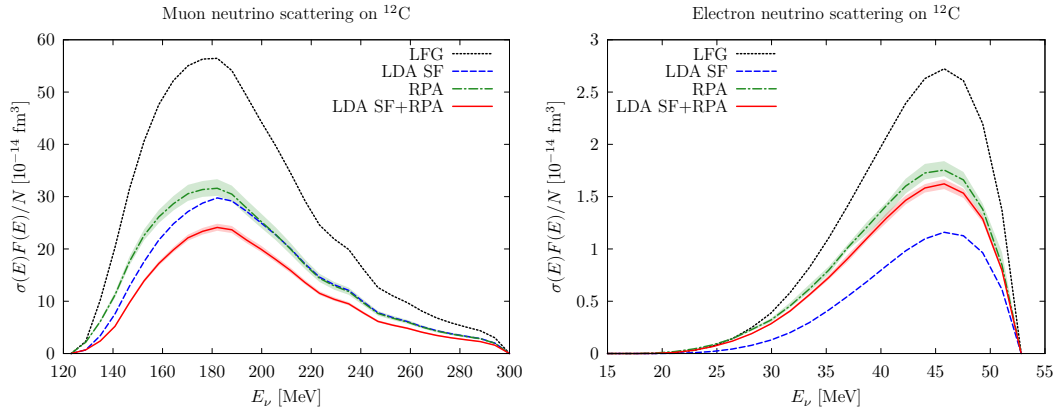

FIGURE 4.5: Predictions for the LSND measurement of the ^{12}C $(\nu_\mu, \mu^-)X$ reaction (left panel) and the ^{12}C $(\nu_e, e^-)X$ reaction near threshold (right panel). Neutrino cross sections have been convoluted with the corresponding flux. Error bands on the RPA predictions show MC 68% CL intervals derived from the uncertainties in the $ph(\Delta h)$–$ph(\Delta h)$ effective interaction as discussed in Sec. 2.5.2.

SF corrections and provides a description of these low energy cross sections as good, if not better, that any of them.

With all kinds of precautions, minding the low excitation energies involved, the LFG model of interacting nucleons, supplemented with a proper energy balance and RPA collective effects, provides a more than reasonable combined description of the inclusive muon capture in ^{12}C and of the measurements of the ^{12}C $(\nu_\mu, \mu^-)X$ and ^{12}C $(\nu_e, e^-)X$ reactions near threshold.

4.2.2 Intermediate energy transfers

The use of nonrelativistic kinematics is sufficiently accurate for the computation of hole SF, but its applicability to the ejected nucleon limits the range of energy (q^0) and momentum ($|\vec{q}|$) transfers to regions where, at least, $|\vec{q}| < 500 - 600$ MeV. The energy of the projectile is an issue for totally integrated cross sections because if it is high, there will be phase space regions where the q^0 and $|\vec{q}|$ will be too large to accept the accurateness of our nonrelativistic description of the particle SF. For differential cross sections, however, we could address large projectile energies at forward angles to keep $|\vec{q}|$ sufficiently small. On the other hand, RPA effects decrease as $-q^2$ increases, and become necessarily small when the associated wave-length of the electroweak probe is much shorter than the nuclear size. As the energy of the projectile increases, the

	LFG	RPA	LDA SF	LDA SF+RPA	SM [161]	SM [162]	CRPA [163]
$\bar{\sigma}(\nu_\mu,\mu^-)$	23.1	13.2 ± 0.7	12.2	9.7 ± 0.3	13.2	15.2	19.2
	Experiment						
	LSND [160] $8.3\pm0.7\pm1.6$		LSND [164] $11.2\pm0.3\pm1.8$		LSND [165] $10.6\pm0.3\pm1.8$		
	LFG	RPA	LDA SF	LDA SF+RPA	SM	SM	CRPA
$\bar{\sigma}(\nu_e,e^-)$	0.200	0.143 ± 0.006	0.086	0.138 ± 0.004	0.12	0.16	0.15
	Experiment						
	KARMEN [151] $0.15\pm0.01\pm0.01$		LSND [152] 0.15 ± 0.01		LAMPF [153] 0.141 ± 0.023		

TABLE 4.4: Experimental and theoretical flux averaged $^{12}\mathrm{C}(\nu_\mu,\mu^-)X$ and $^{12}\mathrm{C}(\nu_e,e^-)X$ cross sections in 10^{-40} cm^2 units. Theoretical errors in the RPA predictions show MC 68% CL intervals derived from the uncertainties on the $ph(\Delta\mathrm{h})$–$ph(\Delta\mathrm{h})$ effective interaction. We also quote results from other calculations (see text for details).

available phase-space includes larger regions where one might expect that RPA effects are small. However, one should admit larger uncertainties in the RPA corrections at these large values of $-q^2$, because their calculation probes NN, $N\Delta$ and $\Delta\Delta$ interactions at high virtualities. The model used here includes some exchanges of virtual mesons, and it has been shown to work well at intermediate energies in different hadronic processes. Thus, with some precautions, the idea is that we could realistically compute RPA corrections up to a region of $-q^2$ values where they become quite small and hence, the possible existence of some systematic errors on their computation will have little effect in the final observables. Indeed, the present model for RPA corrections has been successfully applied to describe MiniBooNE [74] (see Fig. 4.10 below) and MINERνA [79] CCQE integrated cross sections.

In Tables 4.5 and 4.6, we present results in oxygen for inclusive electron and muon (anti) neutrino-nucleus scattering and energy transfers up to 400 MeV. We examine RPA and the LDA SF corrections and their dependence on the energy. First, we observe the differences stemming from the use of nonrelativistic and relativistic Lindhard functions. (As mentioned, in the case of nonrelativistic kinematics, we use the nonrelativistic nucleon dispersion relations and set to one the factors M/E_p and M/E_{p+q} in Eq. (2.80).) For the highest considered energies ($E_{\nu_\mu}=500$ MeV), relativistic effects are approximately $7-10\%$ and decrease down to $3-4\%$ for $E_{\nu_\mu}=250$ MeV. We should be aware of this fact when considering LDA SF+RPA corrections because they have been computed using nonrelativistic kinematics.

Next, we pay attention to both RPA and LDA SF corrections that suppress the total cross sections. Results are graphically shown in Fig. 4.6. For a free LFG, the RPA effects[5] are especially significant at lower energies, where we find a very drastic reduction of about $35-40\%$, the corrections being still large (of the order of 20–25%) for the higher energies examined in Table 4.5. SF effects change importantly both, the integrated and the shape of the differential cross sections, as we will see. When medium polarization (RPA) effects are not considered, the LDA SFs provide significant reductions (20–35%) of the neutrino cross sections, and somewhat smaller effects in the case of antineutrinos[6]. The LDA SF corrections decrease as the (anti-)neutrino energy increases. However, when RPA correlations are included, the reductions

[5]For both the nonrelativistic and SF set of results, the real part of the $ph-$Lindhard function that appear in the RPA denominators has been computed using its nonrelativistic expression derived in a free LFG.

[6]The SF effects reported in Ref. [3] were smaller because in that work, the imaginary part of the hole self-energy was neglected.

		$\sigma(\nu_\mu + {}^{16}\mathrm{O} \to \mu^- + X)\,[10^{-40}\mathrm{cm}^2]$		
		Nonrelativistic	Relativistic	LDA SF
500 MeV	Pauli	625	580	494
	RPA	520 ± 40	470 ± 40	445 ± 27
375 MeV	Pauli	443	418	328
	RPA	329 ± 24	308 ± 22	274 ± 14
250 MeV	Pauli	199	192	132
	RPA	123 ± 7	118 ± 7	101 ± 5
		$\sigma(\bar{\nu}_\mu + {}^{16}\mathrm{O} \to \mu^+ + X)\,[10^{-40}\mathrm{cm}^2]$		
		Nonrelativistic	Relativistic	LDA SF
500 MeV	Pauli	143.8	134.4	118.9
	RPA	106.3 ± 1.9	98.5 ± 1.9	105.6 ± 1.5
375 MeV	Pauli	99.8	94.1	78.2
	RPA	71.6 ± 1.4	66.9 ± 1.3	68.6 ± 1.2
250 MeV	Pauli	51.5	49.0	37.6
	RPA	34.3 ± 0.8	32.5 ± 0.8	31.0 ± 0.7

TABLE 4.5: Muon neutrino and antineutrino inclusive QE integrated cross sections from oxygen. We present results for relativistic and nonrelativistic nucleon kinematics. In this latter case, we present results with and without LDA SFs effects. Results, denoted as RPA and Pauli have been obtained with and without including RPA and Coulomb corrections, respectively. LDA SF results have been computed using a complex self-energy to dress both particle and hole nucleon lines. Theoretical errors on the RPA predictions show MC 68% CL intervals derived from the uncertainties in the $ph(\Delta\mathrm{h})$–$ph(\Delta\mathrm{h})$ effective interaction, as detailed in Subsec. 2.5.2.

become more moderate, around 15% for neutrino reactions, and much smaller for antineutrinos. Indeed, in this latter case and for the higher energies examined in the Tables 4.5 and 4.6, the integrated cross sections remain practically unchanged. LDA SF effects are responsible for a certain quenching of the QE peak and a redistribution of its strength as can be seen in Fig. 4.7, where (anti-)neutrino differential cross sections from ^{16}O at various energies are shown. The use of non-free SFs produces a tail which goes to higher energies inducing in general a significant change of the $(q^0, |\vec{q}\,|)$-region accessible in the process. It does not change the strength of the interaction between the gauge boson and the nucleons (the form–factors), which is how the RPA effect is included in our formalism.

As mentioned above, when we take into account RPA corrections, the differences between SF and nonrelativistic LFG total cross sections are small, and in general mostly covered by the theoretical errors of the RPA predictions (see Fig. 4.6), derived from the uncertainties on the $ph(\Delta\mathrm{h})$–$ph(\Delta\mathrm{h})$ effective interaction. This is because the LDA SFs diminish the height of the QE peak and increase the cross section for the high energy transfers. But for nuclear excitation energies higher than those around the QE peak, the RPA corrections are certainly less important than in the peak region. Hence, the RPA suppression of the LDA SF distribution is significantly smaller than the RPA reduction of the distributions determined by the ordinary Lindhard function. In Fig. 4.7, we also observe that antineutrino distributions are narrower than neutrino ones and more significantly peaked towards lower energy transfers. Also in these plots, we can see (stripped pattern bands) the size of the relativistic effects. These introduce a systematic error in our predictions in the higher energy transfer region of the differential cross sections, because LDA SF+RPA corrections have been computed within a nonrelativistic scheme.

In Fig. 4.6 we present how the size of the nuclear effects depends on the energy of the incoming (anti)neutrino. We appreciate some differences between neutrino and antineutrino reactions. Both LDA SF and RPA effects suppress the cross section and as already mentioned,

		$\sigma(\nu_e + {}^{16}\mathrm{O} \to e^- + X)\,[10^{-40}\mathrm{cm}^2]$		
		Nonrelativistic	Relativistic	LDA SF
310 MeV	Pauli	370	350	271
	RPA	259 ± 18	244 ± 16	219 ± 11
220 MeV	Pauli	191	183	131
	RPA	117 ± 7	112 ± 6	101 ± 5
130 MeV	Pauli	44.6	43.1	28.3
	RPA	25.6 ± 1.2	24.8 ± 1.1	23.2 ± 0.8
		$\sigma(\bar{\nu}_e + {}^{16}\mathrm{O} \to e^+ + X)\,[10^{-40}\mathrm{cm}^2]$		
		Nonrelativistic	Relativistic	LDA SF
310 MeV	Pauli	81.6	77.3	63.1
	RPA	57.9 ± 1.1	54.2 ± 1.1	55.6 ± 0.9
220 MeV	Pauli	49.2	47.0	36.2
	RPA	32.3 ± 0.8	30.8 ± 0.8	30.4 ± 0.7
130 MeV	Pauli	17.9	17.3	12.2
	RPA	10.3 ± 0.3	9.8 ± 0.3	9.6 ± 0.3

TABLE 4.6: As in Table 4.5 but for electron neutrino and antineutrino inclusive QE scattering.

these two combined effects yield results similar to those obtained when only RPA correlations are considered. On the other hand, for antineutrinos, the use of non-free SFs leads to smaller effects.

Theoretical errors practically cancel out in the ratio $\sigma(\nu_\mu)/\sigma(\nu_e) \equiv \sigma(\nu_\mu + {}^A Z \to \mu^- + X)/\sigma(\nu_e + {}^A Z \to e^- + X)$, and in the equivalent one constructed for antineutrinos. These ratios are depicted in Fig. 4.8 for carbon, oxygen and argon. Theoretical uncertainties on these ratios turn out to be much smaller than 1% and are hardly visible in the plots. On the other hand, predictions for these ratios obtained from a simple Lindhard function[7] incorporating a correct energy balance in the reaction (lines denoted as "LFG" in the plots) differ from the most realistic ones obtained including also LDA SF+RPA effects at the level of 5-10% for neutrino energies above 300 MeV, in sharp contrast with the situation found for each of the individual $\sigma(\nu_\mu + {}^A Z \to \mu^- + X)$, $\sigma(\nu_e + {}^A Z \to e^- + X)$, $\sigma(\bar{\nu}_\mu + {}^A Z \to \mu^+ + X)$ and $\sigma(\bar{\nu}_e + {}^A Z \to e^+ + X)$ cross sections (see Fig. 4.6). However, these differences are much larger at low energies, especially for the antineutrino ratios. Note that RPA corrections greatly cancel out, especially in carbon and oxygen, in the neutrino ratios calculated with full SFs. For antineutrino ratios, though, RPA effects are clearly visible when LDA SFs are used. Besides, we should note that in the ratio $\sigma(\nu_\mu)/\sigma(\nu_e)$, relativistic nucleon kinematics effects are quite small, being always smaller than 1% in the whole energy interval studied here, as it was pointed out in Ref. [122] (see Fig. 6 of that reference).

4.2.3 Comparison with other approaches

Here, we briefly discuss predictions obtained within other approaches. As we commented, there is an abundant literature in the field, and we do not aim at performing an exhaustive comparison, but we will rather focus on some representative works, where RPA or SF effects have been examined.

We will begin with the continuum RPA (CRPA) scheme examined in Ref. [163]. As explained in this latter reference, the main difference between RPA and CRPA approaches lies in the treatment of the excited states. In the case of RPA, all of them are treated as bound states,

[7] It is to say from a local Fermi gas model of noninteracting nucleons.

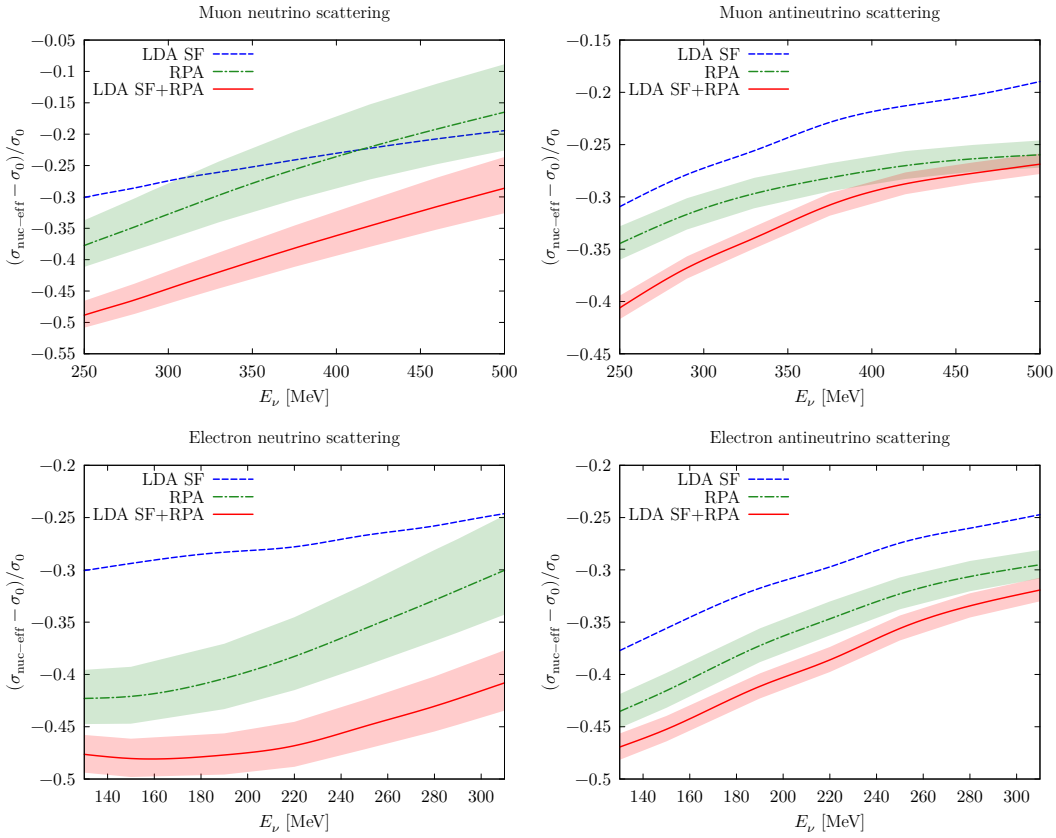

FIGURE 4.6: Importance of nuclear effects compared to the nonrelativistic free LFG cross section (σ_0). We display $(\sigma_{\rm nuc\ eff}-\sigma_0)/\sigma_0$ where "nuc eff" stands for a nuclear effect (RPA, LDA SF or LDA SF+RPA). The bands show 68% CL intervals derived from the uncertainties on the $ph(\Delta h)$–$ph(\Delta h)$ effective interaction.

leading to a discrete excitation spectrum, while within a CRPA scheme, the final states asymptotically have the appropriate scattering wave-function for energies above the nucleon-emission thresholds; consequently the excitation spectrum in the CRPA is continuous. In this sense, it is clear that the approach followed here (see Subsec. 2.5.2) should be understood as a CRPA one.

In Ref. [163], it is argued that the RPA or CRPA are the methods of choice at intermediate neutrino energies. The CRPA calculations carried out in this reference used a finite range residual force based on the Bonn potential, and all multipole operators with $J \leq 9$ and both parities were included. Free nucleon form factors were used in [163], with no quenching, and thus this RPA approach provided a realistic description of collective nuclear excitations due to one-particle one-hole excitations of the correlated ground state. However, neither short range nucleon-nucleon correlation effects included in realistic SFs, nor the excitation of Δh components in the RPA responses are taken into account in the scheme of Ref. [163].

In Fig. 4.9, we compare our RPA predictions for $d\sigma/d(\cos\theta)$ with those obtained in [163] for oxygen and two different electron–neutrino energies. We find a reasonable agreement, which is substantially improved when Δh excitations are not allowed in our approach (black dashed curves). (The role played by the inclusion of Δh components in the RPA series at intermediate energies was already mentioned in Ref. [3].) There exist some discrepancies for $E_\nu = 500$ MeV and $\theta > 90^0$. In this region, the momentum transfers are larger than those for which our nonrelativistic RPA treatment is adequate. Nevertheless, we clearly see that in both approaches, RPA corrections lower the cross section at forward angles, but raise it at more backwards angles. This is also seen for $E_\nu = 300$ MeV.

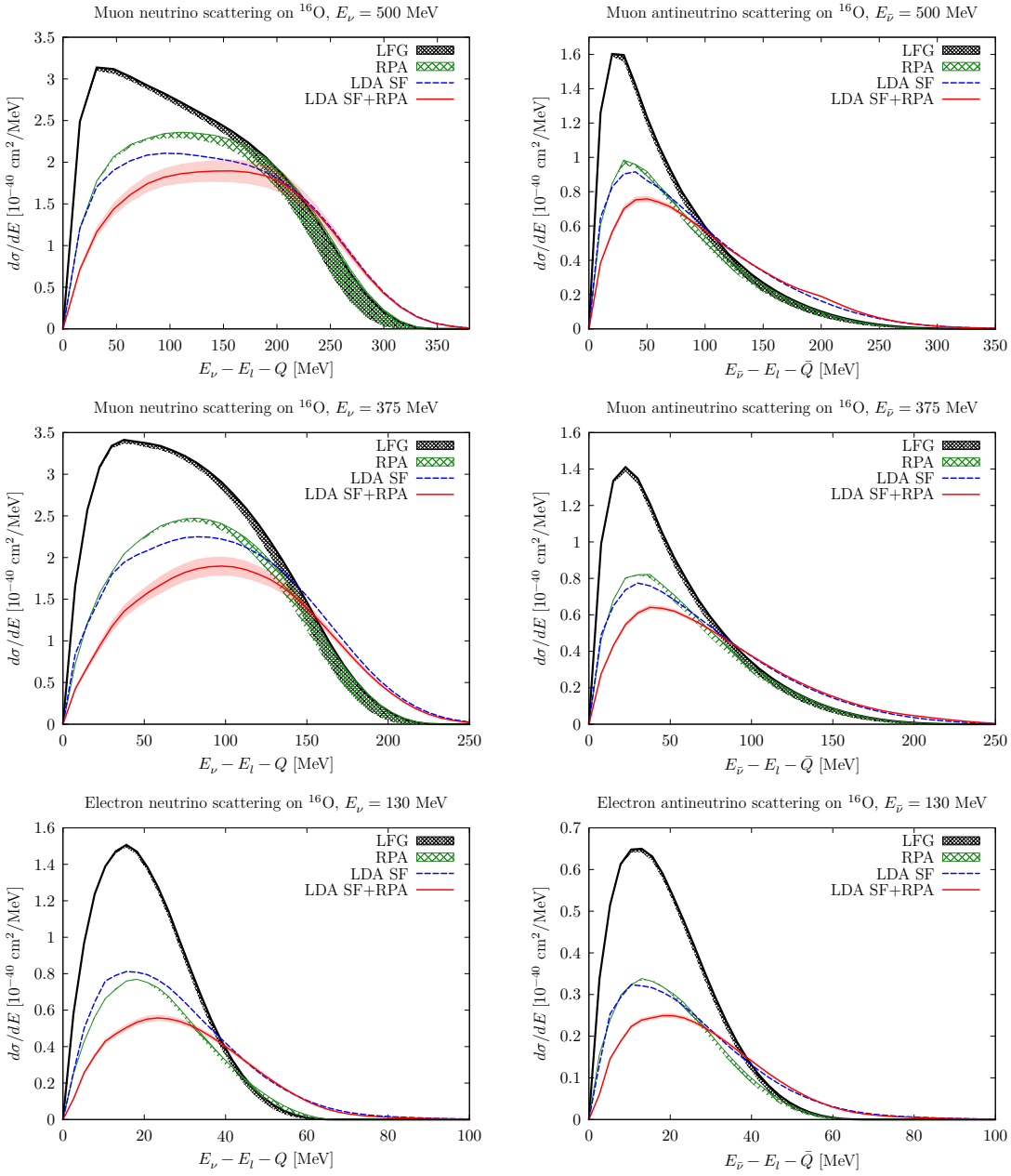

FIGURE 4.7: Neutrino and antineutrino differential cross sections from ^{16}O at various energies. "LFG" and "RPA" curves were calculated with nonrelativistic kinematics. The use of relativistic kinematics causes a decrease of the cross section shown as striped pattern bands below those curves. LDA SF results have been computed using a complex self-energy to dress both, particle and hole nucleon lines. Theoretical errors on the LDA SF+RPA predictions show MC 68% CL intervals (red bands).

The double differential neutrino-carbon quasielastic cross sections measured by the MiniBooNE collaboration triggered an enormous theoretical activity, since a large value of the axial nucleon mass, M_A, is needed to describe the data when RPA and $2p2h$ nuclear effects are not considered [166]. The solution to this puzzle came from the consideration of these nuclear corrections, which were computed by two different groups: Lyon [75] and IFIC [74]. The latter one included RPA corrections using the many-body scheme described in Subsec. 2.5.2, while the Lyon group accounted for RPA effects as described in Ref. [72]. In Fig. 4.10, we show results [74], for the QE contribution to the CC quasielastic $\nu_\mu - ^{12}$C double differential cross section convoluted with the MiniBooNE flux. There, we also display results from the Lyon

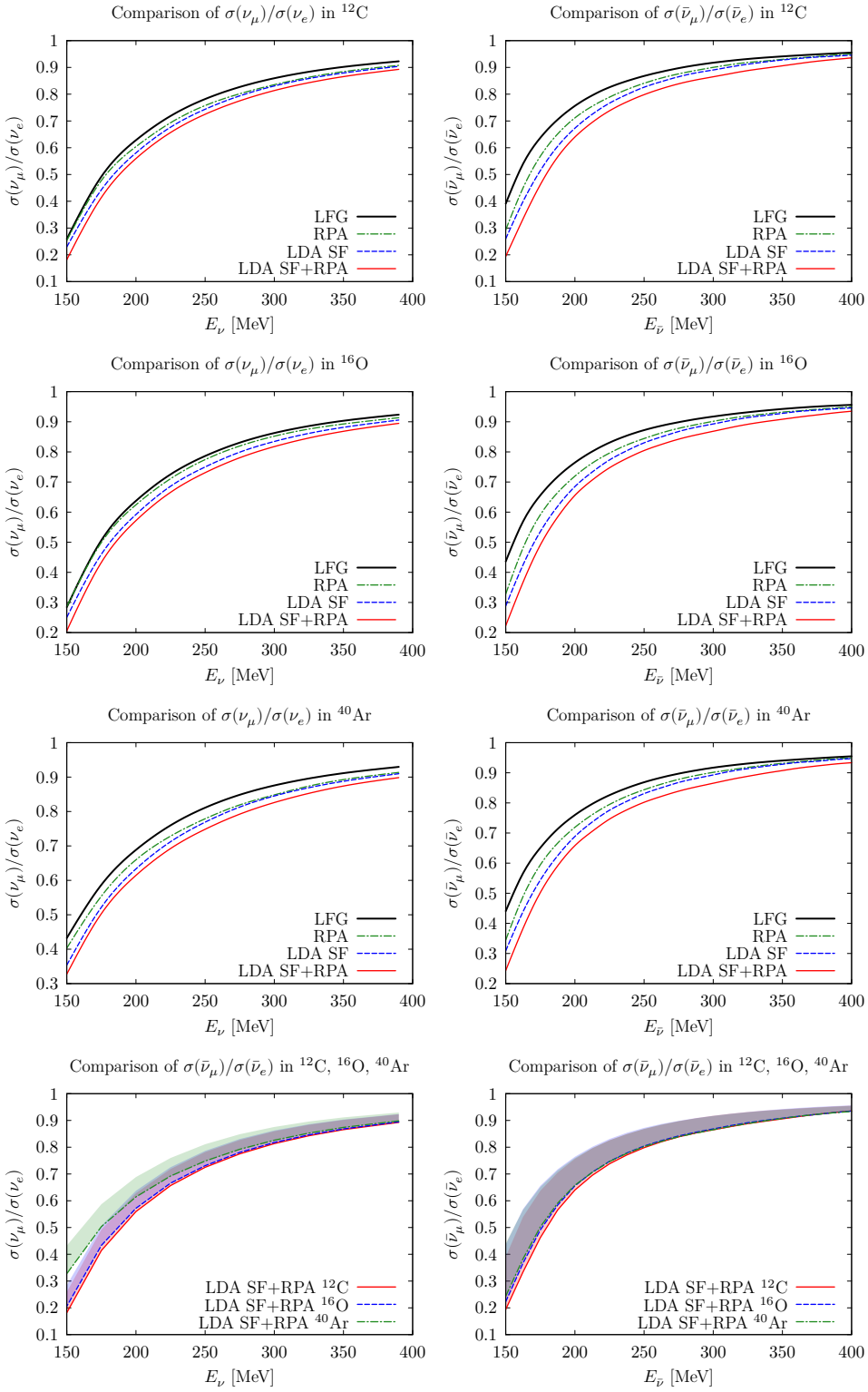

FIGURE 4.8: Ratio $\sigma(\mu)/\sigma(e)$ of inclusive neutrino (first row) and antineutrino (second row) QE cross sections for carbon, oxygen and argon, as a function of the incoming (anti-)neutrino energy. We show nonrelativistic free LFG, RPA, LDA SF and LDA SF+RPA results. In the two bottom plots, we show bands (red for carbon, blue for oxygen and green for argon) whose upper and lower limits are given by the LFG and LDA SF+RPA predictions, respectively.

model taken from [75]. Both sets of predictions for this genuine QE contribution, with and

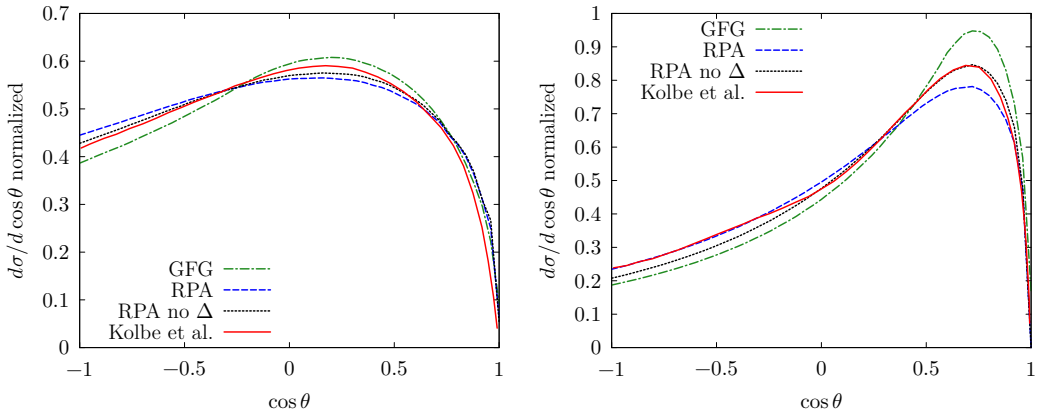

FIGURE 4.9: Angular distributions of the emitted electron in the $\nu_e + {}^{16}\mathrm{O} \to e^- + X$ inclusive reaction for $E_\nu = 300$ MeV (left) and 500 MeV (right). The curves labeled by GFG and Kolbe et al. are taken from the bottom panel of Fig. 3 of Ref. [163], and stand for the relativistic global Fermi gas model and the CRPA calculations presented in that work, respectively. In addition, we also show our full RPA predictions and the distributions obtained when the excitation of Δh components in the RPA responses are not taken into account (this amounts to setting U_Δ to zero in the denominators of Eq. (2.99)). Relativistic free LFG (noninteracting) SFs have been used in all cases.

without RPA effects, turn out to be in an excellent agreement, despite the large corrections produced by the RPA re-summation. Note that the comparison in Fig. 4.10 is quite appropriate, not only for the repercussion of the M_A puzzle, but also because the MiniBooNE flux peaks at muon-neutrino energies around 600 MeV [167], below 1 GeV that is the energy used to show predictions in Ref. [72]. Our RPA treatment is nonrelativistic and it should be used with some caution, as discussed at the beginning of Subsec. 4.2.2, for neutrino energies well above those compiled in Table 4.5. We understand that some relativistic corrections could also limit the validity of the RPA predictions of Ref. [72].

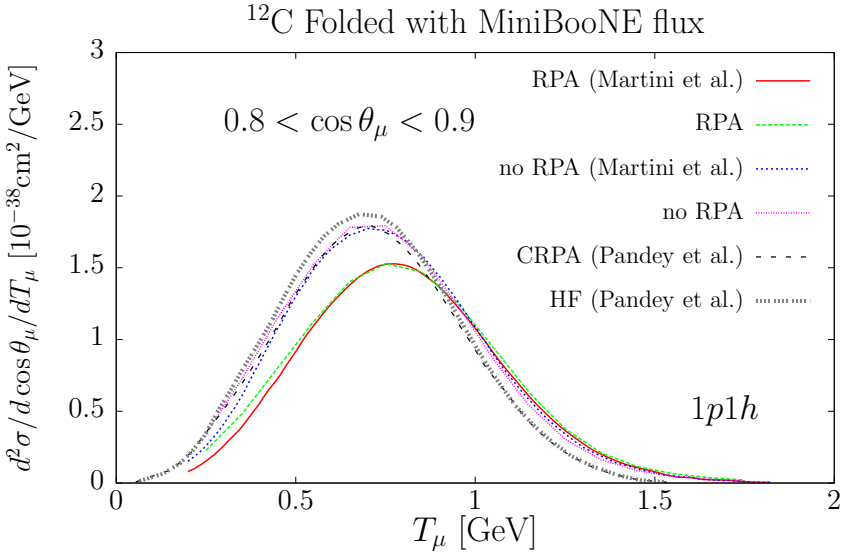

FIGURE 4.10: RPA effects on the QE contribution to the MiniBooNE flux–averaged $\nu_\mu - {}^{12}\mathrm{C}$ double differential cross section per neutron for $0.8 < \cos\theta_\mu < 0.9$, as a function of the outgoing muon kinetic energy. The curves labeled by Martini et al. and Pandey et al. are taken from Fig. 6 of Ref. [75] and Fig. 4 of Ref. [24], respectively, while the other two curves have been calculated using the model presented in this work, and they were first shown in Fig. 3 of Ref. [74]. Relativistic free LFG (noninteracting) SFs have been used in our predictions.

There exist other RPA or CRPA approaches available in the literature. Thus, for instance a detailed study of a CRPA approach to QE electron-nucleus and neutrino-nucleus scattering has been recently presented in Ref. [22] and briefly described in Subsec. 3.3.4. There, a special attention to low-energy excitations is paid, together with an exhaustive comparison of the $^{12}\mathrm{C}(e,e')$ and $^{16}\mathrm{O}(e,e')$ experimental double differential cross sections with CRPA and Hartree-Fock (HF) predictions. The work of Ref. [22] is in principle self-consistent, because the same interaction is used in both the HF and CRPA calculations. This is however not completely true, since the parameters of the momentum-dependent nucleon-nucleon force used in [22] were optimized against ground-state and low-excitation energy properties [168], and this force tends to be unrealistically strong at large $Q^2 = -q^2$ values. This is corrected in [22] by introducing a phenomenological dipole hadronic form factor at the nucleon-nucleon interaction vertices. Qualitative features reported in [22] agree with our model. To be more specific, let us focus in the $^{12}\mathrm{C}(e,e')$ cross sections showed for different kinematics in Fig. 5 of this reference. There, we see that being a collective effect, RPA corrections decrease as the associated wave-length of the virtual photon becomes significantly shorter than the typical size of the nucleus [79]. Thus, RPA effects become little relevant for the highest Q^2-panels showed in that figure, which in general correspond to incoming electron energies above 1 GeV or in the case of smaller energies to large scattering angles. However, large RPA corrections are clearly visible for the lowest electron energies (first seven panels of the figure), where in addition $Q^2 < 0.1$ GeV^2. Indeed, in most of these panels, where Q^2 is even smaller than 0.025 GeV^2, we see how the consideration of RPA correlations lead to the appearance of peaks in some regions. In the previous subsection (Subsec. 4.2.1), where the predictions of our model for low energies are discussed, we will see how something similar also occurs within our model, and in some regions we find clear enhancements of the LDA SF+RPA distributions as compared to those obtained without including RPA corrections.

In general, and besides the extremely low Q^2-panels, we conclude from Fig. 5 of Ref. [22] that RPA effects on top of the HF results are moderately small. This is in good agreement with our observation that RPA corrections are smaller when realistic SFs are taken into account. (Note that within a HF scheme, the nucleons acquire a real self-energy, and thus somehow this would be equivalent to use SFs obtained neglecting the particle and hole widths). The less important role played by RPA corrections, at sufficiently high Q^2 values when some realistic MF potentials are used, could provide some understanding of the success of the SuSA [21, 169, 170, 171, 172, 148] or the bound local FG model (used in the GiBUU–Giessen Boltzmann-Uehling–Uhlenbeck- transport approach [64]), in predicting neutrino cross sections despite not incorporating RPA effects.

Nevertheless, the approach of Ref. [22] has some limitations mostly because zero-range Skyrme interactions do not properly describe processes involving momentum transfers, significantly larger than m_π. Indeed, though a zero-range Skyrme force might be adequate for a microscopic description of both ground- and excited-state properties of nuclei, it might not be well suited to describe the dynamics of the ejected nucleon (S_p) or to compute RPA corrections for large momentum and energy transfers (let us say above 150 MeV). In this latter case, including $\Delta(1232)$ degrees of freedom (as we have shown in the discussion of the results of Ref. [163]), or considering explicitly pion exchange contributions to the interaction produce significant effects. This has been shown in a multitude of works [119, 173, 106, 2, 174, 175, 176, 177, 121, 178, 179, 7, 180, 7, 181, 182, 6, 183, 184, 185], where photon, electron, pion, kaon, $\Lambda,\Sigma-$hyperons etc. interactions with nuclei have been described within the many-body framework used here. Thus, as an example, in Fig. 4.11, we compare with data the predictions of the approach of Ref. [22] for inclusive QE cross section for scattering of electrons on carbon at 560 MeV and 60° ($|\vec{q}| = -0.508$ GeV). We observe that the results of Ref. [22] already describe the data in the region of QE peak, leaving almost no room for 2p2h contributions, which according to the empirical fit to electron-nucleus scattering data carried out in [186] provide

a significant cross section in that region. Note that the LDA SF+RPA QE predictions (RPA effects are moderately small, as one can expect for this value of q^2) lie below the data, and one might expect that some 2p2h contributions would improve notably the agreement with data[8]. In addition, one should bear in mind that our results for the energy transfers larger than that of the QE peak are affected from relativistic corrections, which will make the distribution narrower, as can be inferred from the reddish-shaded region shown in Fig. 4.11. Indeed, the position of the QE peak is also affected and a relativistic calculation will shift its position around 10 MeV towards lower energy transfers.

We should note that the GiBUU 2016 QE plus 2p2h cross sections, supplemented by $\Delta(1232)-$driven mechanisms and some non-resonant pion background terms provide a fairly good description of the data for all energy transfers shown in Fig. 4.11, as can be seen in the original Fig. 3 of Ref. [64].

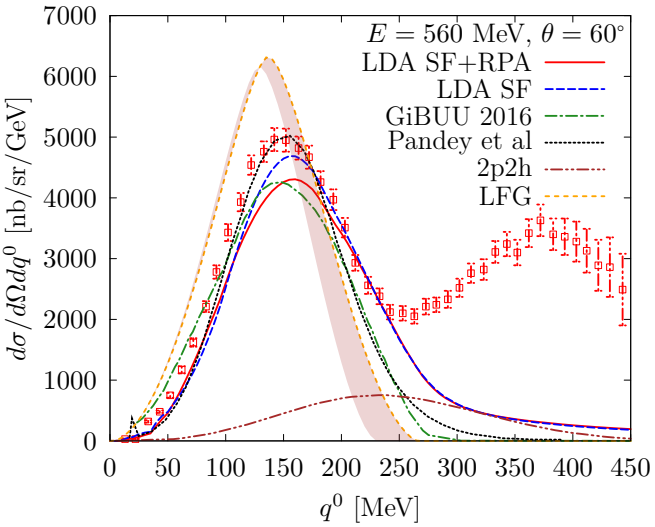

FIGURE 4.11: Inclusive QE cross section for scattering of electrons on carbon at 560 MeV and 60° ($q^2 = -0.242$ GeV^2 at the QE peak). Besides the LDA SF and LDA SF+RPA results (RPA corrections are included as in the case of the vector contributions to the neutrino-induced inclusive QE reaction driven by the electroweak NC studied in Ref. [113]; see also [6]), predictions from Refs. [22] (Pandey et al.) and [64] (GiBUU 2016) are also shown. These latter curves are taken from panel j of Fig. 5 of [22] and Fig. 3 of [64], respectively. The 2p2h curve, taken also from Fig. 3 of [64], stands for contributions of meson exchange currents (genuine 2p2h), and it might include also short-range and RPA effects [64]. It is obtained from an empirical fit to electron-nucleus scattering data carried out in [186]. Finally, the reddish-shaded region shows the difference between relativistic and nonrelativistic noninteracting LFG predictions. Data taken from Ref. [187].

The HF and CRPA approaches of Ref. [22] were used in Ref. [24] to evaluate the QE contribution to the CC quasielastic $\nu_\mu - {}^{12}$C double differential cross section convoluted with the MiniBooNE flux. These latter results for $0.8 < \cos\theta_\mu < 0.9$, as a function of the outgoing muon kinetic energy, are also displayed in Fig. 4.10. The size of the quenching is smaller in the CRPA model of Refs. [22, 24], resulting in a larger predicted cross section for the QE process, than in the approaches of Refs. [74] and [75]. We expect here a situation similar to that discussed in Fig. 4.11 for electron scattering, since all the available estimates [74, 75, 66, 64]

[8]We cannot simply add up the 2p2h contribution displayed in Fig. 4.11 to our predicted cross section. This is because our model for the SFs contains contributions from the 2p2h diagram depicted in Fig. 3.4, and then the addition of the rest of 2p2h contributions will include some interference terms which sign is not defined. Moreover and according to Ref. [64], the 2p2h curve also accounts for some short-range and RPA effects.

for the 2p2h contribution to the CCQE-like cross section measured by MiniBooNE will lead to the CRPA or HF models used in [24] to overestimate the data[9].

Next we pay attention to schemes involving realistic SFs. We begin with the CBF SF formalism, based on factorization and a state-of-the-art model of the nuclear SFs, used in Refs. [15, 16, 17, 18, 19] to describe neutrino-nucleus interactions. Such scheme has been extensively and successfully tested in electro-nuclear reactions at relatively large energies. We first compare in Fig. 4.12 our results with the most recent QE neutrino predictions reported in Ref. [19]. The

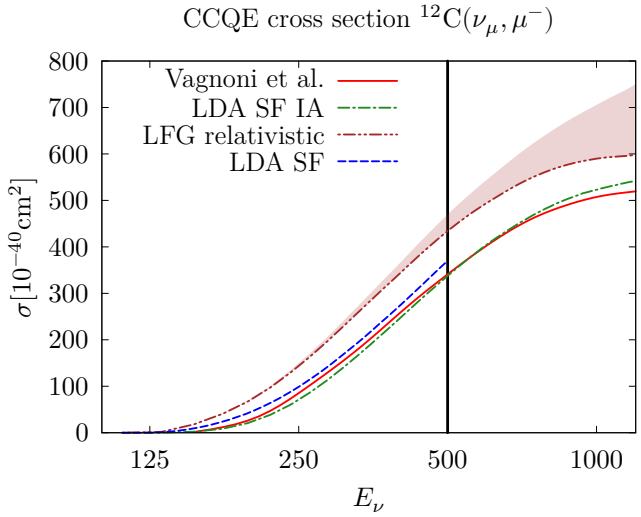

FIGURE 4.12: CCQE cross section of the reaction $\sigma(\nu_\mu + ^{12}\mathrm{C} \to \mu^- + X)$ as a function of neutrino energy. Besides the results taken from the bottom panel of Fig. 3 of Ref. [19], and labeled as Vagnoni et al., we also display (blue dashed line) our LDA SF predictions up to 500 MeV, and relativistic and nonrelativistic free LFG (upper limit of the reddish band) cross sections for the entire neutrino energy range. We also show results LDA SF IA obtained using the hadron tensor of Eq. (3.10), keeping the full hole LDA SF while treating the outgoing nucleon as a free particle.

calculation of Ref. [19] considers a fully dressed nucleon-hole, but uses a free particle SF, i.e., it employs a plane wave for the outgoing nucleon, satisfying a free relativistic energy-momentum dispersion relation. In the terminology of this reference, FSI effects are not taken into account. In spite of this, we see that our results, obtained dressing both particle and hole nucleon lines with a complex self-energy, agree quite well with the predictions given in Ref. [19] up to $E_\nu = 500$ MeV, where relativistic corrections could start being relevant. This confirms the validity of the approximation, sometimes used by this group, of neglecting FSI nuclear effects when studying inclusive total cross sections[10]. To extend the comparison to higher energies, we have adopted the same approximation as in [19], and replaced S_p in Eq. (2.87) by an energy conserving delta function[11], including also the M/E_{p+q} factor that appears in the evaluation of the Lindhard function when relativistic kinematics is used. The green dash-dotted curve, labeled as LDA SF IA, in Fig. 4.12 shows the results of this new calculation. The agreement

[9] See for instance the results for the QE and 2p2h cross sections given in Fig. 5 of Ref. [64], which sum describes fairly well the MiniBooNE data.

[10] FSI effects on inclusive integrated cross sections are mostly produced by the consideration of the real part of the self-energy in the energy conservation equation, and are in general small.

[11] As discussed in Subsec. 3.3.1, the real part of the nucleon self-energy is evaluated in [2] up to momentum independent pieces that appear both in the hole and particle self-energies and that cancel in the computation of the imaginary part of the fully dressed Lindhard function. However, to obtain results using a dressed hole and an undressed particle, an absolute value for the real part of the nucleon-hole self-energy is needed. Here, we include phenomenologically a constant term $C\rho$ in the nucleon self-energy, with $C = 0.8$ fm^2 for carbon, fixed to a binding energy per nucleon $|\varepsilon_A| = 7.8$ MeV (see Subsec. 3.2.3).

with the predictions of Ref. [19] is remarkable for the entire neutrino energy range displayed in the figure, even above 1 GeV.

Note that the use of a realistic hole SF produces significant corrections, which clearly need to be accounted for to achieve an accurate description of the cross section.

FSI effects (use of a nontrivial particle SF) in the scheme of Refs. [15, 16, 17, 18] are taken into account by means of a convolution [144, 14], which involves the real part of a nucleon-nucleus optical potential–responsible for a certain shift in the QE peak position–, the nuclear transparency, and the in-medium NN scattering cross section. The imaginary part of the Lindhard function calculated using the SFs of Ref. [2] also nicely agrees with that deduced within the scheme of Refs. [15, 16, 17, 18] when FSI effects are taken into account. In a comparison presented in Ref. [188] and in Chpt. 5 the scaling function [189, 190, 191] is computed and compared in both approaches (the scaling function is essentially, up to a factor $|\vec{q}|$ and some other constants, the imaginary part of the Lindhard function [25]).

In Fig. 4.13, we have also compared the results of our approach in the QE region for several $e+^{12}\mathrm{C} \to e'X$ double differential distributions at different scattering angles and incoming electron energies with data and with the predictions of Ref. [14]. The approach of Ref. [14], in addition to the use of a realistic hole spectral function, takes also into account the effects of FSI (nontrivial particle SF) between the struck nucleon and the residual nucleus through the convolution mentioned above. Our LDA SF results agree reasonably well with the predictions of Ref. [14] for all examined kinematics. Nevertheless in the bottom panels, for which $|\vec{q}| > 365$ MeV, our distributions are wider than those obtained within the approach of Ref. [14], showing clear differences above the QE peak. Relativistic corrections will make our distributions narrower, as can be inferred from the reddish-shaded regions in Fig. 4.13.

We finish these comparisons discussing the similarities of our approach with the GiBUU framework used in Ref. [145] to make predictions for CC and NC inclusive scattering of oxygen at beam energies ranging from 0.5 to 1.5 GeV. The scheme takes into account various nuclear effects: the LDA for the nuclear ground state, mean-field potentials, and in-medium spectral functions. For the spectral function of the initial state nucleon, it was considered only the real part of the self-energy generated by a MF potential and neglected the imaginary part[12]. All these in-medium modifications were tested by comparing the predictions of the model with electron scattering results.

In Fig. 4.14, we show the CCQE predictions for oxygen at $E_\nu = 0.5$ GeV given in the top panel of Fig.13 of Ref. [145] (orange-dotted curve labeled as Leitner et al in Fig. 4.14), together with our LDA SF and free LFG results. The agreement is not as good as in the previous cases, and our full SF distribution at the QE peak is smaller (around 30%) than that obtained in Ref. [145], and it is also significantly wider. The agreement improves when the results of Ref. [145] are compared with the differential cross section obtained within our model neglecting the imaginary part of the hole self-energy, as in [145].

We should note that the GiBUU framework used in [145] overestimates the similar (e,e') differential QE cross sections for incoming electron energies and outgoing scattering angles close to those examined in Fig. 4.14. This can be seen in Figs. 10 and 11 of the same reference [145]. Indeed looking at the top panels of these two figures, one can appreciate deviations from data of around 20-25% at the QE peak. Moreover, the discrepancies seem to increase when both the incoming electron energy and scattering angle decrease. (Note that in the top panels of Figs. 10 and 11, both scattering angle and energy are larger than those examined in Fig. 4.14.) One certainly expects that the approximate SF-treatment used in [145] should work much better and be quite accurate for angular-integrated cross sections.

[12]Neglecting the hole width is a priori a reasonable approximation, as can be inferred from Fig. 3.6, and it was also used in Ref. [3]. Note however that in this latter work, the Jacobian determinant discussed in Eq. (3.21) was further approximated to one.

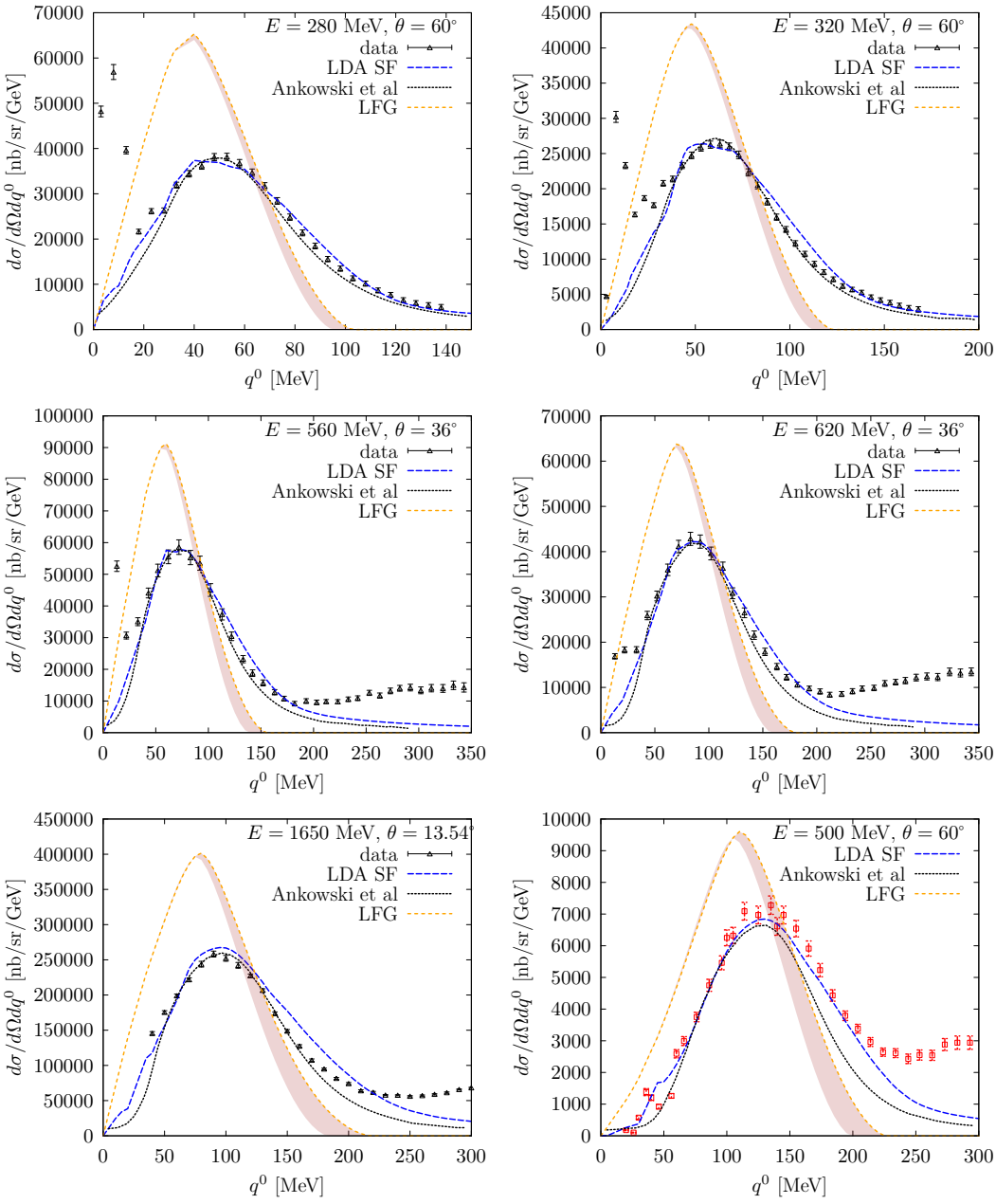

FIGURE 4.13: Inclusive QE cross sections for scattering of electrons on carbon at different scattering angles and incoming electron energies. Besides LDA SF results, predictions (Ankowski et al.) taken from panels (d)–(i) of Fig. 2 of Ref. [14] are also shown. At the QE peaks, the momentum transfers $|\vec{q}|$ are 259, 295, 331, 366, 390 and 450 MeV, respectively. Data taken from Refs. [192, 193, 194]. As in Fig. 4.11, the reddish-shaded regions show the difference between relativistic and nonrelativistic noninteracting LFG predictions.

A new release of GiBUU became available in 2016 [64], among other improvements, a better preparation of the nuclear ground state and its momentum distribution are implemented. This corresponds in our language to use more accurate SFs. The new result is also shown (blue-dashed curve, labeled as GiBUU 2016) in Fig. 4.14, where we could see the agreement with the two versions of the present work is now quite good.

Moreover, the update GiBUU version provides an excellent description of electron data, not only for QE scattering here discussed, but also in the dip and $\Delta-$peak regions [64, 195].

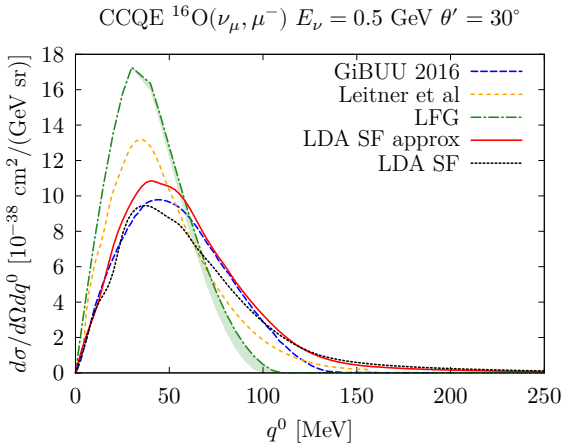

FIGURE 4.14: CCQE neutrino double differential cross section $d^2\sigma/d\Omega(\hat{k}')dE'$ on ^{16}O as a function of the energy transfer at $E_\nu = 0.5$ GeV and a scattering angle of $\theta = 30^o$. The orange-short-dashed curve, labeled by Leitner et al., stands for the full calculation of Ref. [145] (full in-med. SF curve of top panel of Fig. 13 of this reference). We also show relativistic and nonrelativistic free LFG, and the LDA SF and approximated LDA SF (neglecting the hole width) sets of predictions. Finally the blue-dashed curve, labeled as GiBUU 2016, has been obtained with the 2016 updated version of the GiBUU code [64].

4.3 Electron scattering

In this section, we will confront the nuclear effects incorporated by the means of realistic SFs with electron scattering data. It is based on the findings of Ref. [150].

4.3.1 Electron selection criterion

There is a large set of electron-nucleus cross-section measurements. In order to perform a comparison with electron data we will choose the data sets that are most important for the T2K experiment. To do this, we consider the flux-averaged differential cross section $(d\sigma/d|\vec{q}|dq^0)^{\rm CCQE}$ from carbon. The muon neutrino flux used in the T2K experiment, $\mathscr{F}(E)$, is shown in Fig. 4.15. The cross section averaged over the flux is given by:

$$\frac{d\sigma}{d|\vec{q}|dq^0}\Big|_{\rm T2K} = \frac{1}{\mathscr{F}}\int dE \frac{d\sigma^{\rm CCQE}}{d|\vec{q}|dq^0}\mathscr{F}(E), \quad \mathscr{F} = \int dE\mathscr{F}(E). \tag{4.18}$$

We have also looked at the distribution of the oscillated neutrinos investigated in both the appearance and the disappearance measurements, taking into account the probability of oscillation $\mathscr{P}_{\nu_\mu\to\nu_e}$ for the ND280 near detector with parameters given in [51]. It shifts slightly the peak and makes it narrower (see Fig. 4.15). Thus we consider now:

$$\frac{d\sigma}{d|\vec{q}|dq^0}\Big|^{\rm osc}_{\rm T2K} = \frac{1}{\mathscr{W}}\int dE \frac{d\sigma^{\rm CCQE}}{d|\vec{q}|dq^0}\mathscr{F}(E)\mathscr{P}_{\nu_\mu\to\nu_e}(E),$$
$$\mathscr{W} = \int dE\mathscr{F}(E)\mathscr{P}_{\nu_\mu\to\nu_e}(E). \tag{4.19}$$

The results of the analysis done with Eqs. (4.18) and (4.19) are very similar because the spectra for the muon neutrinos and oscillated neutrinos are very much alike (see Fig. 4.15). In what follows, the latter option will be chosen. In order to calculate $(d\sigma/d|\vec{q}|dq^0)^{\rm CCQE}$ we have used the LDA SF IA model (with a free particle spectral function, see Sec. 3.2.3 because of its fast numerical performance). The results are shown in Fig. 4.16, where we can also see the position of the QE peak, defined as the maximal value of $(d\sigma/d|\vec{q}|dq^0)^{\rm CCQE}$ for a given q^0 (note that its

position is very close to $\vec{q}^2 = (q^0)^2 + 2Mq^0$). The use of different models might slightly change the shape shown in Fig. 4.16 (*e.g.* shift the position of the QE peak, spread it, etc.); however, it would not influence the final conclusions of this analysis since it is used only to sieve the electron data.

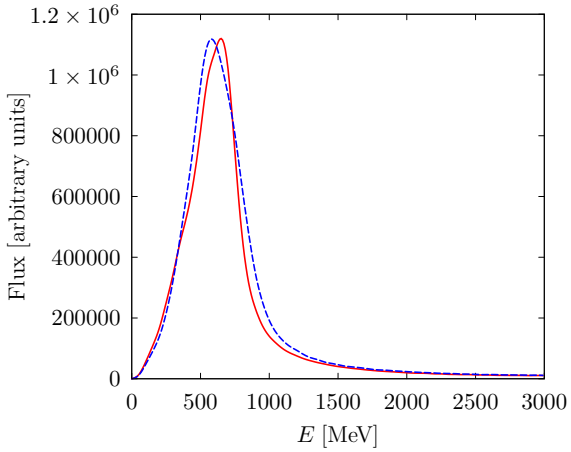

FIGURE 4.15: The muon neutrino flux in the ND280 detector of the T2K experiment, taken from [196]. The dashed line shows the flux, the solid curve shows the flux multiplied by the oscillation probability $\mathscr{P}_{\nu_\mu \to \nu_e}$ [51]. Both curves are normalized to the same area.

In total there are 66 data sets of electron-carbon scattering data gathered in [187]. They cover a wide range of incoming electron energies and scattering angles which can be translated into energy and momentum transfer variables. Using this change of variables, one can plot them all on the $(q^0, |\vec{q}|)$ plane, just as shown in Fig. 4.16 for three example data sets. The usage of $(q^0, |\vec{q}|)$ variables is more natural because they are the arguments of the nuclear response functions, which play the same role for neutrino and electron scattering processes (the difference lies in the interaction vertex). In Fig. 4.16 we show how three typical electron data sets coincide with the CCQE region for the T2K flux.

The next problem is to define a criterion to select which data sets are most important for neutrino studies. We propose to quantify the significance of data using the following procedure:

1. Calculate $d\sigma/d|\vec{q}|dq^0\big|^{\text{osc}}_{\text{T2K}}$ for the range of $q^0 \in (0, 500)$ MeV, $|\vec{q}| \in (0, 1000)$ MeV.

2. We look at the QE peak defined as the maximal value of $d\sigma/d|\vec{q}|dq^0\big|^{\text{osc}}_{\text{T2K}}$ for a given q^0 (it leads to a "CCQE line" marked as a black solid curve in Fig. 4.16)

3. Plot the different electron data sets on the (q^0, $|\vec{q}|$) plane.

4. Choose only those data sets which CCQE value (the value of $d\sigma/d|\vec{q}|dq^0\big|^{\text{osc}}_{\text{T2K}}$ at the crossing point with the "CCQE line") is at least 67% of the maximal value taken by this flux-averaged differential cross section along the "CCQE line", see Fig. 4.17.

This procedure largely reduces the available electron scattering data, basically removing those with low or high energy transfers in the QE peak. There are in total 33 data sets fulfilling this condition. To introduce further order, we divide them into three groups according to their importance, calculating again the value of the CCQE peak that corresponds to their position. In Fig. 4.17 we plot the dependence of the CCQE peak height on the energy transfer q^0 (using the LDA SF IA model) and mark three regions. In the energy range $30 - 200$ MeV the height varies from 43.7 to $62.5 \times 10^{-38} \text{cm}^2/\text{GeV}^2$. The maximal value is reached for $q^0 \sim 80$ MeV. The three regions that we consider are:

- **Region I (energy transfer 30-50 MeV)**. The momentum transfer in this region is $|\vec{q}| <$ 300 MeV, which means that one is actually beyond the limit of usability of the Impulse Approximation and giant resonances might be visible in the data. This is also the smallest sample with only five data sets.

- **Region II (energy transfer 50-125 MeV)**. This will be our main region of interest, it covers data with at least 95% of the maximal height. There exist eighteen data sets in this region.

- **Region III (energy transfer 125-200 MeV)**. The importance of this region is similar to that of Region I, however, they are separated for the sake of a clearer analysis (since theoretical models behave differently in Regions I and III). There are ten data sets in this region of energy transfer.

4.3.2 Data sets

The selected 33 data sets are gathered in Tables 4.7 (Region II) and 4.8 (Regions I and III). Each data set is identified by the energy of the incoming electron and the scattering angle (columns 1 and 2), and for all of them we find the point $(q^0, |\vec{q}|)$ for which $d\sigma/d|\vec{q}|dq^0|^{\rm osc}_{\rm T2K}$ is maximal. The point coordinates are denoted by $((q^0)^{\rm QE}, |\vec{q}|^{\rm QE})$ and shown in columns 3 and 4. The numerical value of $d\sigma/d|\vec{q}|dq^0|^{\rm osc}_{\rm T2K}((q^0)^{\rm QE}, |\vec{q}|^{\rm QE})$ is given in the fifth column. Finally, the ratio of these latter values and the absolute maximal one for $d\sigma/d|\vec{q}|dq^0|^{\rm osc}_{\rm T2K}$ are collected in the column number six (among all the sets it corresponds to the kinematics E=1500 MeV, $\theta = 13.54^\circ$ and $q^0 \sim 80$ MeV). This serves as a measure of the importance of the set.

We will consider different theoretical models and compare the various predictions to the inclusive electron-nucleus scattering data. We will restrict this study to the QE region. For future discussions we estimate also contributions from the longitudinal and transverse responses. For electron-nucleus scattering, the cross section is the sum of two contributions from either a transverse or longitudinally polarized virtual photon. It can be expressed in terms of $R_T(q)$, $R_L(q)$ response functions which enter in the definitions of $\sigma_{L,T}$ (see Eq. (5.1) of the next chapter):

$$\frac{d^2\sigma}{d\Omega_{k'}dq^0} = \left(\frac{d\sigma}{d\Omega_{k'}}\right)_{\rm Mott}\Big[\sigma_L + \sigma_T\Big], \tag{4.20}$$

It is well known that non-QE processes, like 2p2h excitations or the Δ production, mostly contribute to the σ_T part. Therefore, for $\sigma_L \gg \sigma_T$ one might expect those mechanisms to give small contributions in the QE region. We will come back to this point in Sec. 4.3.4. Thus, in the column 7, σ_T/σ_L is also shown. Those ratios are calculated at the QE peaks and provide some information on how large contributions from 2p2h and Δ mechanisms should be expected.

4.3.3 Analysis

In the following section, the results predicted by different models are described. We will include LDA SF (Sec. 3.2), CBF SF (Subsec. 3.3.1), GiBUU (Subsec. 3.3.2) and – as a benchmark – LFG and GFG relativistic models. In order to make the plots legible, the results of CBF SF without including FSI are not depicted. However, its behaviour is briefly mentioned in the discussion. Also, CBF SF+FSI results will be shown in the figures included in Subsec. 4.3.4. Since we are comparing theoretical QE approaches with inclusive electron scattering data, one must be careful in drawing definite conclusions about precision of the different models. In some kinematical setups the 2p2h and the Δ production mechanisms might give sizable contributions in the QE peak region. Therefore, one should not expect a perfect agreement of the QE theoretical models with data. This issue will be separately discussed for each region.

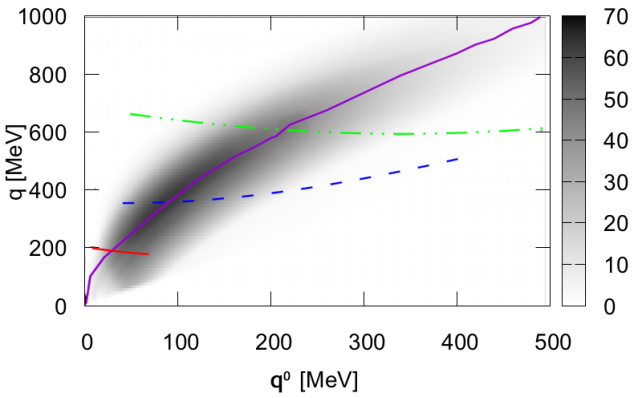

FIGURE 4.16: $d\sigma/d|\vec{q}|dq^0|^{\rm osc}_{\rm T2K}$ [10^{-38}cm^2/GeV^2] in carbon for the T2K flux (using the LDA SF IA model), see Eq. (4.19). The position of the CCQE peak is marked with the solid line. Three typical electron data sets are also shown (experimental points are connected by lines for better legibility): solid line E= 200 MeV, $\theta = 60°$; dashed line E= 1500 MeV, $\theta = 13.54°$, dotted-dashed line E= 680 MeV, $\theta = 60°$. Each of them crosses the black solid curve ("CCQE line") at different points. The value of $d\sigma/d|\vec{q}|dq^0|^{\rm osc}_{\rm T2K}$ in this crossing point is taken as the measure of the importance of the data set.

I Region (energy transfer 30-50 MeV)

In this region, the longitudinal part of the cross section is overwhelmingly dominant (see Table. 4.8), and contributions of the 2p2h and the Δ mechanisms are supposed to be quite small, hardly influencing the analysis. Thus, one can compare the models directly to the data. On the other hand, this region is sensitive to collective effects, which are clearly visible in the data (Figs. 4.18a-4.18e). With such small energy transfers, one is on the verge of the applicability of some models, and the data points lying on the left of the QE peak are usually not correctly described using just spectral functions.

In these kinematical setups, the importance of SF nuclear effects is clearly visible. The LFG predicts the QE peak sometimes twice higher than data and shifted (up to 15 MeV). The GFG predictions are slightly lower but also clearly overestimate the experimental cross section. CBF SF (not shown in the plots) misplaces the QE peak (even by 20-25 MeV) and overestimates it (up to 10% effect), confirming that it is not enough to describe properly the data using only a realistic hole SF. When applying the complete models: LDA SF, CBF SF+FSI and GiBUU, the results are close to the data and all the models work remarkably well (Figs. 4.18a-4.18e).

LDA SF and CBF SF+FSI performances are probably slightly better than that of GiBUU. The latter model overestimates slightly the strength of the QE peak and the slope of the data. Also, one observes that LDA SF and CBF SF+FSI produce a long tail which is not present in GiBUU results; however, this influences only the high energy transfer region. The tail would appear also for GiBUU if the collisional broadening had been taken into account (here we present the results of the standard calculation where these effects were neglected).

In this region, the fact of using nonrelativistic kinematics hardly influences the results. This can be observed for the LFG model, where the difference between relativistic and nonrelativistic kinematics is small (see the gray band on Fig. 4.18a-4.18e).

II Region (energy transfer 50-125 MeV)

This is the most important region where the highest $d\sigma/d|\vec{q}|dq^0|^{\rm osc}_{\rm T2K}$ cross sections are found. There are many data sets (18) to compare with, for various kinematical setups (both low and intermediate scattering angles). Results are shown in Figs. 4.19, 4.20 and 4.21.

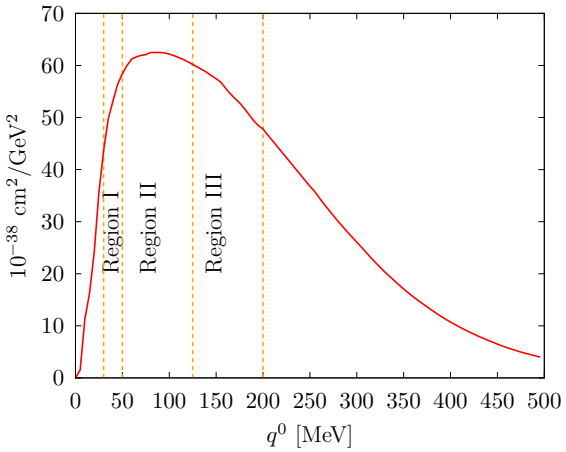

FIGURE 4.17: Flux (T2K) average CCQE $d\sigma/d|\vec{q}|dq^0|^{\text{osc}}_{\text{T2K}}$ [10^{-38}cm^2/GeV^2] cross section in carbon at the QE peak as a function of the energy transfer. The LDA SF IA model has been used to evaluate the nuclear cross section.

First of all, one notices that GiBUU, CBF SF+FSI and LDA SF predictions stay in a very good agreement with the data in this region. For higher energy transfers (above the QE peak) LDA SF predicts broader QE distributions than the other two models, however, this can be explained by the nonrelativistic kinematics that is employed. GiBUU and CBF SF+FSI models in some cases underestimate the data (especially on the right side of the peak). This can, however, be partially understood by the 2p2h contribution that is not included in the calculations, as will be discussed in Subsec. 4.3.4 (see Figs. 4.21a, 4.21e and 4.21f). The difference between the models at the QE peak is rather small (a few percent difference, with GiBUU lying below). For the lower energy transfers (below 50-75 MeV) the discrepancies are more pronounced. GiBUU in some cases slightly overestimates the data (e.g. Fig. 4.21f), while CBF SF+FSI and LDA SF underestimate it (*e.g.* Fig. 4.21c). We also see in Figs. 4.19a, 4.19c, 4.19d, 4.19f, 4.20a, 4.20b, 4.20e, 4.20f some additional low-energy structures which might be described by collective modes.

Fermi gas models have a tendency to overestimate the QE peak. The LFG predicts the QE peak far too high, for the lower energy transfers almost twice as high, going down to $40-60\%$ effect. It is also displaced for about $10-15$ MeV in the case of a high-energy incoming electron and a small scattering angle (see for instance Figs. 4.20c, 4.20d, 4.21b). Even though the change of the binding energy would move the QE peak position, it is impossible to choose a unique value which would be correct for all kinematics.

If one neglects FSI, using CBF SF, the QE peak is shifted - up to 25 MeV - and slightly overestimated (what is especially pronounced for low scattering angles). The latter effect is, however, rather small (few percent). Similarly to Region I, CBF SF+FSI and LDA SF predict a long tail spreading to the high energy transfer. There, the two approaches describe the data remarkably well, as can be observed *e.g.* in Fig. 4.19. In this region in general $\sigma_T/\sigma_L < 1$ but – as can be seen in Figs. 4.21d-4.21f – where $\sigma_T/\sigma_L \approx 1$ other mechanisms start to be visible in the data and lead to some enhancement in the cross section for large q^0.

Region III (energy transfer 125-200 MeV)

In this region, $\sigma_T \sim \sigma_L$ and therefore 2p2h and Δ mechanisms are expected to overlap with the QE peak in a significant way. However, as will be shown in Subsec. 4.3.4, the effect of these reaction channels is not drastic in the vicinity of the peak. It influences mostly the slope at the

Energy [MeV]	Angle [degrees]	$(q^0)^{\rm QE}$ [MeV]	$\lvert\vec{q}\rvert^{\rm QE}$ [MeV]	$\frac{d\sigma}{d\lvert\vec{q}\rvert dq^0}{}^{\rm osc}_{\rm T2K}$ $((q^0)^{\rm QE},\lvert\vec{q}\rvert^{\rm QE})$ [10^{-38} cm^2/GeV^2]	$\frac{\text{height}}{\text{max height}}[\%]$	σ_T/σ_L $((q^0)^{\rm QE},\lvert\vec{q}\rvert^{\rm QE})$
280	60°	53	258	60.1	96.1	0.4
1300	11.95°	60	271	61.2	98.0	0.2
480	36°	62	284	61.5	98.3	0.3
320	60°	63	294	61.3	98.1	0.5
1500	11.95°	70	313	61.7	98.8	0.3
1300	13.54°	70	306	61.9	99.1	0.3
560	36°	72	331	62.2	99.4	0.4
361	60°	73	331	62.2	99.5	0.6
1650	11.95°	80	345	62.1	99.4	0.4
1500	13.54°	80	353	62.4	100	0.4
401	60°	88	365	62.3	99.7	0.7
620	36°	92	365	62.3	99.7	0.5
440	60°	98	400	61.7	98.7	0.8
1650	13.54°	100	390	62.0	99.2	0.4
680	36°	102	401	61.5	98.5	0.6
480	60°	112	435	60.5	96.9	0.9
730	37.1°	115	442	60.2	96.3	0.7
500	60°	125	451	59.9	95.8	1.0

TABLE 4.7: Data sets of Region II sorted by $(q^0)^{QE}$. Columns 3 and 4: coordinates $((q^0)^{\rm QE}, |\vec{q}|^{\rm QE})$ in Fig. 4.16 for which $d\sigma/d|\vec{q}|dq^0|^{\rm osc}_{\rm T2K}$ in carbon is maximum for the given electron data set, being the latter value collected in the fifth column. Column 6: ratio of the flux averaged cross section displayed in column 5 ("height") and the absolute maximum one that corresponds to kinematics E=1500 MeV, $\theta = 13.54°$ ("max height"). Finally, in the last column we give the ratio σ_L/σ_T (Eq. (4.20)) for electron-nucleus scattering. The numbers given in the last column where obtained in the LFG model. The results of column 5 have been evaluated using the LDA SF IA nuclear model. For some more details see the text in Subsec. 4.3.2.

right hand side of the QE maximum, though in some cases it might even change the height of the peak.

The higher energy transfers are, the less visible SF nuclear effects become. Comparing to Regions I and II, the differences between the Fermi gas and other models are less pronounced. Surprisingly, the GFG gives predictions very similar to models which contain nuclear corrections while the LFG overestimates the peak (as is Regions I and II). Here the effect is not so drastic, yet clearly visible, about 35% of the discrepancy.

CBF SF model also slightly misplaces the peak (up to 15 MeV towards high energies), however, not overestimating it. The inclusion of FSI, which caused quite a strong quenching in Regions I and II, here produces a rather small effect. The peak gets shifted towards lower energies because of the real part of the optical potential U_V.

In this region, because of the large relativistic effects, for all the cases but the four corresponding to the lowest energy transfers (Figs. 4.22a, 4.22b, 4.22c, 4.22d) we have used an approximated version of the LDA SF model, where the particle spectral function is approximated by the free relativistic one (LDA SF IA). We have neglected FSI effects and we have used the approximated expression of Eq. (3.11). The results are shown in Figs. 4.22e, 4.22f and 4.23. Comparing the predictions of the latter model with those obtained with the GiBUU and CBF SF+FSI ones, the peak is around 10-15% higher and slightly broader on the right side of the QE peak, which makes them closer to data, however not leaving much room for the inclusion of 2p2h and Δ effects.

Energy [MeV]	Angle [degrees]	$(q^0)^{\mathrm{QE}}$ [MeV]	$\lvert\vec{q}\rvert^{\mathrm{QE}}$ [MeV]	$\frac{d\sigma}{d\lvert\vec{q}\rvert dq^0}^{\mathrm{osc}}_{\mathrm{T2K}}$ $((q^0)^{\mathrm{QE}}, \lvert\vec{q}\rvert^{\mathrm{QE}})$ [10^{-38} cm^2/GeV^2]	$\frac{\text{height}}{\text{max height}}[\%]$	σ_T / σ_L $((q^0)^{\mathrm{QE}}, \lvert\vec{q}\rvert^{\mathrm{QE}})$
200	60°	43	182	50.3	80.5	0.2
320	36°	43	189	51.9	83.0	0.2
240	36°	48	141	44.7	71.5	0.1
240	60°	48	220	56.8	90.9	0.3
400	36°	52	236	58.3	93.3	0.2
519	60°	131	468	59.0	94.3	1.0
560	60°	142	504	57.0	91.2	1.2
2020	15.022°	150	530	54.2	86.7	0.7
2000	15°	150	524	55.0	88.0	0.7
1930	16°	164	539	53.2	85.1	0.8
620	60°	168	555	51.6	82.6	1.3
2130	16°	179	595	47.2	75.5	0.9
1930	18°	182	603	46.0	73.7	0.9
961	37.5°	183	585	48.7	78.0	1.0
680	60°	188	608	46.0	73.7	1.5

TABLE 4.8: As in Table 4.7, but now the data sample belong to Regions I (first five sets) and III (last ten sets) sorted by $(q^0)^{\mathrm{QE}}$.

GiBUU and CBF SF+FSI models give very similar predictions for the height of the QE peak (a few percent difference with GiBUU ones lying lower), but slightly shifted. One observes that the GiBUU peak is much broader and for this reason in general for lower energy transfers this model better describes the data, though in some occasions overestimate the experimental cross section. CBF SF+FSI and LDA SF models underestimate the data at the left hand side of the QE peak and this cannot be explained by 2p2h or $\Delta(1232)$ excitation mechanisms. This difference between models was already visible in Region II.

4.3.4 Discussion

One encounters various practical problems when trying to perform a more quantitative comparison of the models. The description of the QE peak means not only its position, height and width. The peak's shape also changes, from almost symmetric to some appreciable degree of asymmetry (*e.g.* Figs. 4.18d, 4.20a). Moreover, one does not have enough "direct information" even to measure these basic nuclear quantities. In Regions I and II we cannot calculate the peak's width because the experimental points for low energy transfers are obscured by the existence of giant resonances. On the other hand, in Regions II and III, the contributions from 2p2h and Δ mechanisms broaden the peak, changing also its height and modifying the shape.

In order to overcome these obstacles, we will attempt to subtract the 2p2h and the Δ contributions from the data, using a model from Ref. [197] (this is not a unique possibility; one can use *e.g.* the empirical fit proposed in Ref. [186]). We are well aware of the fact that this is only an approximated procedure because predictions for 2p2h and Δ mechanism contributions are model dependent and there may be non-negligible interference effects. However, we hope that at least basic properties of the different schemes can be analyzed in this way.

We will first concentrate on two characteristics of the QE peak: its position and height. Subtracting the 2p2h and the Δ contributions affects mainly the width of the QE peak, changing the QE peak's height only for the higher energy transfers by less than 10% percent (according to the model from [197]). Lastly, we will compare the QE peak's height and width (defined as

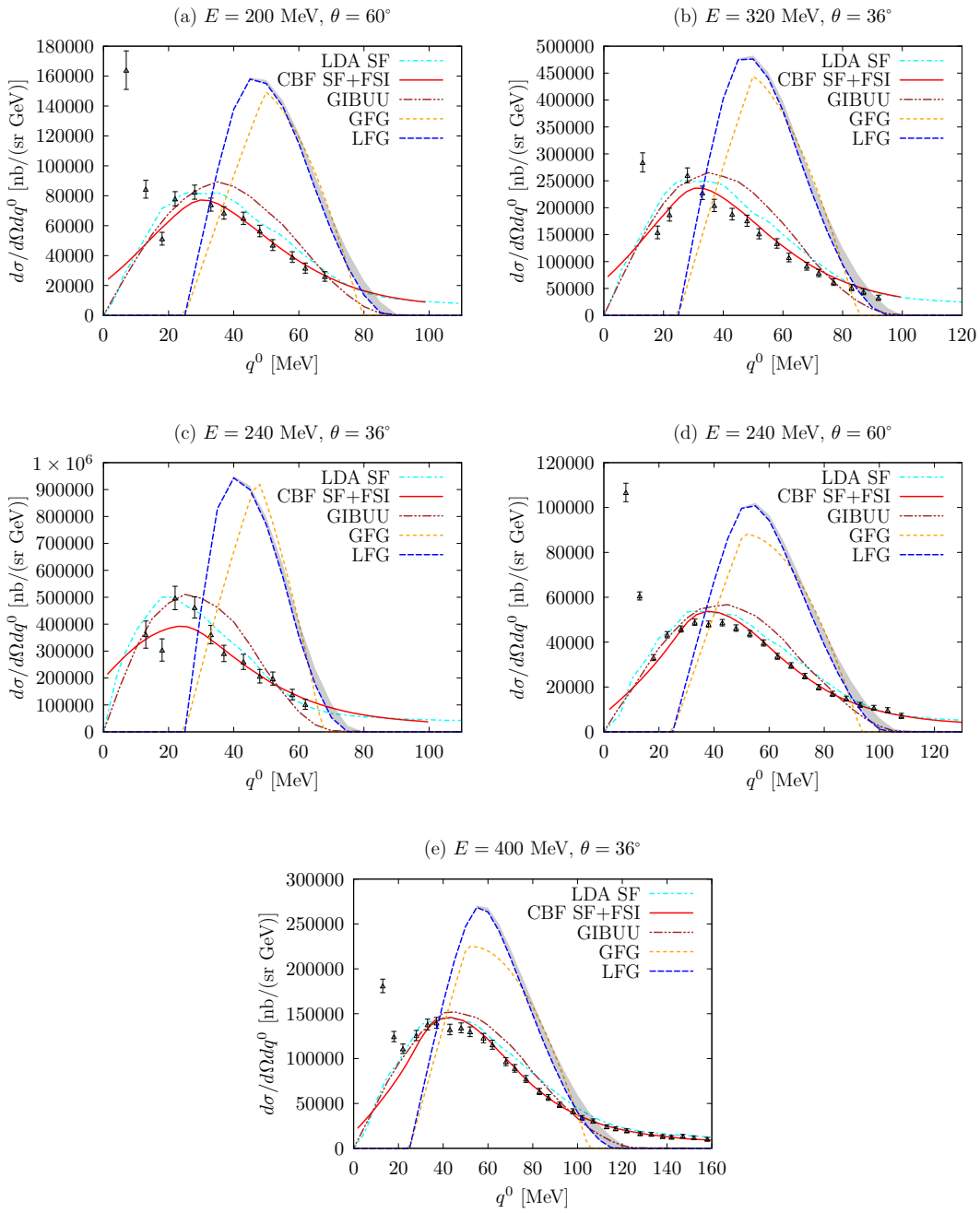

FIGURE 4.18: Comparison of different electron-nucleus scattering models in Region I. For the local Fermi gas, relativistic kinematics is employed and the difference from nonrelativistic results is shown as a gray band.

the distance to the peak position where the strength has been reduced by a factor $1/2$) predicted by various models with those find in the LFG one.

2p2h and Δ contribution

Two particle two hole (2p2h) mechanisms, also called meson-exchange current (MEC) contributions, describe a situation where the lepton interacts with two nucleons from the ground state, creating another pair of nucleons. On the other hand, the virtual photon can also excite a $\Delta(1232)$ resonance that subsequently decays into a πN pair or disappears through nucleon

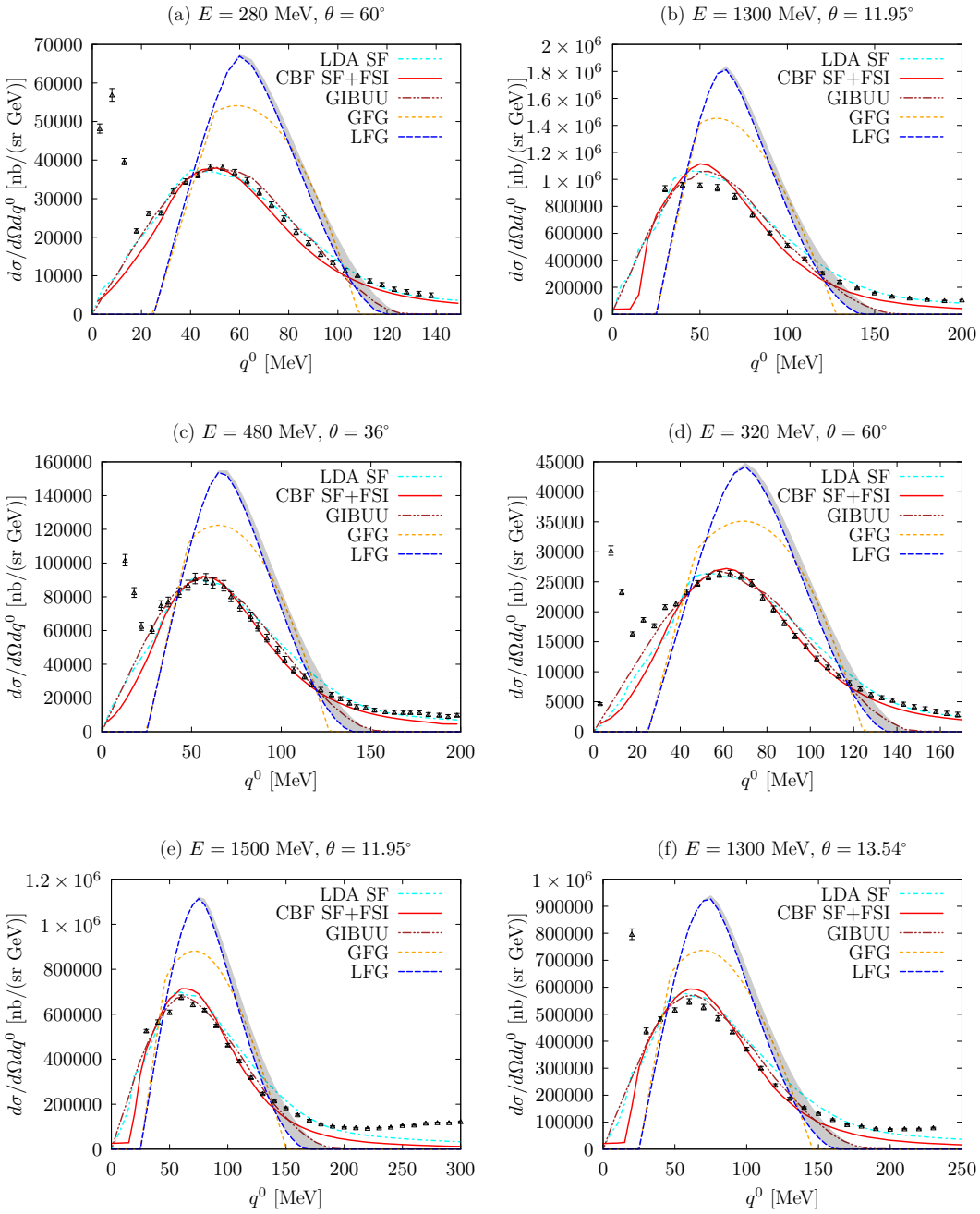

FIGURE 4.19: The same as in Fig. 4.18, but for Region II with $(q^0)^{\mathrm{QE}} \leq 70$ MeV.

collisions $\Delta N \to NN$. In some kinematical regions, the 2p2h and the Δ mechanisms may give a noticeable contribution to the QE region. These new physical reaction channels overlap with the QE peak, as can be observed with a naked eye when looking at the data: the cross section grows instead of diminishing for higher energy transfers (above the QE peak), see *e.g.* Fig. 4.22. This large contribution is in general due to the fact that the transverse response function gives a sizable contribution to the cross section.

In Tables 4.7 and 4.8 the ratio σ_T / σ_L at the QE peak for every data set was shown. In general, for low energy transfers the ratio is small (< 1), increasing for higher energies. A low ratio means that R_T is suppressed and thus one suspects that the 2p2h and the Δ contributions are relatively small. This refers mainly to the data from Region I and partially from Region II.

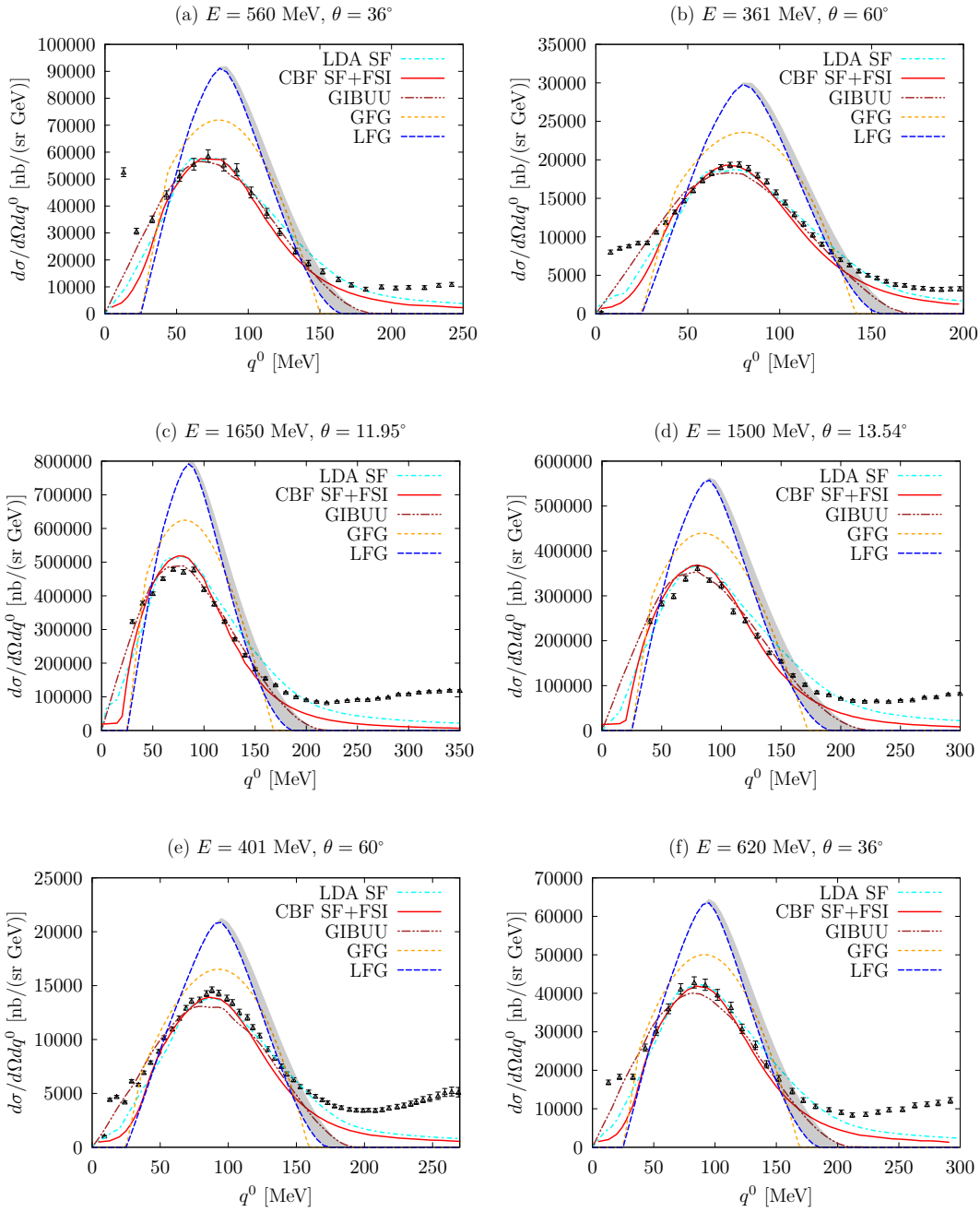

FIGURE 4.20: The same as Fig. 4.19, but $70 < (q^0)^{\mathrm{QE}} \leq 95$ MeV.

However, for a kinematics with a high σ_T / σ_L ratio such conclusion cannot be safely drawn.

We must also note that the CBF SF model includes initial nucleons' correlations which are partially responsible for the 2p2h contributions, so one should expect the sum of the QE and 2p2h mechanisms to exceed experimental data. The same occurs with the LDA SF model which also contains some 2p2h dynamics.

To gauge the effect, in Figs. 4.24a and 4.24b we show two examples (from Region III), where the 2p2h and the Δ play an important role. One may see that all the models (in particular, the CBF SF+FSI and GiBUU ones) underestimate the data, especially at the right hand side of the QE peak. After the approximate subtraction of the 2p2h and the Δ contributions from data, the agreement becomes much better. Nevertheless, even then the height of the QE peak is still

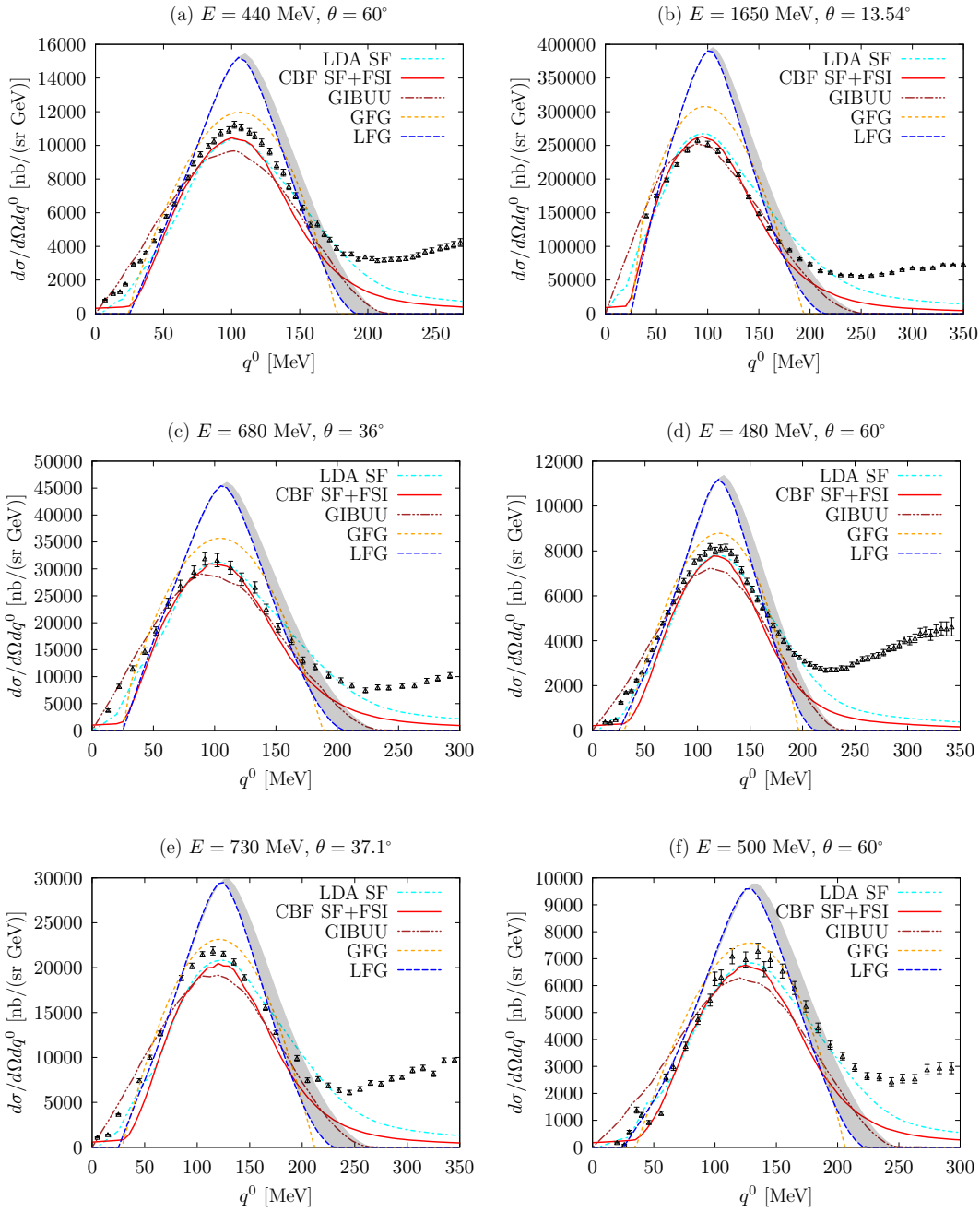

FIGURE 4.21: The same as Figs. 4.19 and 4.20 but for $(q^0)^{\mathrm{QE}} \geq 95$ MeV.

underestimated by GiBUU. The LDA SF model overestimates the corrected (green points) cross sections at the right hand side of the QE peak for both kinematics, but for different reasons. In Fig. 4.24a this is probably due to applying nonrelativistic kinematics while in Fig. 4.24b it is because the approximated LDA SF IA is used.

We want to emphasize that the above analysis is model-dependent and should not be treated quantitatively. It just aims to show the main features of the 2p2h and the Δ inclusion.

QE peak's height and position

In Fig. 4.25 we show the ratio $(d\sigma/d\Omega dq^0)^{model}/(d\sigma/d\Omega dq^0)^{data}$ at the QE peak for various models, as a function of the QE peak position.

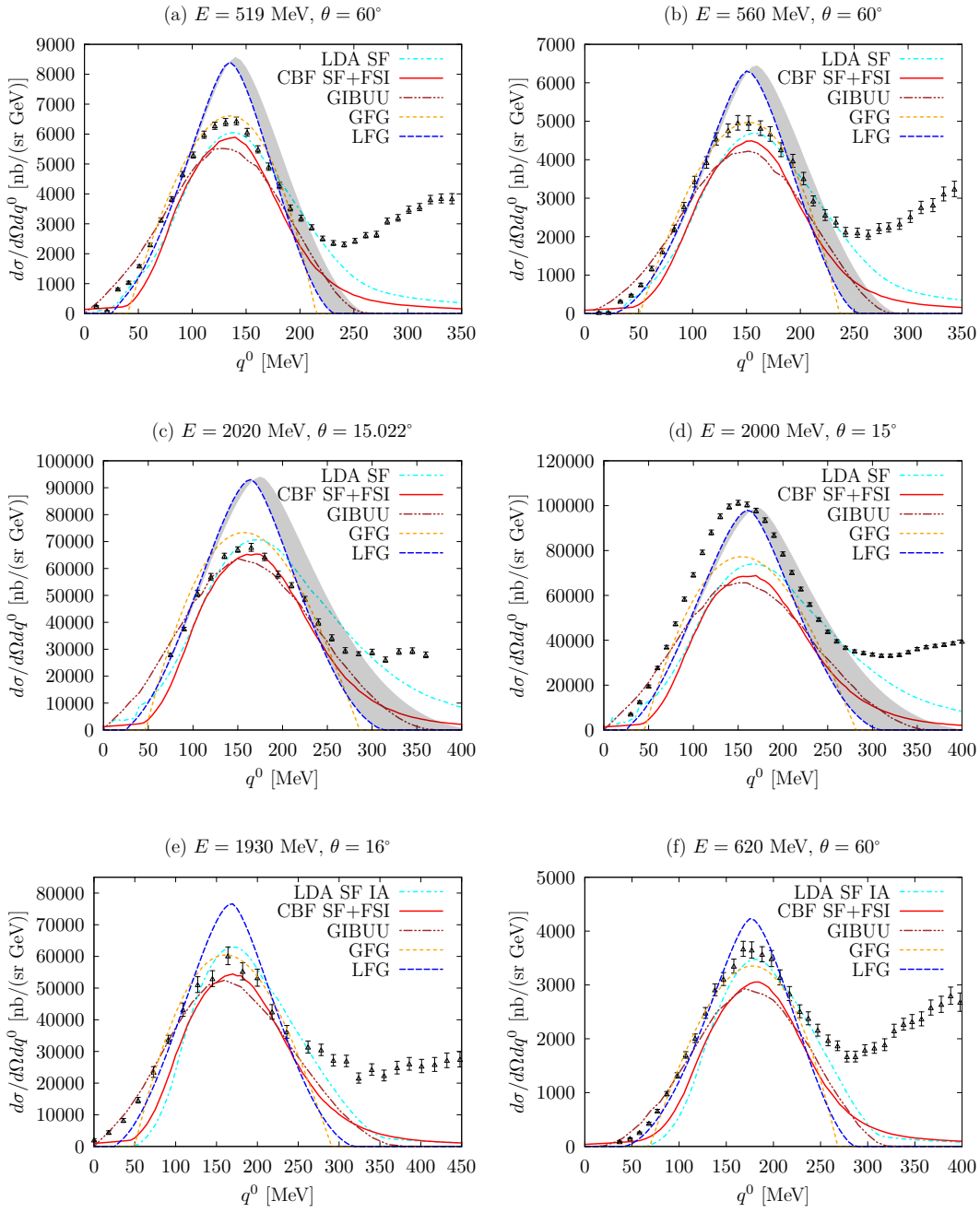

FIGURE 4.22: The same as Fig. 4.18, but for Region III with $(q^0)^{\mathrm{QE}} \leq 180$ MeV. For the last two panels, the predictions of the LDA SF model have been obtained using a free relativistic particle SF (see Eq. (3.10)). In general the 2p2h and Δ contributions are large and influence the QE region.

We see how the ratio changes drastically for both relativistic Fermi gas models, which overestimate the QE peak height very strongly, especially for low energy transfers. The GFG model describes reasonably well the data for $q^0 > 100$ MeV.

In the other more realistic models, the ratio does not depend so strongly on the values of the energy transfer and their predictions are quite similar. GiBUU slightly overestimates the data for low energies and then underestimates it for moderate and high energy transfers. The LDA SF and the CBF SF+FSI models provide similar results, although for high energy transfers – where the approximation of neglecting nuclear effects on the particle SF is used – the former

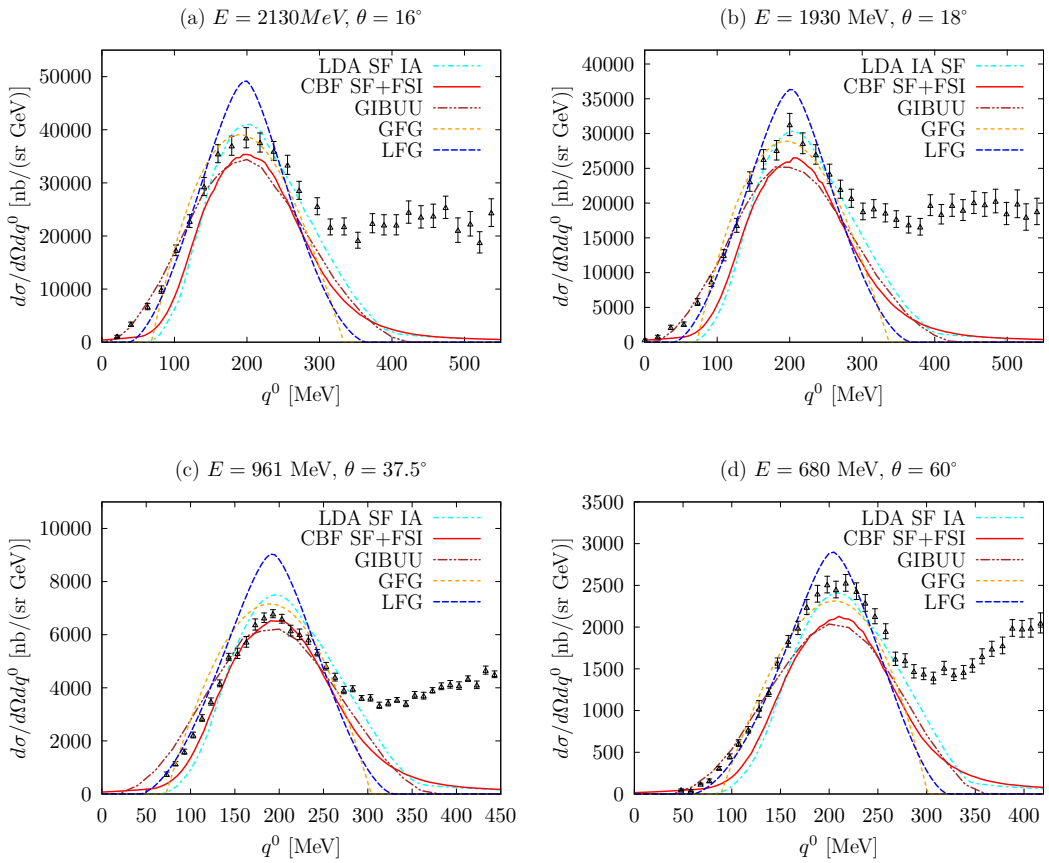

FIGURE 4.23: The same as Fig. 4.22 but for $(q^0)^{\mathrm{QE}} > 180$ MeV.

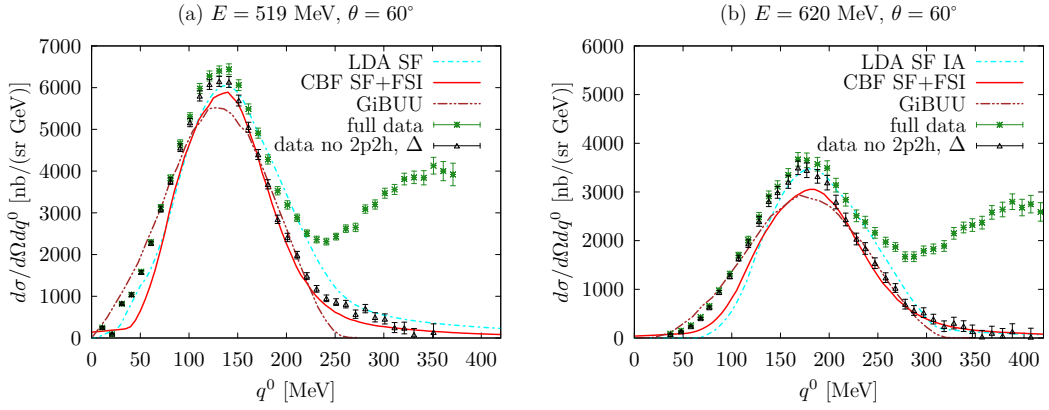

FIGURE 4.24: Comparison of GiBUU, LDA SF and CBF SF+FSI models, with data (green points). We also display some data-points for which 2p2h and the Δ contributions have been subtracted using results from [197] (black points). In the left panel: the full LDA SF model (nonrelativistic) is used, while in the right panel, the particle SF is approximated by the relativistic free one in this latter model.

one overestimates the data.

In Fig. 4.26 we compare the position of the QE peak, according to the various models, with that inferred from data, as a function of the energy transfer. In Region I the Fermi gas models shift the peak by more than 10-20 MeV towards higher energy transfers. In Region II the effect is smaller and the predictions are already comparable with those obtained from the

other models. Surprisingly, for Region III the LFG model seems to be the closest one to data. One must, however, remember that here the 2p2h contribution might be responsible for moving slightly the peak towards higher energy transfers.

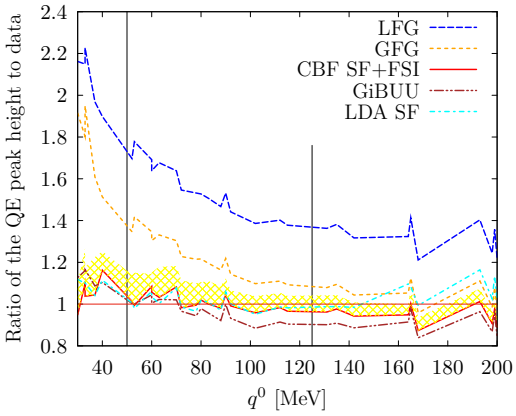

FIGURE 4.25: Ratio $(d\sigma/d\Omega dq^0)^{\text{model}}/(d\sigma/d\Omega dq^0)^{\text{data}}$ at the QE peak for various models. The band above the CBF SF+FSI curve shows the difference from the predictions obtained within the CBF SF model, where the FSI effects are not considered. Two vertical lines at 50 and 125 MeV tentatively mark Regions I, II and III.

Comparison to the LFG for the QE peak width and height

The Fermi gas model is a reasonable benchmark to estimate the importance of nuclear effects. Hence we want to show how the SF nuclear corrections influence the height and the width of the QE peak and how these modifications depend on the energy transfer. Though a comparison of the peak's width with data is not possible to perform, such analysis can be done for the predictions of theoretical models. In the left panel of Fig. 4.27 an analogous plot to Fig. 4.25, for the ratio $(d\sigma/d\Omega dq^0)^{\text{model}}/(d\sigma/d\Omega dq^0)^{\text{LFG}}$ at the QE peak is shown. The difference between the LFG and all the models is more pronounced at low energy transfers. CBF SF+FSI causes stronger quenching of the QE peak with respect to the CBF SF model (the difference is marked by a band). The GiBUU predictions lie even lower; however, the general behaviour is the same for these models: the ratio starts around 0.5 and grows up to $\approx 0.7-0.8$ for 200 MeV. The LDA SF ratios for low energy transfers (Region I) follow GiBUU but for $q^0 > 90$ MeV get closer to the CBF SF+FSI ratio. In Region III, above the 150 MeV, the LDA SF ratios are higher than those found with the other two models because nuclear effects in the particle spectral function are neglected. The introduction of such effects would produce some quenching of the peak, similar of what can be seen for the CBF model.

The behaviour of the QE peak's width is shown in the right panel of Fig. 4.27. It is defined as $q^0_R - q^0_L$ where $q^0_{R,L}$ correspond to the energy transfer at the right/left of the QE peak, where the cross section is a half of that at the peak. Again the largest nuclear effects are visible in Region I. There, one can see that CBF SF+FSI, GiBUU and LDA SF give very similar results. In Region II, however, CBF SF+FSI distributions are narrower. Looking at the data sets, one can see that the difference comes from the low-energy transfer region (below the QE peak). For higher energy transfers one should remember that relativistic effects are already visible and that LDA SF peak's width is overestimated. One can also observe that when neglecting nuclear effects in the particle spectral function, the LDA SF model gives narrower distributions (for energy transfers $q^0 > 150$ MeV).

The general energy dependence in all three models is similar (the ratio diminishes for growing energies comparing to Region I). The spreading of the peak caused by the FSI is also well visible.

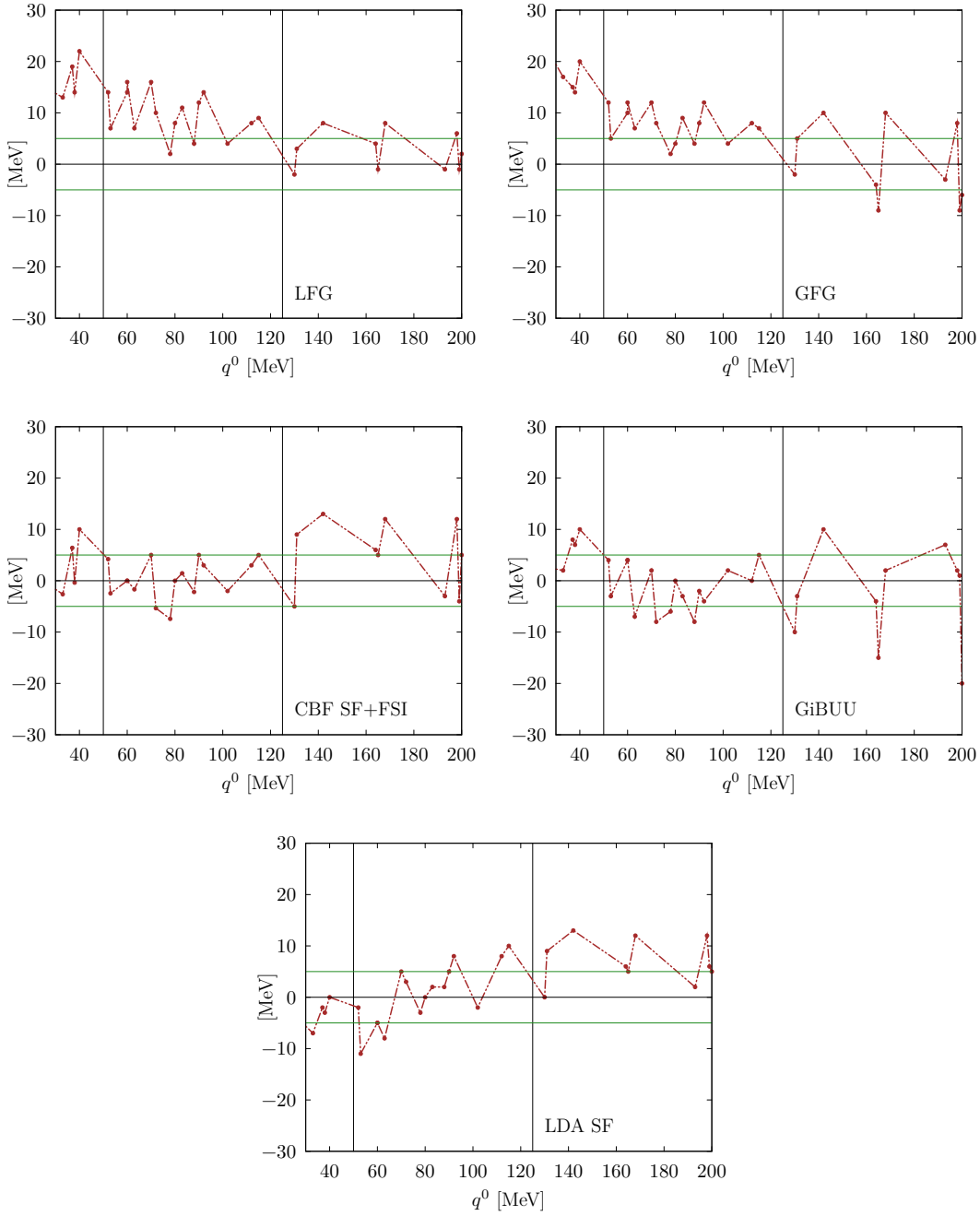

FIGURE 4.26: Position of the QE peak with respect to the data (difference between the position of the maximum of the experimental differential cross section and that of the theoretical prediction for various models). Because of the discrete nature of experimental points, an error band of 5 MeV is also shown with a dotted line. The two vertical lines at 50 and 125 MeV tentatively mark Regions I, II and III. In the bottom panel (LDA SF), the last six points ($q^0 > 150$ MeV) have been obtained using a free relativistic Pauli-blocked particle SF.

Conclusions

We have analyzed how various SF models of electron-nucleus QE scattering behave in the kinematical region important to the T2K experiment.

The conclusions drawn from inclusive electron-nucleus data analysis cannot be straightforwardly applied to the neutrino case. This is not only because of the different interaction

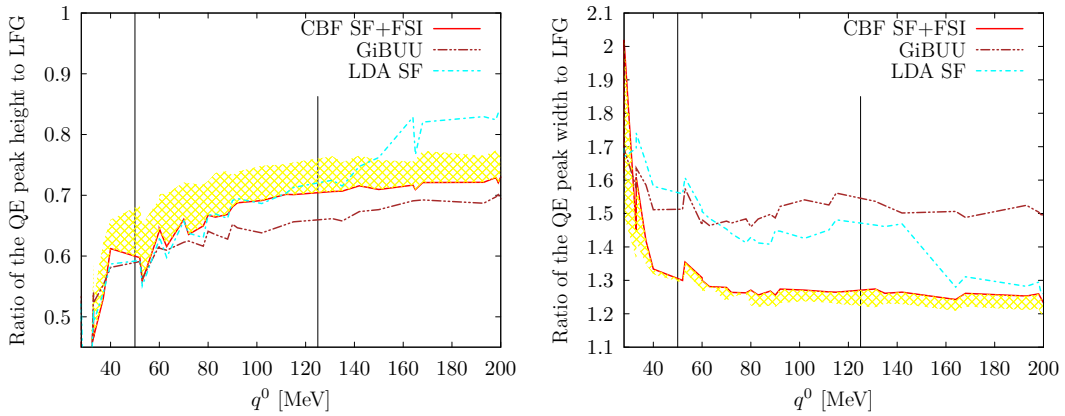

FIGURE 4.27: Left: Ratios $(d\sigma/d\Omega dq^0)^{\text{model}}/(d\sigma/d\Omega dq^0)^{\text{LFG}}$ at the QE peak for CBF SF+FSI, GiBUU and LDA SF models. Right: Ratios $((q_R^0)^{\text{model}} - (q_L^0)^{\text{model}})/((q_R^0)^{\text{LFG}} - (q_L^0)^{\text{LFG}})$ with q_R^0, q_L^0 the energy transfer values for which the strength of the differential cross section gets reduced to one half of the value at the maximum (for $q^0 = [(q^0)^{\text{QE}}]$). The bands above/below the CBF SF+FSI curve show the prediction obtained with the CBF SF model (neglecting the FSI effects). As in Fig. 4.26, for $q^0 > 150$ MeV the LDA SF predictions were calculated using a free relativistic Pauli-blocked particle SF. The two vertical lines at 50 and 125 MeV tentatively mark Regions I, II and III.

vertex (the neutrino-nucleon interaction has an additional axial part) but mainly because neutrino fluxes are not monochromatic. Integration over the incoming neutrino beam blurs the picture. As we have seen, each electron-nucleus scattering model works differently for various kinematical regions (depending on the scattering angle and the energy) and some effects may be enhanced or canceled out in integrated distributions (*e.g.* an overestimation in one region and an underestimation in another may accidentally sum up to a good result).

The LFG model, in general, overestimates the height of the QE peak. The effect grows as the energy transfer decreases, starting from a $20-40\%$ in Region III, through $40-80\%$ in Region II, up to 100% in Region I. The GFG model, comparing with the LFG one, describes the data much better. It does not overestimate the QE peak so strongly – yet, the effect is also fairly visible. In both models, the position of the peak is sometimes shifted (even by 25 MeV) but this is important only for low energy transfers and depends strongly on the scattering angle. We have seen that a binding energy suitable for all the setups cannot be chosen. The peak's shape is also far from the experimental one, failing to spread to higher energies. The inclusion of the nuclear corrections encoded in realistic SFs is needed to bring the predictions closer to reality.

Taking into account the hole CBF SF causes quenching of the QE peak, but still overestimating it (up to 10% effect which is more pronounced for low energy transfers; for Region II it is only a few percent effect). It displaces the peak's position (up to 25 MeV). However, its shape is much closer to the experimental data, which can be especially observed in Region II where the spectral function recovers a high energy tail present in the data. The shortcoming of the CBF SF model are greatly healed by introducing FSI effects. The peak is shifted and slightly suppressed so that it matches the experimental points almost perfectly in the QE peak region. However, for Regions II and III at lower energy transfers, (at the left of the QE peak) the cross sections are underestimated.

LDA SFs describe in general the data well, in a very similar way to the CBF SF+FSI model. The main drawback is the nonrelativistic treatment of the nucleons, which has forced us to neglect nuclear effects in the particle spectral function for the highest energy transfers studied here (Region III). This approximation leads to a slight overestimation of the QE peak.

The GiBUU predictions also describe the data with good precision. The GiBUU model

slightly overestimates the QE peak height in Region I and underestimates it in Regions II and III; however, one cannot say exactly how much because of the unknown 2p2h contributions. Still, we expect effects below 10%. The GiBUU predictions for the low-energy part of the QE spectrum differ a little with respect to those obtained with the CBF and LDA models. In general, the GiBUU broader widths fit better with the data, yet, overestimating some measurements (for Region II).

Among all the analyzed models, it is difficult to choose the one which would reproduce electron data with the greatest accuracy in all three regions. What is absolutely clear is that Fermi Gas models are not able to properly describe the data. This study clearly shows the need of incorporating more sophisticated nuclear corrections. It is also clear that a good model of the 2p2h and the Δ contributions is also necessary to accurately model the QE peak region.

Chapter 5

Scaling in the Spectral Function approach

The analysis of scaling properties of a composite system interacting with a weak probe was proposed in the field of particle physics already in the 1960s, as a tool to understand the underlying dynamics of the many-body system. The idea standing behind the concept of scaling is the fact that at sufficiently high energies the probe scatters on the single constituents of the interacting system. With the increasingly higher resolution this property does not change. Therefore, the inclusive cross section which in general depends on two variables (e.g. energy and momentum transfer), becomes a function of just one, while it stays independent of the resolution scale. One of the examples of this phenomena is the famous $x-$scaling in the deep inelastic region, proposed by Bjorken in [198]. His theoretical idea, together with experimental data from SLAC allowed to get insight into the quark structure of nucleons through scattering of high energetic leptons.

Afterwards, this concept was introduced by West for a lower energy regime to probe the structure of nuclei and was called in analogy as y-scaling [199]. In this case the point-like constituents are nucleons, which knocked out at sufficiently high momentum transfer hardly interact with the rest of the nuclear system. In the limit where the final state interactions can be neglected, the electron scattering cross section is expressed in terms of a factor which encodes physics of electron-nucleon scattering (and kinematical setup of the reaction), multiplied by a function which exhibits scaling properties (*i.e.* depends only on $y(q^0, |\vec{q}|)$ but not separately on $\vec{q}$ and q^0). The first analysis of y-scaling properties was done using nonrelativistic kinematics of nucleons and later generalized to relativistic energies in Ref. [189]. This property was called the scaling of the first kind.

The scaling analysis can be applied not only to the cross section, but also separately to the electromagnetic transverse and longitudinal nuclear responses. For energies above the QE peak there are other physical mechanisms contributing to the response of the system, which cause breaking of the scaling property. They are visible in the transverse channel, while the longitudinal one, dominated by the QE mechanism, exhibits scaling properties even in higher energy transfer region.

In Ref. [200], authors moved a step further and proposed a modified scaling variable ψ' which would additionally be independent of nuclear species, calling it second kind scaling. Both properties - scaling of the first and second kind - was then named superscaling [189].

The analysis of scaling properties of nuclear response functions has proven to be a useful tool to unveil information on the underlying nuclear structure and dynamics [199, 201, 202]. Indeed, singling-out individual-nucleon interactions allows to disentangle the many-body aspects of the calculation [203, 204]. These properties are relevant for interpreting electron-scattering data and to predict quantities of interest for neutrino-oscillation experiments. It has been proposed that an empirical scaling function extracted from electron scattering data can be used to predict neutrino-nucleus cross sections or to validate neutrino-nucleus interaction models [205,

206, 207, 148]. In particular, the use of RMF in such calculations has found support in its capability of properly reproducing the asymmetric shape and the transverse enhancement of the empirical scaling function [205].

Recently, an analysis of the scaling properties of the electromagnetic response functions of ^{4}He and ^{12}C nuclei computed by the Green's Function Monte Carlo (GFMC) approach [208], retaining only one-body current contributions, was carried out in Ref. [25]. The results of this work are consistent with scaling of zeroth, first and second kind and show that the characteristic asymmetric shape of the experimental scaling function emerges in the calculations in spite of the nonrelativistic nature of the model. A novel interpretation of the longitudinal and transverse scaling functions in terms of a universal scaling function, defined in terms of the nucleon-density response function was discussed. However, the reason why the nucleon-density scaling function depends on the energy and momentum transfers only through the scaling variable is yet to be fully understood.

In this chapter based on Ref. [188], we will perform a comparison and analysis of the scaling properties of two nucleon-density response functions obtained within different spectral function models.

The chapter is organized as follows. In Sec. 5.1 we present the definitions of longitudinal and transverse responses. Next, in Sec. 5.2 the scaling variables are introduced and we perform an analysis of scaling properties in the Fermi gas model, following Ref. [189]. In Sec. 5.4 – as suggested in Ref. [25] – we introduce the nucleon-density response expressed in terms of spectral functions. The origin of scaling in the interacting many-body systems is much more complicated than in the case of the Fermi gas model. In Sec. 5.5 we perform a short analysis of how various approximations affect the scaling properties of the models for nuclear effects. Finally, in Sec. 5.6 we present the results of the comparison of the two realistic approaches outlined in Sec. 3.2 and 3.3.1, paying special attention to the role played by the final state interactions.

5.1 Responses for electron scattering

The cross section for electron-nucleus interaction can be split into longitudinal and transverse components

$$\frac{d\sigma^2}{dE_{k'}d\Omega_{k'}} = \left(\frac{d\sigma}{d\Omega_{k'}}\right)_{\text{Mott}} \left[A_L(q^0,|\vec{q}|,\theta)R_L(q^0,|\vec{q}|) + A_T(q^0,|\vec{q}|,\theta)R_T(q^0,|\vec{q}|)\right] \tag{5.1}$$

where the Mott cross section is given by

$$\left(\frac{d\sigma}{d\Omega_{k'}}\right)_{\text{Mott}} = \left(\frac{\alpha\cos(\theta/2)}{2E_{k'}\sin^2(\theta/2)}\right)^2 \tag{5.2}$$

It describes scattering on a point-like spinless target in laboratory reference frame. The kinematic factors A_L and A_T depend on the scattering angle θ of outgoing electron, while the response functions encompass the dynamics of the hadronic system:

$$A_L = \left(\frac{q^2}{|\vec{q}|^2}\right)^2, \qquad A_T = -\frac{1}{2}\frac{q^2}{|\vec{q}|^2} + \tan^2\frac{\theta}{2} \tag{5.3}$$

The electromagnetic longitudinal and transverse response functions are given by

$$R_\alpha(q^0,\vec{q}) = \sum_f \langle f|J_\alpha(\vec{q},q^0)|i\rangle\langle i|J^\dagger_\alpha(\vec{q},q^0)|f\rangle\delta(q^0 - E_f + E_i)\,, \tag{5.4}$$

where $|i\rangle$ and $|f\rangle$ represent the nuclear initial ground-state and final bound- or scattering-state of energies E_i and E_f, respectively, and $J_\alpha(\vec{q},q^0)$ ($\alpha = L,T$) denotes the longitudinal and transverse components of the electromagnetic current.

We can relate the responses to the hadron tensor defined in Eq. (2.64), for j^μ_{em} instead of j^μ_{cc}, assuming that $\vec{q}||\hat{z}$:

$$R_L = W^{00}, \qquad R_T = W^{xx} + W^{yy} \tag{5.5}$$

5.2 Scaling in the Fermi gas model

The scaling properties of the nuclear responses were analyzed in the framework of the relativistic global Fermi gas (GFG) model for the first time in Ref. [189].

The transverse and longitudinal responses of Eq. (5.5) are obtained from the hadronic tensor, which for the case of CC and LFG was developed in Eq. (2.80). Here, we follow the normalization of Ref. [189] to keep contact with previous calculations:

$$W^{\mu\nu}(q) = \frac{3\mathscr{N}}{4\pi p_F^3}\int d^3p \frac{M}{E_p}\frac{M}{E_{p+q}}\delta(q^0+E_p-E_{p+q}) \\ \times \theta(p_F-|\vec{p}|)\theta(|\vec{p}+\vec{q}|-p_F)A^{\mu\nu}_{\rm EM}(p,q) \tag{5.6}$$

where $\mathscr{N}$ is the number of protons or neutrons (we consider only symmetric nuclei). The single-nucleon hadron tensor, $A^{\mu\nu}_{\rm EM}$, describes the response

$$A^{\mu\nu}_{\rm EM}(p,q) = -W_1(q^2)\left(g^{\mu\nu}-\frac{q^\mu q^\nu}{q^2}\right)+W_2(q^2)\frac{1}{M^2}\left(p^\mu-\frac{p\cdot q}{q^2}q^\mu\right)\left(p^\nu-\frac{p\cdot q}{q^2}q^\nu\right) \tag{5.7}$$

The structure functions can be written in terms of Sachs form factors:

$$W_1(q^2) = \tau G_M^2(q^2) \\ W_2(q^2) = \frac{1}{1+\tau}\left(G_E^2(q^2)+\tau G_M^2(q^2)\right) \tag{5.8}$$

with $\tau = -\frac{q^2}{4M^2}$ and

$$G_E(q^2) = G_E^p(q^2)\frac{1}{2}(1+\tau_{z,i}) + G_E^n(q^2)\frac{1}{2}(1-\tau_{z,i}) \\ G_M(q^2) = G_M^p(q^2)\frac{1}{2}(1+\tau_{z,i}) + G_M^n(q^2)\frac{1}{2}(1-\tau_{z,i}) \\ \tau_{z,p/n} = \pm 1 \tag{5.9}$$

In order to make contact with previous studies, we introduce the following set of dimensionless variables [189]

$$\lambda = q^0/2M\,, \qquad \kappa = |\vec{q}|/2M\,, \qquad \tau = \kappa^2-\lambda^2\,, \\ \eta_F = p_F/M\,, \qquad \varepsilon_F = \frac{\sqrt{p_F^2+M^2}}{M}, \qquad \xi_F = \varepsilon_F - 1\,. \tag{5.10}$$

We also define:

$$\lambda_0 = \frac{1}{2}\left(\sqrt{1+4\kappa^2}-1\right) \tag{5.11}$$

which corresponds to the value of λ in the QE peak.

Next we introduce

$$\Delta \equiv \frac{\tau}{\kappa^2}\left(\frac{1}{3}\left(\varepsilon_F^2+\varepsilon_F\Gamma+\Gamma^2\right)+\lambda\left(\varepsilon_F+\Gamma\right)+\lambda^2\right)-(1+\tau) \tag{5.12}$$

with

$$\Gamma \equiv \max\left\{\varepsilon_F-2\lambda, \Gamma_2 \equiv \kappa\sqrt{1+\frac{1}{\tau}}-\lambda\right\} \tag{5.13}$$

With the above definitions the responses can be cast into form:

$$R_{L,T} = \frac{3\mathcal{N}}{4M\kappa\eta_F^3}(\varepsilon_F-\Gamma)\theta(\varepsilon_F-\Gamma)\begin{cases}\times G_L(q^2) & \text{for } R_L\\ \times G_T(q^2) & \text{for } R_T\end{cases} \tag{5.14}$$

Different factors in R_L and R_T coming from integration over $A^{\mu\nu}_{\rm EM}$ in Eq. (5.6) are given by:

$$\begin{aligned} G_L &= \frac{\kappa^2}{\tau}\left(\left((1+\tau)W_2(q^2)-W_1(q^2)\right)+\Delta W_2(q^2)\right)\\ G_T &= 2W_1(q^2)+\Delta W_2(q^2)\end{aligned} \tag{5.15}$$

The common kernel of R_T and R_L is written in such a way that all the information about the q dependence is hidden in $(\varepsilon_F-\Gamma)/\kappa$. Let us notice that in the limit in which $|\vec{q}| \geq 2p_F$ the outgoing nucleon is not Pauli-blocked. In this regime of high momentum transfer we have that $\Gamma = \Gamma_2$.

Both responses can be mapped into a parabola if we properly define a dimensionless scaling variable

$$\psi \equiv \text{sign}(\lambda-\lambda_0)\frac{1}{\sqrt{\xi_F}}\sqrt{\Gamma_2-1} = \frac{1}{\sqrt{\xi_F}}\frac{\lambda-\tau}{\sqrt{(1+\lambda)\tau+\kappa\sqrt{\tau(1+\tau)}}}. \tag{5.16}$$

The longitudinal and transverse scaling functions are obtained by dividing the response functions $R_{L,T}$ by appropriate prefactors, encompassing single-nucleon dynamics within the GFG model in Eq. (5.15).

$$f_{L,T}(\psi) = p_F \times \frac{R_{L,T}}{G_{L,T}}. \tag{5.17}$$

It has to be noted that the GFG longitudinal and transverse scaling functions coincide (the model exhibits zeroth kind scaling). The analytical expression of the common function, symmetric and centered in $\psi = 0$, reads

$$f_L^{\rm GFG}(\psi) = f_T^{\rm GFG}(\psi) = \frac{3\xi_F}{2\eta_F^2}(1-\psi^2)\theta(1-\psi^2)\,. \tag{5.18}$$

5.3 Nucleon-density scaling function

In the following we discuss how the inclusion of nuclear interactions affects the shape of the scaling functions, possibly leading to scaling violations. In Ref. [25] it has been suggested that, for large momentum transfers, the longitudinal and transverse scaling functions can be interpreted in terms of the proton and neutron-density responses

$$R_{p(n)}(\vec{q},q^0) = \sum_f \langle i|\rho^\dagger_{p(n)}(\vec{q})|f\rangle\langle f|\rho_{p(n)}(\vec{q})|i\rangle\,\delta(q^0-E_f+E_0)\,, \tag{5.19}$$

where the proton (neutron)-density operator is given by

$$\rho_{p(n)}(\vec{q}) \equiv \sum_j e^{i\vec{q}\cdot\vec{r}_j} \frac{(1 \pm \tau_{j,z})}{2}. \tag{5.20}$$

In isospin-symmetric nuclear matter, the proton- and neutron-density responses coincide. It is convenient to refer to them as the nucleon-density response, proportional to the imaginary-part of the polarization propagator

$$R_\rho(\vec{q},q^0) = \frac{1}{\pi} \text{Im}\, \Pi(\vec{q},q^0), \tag{5.21}$$

with

$$\Pi(\vec{q},q^0) = \langle i|\rho_q^\dagger \frac{1}{\mathscr{H} - E_0 - q^0 - i\varepsilon} \rho_q |i\rangle \,, \tag{5.22}$$

where $\mathscr{H}$ is the Hamiltonian, $\rho_{\vec{q}} = \sum_{\vec{p}} a^\dagger_{p+q} a_p$ is the proton- or neutron-density fluctuation operator and $a^\dagger_p$ and a_p are either the proton or the neutron creation and annihilation operators, respectively. In the limit of large momentum transfer and for isospin symmetric nuclei, where the effect of collective excitation modes is expected to be negligible, the polarization propagator in nuclear matter reduces to

$$\Pi(\vec{q},q^0) = 2iV \int \frac{d^3p}{(2\pi)^3} \frac{dE}{2\pi} \, G(\vec{p},E) G(\vec{p}+\vec{q},q^0+E) \tag{5.23}$$

where the discrete sum $\sum_p$ has been replaced by $V \int d^3p/(2\pi)^3$, with V being the volume of the system, and the factor 2 stems from the spin sums. The one-body Green's function $G(\vec{p},E)$ in nuclear matter was defined in Eq. (2.52). Let us notice that $\Pi(\vec{q},q^0)$ is proportional to Lindhard function defined in Eq. (2.81). The nucleon-density response for positive excitation energies ($q^0 > 0$) is then given by

$$R_\rho(\vec{q},q^0) = -\frac{2V}{\pi^2} \int \frac{d^3p}{(2\pi)^3} dE \; \text{Im}G_h(\vec{p},E) \text{Im}G_p(\vec{p}+\vec{q},q^0+E). \tag{5.24}$$

using $\bar{S}_h(\vec{p},E) = 2V S_h(\vec{p},E)/\mathscr{N}$, as introduced in Eq. (3.2) and employing the definition given in Eq.(2.53) for the hole and particle SFs, the nucleon-density response reads

$$R_\rho(\vec{q},q^0) = \mathscr{N} \int \frac{d^3p}{(2\pi)^3} dE \bar{S}_h(\vec{p},E) S_p(\vec{p}+\vec{q},E+q^0) \tag{5.25}$$

When a relativistic fermion propagator is employed, its imaginary part is a matrix in the Dirac space and contains the factor $(\not{p}+M)/2E_p$ (with dimensionless spinors normalized as $u_r^\dagger u_s = \delta_{r,s}$). This can be rewritten as $[(\not{p}+M)/2M] \times [M/E_p]$. The first term enters in the matrix elements of the external current, while the second one is included in the definition of the nucleon-density response. For the spinor normalization used in the previous chapters, $\sum \bar{u}u = (\not{p}+M)$, we have an additional factor $1/2M$ which enters into the definition of hadron tensor, see Eq. (2.80). Therefore in the relativistic case the nucleon-density response is:

$$R_\rho(\vec{q},q^0) = \mathscr{N} \int \frac{d^3p}{(2\pi)^3} \, dE \, \frac{M}{E_p} \frac{M}{E_{p+q}} \bar{S}_h(|\vec{p}|,E) S_p(|\vec{p}+\vec{q}|,E+q^0) \,. \tag{5.26}$$

The factors M/E_p, which reduce to one in the nonrelativistic limit, become relevant when the struck particle is relativistic. The GFG SFs defined in Eq. (3.1), with the relativistic energy of

Eq. (3.5), yield the scaling function of Eq. (5.18).

5.4 Responses in LDA and CBF models

For the sake of clarity, we explicitly give here the definitions of the nucleon-density responses (and scaling functions) obtained within the models of Secs. 3.2 and 3.3.1, used for comparisons in this chapter.

- For the model of Ref. [2], we consider both hole and particle spectral functions, $S_{p,h}^{\text{LDA rel}}(\vec{p},E)$ defined in Eq. (3.20). After performing the integration over the nuclear volume:

$$\mathrm{R}_{\rho}^{\text{LDA SF}}(\vec{q},q^0) = \frac{\theta(q_0)}{4\pi^3}\int d^3r \int d^3p \int_{\mu-q_0}^{\mu} dE \frac{M}{E_p}\frac{M}{E_{p+q}} S_h^{\text{LDA rel}}(\vec{p},E) \times S_p^{\text{LDA rel}}(\vec{p}+\vec{q},E+q_0)\,. \tag{5.27}$$

- When in the model of Ref. [2], only nuclear effects in the hole spectral function (defined in Eq. (3.13)) are included, while the particle is taken as a free state, we have:

$$\mathrm{R}_{\rho}^{\text{SF LDA IA}}(\vec{q},q^0) = \frac{\theta(q_0)}{4\pi^3}\int d^3r \int d^3p \int_{\mu-q_0}^{\mu} dE \frac{M}{E_p}\frac{M}{E_{p+q}} S_h^{\text{LDA}}(\vec{p},E) \times \delta(q^0+E+M-E_{p+q})\theta(|\vec{p}+\vec{q}|-p_F(\rho))\,. \tag{5.28}$$

- For the model of Sec. 3.3.1, in which the FSI effects are not taken into account, we have:

$$R_{\rho}^{\text{CBF SF}}(\vec{q},q^0) = \mathscr{N}\int \frac{d^3p}{(2\pi)^3}\int dE \bar{S}_h^{\text{CBF}}(\vec{p},E)\frac{M}{E_p}\frac{M}{E_{p+q}} \times \delta(q^0+E+M-E_{p+q})\,\theta(|\vec{p}+\vec{q}|-p_F)\,. \tag{5.29}$$

- In the case when the FSI are also included in terms of the convolution scheme, we have:

$$R_{\rho}^{\text{CBF SF+FSI}}(\vec{q},q^0) = \mathscr{N}\int \frac{d^3p}{(2\pi)^3}\int dE \int d\omega' f_{p+q}(q^0-\omega') \times \frac{M}{E_p}\frac{M}{E_{p+q}}\bar{S}_h^{\text{CBF}}(\vec{p},E)\delta(\omega'+E+M-\tilde{E}_{p+q})\theta(|\vec{p}+\vec{q}|-p_F)\,. \tag{5.30}$$

  We recall that $\tilde{E}_{p+q}$ corresponds to energy of outgoing nucleon shifted with the optical potential, as discussed in Eq. (3.42).

The corresponding scaling functions are then defined as:

$$f^X(\psi) = p_F \times 2\kappa R_{\rho}^X/\mathscr{N} \tag{5.31}$$

with X denoting SF LDA, SF LDA IA, CBF SF or CBF SF+FSI.

5.5 Origin of scaling

The origin of the scaling exhibited by the nuclear responses has a simple and exact formulation within the GFG model, which, however, largely fails to reproduce experimental data. Understanding the scaling features of nuclear responses becomes challenging when the nucleus is treated as a fully-interacting many-body system.

In order to avoid the complications arising when GFG model prefactors are used to remove single-nucleon dynamics, we will focus on the nucleon-density scaling function, defined in Eq.(5.31). To address the dynamical origin of first-kind scaling, we will consider a simplified description of the nucleus, yet retaining the key aspects of the many-body problem. For simplicity, our analysis is limited to nonrelativistic kinematics. Hence, in the following we will use the nonrelativistic scaling variable [25]

$$\psi^{nr} = \frac{1}{p_F}\left(\frac{Mq^0}{|\vec{q}|} - \frac{|\vec{q}|}{2}\right). \tag{5.32}$$

A generalization to the relativistic case does not involve conceptual difficulties.

PWIA model

Within the CBF SF, the nonrelativistic nucleon-density scaling function is defined as

$$f^{\text{CBF SF}}(\vec{q},q^0) = 2\kappa p_F \int \frac{d^3p}{(2\pi)^3}\, dE \bar{S}_h^{\text{CBF}}(|\vec{p}|,E)\theta(|\vec{p}+\vec{q}|-p_F)\delta\left(q^0+E-(\vec{p}+\vec{q})^2/2M\right), \tag{5.33}$$

The above expression can be further simplified within the plane wave impulse approximation (PWIA), which amounts to neglect information on the target removal energy distribution. The hole SF is written in the approximate form

$$\bar{S}_h(\vec{p},E) \simeq \bar{n}(|\vec{p}|)\delta\left(E-\vec{p}^{\,2}/2M\right), \tag{5.34}$$

where the momentum distribution is defined as

$$\bar{n}(|\vec{p}|) = \int dE \bar{S}_h(|\vec{p}|,E) \quad , \quad \int \frac{d^3p}{(2\pi)^3}\bar{n}(|\vec{p}|) = 1\,. \tag{5.35}$$

We will use a state-of-the-art momentum distribution computed within variational Monte Carlo in Ref. [209].

Within the PWIA, the nucleon-density scaling function reads

$$f^{\text{PWIA}}(|\vec{q}|,q_0) = 2\kappa p_F \int \frac{d^3p}{(2\pi)^3}\, \bar{n}(\vec{p})\theta(|\vec{p}+\vec{q}|-p_F)\delta\left(q_0+\vec{p}^{\,2}/2M-(\vec{p}+\vec{q})^2/2M\right). \tag{5.36}$$

To better elucidate the emergence of first-kind scaling and the asymmetry of the scaling function, we consider three different scenarios with increasing sophistication for the description of the energy spectrum.

Let us first assume a free energy spectrum for both the hole and particle states in the energy-conserving δ function

$$\delta(q^0+\vec{p}^{\,2}/2M-(\vec{p}+\vec{q})^2/2M) = \delta\Big(q^0-\frac{|\vec{q}|^2}{2M}-\frac{|\vec{p}||\vec{q}|\cos\theta}{M}\Big), \tag{5.37}$$

where θ is the angle between $\vec{p}$ and $\vec{q}$. The integration over $\cos\theta$ can be performed using the δ-function, which gives rise to a Jacobian

$$\mathscr{J} = \frac{M}{|\vec{p}||\vec{q}|} = \frac{1}{2|\vec{p}|\kappa}. \tag{5.38}$$

The fact that $|\cos\theta| \leq 1$ provides a lower bound to the momentum of the hole

$$|\vec{p}| \geq p_F\,|\psi^{nr}|. \tag{5.39}$$

An additional constraint comes from the step function $\theta(|\vec{p}+\vec{q}| - p_F) = \theta(\vec{p}^{\,2}/2M + q^0 - p_F^2/2M)$, yielding

$$|\vec{p}|^2 \geq p_F^2 - 2Mq^0. \tag{5.40}$$

The latter constraint is always satisfied for sufficiently large values of q^0, in which case the integration range of $|\vec{p}|$ is limited by Eq. (5.39) only. For low momentum and energy transfers, the lower limit is instead the one of Eq. (5.40) leading to violations of first-kind scaling, unless a piecewise definition of $|\psi^{nr}|$ is adopted [189].

Since the factor κ that appears in Eq. (5.36) simplifies with the Jacobian, the result of the integration only depends upon the lower integration limit, $p_F|\psi^{nr}|$, and thus it is easily found that f^{PWIA} is a symmetric function of ψ^{nr}, as it only depends on the modulus of this variable.

Figure 5.1 shows the PWIA nucleon-density scaling functions of ^{12}C, using the energy-conserving δ function of Eq. (5.37), for different momentum transfers. Scaling is perfectly satisfied: the curves are peaked around $\psi^{nr} = 0$ and do not show any asymmetry, as expected from the above discussion. The only difference with the GFG case is that the scaling function extends to values of $|\psi^{nr}|$ larger than 1. This is due to the fact that $\bar{n}(p)$ does not vanish above p_F.

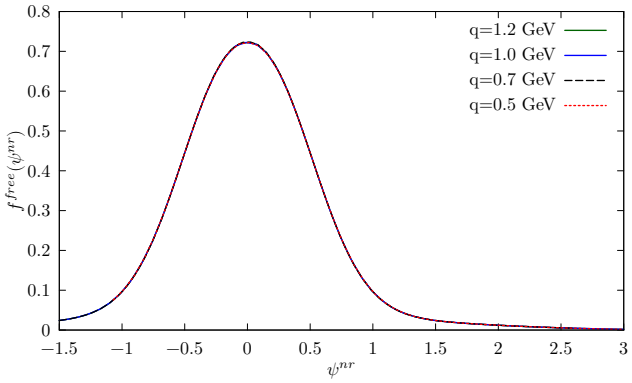

FIGURE 5.1: Non-relativistic PWIA scaling responses, using the momentum distribution of ^{12}C derived in Ref. [209] for $|\vec{q}| = 0.5,\ 0.7,\ 1$ and 1.2 GeV. The Fermi momentum has been fixed to $p_F = 225$ MeV.

As a second step, we treat the hole as a bound state using the energy spectrum of nuclear matter at saturation density of Ref. [210] (see also the recent work of Ref. [211]). In this case the energy conserving δ-function is given by

$$\delta\left(q^0 + \mathscr{U}(\vec{p}) - \frac{|\vec{q}|^2}{2M} - \frac{|\vec{p}||\vec{q}|\cos\theta}{M}\right). \tag{5.41}$$

where the single-particle potential $\mathscr{U}(\vec{p}) < 0$ has been added to $\vec{p}^{\,2}/2M$. Modifying the hole energy spectrum does not change the Jacobian of Eq. (5.38). However, the lower bound of

Eq. (5.39) now reads

$$|\vec{p}| \geq \left| p_F \ \psi^{nr} + M \frac{\mathscr{U}(\vec{p})}{|\vec{q}|} \right| . \tag{5.42}$$

The term $\mathscr{U}(\vec{p})/|\vec{q}|$ introduces further dependencies on $|\vec{q}|$ and leads to violations of first-kind scaling. These violations are apparent in the results displayed in Fig. 5.2, where the $|\vec{p}|$-dependent term in the energy-conserving δ-function leads to a shift of the different curves. The peaks move to higher excitation energies, as expected for an attractive average hole potential. For $|\vec{q}|$=1.0, 1.2 GeV, the curves peak approximately at $\psi^{nr} = 0$ and the result found in the free energy case is recovered to a very large extent. This can be easily understood, since the average $\mathscr{U}(\vec{p})^{\text{avg}}/|\vec{q}|$ correction becomes small for large values of the momentum transfer. The shape of the scaling functions, which is still symmetric around $\psi^{nr} = 0$, is almost unaffected by the single-particle potential.

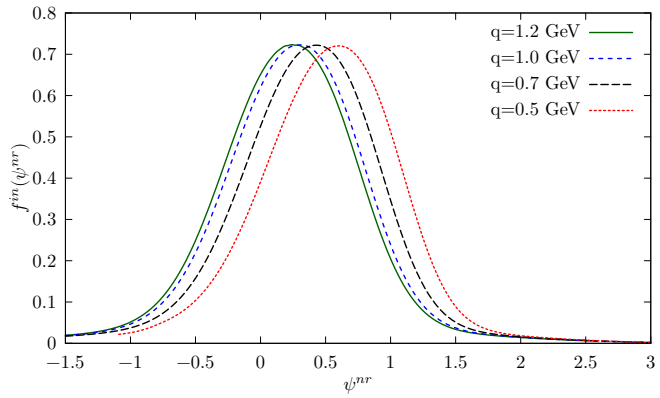

FIGURE 5.2: Non relativistic scaling responses obtained within PWIA (Eq. (5.36)) as a function of ψ^{nr} for $|\vec{q}| = 0.5,\ 0.7$, and 1 GeV. The momentum distribution of ^{12}C derived in Ref. [209] has been used, and the energy of the hole state has been extracted from the calculations of the nuclear matter energy spectrum of Ref. [210] and implemented in the energy conservation (see Eq. (5.41)). The Fermi momentum, p_F, has been fixed to 225 MeV.

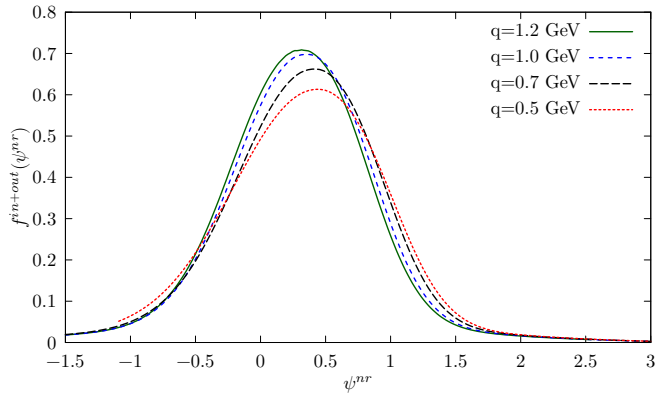

FIGURE 5.3: Same as in Fig.5.2, but nuclear potentials have been used to determine both the hole and particle state energies (see Eq. (5.43)).

Finally, we consistently include a single-particle potential in the hole and particle energy spectra. The energy conserving δ-function reads

$$\delta\left(q^0 - \frac{|\vec{q}|^2}{2M} - \frac{|\vec{p}||\vec{q}|\cos\theta}{M} + \mathscr{U}(|\vec{p}|) - \mathscr{U}(|\vec{p}+\vec{q}|)\right) . \tag{5.43}$$

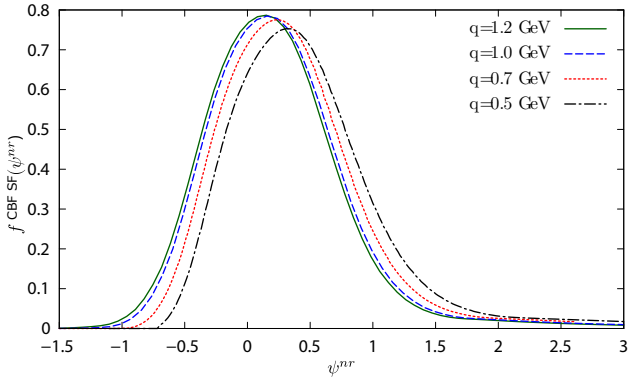

FIGURE 5.4: Scaling functions for ^{12}C obtained with the nonrelativistic kinematics, Eq. (5.33), using the hole CBF SF for $|\vec{q}| = 0.5$, 0.7, 1.0, and 1.2 GeV.

The nontrivial dependence on $\cos\theta$ hidden in $\mathscr{U}(|\vec{p}+\vec{q}|)$ prevents, in general, from analytically solving the integral. To circumvent this problem, we performed a numerical integration, treating the δ-function as the limit of a Gaussian. This allows us to properly evaluate the Jacobian, which differs from the one reported in Eq. (5.38). This introduces a first source of scaling violations, as the κ factor of Eq. (5.36) does not exactly cancel with the Jacobian. Nevertheless, the cancellation is still partially produced and becomes exact in the $|\vec{q}| \gg |\vec{p}|$ limit. Fig. 5.3 displays the scaling functions computed using Eq. (5.43) for the energy-conserving δ function for the same kinematical setups as in Figs. 5.1 and 5.2. The curves are still shifted[1] compared to the free case, although the position of the peaks is closer to $\psi^{nr} = 0$ than in Fig. 5.2. This indicates a partial cancellation of single-particle potentials in the hole and particle spectra, as discussed in Ref. [4]. At $|\vec{q}| = 0.5$ GeV including the single-particle potential in the particle energy spectrum shifts the peak to lower ψ^{nr}, at $|\vec{q}| = 0.7$ GeV the peak position does not change, while at $|\vec{q}| = 1.0$ GeV and $|\vec{q}| = 1.2$ GeV the peak is shifted to higher ψ^{nr}. This is due to the sign of the single particle potential: $\mathscr{U}(\vec{p}+\vec{q})$ is negative (positive) for small (large) values of the momentum transfer. As alluded to earlier, the new Jacobian introduces a residual dependence on $|\vec{q}|$, specifically in the magnitude of the scaling functions. First kind scaling is almost recovered for $|\vec{q}| \geq 1$ GeV, although scaling violations are already small for $|\vec{q}| = 0.7$ GeV. As in the other cases, scaling functions exhibit only a small asymmetry.

Up to now, we have neglected the imaginary part of the in-medium potentials. As discussed in Refs. [2, 4], effects on the ejected-nucleon are expected to be larger than in the hole state. The corrections induced by the imaginary part of the optical potential on the particle states can be estimated, following the approach detailed in Subsec. 3.3.1, by convoluting the PWIA scaling function as in Eq. (5.30). Since Eq. (5.43) consistently includes the single-particle potential, both in the hole and particle energy spectra, the real part of the potential does not have to be included in the argument of the folding function. Analogously to the discussion in Fig. 5.7, the corrections are very small and have little effects on the discussion about the origin of the scaling. Moreover, these FSI corrections do not induce any appreciable asymmetry in the scaling functions.

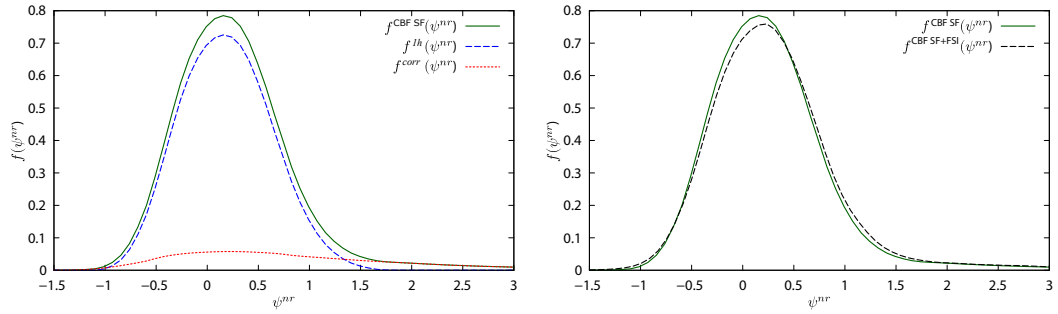

FIGURE 5.5: Left: Breakdown of the scaling response of ^{12}C at $|\vec{q}|$=1.2 GeV showed in Fig. 5.4 into the total, hole, and background contributions. Right: Dashed (black) and solid (green) lines correspond to the scaling function calculated with and without the inclusion of FSI effect at $|\vec{q}| = 1$ GeV in ^{12}C. The CBF SF curve corresponds to that displayed in Fig. 5.4, and it is used in the convolution detailed in Eq. (5.30) to incorporate the FSI effects.

Beyond PWIA

The hole SF $\bar{S}_h(|\vec{p}|,E)$ is a function of two independent variables, which are related in a nontrivial way. It is long known that the PWIA of Eq. (5.35), which disregards the dependence on the removal energy of the nucleus, is inaccurate. Realistic $S_h(|\vec{p}|,E)$ exhibits a strong correlation between momentum and removal energy, implying that large momenta always correspond to large removal energies. For instance, for nuclear matter hole SF calculated within the CBF approach, around 50% of the strength at $|\vec{p}| = 3$ fm^{-1} resides at $E > 200$ MeV [29]. Furthermore, the shell structure of the nucleus is completely disregarded in the PWIA of Eq. (5.35).

In the following, we argue that the use of a realistic hole SF produces noticeably different scaling features of the nucleon-density response from those obtained within the PWIA model. In the IA, the energy conserving δ function of Eq. (5.29) reads

$$\delta\left(q^0 + E - \frac{|\vec{p}|^2}{2M} - \frac{|\vec{q}|^2}{2M} - \frac{|\vec{p}||\vec{q}|\cos\theta}{M}\right) . \tag{5.45}$$

Imposing $|\cos\theta| \leq 1$ gives a boundary condition on both E and $|\vec{p}|$, which are related through $\bar{S}_h(\vec{p},E)$. The Jacobian still yields a factor κ that cancels the one of Eq. (5.36). The binding energies associated with the continuum part of the hole SF are generally larger than $|\vec{p}|^2/2M + \mathscr{U}(|\vec{p}|)$. This feature is particularly relevant for $\psi^{nr} > 1$, as larger values of q^0 are needed to compensate for the large removal energy. Hence, for sufficiently large momentum transfers we expect violations of first-kind scaling, and the appearance of a more significant tail at the right of the QE peak that will enhance the asymmetry of the scaling function compared to the PWIA case.

Scaling violations are apparent in Fig. 5.4, as the positions of the peaks of the scaling functions depend upon the momentum transfer. These shifts are likely to be ascribed to the energy of the bound hole state described by the hole SF, analogously to Fig. 5.2. However, the scaling functions obtained using the hole SF show a more pronounced asymmetric shape than those displayed in Fig. 5.2.

In the left panel of Fig.5.5 we show the breakdown of the scaling response at $|\vec{q}| = 1$ GeV into the one-hole and correlation contributions, coming from the pole and the continuum part

[1]The resulting breaking scaling pattern can be understood taking into account that

$$\mathscr{U}(|\vec{p}|) - \mathscr{U}(|\vec{p}+\vec{q}|) < 0 \tag{5.44}$$

and that in the large momentum transfer, this difference becomes independent of $\cos\theta$, and has little influence in the lower limit of the $|\vec{p}|-$integration.

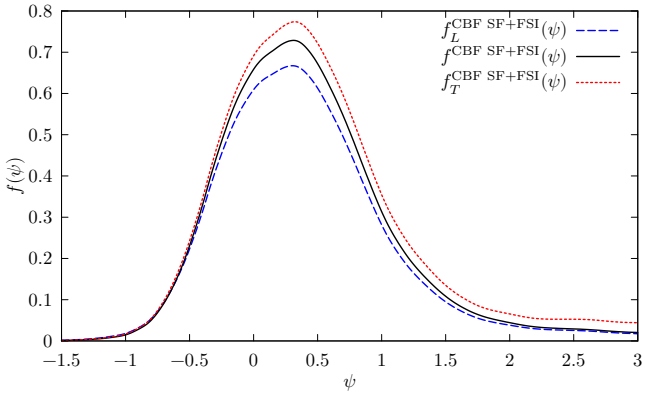

FIGURE 5.6: Transverse (red dotted), longitudinal (blue dashed) and nucleon-density (black-solid) scaling functions of ^{12}C at $|\vec{q}| = 1.0$ GeV obtained from the CBF SF approach including FSI corrections.

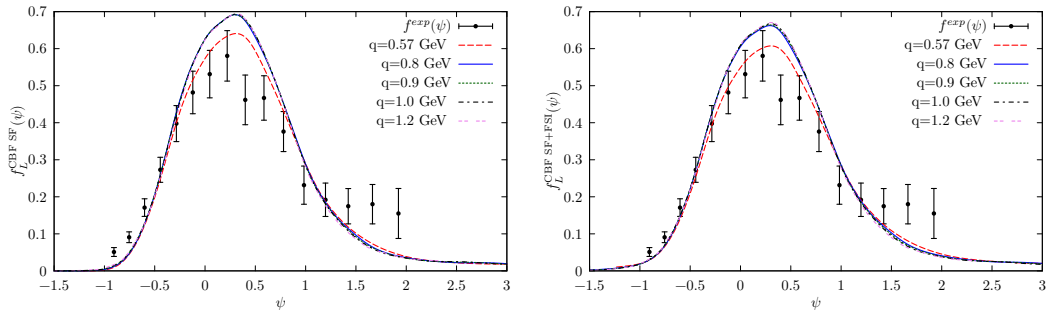

FIGURE 5.7: Longitudinal scaling functions in ^{12}C computed using the hole SF (Eq. (3.32)) of Ref. [27] for $|\vec{q}| = 0.57$, 0.8, 0.9, 1.0, and 1.2 GeV. Results neglecting the nuclear effects of the particle SFs are shown in the left panel, while those including FSI effects are displayed in the right one. The standard definition of the longitudinal prefactor given in Eq. (30) of Ref. [25] has been used to get both the theoretical curves and the experimental points obtained from the $|\vec{q}| = 0.57$ GeV data of Ref. [192]

.

of the hole Green's function. The asymmetric shape is mostly determined by the background contribution, with a large tail in the region of large ψ. Interestingly, the scaling response obtained by retaining only the one-hole contribution in the SF is not completely symmetric. This has to be ascribed to the presence of two independent integration variables, *i.e.* $|\vec{p}|$ and E. This more sophisticated description of nuclear dynamics likely contributes to the asymmetry observed in the experimental data. In the right panel of the figure, we show how FSI affect the scaling function for $|\vec{q}| =$ 1 GeV, comparing the CBF SF (dashed black) and the CBF SF+FSI (solid green) results. Although FSI are significant for moderate momentum transfer, they are practically negligible in the kinematical region displayed in the figure. Overall FSI provide a shift and a redistribution of the strength of the scaling function, bringing about an enhancement of the asymmetry.

5.6 Results

In this section we present the ^{12}C electromagnetic scaling functions obtained using the SF approaches outlined in Secs. 3.2 and 3.3.1. When defining the scaling variable ψ, we used $p_F = 225$ MeV, accordingly to the analysis of electron-scattering data of Ref. [147]. As discussed above, the model described in Sec. 3.2 makes an extensive use of the LDA. In this case, the response of the nucleus is obtained by averaging the nuclear-matter responses obtained for a given value of ρ over the density profile $\rho(r)$. As for the CBF spectral function, the LDA is

employed to estimate the correlated part of the hole spectral function deduced from the CBF calculations carried out in isospin-symmetric nuclear matter (see Eq. (3.34)). In the following we employ for ^{12}C a harmonic-oscillator density profile introduced in Subsec. 2.3.2. To obtain the point-proton density from the charge density we unfold the charge form factor of the proton. This procedure relies on the tenet that the contribution of longitudinal two-body currents to the charge form factor is small, as proven, for instance, in Ref. [212].

In the following we denote with "CBF SF+FSI" the results of the CBF hole SF supplemented by the convolution scheme and with "CBF SF" those in which FSI are neglected, as in Eq. (5.29). With "SF LDA" we indicate the semi-phenomenological approach of Sec. 3.2 consistently adopted for both the hole and particle SFs (using the relativistic definition of Eq. (3.20)). When a relativistic free nucleon in the final state (delta distribution for the particle SF) and a fully dressed hole are considered, the curves are labeled as "SF LDA IA". This is consistent with the definitions of Sec. 5.4.

In Fig. 5.6, the transverse, longitudinal and nucleon-density scaling functions obtained using the CBF SF are compared. In all cases FSI effects are included. Despite only one-body current contributions are considered, an enhancement in the transverse channel (red dotted curve) with respect to the longitudinal one (blue dashed curve) is apparent. The nucleon-density scaling function (solid black curve) lies between the transverse and the longitudinal ones, corroborating this choice of the scaling function. Our analysis suggests that the differences between the three curves have to be ascribed to the use of the GFG model prefactors in the scaling functions.

FSI effects in the CBF SF scheme can be appreciated from Fig. 5.7. The CBF SF and CBF SF+FSI longitudinal scaling functions at $|\vec{q}| = 0.57$, 0.8, 0.9, 1.0, and 1.2 GeV, obtained within the CBF SF approach using the hole SF of Ref. [27], are displayed in the left and right panels, respectively. FSI do not play a major role, leading to very small modifications of the CBF SF results except for $|\vec{q}| = 0.57$ GeV, where they improve the agreement with experimental data. Our findings are at variance with those of Ref. [28], where the violation of zeroth-kind scaling are ascribed to relativistic effects in the FSI. The asymmetric shape of the theoretical scaling functions, mildly affected by the inclusion of FSI, is clearly visible, although less pronounced than in the data. It has to be noted that the scaling functions of Fig. 5.7 peak at slightly larger values of ψ compared to those obtained within the GFMC approach in Ref. [25]. The origin of this difference is probably twofold. On the one hand, whilst the GFMC predictions give full account of nuclear dynamics in the final state, SF approaches are based on the factorization ansatz; the dynamics of the knocked-out nucleon is taken care in a somewhat simplified fashion, by means of either the particle spectral function or a convolution scheme. On the other hand, as stated in Refs. [213, 214], the GFMC Euclidean response functions are obtained from variational estimates of the ground-state wave function rather then from the evolved GFMC wave function. Hence, the ground-state energy E_0 in the energy-conserving delta-function entering the definitions of the response functions of Eq.(5.4) is approximated by the variational energy E_T. Since the best variational wave-function for ^{12}C underbinds the nucleus by $E_T - E_0 \simeq 20$ MeV, the GFMC response functions could be shifted to lower values of q^0 compared to the experimental ones. This can be best appreciated by looking at Fig. 4 of Ref. [25]. The variational energy for ^{4}He is much closer to the experimental ones, $E_T - E_0 \simeq 1$ MeV. This might well explain why the longitudinal scaling functions of ^{4}He are shifted to larger values of ψ compared to those of ^{12}C (see Fig. 14 of Ref. [25].)

In Fig. 5.8 we compare the nucleon-density scaling functions obtained using the relativized SF LDA approach against those of the CBF SF+FSI, for the same momentum transfer values of Fig. 5.7. Both approaches provide asymmetric scaling functions that satisfy scaling of the first kind. The comparison between LDA and CBF predictions can be better appreciated in Fig. 5.9, where results for $|\vec{q}| = 0.57$ and 0.9 GeV are highlighted. In the left panel, CBF SF+FSI and SF LDA results nicely agree for both momentum transfers. In the right panel, we show that

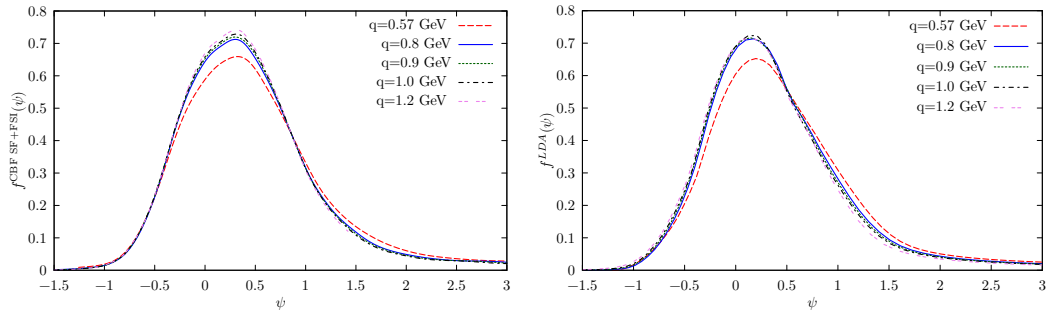

FIGURE 5.8: Nucleon-density scaling functions for ^{12}C computed for $|\vec{q}| = 0.57$, 0.8, 0.9, 1.0 and 1.2 GeV. In the left (right) panel, results obtained using CBF SF+FSI (LDA SF) are shown

the consistency between the two approaches is preserved also also when the FSI effects are suppressed, provided the $C\rho$ term is included in the real part of the LDA self-energy (see discussion in Subsec. 3.2.3). Comparing the left and right panels, we find appreciable FSI effects only for $|\vec{q}| = 0.57$ GeV. The mean value of ψ, defined by $\int \psi f(\psi) d\psi / \int f(\psi) d\psi$ becomes smaller when FSI are included. Indeed, a redistribution of the strength is produced, which slightly enhances the asymmetry of the nucleon-density scaling functions. The differences in the position of the quasielastic peak – the CBF SF curves are shifted towards larger excitation energies compared to those of the LDA SF – have to be ascribed to the more accurate description of the structure of ^{12}C provided by the CBF SF. This is encoded in the MF contribution $\bar{S}_h^{1h}(|\vec{p}|, E)$, extracted from $(e, e'p)$ experiments, and cannot be encompassed by the LDA SF approach of Sec. 3.2. It is also remarkable that the LDA SF model leads to tails of the scaling functions comparable to those arising in the CBF SF formalism. In the latter case, these tails are mostly provided by the correlation contribution $\bar{S}_h^{\rm corr}(|\vec{p}|, E)$ of the hole SF, and hence they are quite sensitive to short-range correlations. In the LDA SF approach these correlations are incorporated in the in-medium NN potential obtained from the experimental elastic NN scattering cross section, modified to include some medium polarization corrections.

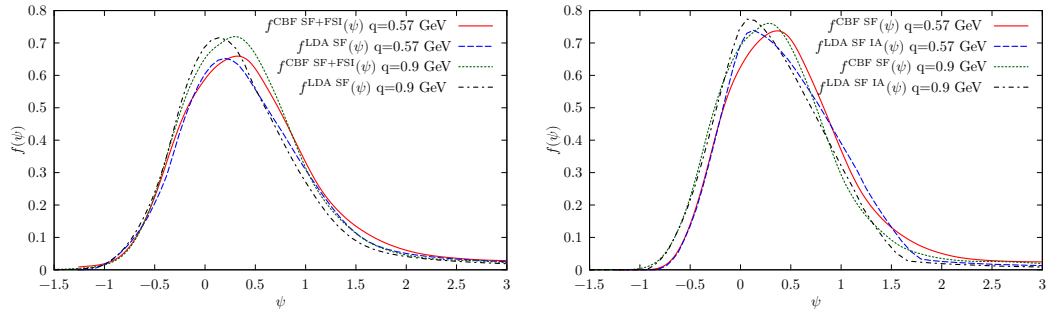

FIGURE 5.9: Scaling functions for ^{12}C computed for $|\vec{q}| = 0.57$, and 0.9 GeV. In the left (right) panel results are obtained within the CBF SF+FSI(CBF SF) and SF LDA (SF LDA IA) approaches.

Chapter 6

Weak production of strange and charmed ground-state baryons in nuclei

In this chapter we analyze the QE weak production of Λ and Σ hyperons induced by $\bar{\nu}$ scattering off nuclei. Electroweak CC can induce the production of strange particles through both the $\Delta S = 0$ and $\Delta S = 1$ channels, where S denotes the strangeness quantum number. We focus our analysis on $\Delta S = 1$ processes, for initial $\bar{\nu}$ energies in the range $E_\nu = 1 - 3$ GeV, of interest for accelerator neutrino experiments. Although $\Delta S = 1$ transitions are generally suppressed with respect to $\Delta S = 0$ reactions by a factor $\tan\theta_C$, in this energy region the latter is strongly reduced by the available phase space and the rates of two processes become comparable. To describe the propagation of hyperons in the nuclear medium we have devised a Monte Carlo cascade (MCC) algorithm. We treat the rescattering processes that the hyperon undergoes before exiting the nucleus in a classical way, using the experimental data for the hyperon-nucleon cross sections as an input.

Our analysis improves upon the pioneering work of Ref. [30], where nuclear effects were for the first time included in the description of $\Delta S = 1$ processes, although a simplified description of the initial nuclear target – the LFG model – was employed. Here we provide a realistic description of the nuclear structure, employing two distinct hole SFs. We analyze the role of nuclear correlations in the ground-state and FSI between the produced hyperon and the spectator nucleons, in double and single-differential, and total inclusive $\bar{\nu}_l + {}^{16}\mathrm{O}$ cross sections in which Λ and Σ hyperons are produced. The dependence of these effects on the initial nuclear species is also discussed by comparing the results obtained for total cross sections in ${}^{12}\mathrm{C}$,${}^{16}\mathrm{O}$, and ${}^{40}\mathrm{Ca}$. All these findings might have important implications in the analysis of SciBooNE [215], MicroBooNE [216], MINERvA [217] and ArgoNeuT [218] experiments once the data collected using $\bar{\nu}$ beams become available.

The BESIII Collaboration has recently reported on the absolute measurement of the branching ratios of $\Lambda_c \to \Lambda e^+ \nu_e$ [219] and $\Lambda_c \to \Lambda \mu^+ \nu_\mu$ [220], which can serve as an important benchmark to compare various theoretical predictions. These decays have been studied within several relativistic and nonrelativistic constituent quark models (CQMs), which provide predictions for the transition form factors [35, 34, 32, 221]. Some of the groups have also presented results for the $\Lambda_c \to N$ form factors [33, 32]. The first lattice QCD (LQCD) calculation of the $\Lambda_c \to \Lambda$ and $\Lambda_c \to N$ form factors reported in Refs. [222] and [31], respectively, deserves special mention.

Capitalizing on these recent developments, we also present realistic results for the weak Λ_c production cross section in nuclei, providing estimates of the theoretical uncertainty of our predictions. We limit our analysis to relatively-low neutrino energies, close to threshold, and we assume that the QE mechanism, $W^+ n_b \to \Lambda_c$ where n_b is a neutron bound in the nucleus, is the dominant one. To estimate the theoretical uncertainties related to the elementary amplitudes, we consider two different scenarios. In the first one, we relate the $\Lambda_c \to \Lambda$ and $\Lambda_c \to N$ form

factors by a SU(3) rotation, neglecting the effects of SU(3) symmetry breaking. In the second one, we directly use $\Lambda_c \to N$ form factors from theoretical calculations, whenever available.

The kinematical region of interest for neutrino experiments corresponds to $q^2 \in (-5,0)$ GeV^2. Since the semileptonic Λ_c decay occurs for $q^2 > 0$, the analysis of the neutrino cross section requires an extrapolation of the form factors to negative q^2, which is not expected to be completely free of uncertainties. Therefore, in our analysis, we select models that are capable to reproduce the measured $\mathrm{BR}(\Lambda_c \to \Lambda e^+ \nu_e)$ branching ratio, and whose form factor parametrizations do not lead to pathological behaviors in the $q^2 < 0$ region. We use four different models for the $\Lambda_c \to N$ form factors to compute the $\nu_\mu + {}^{16}\mathrm{O} \to \mu^- \Lambda_c X$ total cross section. Particular emphasis shall be devoted to the results obtained employing the analytical continuation of the LQCD calculations of Ref. [31]. The latter are supplemented by estimates of the theoretical uncertainties that we propagate throughout our calculations to the neutrino cross sections. A more conservative theoretical uncertainty is obtained from the spread of the predictions found when the different sets of CQM form factors are also considered.

Finally, we would like to point out that since the calculation of the total nuclear cross section and the semileptonic $\Lambda_c \to \Lambda$ decay width are sensitive to different kinematical regions, and therefore presumably to different form factors, the combined study of the two processes allows to better elucidate the differences between models.

This chapter follows the findings of Ref. [223]. In Sec. 6.1, we provide the general expressions for hyperon production cross section in the vacuum. In Sec. 6.2, we outline the main features of the different schemes examined in the case of the $N \to \Lambda_c$ transition. Our approach to account for SF and FSI nuclear effects is described in Sec. 6.3, while the main results of this study are presented in Sec. 6.4.

6.1 Cross section for $\bar{\nu}_\ell + N \to \ell^+ + Y$

The unpolarized differential cross section for the $\bar{\nu}_\ell(k) + N(p) \to \ell^+(k') + Y(p')$ reaction, in which an antineutrino $\bar{\nu}_\ell$ scatters off a nucleon N, and in the final state the charged lepton ℓ^+ and the hyperon Y are produced, is given in the laboratory frame by[1]

$$\frac{d\sigma}{dE_{k'}d\Omega_{k'}} = \frac{G_F^2}{4\pi^2}\frac{|\vec{k}'|}{|\vec{k}|}L^{(\bar{\nu})}_{\mu\sigma}(k,k')W_N^{\mu\sigma}(p,q)\,. \tag{6.1}$$

The lepton tensor is given in Eq. (2.19) and nucleon tensor reads

$$\begin{aligned} W_N^{\mu\sigma}(p,q) &= \frac{\sin^2\theta_C}{2M}\int \frac{d^3p'}{2E^Y_{p'}}\delta^4(q+p-p')A_Y^{\mu\sigma}(p,q,p') \\ &= \frac{1}{ME^Y_{p'}}\delta(q^0+M-E^Y_{p'})A_Y^{\mu\sigma}(p,q,p+q) \end{aligned} \tag{6.2}$$

and

$$A_Y^{\mu\sigma}(p,q) = \frac{1}{2}\mathrm{Tr}\left[(\not{p}+\not{q}+M_Y)\Gamma_Y^\mu(\not{p}+M)\gamma^0\Gamma_Y^{\sigma\dagger}\gamma^0\right] \tag{6.3}$$

The Dirac operator Γ_Y^μ is given in Eq. (2.33). The explicit structure of $N \to \Lambda, \Sigma^0, \Sigma^-$ form factors can be found in Sec. 2.2.3.

[1] In the case of Λ_c production, the reaction is obviously induced by neutrinos instead of antineutrinos. We will come back to this point below.

The integration over $E_{k'}$ needed to obtain the angular cross section can be carried out exploiting the energy-conserving delta function of Eq. (6.2)

$$I(|\vec{k}|,\cos\theta) = \int dE_{k'}|\vec{k}'| \frac{\delta\left(q^0 + M - \sqrt{M_Y^2 + \vec{q}^2}\right)}{\sqrt{M_Y^2 + \vec{q}^2}} = \frac{|\vec{k}'|}{M + |\vec{k}| - \frac{E_{k'}}{|\vec{k}'|}|\vec{k}|\cos\theta} \tag{6.4}$$

where $|\vec{k}'|$ depends on the lepton scattering angle θ through the energy conservation equation $E_{k'} = |\vec{k}| + M - \sqrt{M_Y^2 + \vec{q}^2}$, with $\vec{q}^2 = \vec{k}^2 + \vec{k}'^2 - 2|\vec{k}||\vec{k}'|\cos\theta$, $E_{k'} = \sqrt{\vec{k}'^2 + m_\ell^2}$ and m_ℓ is the mass of the outgoing lepton. Neglecting m_ℓ, the expressions simplify to

$$\frac{d\sigma}{d\Omega_{k'}} = \frac{G_F^2 \sin^2\theta_C}{4\pi^2} \frac{|\vec{k}'|^2}{|\vec{k}|^2} \frac{L_{\mu\sigma}^{(\bar{\nu})}(k,k') A_Y^{\mu\sigma}(p,q)}{1 + \frac{M^2 - M_Y^2}{2|\vec{k}|M}}, \tag{6.5}$$

with

$$E_{k'} = |\vec{k}'| = \frac{|\vec{k}|M + (M^2 - M_Y^2)/2}{M + |\vec{k}|(1 - \cos\theta)} \tag{6.6}$$

The differential cross section for the neutrino $\nu_\ell(k) + N(p) \to \ell^-(k') + Y_c(p')$ charm production reaction can be obtained from the above expressions replacing $L_{\mu\sigma}^{(\bar{\nu})}$ by $L_{\mu\sigma}^{(\nu)} = L_{\sigma\mu}^{(\bar{\nu})}$ and using the appropriate masses and form factors.

6.2 Form factors for $N \to \Lambda_c$ transition

The study of charmed baryon production in weak processes is still in its infancy; it involves non-trivial theoretical calculations and scarce experimental data are available. The CHORUS collaboration recently measured the ratio of the cross section for Λ_c production in neutrino-nucleon CC interaction to the total charged-current cross section, $\sigma(\Lambda_c)/\sigma(CC) = (1.54 \pm 0.35(\text{stat}) \pm 0.18(\text{syst})) \times 10^{-2}$ for a highly energetic neutrino beam, $E_\nu = 27$ GeV [224]. However, in this energy region no reliable theoretical predictions for the form factors are currently available.

Previous analyses on Λ_c weak production in QE processes [225] do not seem to provide robust predictions for the total nuclear cross section. In fact, they rely on theoretical models for the $N \to \Lambda_c$ form factors whose predictions, never confronted with experimental data, differ by an order of magnitude for $E_\nu = 10$ GeV. Here, we compute the total cross section of Λ_c weak production adopting form factors calculated within four independent approaches: the LQCD simulation of Refs. [222, 31] and the CQMs of Refs. [32, 33, 34, 35]. The LQCD results for both $\Lambda_c \to N$ and $\Lambda_c \to \Lambda$ have been obtained using two different lattice spacings and including one ensemble with a physical pion mass, $m_\pi = 139(2)$ MeV. The nonrelativistic harmonic-oscillator basis (NRHOQM) approach of Ref. [35] calculates the form factors with the parameters for the baryon wave functions derived in Ref. [226]. A relativistic CQM (RCQM) with infrared confinement [227, 228, 229] is employed in Ref. [33] to perform a detailed analysis of the $\Lambda_c \to n\ell^+\nu_\ell$ invariant and helicity amplitudes, form factors, angular decay distributions, decay width, and asymmetry parameters. Lastly, a quark-model picture was used to obtain the results of Ref. [32], improving previous predictions [230] for the semileptonic decays of $\frac{1}{2}^+$ charm baryons, belonging to the representation **20** of SU(4), obtained in the four-flavor symmetric limit. Some SU(4) symmetry-breaking corrections, calculated within the MIT bag model (MBM) [231, 232] and a nonrelativistic quark model (NRQM) [233], are included.

The q^2 parametrizations of the above mentioned models, validated against the experimental data for the Λ_c semileptonic decay reported by the BESIII Collaboration [219, 220], can be extended to the $q^2 < 0$ region, relevant for neutrino scattering. The same strategy is not applicable to the form factors of Ref. [221], as they have poles for $q^2 < 0$. As mentioned, the measurement of the $\Lambda_c \to \Lambda \ell^+ \nu_\ell$ ($\ell = e, \mu$) decay width provides a constraint for the $\bar{\nu}_\ell \Lambda_c \to \Lambda \ell^+$ transition form factors. In the limit of unbroken SU(3) symmetry, the latter can be related to the $\bar{\nu}_\ell \Lambda_c \to n \ell^+$ form factors by performing a rotation in the SU(3) space – the resulting Clebsh-Gordan coefficient being $\sqrt{3/2}$ [33].

In the following we briefly review the four approaches utilized to compute the form factors relevant for the $N \to \Lambda_c$-transition considered here and we provide their explicit expressions.

6.2.1 Theoretical models for the form factors

The NRHOQM is used to compute the $\Lambda_c \to \Lambda$ semileptonic decay width, but not the $\Lambda_c \to n$ transition. The calculated branching fractions are $\Gamma(\Lambda_c \to \Lambda \ell^+ \nu_\ell)/\Gamma_{\Lambda_c} = 3.84\%$ and 3.72% for the electron and muon modes[2], respectively. Though theoretical uncertainties were not provided, these predictions agree rather well with the experimental fractions, $(3.63 \pm 0.38 \pm 0.20)\%$ [e] and $(3.49 \pm 0.46 \pm 0.27)$ [μ] measured by BESIII. In addition, in Ref. [35] semileptonic decays to excited Λ^* resonances are calculated and leading order heavy-quark effective theory predictions are also derived, the latter being largely consistent with the quark-model form factors used in that work. Assuming SU(3) invariance, the form factors of the $\Lambda_c \to \Lambda$ transition can be used to estimate the weak production of the Λ_c charm hyperon off a neutron by multiplying them by the appropriate Clebsh-Gordan coefficient. The matrix elements of the vector and axial $c \to s$ currents are expressed in Ref. [35] in terms of the $F_{1,2,3}(q^2)$ and $G_{1,2,3}(q^2)$ form factors, which are related to those introduced in Eq. (2.33) by

$$
\begin{aligned}
f_1(q^2) &= \sqrt{\frac{3}{2}}\left(F_1(q^2) + \frac{M_{\Lambda_c} + M_\Lambda}{2M_{\Lambda_c} M_\Lambda} \left(M_\Lambda F_2(q^2) + M_{\Lambda_c} F_3(q^2) \right) \right), \\
f_2(q^2) &= -\sqrt{\frac{3}{2}} \times \frac{1}{2}\left(F_2(q^2) + \frac{M_{\Lambda_c}}{M_\Lambda} F_3(q^2) \right), \\
g_1(q^2) &= \sqrt{\frac{3}{2}}\left(G_1(q^2) - \frac{M_{\Lambda_c} - M_\Lambda}{2M_{\Lambda_c} M_\Lambda} \left(M_\Lambda G_2(q^2) + M_{\Lambda_c} G_3(q^2) \right) \right), \\
g_2(q^2) &= \sqrt{\frac{3}{2}} \times \frac{1}{2}\left(G_2(q^2) + \frac{M_{\Lambda_c}}{M_\Lambda} G_3(q^2) \right)
\end{aligned}
\tag{6.7}
$$

where the $\sqrt{3/2}$ Clebsh-Gordan coefficient has been explicitly included to use these for the $n \to \Lambda_c$ transition. The NRHOQM form factors of Ref. [35] have the simple form

$$
\left.
\begin{matrix}
F_{1,2,3}(q^2) \\
G_{1,2,3}(q^2)
\end{matrix}
\right\}
= (A + Bq^2 + Cq^4) e^{-\frac{3}{2}\left(\frac{m_q p_\Lambda}{\alpha M_\Lambda}\right)^2}
\tag{6.8}
$$

where $m_q = 0.2848$ GeV, $\alpha^2 = (0.424^2 + 0.387^2)/2$ GeV and $p_\Lambda = \lambda^{1/2}(M_{\Lambda_c}^2, M_\Lambda^2, q^2)/2M_{\Lambda_c}$, with $\lambda(x,y,z) \equiv x^2 + y^2 + z^2 - 2xy - 2xz - 2yz$. The coefficients A, B, and C can be found in Table 6.1.

The RCQM scheme predicted an absolute branching fractions of $\Lambda_c \to \Lambda \ell^+ \nu_\ell$, which turned out to be 2.78% and 2.69% for the electron and muon channels, respectively – no theoretical uncertainties are provided [34] . These values are consistent with the lower limits of the data

[2] Γ_{Λ_c} is the total decay width of the Λ_c hyperon.

	A	B [GeV^{-2}]	C [GeV^{-4}]
$F_1(q^2)$	1.382	-0.073	0
$F_2(q^2)$	-0.235	0.022	0.006
$F_3(q^2)$	-0.146	-0.003	-0.001
$G_1(q^2)$	0.868	0.013	0.004
$G_2(q^2)$	-0.440	0.116	0.003
$G_3(q^2)$	0.203	-0.009	0

TABLE 6.1: Parameters introduced in Eq. (6.8) to describe the q^2-dependence of the form factors used in the NRHOQM of Ref. [35]. Note that the we have changed the sign of the B coefficient of the G_2 form factor, with respect to that quoted in Table III of Ref. [35]. Only in this way, we could reproduce the form factor displayed in Fig. 4(a) of this latter reference.

from the BESIII Collaboration [219, 220]. They also agree rather well with those ($2.9 \pm 0.5\%$ and $2.7 \pm 0.6\%$) quoted in the 2014 edition of the Review of Particle Physics [234], obtained from the first model-independent measurement of the branching fraction of the $\Lambda_c^+ \to pK^-\pi^+$ mode, reported in 2013 by the Belle Collaboration [235]. Within the RCQM, the q^2 behavior of the form factors is well represented by a double-pole parametrization of the form

$$\left.\begin{array}{l} f_{1,2}(q^2) \\ g_{1,2}(q^2) \end{array}\right\} = \frac{A}{1 - B(q^2/M_{\Lambda_c}^2) + C(q^2/M_{\Lambda_c}^2)^2}\,. \tag{6.9}$$

For convenience, the parameters A, B, and C, taken form these references, are reported in Table 6.2.

	A	B	C
$f_1(q^2)$	0.470	1.111	0.303
	0.511	1.736	0.760
$f_2(q^2)$	0.247	1.240	0.390
	0.289	1.970	1.054
$g_1(q^2)$	0.414	0.978	0.235
	0.466	1.594	0.647
$g_2(q^2)$	-0.073	0.781	0.225
	0.025	0.321	8.127

TABLE 6.2: Coefficients employed in Eq. (6.9) to construct the weak Λ_c production form factors from the RCQM results of Refs. [33, 34]. For each form factor, the upper (lower) value corresponds to the $\Lambda_c \to N$ ($\Lambda_c \to \Lambda$) transition. Note that $g_2(q^2) = -f_2^A(q^2)$, being the latter form factor calculated in [33, 34].

The main difference between MBM and NRQM lies in how the initial and final baryon overlap integrations are accounted for: they are limited to the bag space in MBM while in the NRQM they are not. The MBM is expected to be more realistic than the NRQM at the price of introducing additional parameters, such as the bag radius and the masses of the quarks in the bag. Additional corrections to the NRQM and MBM predictions, such as the hard-gluon QCD contributions [32], are also encompassed. Both the monopole and the dipole q^2 dependencies of the form factors have been employed within the MBM and the NRQM. For simplicity we only consider the latter, since monopole form factors overestimate the experimental $\Lambda_c \to \Lambda e^+ \nu_e$ branching ratio. Dipole form factors provide reasonable estimates for this observable: 3.2%

and 3.9% for the MBM and the NRQM, respectively. They have the general form

$$\left.\begin{array}{l} f_{1,2}(q^2) \\ g_{1,2}(q^2) \end{array}\right\} = \frac{A}{(1-q^2/M_R^2)^2}, \tag{6.10}$$

where the values of A and M_R are listed in Table 6.3.

	NRQM		MBM	
	A	M_R [GeV]	A	M_R [GeV]
$f_1(q^2)$	0.22	2.01	0.33	2.01
	0.35	2.11	0.46	2.11
$f_2(q^2)$	0.11	2.01	0.18	2.01
	0.09	2.11	0.19	2.11
$g_1(q^2)$	0.58	2.42	0.41	2.42
	0.61	2.51	0.50	2.51
$g_2(q^2)$	0.04	2.42	0.07	2.42
	0.04	2.51	0.05	2.51

TABLE 6.3: Coefficients employed in Eq. (6.10) to construct the weak Λ_c production form factors for the MBM and NRQM models of Refs. [32, 230]. For each form factor, the upper (lower) value corresponds to the $\Lambda_c \to N$ ($\Lambda_c \to \Lambda$) transition. The values of the form factors at $q^2 = 0$ are taken from [32], and contain some SU(4) breaking corrections, while the pole masses collected in the table are taken from [230]. Note that $g_2(q^2) = -g_2^A(q^2)$, being the latter form factors calculated in [32].

The LQCD works [222, 31] are based on gauge field configurations generated by the RBC and UKQCD collaborations [236, 237] with 2+1 flavors of dynamical domain-wall fermions, for lattice spacings $a \approx 0.11$ fm and 0.085 fm and pion masses in the range $230\,\text{MeV} \leq m_\pi \leq 350\,\text{MeV}$, although in Ref. [222] an additional ensemble with $m_\pi = 139(2)$ MeV was also considered. The form factors are extrapolated to the continuum limit and to the physical pion mass employing a modified $z-$expansions [238]. Taking the Cabbibo-Kobayashi-Maskawa matrix element $|V_{cs}|$ from a unitarity global fit and the Λ_c lifetime from experiments, branching fractions $\mathscr{B}(\Lambda_c \to \Lambda e^+ \nu_e) = (3.80 \pm 0.19 \pm 0.11)\,\%$ and $\mathscr{B}(\Lambda_c \to \Lambda \mu^+ \nu_\mu) = (3.69 \pm 0.19 \pm 0.11)\,\%$ were found in [222], consistent with, and twice more precise than, the BESIII measurements. The LQCD weak transition matrix elements are parameterized in terms of the $f_{\perp,+}(q^2)$ and $g_{\perp,+}(q^2)$ form factors, which are related to those defined in Eq. (2.33) for the Λ_c weak production in the following way[3]:

$$\begin{aligned}
f_1(q^2) &= -\frac{q^2}{s_+(q^2)} f_\perp(q^2) + \frac{(M_{\Lambda_c}+M_1)^2}{s_+(q^2)} f_+(q^2), \\
f_2(q^2) &= \frac{M_{\Lambda_c}(M_{\Lambda_c}+M_1)}{s_+(q^2)} \Big(f_\perp(q^2) - f_+(q^2) \Big), \\
g_1(q^2) &= -\frac{q^2}{s_-(q^2)} g_\perp(q^2) + \frac{(M_{\Lambda_c}-M_1)^2}{s_-(q^2)} g_+(q^2), \\
g_2(q^2) &= \frac{M_{\Lambda_c}(M_{\Lambda_c}-M_1)}{s_-(q^2)} \Big(g_\perp(q^2) - g_+(q^2) \Big)
\end{aligned} \tag{6.11}$$

[3]The additional form factors, f_0 and g_0, computed within LQCD, which only contribute to f_3 and g_3 in Eq. (2.33), are not reported, as they do not contribute to the cross section in the limit of vanishing lepton mass.

where $s_\pm(q^2) = \left[(M_{\Lambda_c} \pm M_1)^2 - q^2\right]$, and M_1 is either M or M_Λ, depending on the Λ_c weak transition considered. The q^2 behavior is parameterized as

$$\begin{aligned} \left.\begin{array}{l} f_{\perp,+}(q^2) \\ g_{\perp,+}(q^2) \end{array}\right\} &= \frac{1}{1 - q^2/M_R^2}\left(A + Bz(q^2) + Cz^2(q^2)\right), \\ z(q^2) &= \frac{\sqrt{t_+ - q^2} - \sqrt{t_+ - t_0}}{\sqrt{t_+ - q^2} + \sqrt{t_+ - t_0}}, \\ t_+ &= \begin{cases} (M_D + M_K)^2 & \text{for } c \to s \\ (M_D + M_\pi)^2 & \text{for } c \to d \end{cases} \end{aligned} \tag{6.12}$$

with $t_0 = (M_{\Lambda_c} - M_1)^2$, $M_D = 1.87$ GeV, $M_K = 0.494$ GeV and $M_\pi = 0.135$ GeV and the A, B, C and M_R coefficients are taken from the nominal fits carried out in Refs. [222, 31], providing the central values and statistical uncertainties of the form factors. We list all these parameters in Table 6.4.

	A	B	C	M_R [GeV]
$f_\perp(q^2)$	1.36 ± 0.07	-1.70 ± 0.83	0.71 ± 4.34	2.01
	1.30 ± 0.06	-3.27 ± 1.18	7.16 ± 11.6	2.112
$f_+(q^2)$	0.83 ± 0.04	-2.33 ± 0.56	8.41 ± 3.05	2.01
	0.81 ± 0.03	-2.89 ± 0.52	7.82 ± 4.53	2.112
$g_\perp(q^2)$	0.69 ± 0.02	-0.68 ± 0.32	0.70 ± 2.18	2.423
	0.68 ± 0.02	-1.91 ± 0.35	6.24 ± 4.89	2.46
$g_+(q^2)$	0.69 ± 0.02	-0.90 ± 0.29	2.25 ± 1.90	2.423
	0.68 ± 0.02	-2.44 ± 0.25	13.7 ± 2.15	2.46

TABLE 6.4: Coefficients, taken from the nominal fits carried out in Refs. [222, 31], of the LQCD form factors used in the parametrization of Eq. (6.12). For each form factor, the upper (lower) value corresponds to the $\Lambda_c \to N$ ($\Lambda_c \to \Lambda$) transition.

The semileptonic branching ratios $\mathrm{BR}(\Lambda_c \to \Lambda e^+ \nu_e)$ calculated with the five different sets of form factors turn out to be in a reasonable agreement with each other and with the BESIII measurement. The predictions range from the 2.78% of the RCQM [33], to the 3.9% obtained within the NRQM scheme [32], corresponding to a $\simeq 30\%$ variation. Hence, one should expect a similar spread among the predictions for the total $\nu_\ell + n \to \Lambda_c^+ + \ell^-$ cross section. However, the theoretical uncertainty on the latter observables could be even larger for the following reasons. (i) Experimental measurements effectively constraint the $\Lambda_c \to \Lambda$ form factors, while we are interested in the $n \to \Lambda_c$ transition. The form factors for $\Lambda_c \to \Lambda$ and $n \to \Lambda_c$ transitions may be related by an SU(3) rotation but, because of SU(3) breaking effects, these are subject to additional corrections. In this regard, one has to note that for most of the models we have also access to direct predictions for the $c \to d$ transition form factors. (ii) The form factors have been fitted to the experimental decay width in the range $0 \leq q^2 \leq (M_{\Lambda_c} - M_\Lambda)^2$, while Λ_c neutrino production is characterized by $q^2 < 0$. The extrapolation of the form factors to moderately large negative q^2 values, corresponding to medium-energy neutrino beams, entails a certain degree of ambiguity. In order to quantify the uncertainty of this procedure, we consider five different sets of form factors characterized by a variety of q^2 dependencies. (iii) The $\Lambda_c \to \Lambda e^+ \nu_e$ decay is mostly sensitive to the axial $g_1(q^2)$ form factor, which dominates the total width. On the other hand, both $f_1(q^2)$ and $g_1(q^2)$ are important in the $\nu_\ell + n \to \Lambda_c^+ + \ell^-$ process. Thus, the $f_1(q^2)$ form factor, being less constrained by the experiment, may introduce an additional error to the

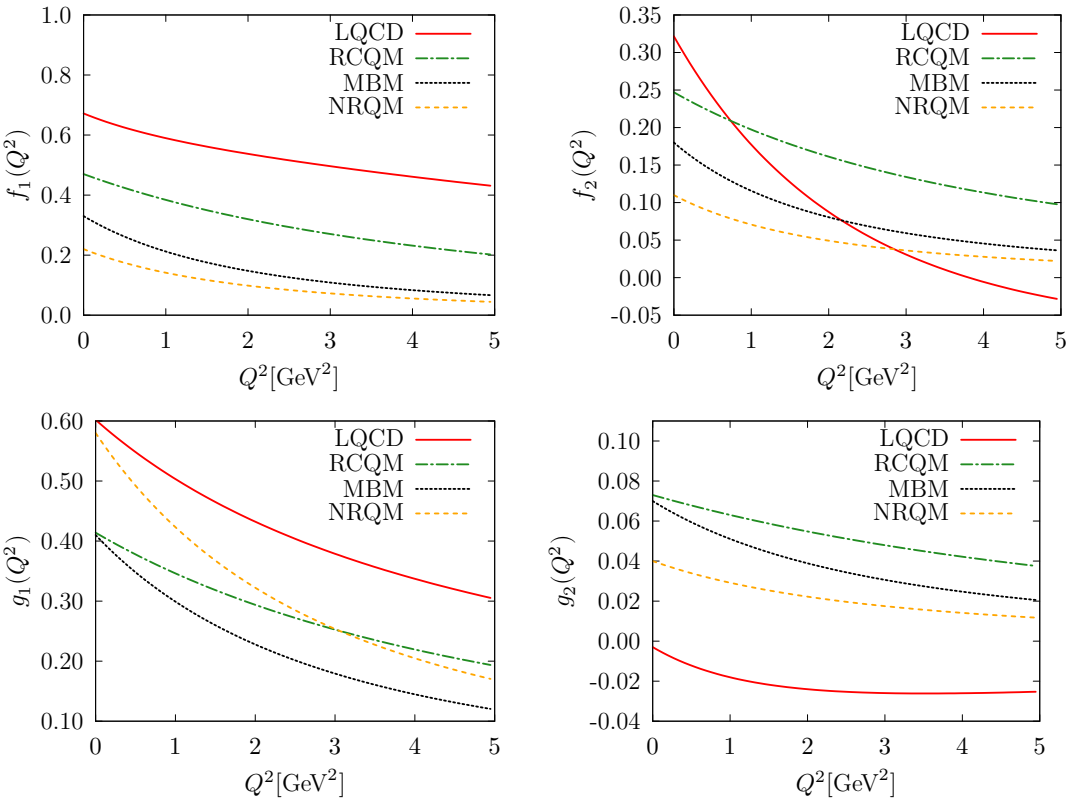

FIGURE 6.1: Form factors for the $n \to \Lambda_c$ transition deduced from extrapolating to $Q^2 = -q^2 > 0$ the results reported in Refs. [31] (LQCD), [33] (RCQM) and [32] (MBM and NRQM).

cross-section prediction.

To evaluate the $\nu_\ell + n \to \Lambda_c^+ + \ell^-$ cross section for the LQCD [222, 31], the RCQM of Refs. [33, 34] and the MBM & NRQM [32] schemes, we pursue two different avenues. The first one corresponds to the unbroken SU(3) limit, in which we take the $\Lambda_c \to \Lambda$ form factors and use the $\sqrt{3/2}$ Clebsh-Gordan coefficient to compute the Λ_c production off the neutron. In the second one, we directly apply the $\Lambda_c \to N$ form factors reported in these references. As for the NRHOQM of Ref. [35], the only available parametrization, obtained from the SU(3) rotation, will be employed.

In Fig. 6.1, we show the form factors for the $N \to \Lambda_c$ transition, for $Q^2 = -q^2 > 0$, corresponding to the kinematics of neutrino production. As we mentioned, the main contribution to the cross section and to the decay width is driven by $f_1(Q^2)$ and $g_1(Q^2)$. LQCD predicts the largest values for these two form factors, while the MBM and NRQM models provide the far lowest ones for $f_1(Q^2)$ and, at high Q^2, for $g_1(Q^2)$. Note that the LQCD and RCQM form factors exhibit similar Q^2 dependencies, except for f_2, being the f_1 and g_1 from RCQM form factors $\sim 30\%$ smaller than those computed within LQCD. Analogous behaviors are observed for the $\Lambda_c \to \Lambda$ form factors, discussed in detail in Subsec. 6.2.2, where further comparisons among the various approaches are provided.

As a final remark, analogously to the case of Λ and Σ production, the f_3 and g_3 form factors have been neglected in the cross-section calculations, as they are suppressed by a factor m_ℓ^2/M^2.

6.2.2 Further details on the $\Lambda_c \to \Lambda, N$ form factors

When computing the $\nu_\mu + n \to \mu^- + \Lambda_c^+$ cross section, we might assume SU(3) symmetry to relate the $\Lambda_c \to \Lambda$ form factors to the $\Lambda_c \to N$ ones. To estimate SU(3)-breaking effects, we have computed the BR$(\Lambda_c \to \Lambda e^+ \nu_e)$ comparing the results obtained using either the rescaled

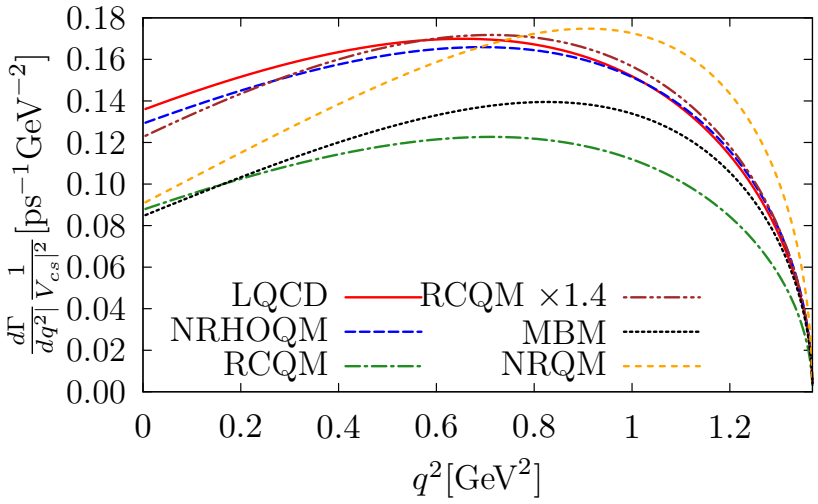

FIGURE 6.2: $\Lambda_c \to \Lambda e^+ \nu_e$ differential decay width from NRHOQM [35], RCQM [34], MBM and NRQM [32], CQM approaches, and the LQCD simulation of Ref. [222].

$\Lambda_c \to N$ or the $\Lambda_c \to \Lambda$ form factors. We performed this comparison for the LQCD, RCQM, NRQM and MBM approaches of Refs. [222, 34, 32]. As for the LQCD form factors, the branching ratios attained assuming SU(3) symmetry are $\sim 20\%$ lower than the direct calculations with the actual $\Lambda \to \Lambda_c$ form factors. This reduction is even more evident, $\sim 40-50\%$, for the RCQM, NRQM, and MBM approaches. This source of uncertainties should be considered when analyzing the different predictions for $\sigma(\nu_\mu + {}^{16}\mathrm{O} \to \mu^- + \Lambda_c + X)/N$ displayed in Fig. 6.10.

The differential widths $d\Gamma(\Lambda_c \to \Lambda e^+ \nu_e)/dq^2$ are shown in Fig. 6.2 for all the approaches used to compute the $\Lambda \to \Lambda_c$ form factors. LQCD, NRHOQM and MBM provide similar distributions, while the NRQM yields significantly different shape, the strength being shifted towards higher values of q^2. Note however, that no major differences in the total width are observed. As discussed in the previous Subsection, the RCQM predicts the lowest branching ratio, about $\sim 40\%$ smaller than the LQCD result reported in Ref. [222]. However, once the RCQM differential distribution [34] is rescaled by a factor 1.4, the shape of $d\Gamma/dq^2$ turns out to be very close to the LQCD one.

The main contribution to the total width ($\sim 65\%$ in most of the models) comes from the axial form factor $g_1(Q^2)$, while the rest of the strength is driven by $f_1(Q^2)$ – there is no axial-vector interference contributing to $d\Gamma/dq^2$. Because of the kinematical reasons, the ratio of the vector to axial parts is different for the $\nu_\mu + n \to \mu^- + \Lambda_c$ reaction, with $f_1(Q^2)$ playing a more important role. Because both f_1 and g_1 dominate the total cross section, it is interesting to pay some further attention to their behavior, when extrapolating them to the region of Q^2 relevant for neutrino scattering. The Q^2 dependence of the $\Lambda_c \to \Lambda$ form factors is displayed in Fig. 6.3. They are multiplied by the factor $\sqrt{3/2}$, as dictated by the SU(3) symmetry to get the $c \to d$ matrix elements from the $c \to s$ ones. Besides the phase-space available in the semileptonic decay, corresponding to $Q^2 < 0$, we also show the behavior of the form factors in the $Q^2 > 0$ region accessible in Λ_c neutrino-production reactions. It is interesting to compare the LQCD, RCQM, NRQM and MBM form factors of Fig. 6.3 with those shown in Fig. 6.1, the latter being computed employing the appropriate $\Lambda_c \to N$ form factors. Such comparison helps estimating the size of SU(3)-breaking contributions, complementing the discussion on integrated $\mathrm{BR}(\Lambda_c \to \Lambda e^+ \nu_e)$ that we alluded to earlier. Focusing on f_1 and g_1, these SU(3)-breaking effects are more apparent in the vicinity of $Q^2 = 0$, while they are less important as Q^2 increases, becoming moderately small for $Q^2 = 5$ GeV^2.

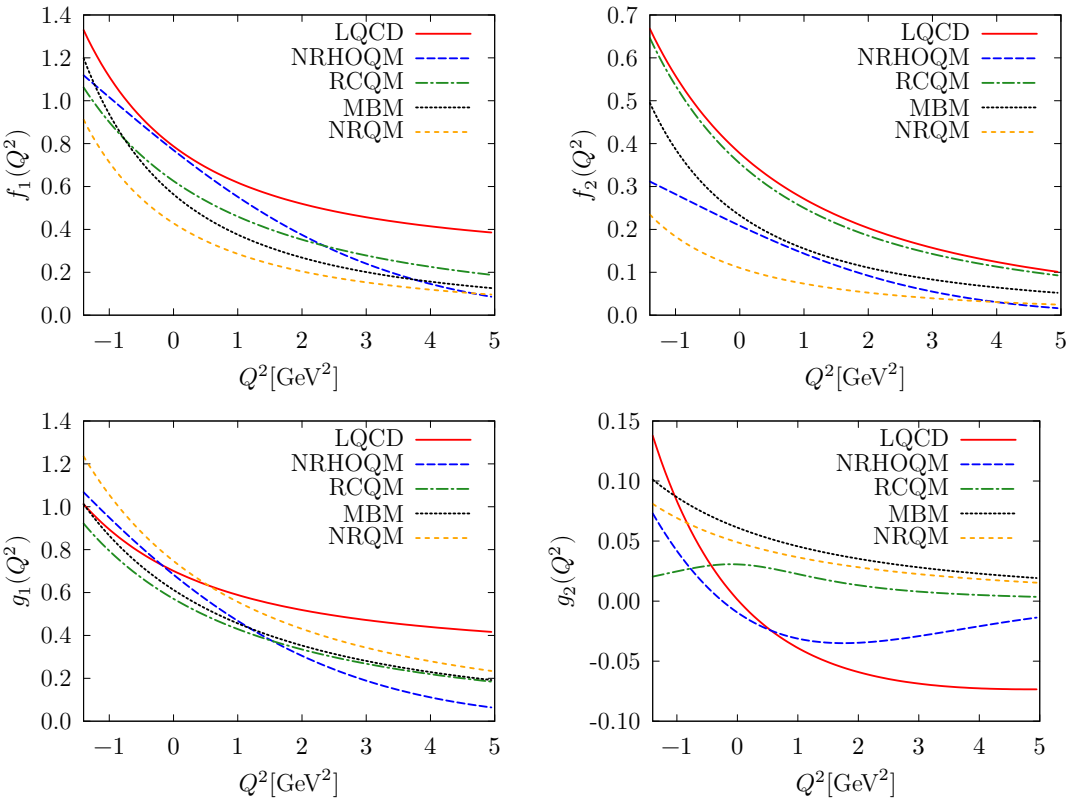

FIGURE 6.3: Vector and axial form factors for the $\Lambda_c \to \Lambda$ transition calculated for the different models as detailed in Sec. 6.2. The form factors are multiplied by the Clebsh-Gordan coefficient $\sqrt{3/2}$ in order to estimate them for the $n \to \Lambda_c$ transition, assuming unbroken SU(3) flavor symmetry. Negative values of Q^2 correspond to the kinematics of the Λ_c semileptonic decay, while Q^2 is positive for the Λ_c neutrino production.

Fig. 6.3 shows that the LQCD and RCQM calculations for $f_1(Q^2)$, $f_2(Q^2)$ and $g_1(Q^2)$ exhibit a similar Q^2 dependence, while their predictions for $g_2(Q^2)$ are quite different. Note, however, that this is not much relevant for the neutrino-induced Λ_c production, since the g_2 contributions for this process are negligible. As for the absolute size, both approaches predict almost the same $f_2(Q^2)$, but the RCQM results for $f_1(Q^2)$ and $g_1(Q^2)$ at $Q^2 < 0$ are $\sim 20\%$ smaller than those of LQCD. This discrepancy is more significant in the region of large Q^2, relevant for scattering processes. This latter behavior is less visible in the $\Lambda_c \to N$ transition form factors shown in Fig. 6.1, where the LQCD and RCQM shapes of f_1 and g_1 turn out to be remarkably similar for the entire range of Q^2, translating into the comparable $d\Gamma/dq^2$ shapes of Fig. 6.2.

We should also note that the Q^2 dependencies of the NRHOQM form factors are significantly different than those of the other models considered here. By only looking at the $d\Gamma/dq^2$ shape in Fig. 6.2, one might expect that the NRHOQM and the LQCD predictions for the neutrino-induced Λ_c production to be similar. However, this is not the case, as shown in Fig. 6.10, where the NRHOQM results lie well below those from LQCD. This is because f_1 and g_1 computed within the NRHOQM becomes smaller with increasing Q^2 much more rapidly than in any of the other models. Finally, both the NRQM and the MBM predict g_1 comparable with those obtained within other schemes. However, their results for f_1 at $Q^2 > 0$ lie below the results of LQCD, RCQM, and NRHOQM. Nevertheless, the NRQM and MBM $\Lambda_c \to \Lambda$ form factors are in an overall better agreement with those of the RCQM than in the case of the $\Lambda_c \to N$ transition shown in Fig. 6.1.

6.3 Nuclear effects

In this Section we generalize the discussion of Sec. 6.1 to the case in which the $\bar{\nu}$ beam scatters off a nucleus with A nucleons producing a hadronic final state comprised of a hyperon Y and an $(A-1)$-nucleon residual system. In the kinematical region in which the IA is expected to be applicable, the nuclear matrix element can be still expressed as in Eq. (6.3), provided that the elementary interactions occur on single bound nucleons. In what follows, we will restrict the discussion to isospin-symmetric nuclei, for which we assume the neutron and proton densities to coincide. Within this scheme, the double-differential cross section is evaluated as in Eq. (6.1), but the hadron tensor is obtained from the convolution of the hole SF and the spin averaged squared amplitude of the hadron matrix element, $A_Y^{\mu\nu}$, reported in Eq. (6.3)

$$W_Y^{\mu\nu}(q) = \frac{\sin^2\theta_C}{4MM_Y}\int\frac{d^3p}{(2\pi)^3}\int dE\bar{S}_h(E,\vec{p})\frac{M}{E_p}\frac{M_Y}{E^Y_{p+q}}\delta(E+M+q^0-E^Y_{p+q})A_Y^{\mu\nu}(p,q)\,. \quad (6.13)$$

In Ref. [30], the LFG model was adopted to describe nuclear dynamics. Generalized Lindhard function in this case (when the mass of outgoing particle is different and hyperons are not Pauli blocked) can be computed analytically and is reported in Appendix C. This amounts to rewriting the hole SF as

$$\bar{S}_h^{\rm LFG}(E,\vec{p}) = \int d^3r\frac{\rho(r)}{2}\frac{6\pi^2}{p_F^3(r)}\theta(p_F(r)-|\vec{p}|)\delta(E+M-\sqrt{\vec{p}^{\,2}+M^2})\,. \quad (6.14)$$

It has long been known that models based on an independent-particle description of the nuclear structure largely fail to account for the complexity of nucleon correlations in nuclei. Here we improved the model of Ref. [30] by considering two different realistic hole SFs: a semi-phenomenological LDA SF (see Sec. 3.2), and CBF SF (see Sec. 3.3.1).

In analogy to Eq. (6.14), the LDA SF of finite nuclei is obtained through the LDA procedure. The infinite nuclear matter hole SF derived in [2], denoted by $S_h^{\rm LDA}(E,\vec{p},\rho)$, is calculated for different values of the nuclear density and integrated over the density profile of the nucleus

$$\bar{S}_h^{\rm LDA}(E,\vec{p}) = \int d^3r\frac{\rho(r)}{2}\frac{6\pi^2}{p_F^3(r)}S_h^{\rm LDA}(E,\vec{p},\rho) = 2\int d^3r S_h^{\rm LDA}(E,\vec{p},\rho)\,. \quad (6.15)$$

However, when computing the cross section, the integration over the nuclear volume is carried out for the full hadron tensor [3, 4]

$$W^{\mu\nu}_{Y,\rm LDA}(q) = \frac{\sin^2\theta_C}{2MM_Y}\int d^3r\int\frac{d^3p}{(2\pi)^3}\int dE\,S_h^{\rm LDA}(E,\vec{p},\rho) \times\frac{M}{E_p}\frac{M_Y}{E^Y_{p+q}}\delta(E+M+q^0-E^Y_{p+q}(\rho))A_Y^{\mu\nu}(p,q)\,. \quad (6.16)$$

For the CBF SF model we make use of the hadron tensor given in Eq. (6.13) with $\bar{S}_h^{\rm CBF}(E,\vec{p})$ normalized to the number of active nucleons.

6.3.1 Final state interaction for hyperons

The hole SF accounts for the complexity of nuclear interactions pertaining to the nucleon in the initial nuclear target. However, in the kinematical region in which the interactions between the struck particle and the spectator system cannot be neglected, the IA results have to be corrected. Here the interactions between the outgoing hyperon and the $A-1$ nucleons are described simply employing a phenomenological MF potential, to modify the hyperon energy spectrum as $\tilde{E}^Y_{p+q}(\rho) = E^Y_{p+q}+V(\rho)$, where $V(\rho) = -30\rho/\rho_0\,$MeV [239], and $\rho_0 = 0.16\,\text{fm}^{-3}$, the nuclear

saturation density. Within the LDA SF, the density-dependent hyperon spectrum is included by replacing the energy conservation delta function in Eq. (6.16) by $\delta(E+M+q^0-\tilde{E}^Y_{p+q}(\rho))$. Nuclear modifications affecting the nucleon tensor $A_Y^{\mu\nu}$ are expected to be much smaller and have not been considered. On the other hand, within the CBF approach, we simply modify the energy-conserving δ function of Eq. (6.13) as $\delta(E+M+q^0-\bar{E}^Y_{p+q})$ with the average hyperon spectrum

$$\bar{E}^Y_{p+q} = E^Y_{p+q} + \frac{1}{A}\int d^3r\rho(r)V(\rho)\ . \tag{6.17}$$

The hyperon produced in the primary vertex travels through the nuclear environment, interacting with nucleons and exchanging momentum and possibly producing a different hyperon. Although a quantum-mechanical description of the scattering processes would be more appropriate, here we use a MC algorithm analogous to that presented in Ref. [30], using as input the available measurements of hyperon-nucleon scattering cross sections. This amounts to treating collisions in a classical fashion, as in most of the available neutrino event generators [240, 241, 242].

According to the total initial cross sections for Σ^0,Σ^- and Λ production, we select the type of hyperon produced in the primary interaction vertex. Then, for this particular hyperon, we compute the differential cross section $d\sigma/(d\Omega_{k'}dE_{k'}d^3r)$ or $d\sigma/(d\Omega_{k'}dE_{k'}d|\vec{p}\,|)$, for the LDA SF or the CBF SF cases, respectively[4]. These are the weights of the events that are taken as input in the MCC.

According to the calculated profiles, we randomly generate the charged lepton energy $E_{k'}\in[m_\ell,E_\nu]$ and scattering angle $\theta\in[0,\pi]$, together with the position $\vec{r}_1=(r_1\cos\theta_1\sin\phi_1,$ $r_1\sin\theta_1\sin\phi_1,r_1\cos\phi_1)$, in which the hyperon has been produced. (Here $r_1\in[0,r_{\rm max}]$, with $r_{\rm max}$ sufficiently large to safely take $\rho_{p(n)}(r_{max})=0$.) Since the elementary cross section obtained using the CBF SF does not depend upon r, we generate $\vec{r}_1$ according to the density profile of the nucleus. When using the LDA SF in the calculation of the cross section, we perform the integration over the initial nucleon momentum beforehand, as in Ref. [30]. In this case, we assume that the momentum of the hyperon produced at the interaction vertex is $\vec{p}_{Y_1}=\vec{q}+\vec{p}_{\rm gen}$, where $\vec{p}_{\rm gen}$ is a randomly generated three-vector below the local Fermi sea ($|\vec{p}_{\rm gen}|\leq p_F(r)$). On the other hand, the CBF SF allows one to consistently generate the momentum modulus of the struck nucleon on an event-by-event basis and to include it in the definition of $\vec{p}_{Y_1}$, choosing randomly an angle between $\vec{p}$ and $\vec{q}$ using a $]0,\pi]$ flat distribution. In both approaches, we assume that this initial hyperon is on-shell, and its energy is given by $E_{Y_1}=\sqrt{M^2_{Y_1}+\vec{p}^{\,2}_{Y_1}}$.

We simulate the hyperon propagation from the interaction vertex until it exits the nucleus by iterating the following steps [30]:

1. Assuming that the hyperon kinetic energy is significantly larger than $V(\rho)$, we propagate it by a short distance $\vec{dl}=\vec{p}_{Y_1}/E_{Y_1}dt$, dt being a small time interval, along its momentum direction. We then randomly select a nucleon from below the Fermi sea, $|\vec{p}_1|<p_F$, and compute the invariant energy $E_{\rm inv}$ of the Y_1+N_1 system. We evaluate the interaction probability per unit length for the various scattering processes permitted by charge conservation $Y_1+N_1\to Y_i+N_i$, where $Y_i=\Lambda,\Sigma^-,\Sigma^0,\Sigma^+$ and $N_i=p,n$. For a given channel i, this is given by $\mathscr{P}_i=\left[\rho_p\sigma_{[Y_1+p\to Y_i+N_i]}(E_{\rm inv})+\rho_n\sigma_{[Y_1+n\to Y_i+N_i]}(E_{\rm inv})\right]$, where the total cross sections $\sigma_{[YN\to Y'N']}(E_{\rm inv})$, extracted from the available experimental data, are compiled in the Appendix of Ref. [30]. The probability that the interaction has occurred is $\mathscr{P}=\sum_i\mathscr{P}_i dl$. Note that dt has to be small enough so that $\mathscr{P}dl\ll 1$. A random number

[4] As for the LDA SF approach, although the initial nucleon momentum is already integrated out, some effects of the hole SF are retained, and they modify the distribution profiles of the outgoing-lepton kinematics. Conversely, the CBF SF scheme enables to sample the magnitude of the momentum of the initial nucleon to be used in the cascade algorithm.

$x \in [0,1]$ is generated. If $x > \sum_i \mathscr{P}_i dl$ the interaction has taken place and we proceed to the next step; otherwise we skip it and go to step 3.

2. We select the interaction channel according to their respective probabilities (cross sections). We generate a random angle for the production of the outgoing (N_i, Y_i) pair in the center-of-mass of $N_1 + Y_1$ system. We boost back to the laboratory frame and we implement Pauli blocking by checking that the momentum of the final nucleon is larger than $p_F(r)$. If this condition is satisfied, we have a new hyperon (possibly of different type) propagating with a new direction and momentum. If not, the interaction did not occur and the hyperon properties remain unchanged.
3. The new position of the hyperon is $\vec{r}_i = \vec{r}_1 + \vec{dl}$. If no interaction has occurred, in this point of the nucleus, the three-momentum and type of hyperon correspond to those of the initial hyperon Y_1. Otherwise, they correspond to those of the outgoing hyperon Y_i after the collision.
4. If the hyperon's kinetic energy is smaller than 30 MeV, we stop the propagation and assume that the hyperon has exited the nucleus without any further interaction. We recall here that the MC code does not include the effects of the real part of the hyperon optical potentials and that straight-line trajectories are always assumed. Quantum effects, neglected in the cascade approach, are expected to become especially important at low energies.

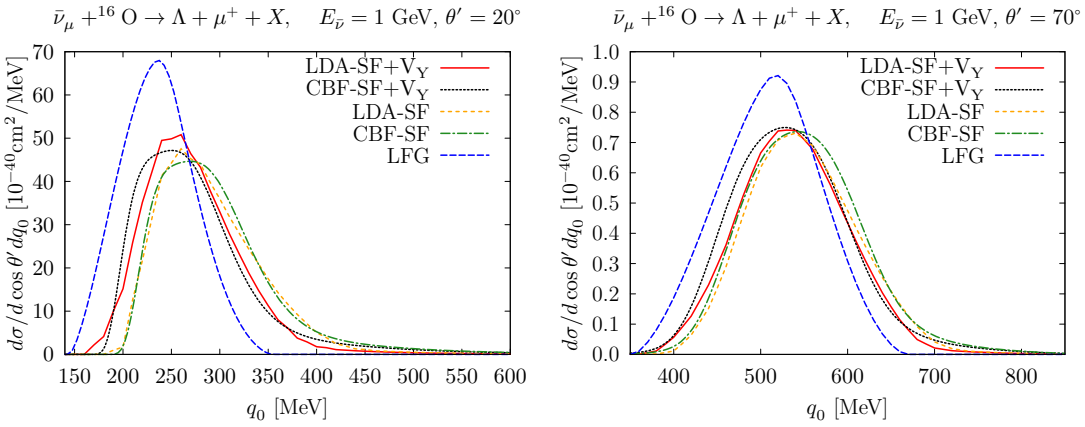

FIGURE 6.4: Differential cross section $d^2\sigma(\bar{\nu}_\mu + {}^{16}\mathrm{O} \to \Lambda + \mu^+ + X)/(d\cos\theta' dq^0)$ for $E_{\bar{\nu}} = 1$ GeV and two fixed antimuon scattering angles, $\theta = 20^\circ$ and $\theta = 70^\circ$, showed in the top and bottom panels, respectively. The blue dashed, green dot-dashed and orange short dashed lines correspond to the LFG, CBF SF and LDA SF calculations, respectively. The red solid and black dotted curves stand for the LDA SF and CBF SF cross sections, when a MF potential is included in the energy spectrum of the hyperon. All the results have been obtained without employing the MCC.

6.4 Results

6.4.1 Strange hyperon production

Let us first focus on the role played by the SFs in the description of the hyperons production. The double-differential cross section $d^2\sigma/(d\cos\theta dq^0)$ of the process $\bar{\nu}_\mu + {}^{16}\mathrm{O} \to \Lambda + \mu^+ + X$ is shown in Fig. 6.4 for different models of the hole SF, and two fixed outgoing lepton scattering angles. Note that the MCC has not been employed to obtain these results. We observe an overall good agreement between the LDA SF and the CBF SF results. As expected, in both cases the

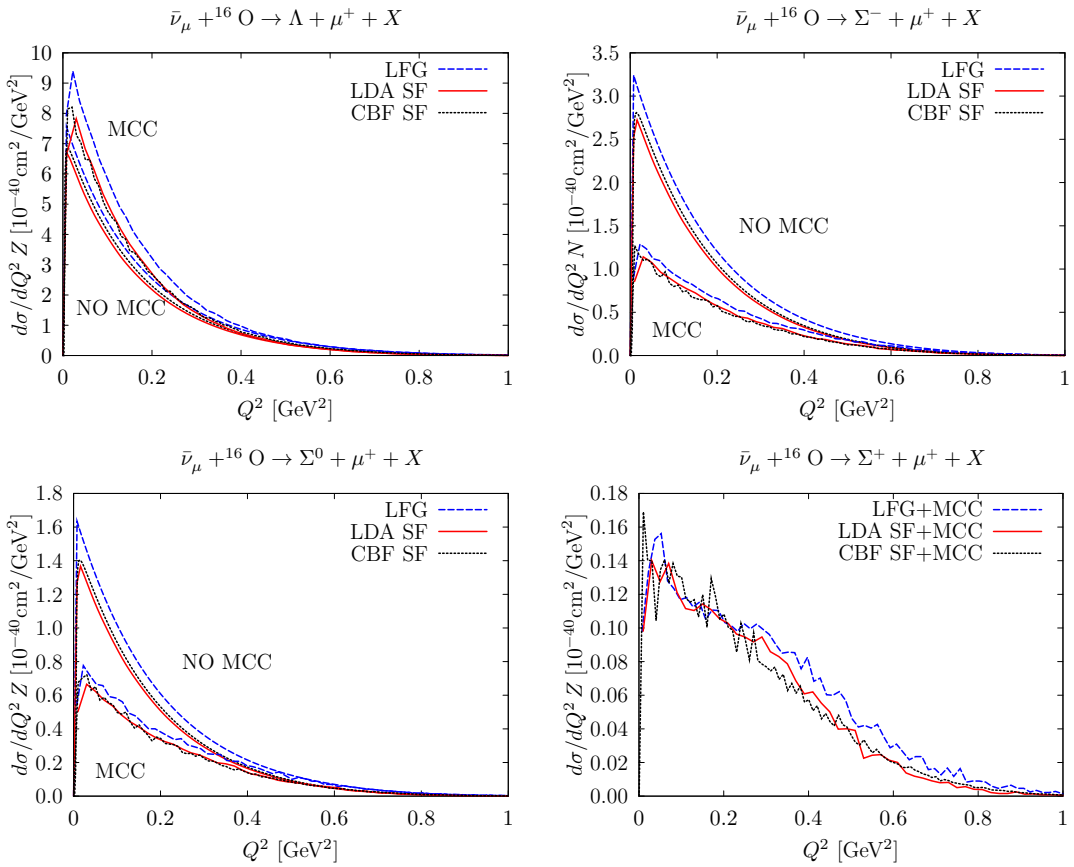

FIGURE 6.5: $d\sigma/dQ^2$ cross sections, per number of target protons or neutrons, for Λ, Σ^-, Σ^0, and Σ^+ production in oxygen and $E_{\bar{\nu}} = 1$ GeV. For each type of hyperon, we show results from the LFG, CBF SF and LDA SF approaches, which are depicted as blue dashed, black dotted and red solid lines, respectively. The MCC and NO MCC labels denote whether the nuclear cascade algorithm has been applied or not.

hyperon MF potential produces a shift of ~ 30 MeV in the position of the QE peak, also leading to an enhancement of its height. The LFG calculations, represented by the blue dashed lines, have been carried out assuming a free energy spectrum for both the initial nucleon and the hyperon, as in Ref. [30]. The comparison with the other curves, in which a more realistic description of the nuclear dynamics is adopted, reveals that nuclear correlations sizably affect the inclusive cross sections. In particular, nuclear correlations in the initial state reduced the height of the QE peak, redistributing the strength to the higher energy-transfer. These effects are more apparent for $\theta = 20^\circ$ than for $\theta = 70^\circ$, being the cross section much bigger (between one to two orders of magnitude) for the lower scattering angle. The q^0 values relevant for the QE cross section increase with θ', and thus one should expect the largest cross sections for relatively small outgoing lepton scattering angles, where the effects of initial-state nuclear correlations are more important.

The differential cross sections, $d\sigma/dQ^2$, for $\Lambda, \Sigma^-, \Sigma^0$ and Σ^+ production from oxygen are shown in Fig. 6.5, for an incoming muon antineutrino energy of 1 GeV and the LFG, LDA SF and CBF SF approaches. We compare the results obtained either applying or not applying the MCC, the corresponding curve labeled as "MCC", or "NO MCC", respectively. Nucleon-nucleon correlations, encoded in the realistic hole SFs, quench the cross sections in all the hyperon-production channels. However, their impact is far less dramatic than for the double-differential cross sections of Fig. 6.4. Considerably more relevant are the effects of the MCC. They strongly modify the initial calculation leading to a non-zero Σ^+ cross section, to a sizable

enhancement of the Λ production and to a drastic reduction – more than 50% – of the Σ^0 and Σ^- distributions. This can be qualitatively understood by analyzing the kinematics of these processes. While traveling through the nucleus, the hyperons dissipate their kinetic energy in the scattering processes. The Σ hyperons are heavier than the Λ baryon, hence their production in the nuclear cascade is generally suppressed. In particular, for low energies the $\Lambda \to \Sigma$ process is kinematically forbidden. Therefore, for low-energy hyperons, the $\Sigma \to \Lambda$ processes dominate. On the other hand, Σ^+ hyperons can be produced only in secondary collisions.

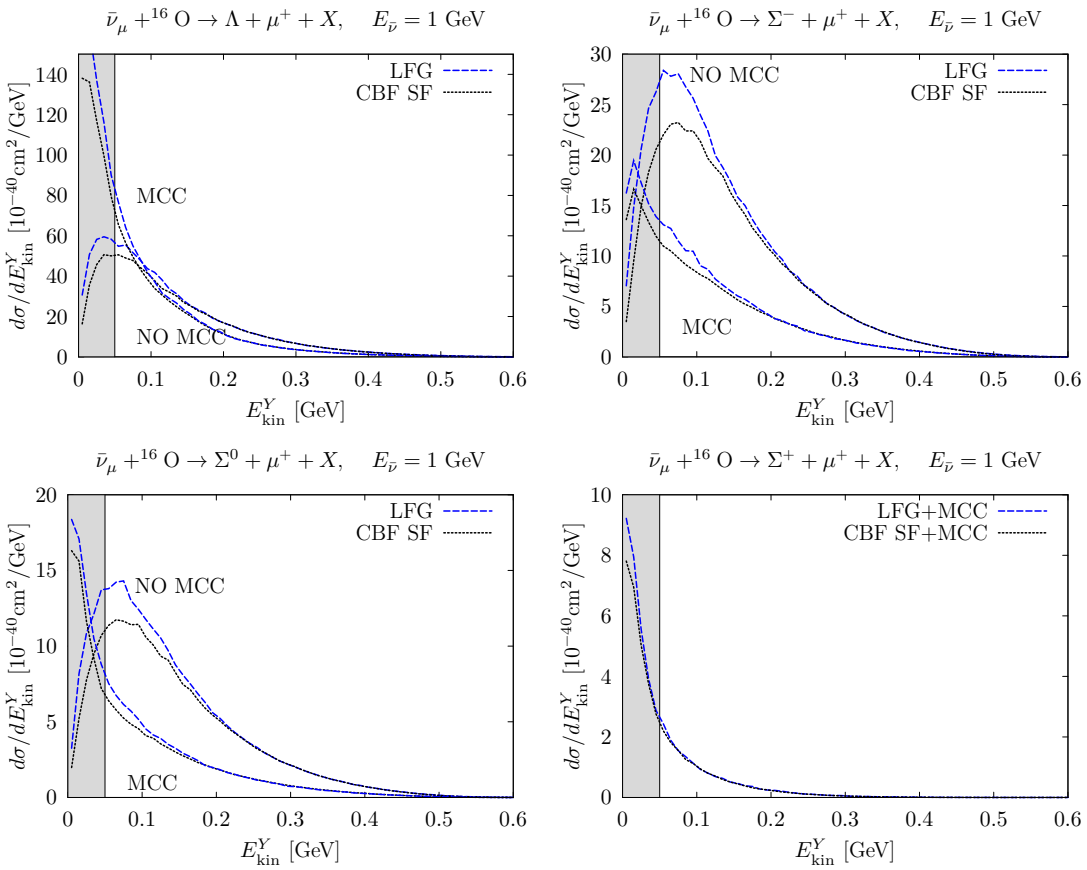

FIGURE 6.6: Hyperon kinetic energy distributions, $d\sigma/dE^Y_{\mathrm{kin}}$, for Λ, Σ^-, Σ^0, and Σ^+ production in oxygen and $E_{\bar{\nu}} = 1$ GeV. The different curves correspond to the LFG and CBF SF predictions, with and without the inclusion of MCC effects. The MF potential corrections to the energy spectrum of the hyperon have not been included. The shaded areas correspond to $E^Y_{\mathrm{kin}} \leq 50$ MeV.

In Fig. 6.6, we display the Λ and Σ hyperon kinetic-energy distributions obtained using the LFG and the CBF SF models. Similar results can be obtained using the LDA SF. For a more direct comparison with Ref. [30], we have not included the hyperon MF potential. Although its effects are not negligible in the double-differential distributions displayed in Fig. 6.4, they become very small in the single-differential and totally-integrated cross sections of Figs. 6.5, 6.6 and 6.7. In the MCC, we used a threshold energy cut of 30 MeV for QE collisions. The shaded areas in Fig. 6.6 correspond to $E^Y_{\mathrm{kin}} \leq 50$ MeV; for such low values of the hyperon kinetic energy the details of the energy spectrum are not meaningful, although the integrals underneath the curves provide estimates of the total number of low-energy hyperons that are produced. In analogy with Fig. 6.5, the inclusion of the MCC leads to sizable modifications of the initial differential cross sections. The Λ channel is sizably enhanced at low E^Y_{kin} and depleted above 100 MeV. The Σ^- and Σ^0 cross sections are strongly quenched, except for very low E^Y_{kin} in the Σ^0 channel. Note, however, that our results are not much reliable in this region. Lastly, the Σ^+ production becomes nonvanishing because of the secondary collisions accounted for the MCC.

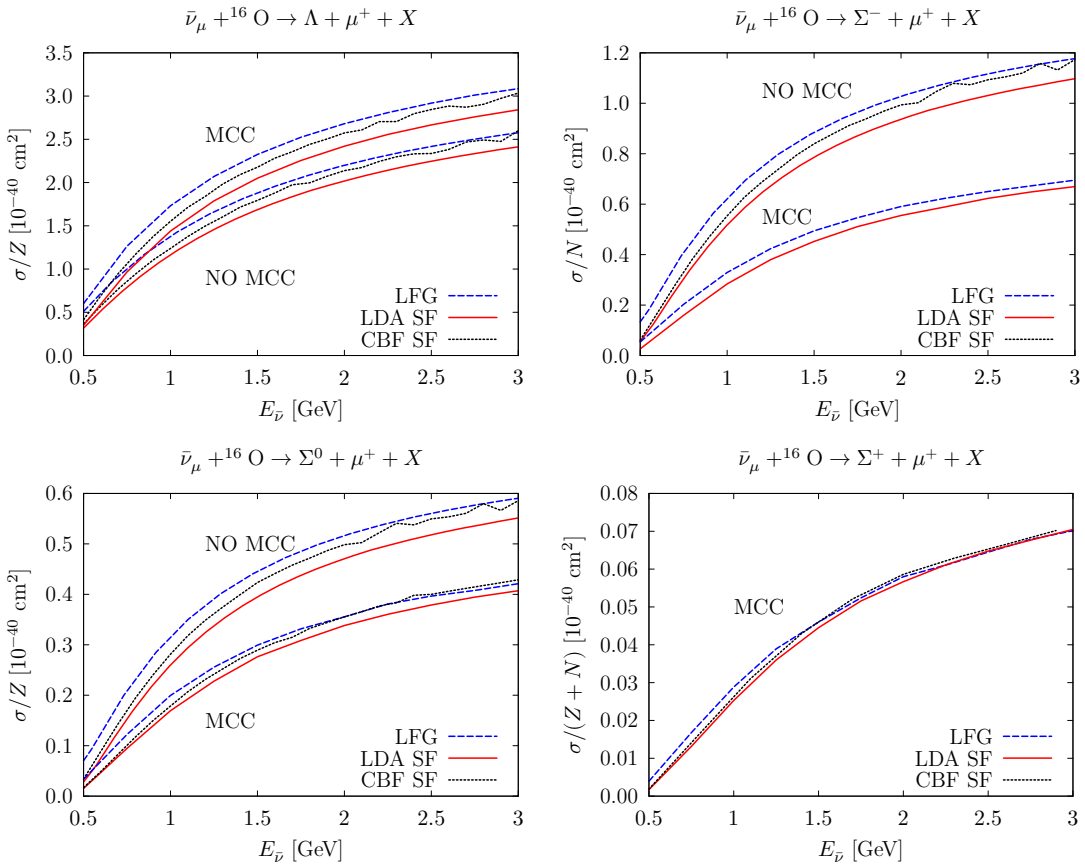

FIGURE 6.7: Total cross sections for Λ, Σ^-, Σ^0 and Σ^+ production on ^{16}O per active nucleon, as a function of the energy of the incoming $\bar{\nu}_\mu$. As for the Λ, Σ^-, and Σ^0 hyperons, we show results obtained with and without the MCC, while the Σ^+ hyperon can only be produced through secondary collisions.

The LFG distributions displayed in Fig. 6.6 should be directly comparable to those shown in the left panels of Fig. 3 of Ref. [30]. While the NO MCC results nicely agree, we see that the effects of the MCC computed in this latter reference turn out to be much smaller and not as visible as those found in the present calculation. We have verified that this discrepancy has to be ascribed to a wrong implementation in Ref. [30] of the Pauli blocking of the outgoing nucleons produced in secondary collisions, leading to an important reduction of the number of interactions experienced by the knocked-out hyperons.

In Fig. 6.7 we show the total cross sections for Λ, Σ^-, Σ^0 and Σ^+ production on oxygen. Consistently with the results of Fig. 6.5, there are small deviations among the curves referring to LDA SF and CBF SF results, which in general agree reasonably well. On the other hand, the application of the MCC noticeably modifies the theoretical predictions for all the hyperon channels; these effects being larger than those associated to the use of realistic hole SFs in place of the LFG model for the initial nuclear state. In absence of the MCC, the production rates of Σ^- and Σ^0 are related by a SU(3) rotation. The associated Clebsh-Gordan coefficient, $\sqrt{2}$, leads to twice as large cross section for Σ^- as for Σ^0. However, the corrections induced by the MCC alter this relation, and the reduction of the Σ^- is about 20% stronger than for Σ^0.

It is interesting to understand how the role played by the MCC depends upon the size of the nucleus. In this regard, in Fig. 6.8 we compare the total cross sections for Λ and Σ^- production on ^{12}C, ^{16}O and ^{40}Ca, obtained using the LDA SF. To make the comparison more transparent, for each nucleus we divided the total cross section by the corresponding number of active nucleons. While the ^{16}O and ^{12}C results are almost indistinguishable, there is around 10% difference with those obtained for ^{40}Ca. This is likely to be ascribed to the longer path that

the hyperons have to travel before exiting the nucleus, implying a larger number of re-scattering processes.

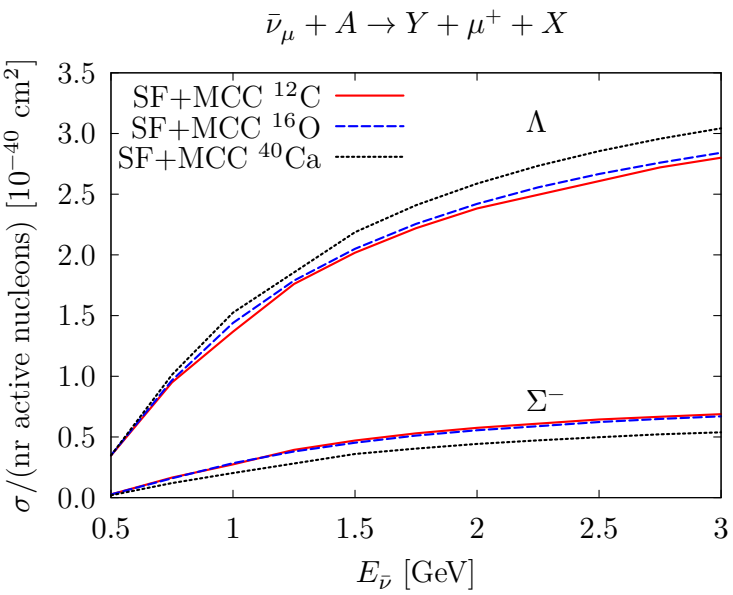

FIGURE 6.8: Total Σ^- and Λ production cross sections in ^{12}C, ^{16}O and ^{40}Ca, as a function of the antineutrino energy. The results are obtained using the LDA SF to model the initial nuclear state and the hyperon secondary collisions are accounted for through the MCC. The three lower (upper) curves correspond to the Σ^- (Λ) production.

6.4.2 Λ_c production

In this subsection, we discuss the results obtained for the $\nu_\mu + ^{16}\text{O} \to \mu^- + \Lambda_c + X$ cross section using the different parametrizations of the $n \to \Lambda_c$ form factors introduced in Sec. 6.2. Our aim is to estimate how the large theoretical uncertainties of these form factors in the free space affect the predictions for the cross section of the Λ_c production in nuclei. For simplicity, in this analysis, nuclear dynamical correlations in the initial state and hyperon FSI have been neglected altogether. Hence, we employ a simple LFG model to describe the initial nuclear target, we assume a free energy spectrum for the struck particle, and we do not employ the MCC. As for the latter, it has to be mentioned that there is no available experimental information on the Λ_c mean free path in a nuclear environment, and the theoretical predictions for the interactions of the Λ_c with nucleons and other charmed baryons suffer from severe uncertainties.

The energy distributions of the incoming neutrino fluxes of MINERvA [243] and DUNE [58] experiments peak at $E_\nu \simeq 3$ GeV and $E_\nu \simeq 5$ GeV, respectively. In Fig. 6.9 we present the differential cross section $d\sigma/dq^2$ for the $\nu_\mu + ^{16}\text{O} \to \mu^- + \Lambda_c + X$ reaction, computed employing the RCQM form factors of Ref. [33], for incoming neutrino energies of up to 5 GeV. The maximum values of Q^2 reached in the production mechanism are 1.5 GeV^2 and 5 GeV^2, for $E_\nu = 3$ GeV and $E_\nu = 5$ GeV, respectively. However, the bulk of to the total cross section stems for Q^2 below 0.5 GeV^2 and 2 GeV^2, for neutrino energies corresponding to the peaks of the MINERvA and DUNE fluxes, respectively. These relatively low values of Q^2 justify the use of form factors fitted to the $\Lambda_c \to \Lambda$ semileptonic decay, corresponding to $Q^2 \in [-1.36, 0]$ GeV^2. However, extrapolating the form factors to moderately large positive Q^2 augment the theoretical uncertainty in our cross-section predictions. To estimate them, we have considered the five sets of form factors reviewed in Sec. 6.2, characterized by the different q^2 dependencies displayed in Fig. 6.1.

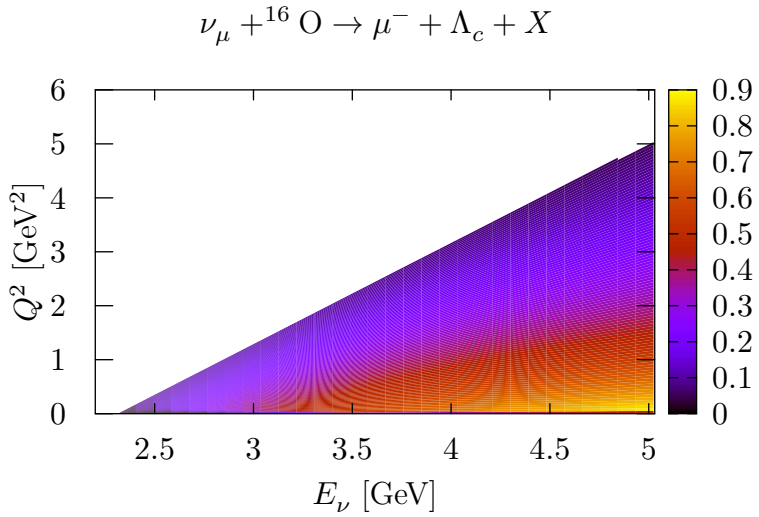

FIGURE 6.9: Differential cross section $d\sigma(\nu_\mu + {}^{16}\mathrm{O} \to \mu^- + \Lambda_c^+ + X)/dq^2$ [10^{-40}cm^{2}GeV^{-2}] per nucleon as a function of E_ν. The results are obtained within the LFG model for the initial nuclear state and assuming a free Λ_c propagation in the final state. The weak-transition form factors are taken from the RCQM of Ref. [33] and are extrapolated to the $Q^2 > 0$ region.

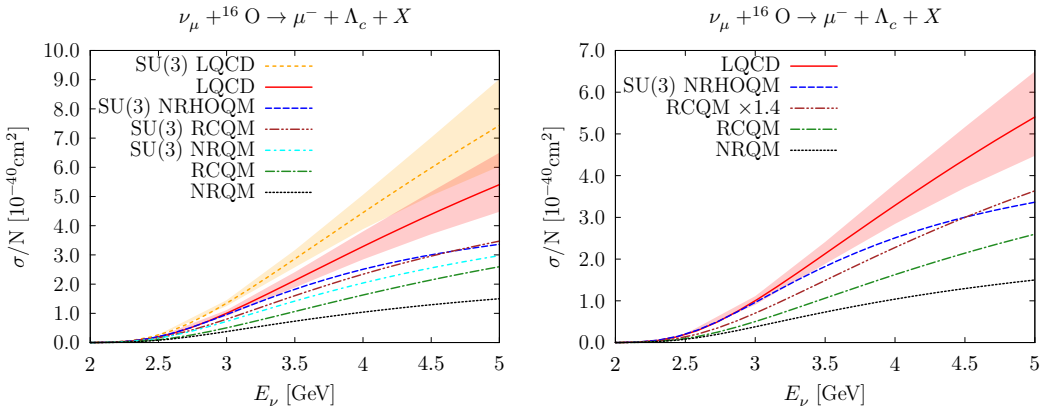

FIGURE 6.10: Total cross section, per number of neutrons, for the $\nu_\mu + {}^{16}\mathrm{O} \to \mu^- + \Lambda_c^+ + X$ reaction, as a function of the incoming neutrino energy. The LFG model for the initial nuclear state is adopted and no FSI for the Λ_c are accounted for. In the left panel the curves represent the set of weak transition form factors analyzed in the text: LQCD [31, 222], NRHOQM [35], NRQM [32], and RCQM [33, 34]. The curves labeled as SU(3) represent the results attained multiplying the $\Lambda_c \to \Lambda$ form factors by the appropriate Clebsh-Gordan coefficient. The 68% CL bands for the LQCD predictions are obtained from the Gaussian covariance matrices of Refs. [222, 31]. In the right panel, we display results corresponding to the direct calculations of the $\Lambda_c \to N$ form factors, the only exception being the SU(3) NRHOQM predictions for which they are not available. The "RCQM $\times 1.4$" curve represents the results of Ref. [33] rescaled by a factor 1.4, as inferred from the discussion on the $\Lambda_c \to \Lambda e^+ \nu_e$ reported in Sec. 6.2.

As for the LQCD [31], the RCQM [33], and NRQM [32] approaches[5], in addition to the $\Lambda_c \to N$ form factors, we have also used those associated to the $\Lambda_c \to \Lambda$ transition, assuming unbroken SU(3) symmetry, and multiplying the matrix element by the appropriate Clebsh-Gordan coefficient ($\sqrt{3/2}$). When employing the latter form factors, the predicted $\nu_\mu + {}^{16}\mathrm{O} \to \mu^- + \Lambda_c + X$ cross sections turn out to be around $10 - 30\%$ higher than those

[5]For the sake of clarity, we will not report results for the MBM model, as it does not add relevant information to our analysis. However, we include this model in the discussion of the $\Lambda_c \to \Lambda$ form factors carried out in Sec. 6.2.

obtained from the direct weak $N \to \Lambda_c$ matrix element – see the left panel of Fig. 6.10 – the smallest differences corresponding to the LQCD form factors. As for the NRHOQM of Ref. [35], the results of Fig. 6.10 have been obtained from the $\Lambda_c \to \Lambda$ form factors assuming SU(3) symmetry, although it might well be that this procedure overestimates the cross section. The 68% CL uncertainty bands pertaining to the LQCD predictions are propagated from the errors and the covariance matrices of the fit parameters listed in Refs. [222, 31]. These theoretical uncertainties grow with the neutrino energy, and become as large as $\sim 20\%$ for $E_\nu = 5$ GeV.

There are sizable discrepancies in the $\nu_\mu + {}^{16}\mathrm{O} \to \mu^- + \Lambda_c + X$ cross sections corresponding to the various form factors, despite that all of them are constrained by the experimental $\Lambda_c \to \Lambda e^+ \nu_e$ decay width. The reason for this behavior is twofold. On the one side, the form factors exhibit major differences in their Q^2 dependence. For instance, those from the NRHOQM [35] are suppressed with increasing Q^2, leading to reduced cross sections, when compared to other approaches – see the detailed discussion of Figs. 6.2 and 6.3 in Sec. 6.2. On the other side, the relative importance of the vector and axial terms of the current to the decay width turns out to be strongly model dependent. The vector contribution amounts to only $\sim 10\%$ of the total $\Lambda_c \to \Lambda$ semileptonic width for the NRQM, it becomes around 30% for the NRHOQM and RCQM, and it is about $\sim 34\%$ in the case of the LQCD approach. The vector form factors, f_1 in particular, play a more important role in the determination of the Λ_c neutrino-production cross section. Hence, it is not surprising that NRQM model, predicting a relatively small vector form factors, leads to the lowest cross section estimates.

In the right panel of Fig. 6.10, we display the cross sections corresponding to the direct calculations of the $\Lambda_c \to N$ form factors within the different approaches. The NRHOQM predictions, for which this option is not available, are rescaled assuming SU(3) symmetry. We also, show the results of RCQM of Ref. [33], rescaled by a factor 1.4, as inferred from the discussion on the $\Lambda_c \to \Lambda e^+ \nu_e$ total and differential widths carried out and represented in Fig. 6.2 of the Sec. 6.2. This factor amounts for the difference in the total semileptonic decay width between the RCQM and the LQCD predictions reported in Refs. [34] and [222], respectively. Note that both approaches provide similar Q^2 dependencies of the leading form factors, f_1 and g_1, not only in the semileptonic decay phase-space, but also for the positive Q^2-values, relevant for the neutrino-production reaction – see the discussions of Figs. 6.1 and 6.3.

The total $\nu_\mu + {}^{16}\mathrm{O} \to \mu^- + \Lambda_c + X$ cross section can be reasonably estimated to lie between the LQCD and the rescaled RCQM predictions. This range also accommodates the SU(3) NRHOQM results, and it leads to theoretical uncertainties below 30% up to $E_\nu \sim 3.5$ GeV. For neutrino energies corresponding to the peaks of the MINERvA and DUNE fluxes, we thus estimate the total cross sections to be $\sigma(E_\nu = 3\,\mathrm{GeV})/N = (0.9^{+0.2}_{-0.1}) \times 10^{-40}\mathrm{cm}^2$ and $\sigma(E_\nu = 5\,\mathrm{GeV})/N = (4.5^{+2.0}_{-0.9}) \times 10^{-40}\mathrm{cm}^2$, respectively. The central value is the average between the LQCD and the rescaled RCQM results, while the errors account for the difference of these two sets of results, taking into account the upper limit of the LQCD uncertainty band. Taking a somewhat less conservative perspective, if the LQCD predictions are assumed to be sufficiently reliable, the corresponding estimates for the cross sections can be readily inferred the plots. Nevertheless, one should also bear in mind that Λ_c FSI effects have not been considered in this preliminary analysis. Although their role is expected to be less relevant than for strange hyperons, they will have some impact in the production rate of Λ_c baryons.

Chapter 7

Polarization effects in quasielastic ν_τ scattering

In the neutrino studies, the ν_τ is experimentally the least explored one among the three neutrino flavours. Its measurement is demanding since the τ lepton, being the product of the ν_τ CC interaction with matter, decays rapidly making its clear identification very challenging. There are very few ν_τ (high energetic) events recorded. They were detected via CC interaction in OPERA [244] and DONuT [245] experiments. In the near future the SHiP facility [246] will start operating, with the ability of measuring the cross sections of ν_τ and $\bar{\nu}_\tau$ with statistics 100 times larger than the DONuT experiment.

One of the advantages of exploring ν_τ and $\bar{\nu}_\tau$ CC interactions is the fact that for a wide range of energies, the outgoing τ is not fully polarized. Each of the τ^- and τ^+ polarization components (longitudinal and transverse ones) is sensitive to different combinations of the nuclear structure functions, making them interesting observables to further explore the differences between various nuclear models. They convey richer information, which is complementary to the knowledge obtained by means of the cross-section predictions. In the limit of high energies $E_\nu \gg m_\tau$, though, the outgoing τ leptons are produced in totally polarized states. Thus, the interesting energy region to be explored is limited to the values of $E_\nu \lesssim 10$ GeV. This relatively moderate energy range can be studied by oscillation experiments, although the measurement is demanding because of the low statistics. From this perspective, the information about the final τ lepton polarization could be helpful because its spin direction affects the angular distribution of the decay products.

We will focus on the QE region in which the single nucleon knock-out is the dominant reaction mechanism. Previous works on ν_τ and $\bar{\nu}_\tau$ scattering have considered the nucleus as an ensemble of free nucleons [247], or used the RPA, and an effective nucleon mass to describe the initial nuclear state [36]. The use of an effective mass for the nucleon is a simplified method to account for the effects due to the change of its dispersion relation inside of a nuclear medium. A proper description, however, is achieved by dressing the nucleon propagators and constructing realistic particle and hole SFs, which incorporate dynamical effects that depend on both the energy and momentum of the nucleons [4]. There was an attempt to include the SF formalism in the study of the polarization of the outgoing lepton produced in CC (anti-)neutrino-nucleus reactions [248]. However, because of the nonrelativistic nature of the nuclear calculations carried out in that study, the predictions were restricted to a very narrow region of the available phase space. Here we perform an analysis which does not suffer from the above-mentioned problem, and we use realistic hole SFs to obtain the $\tau-$polarization vector in the whole available phase-space for neutrino energies below 10 GeV. Moreover, to gauge the model-dependence of the predictions, we perform the calculation using spectral functions obtained within two theoretically different frameworks: a semi-phenomenological one (LDA SF) based on the findings of Ref. [2], and a second one [29, 27] obtained within the CBF theory [249]. Both sets of SFs provide a realistic description of the dynamics including NN correlations in the initial target and in the nuclear remnant. Moreover, combined with a factorization scheme, they have been

successfully used for modeling inclusive electro– and (anti)neutrino–nuclear QE responses [6, 3, 113, 4, 150, 15, 16, 17, 18, 144, 63, 19].

Finally, we would also like to mention that the inclusion of RPA correlations does not change appreciably the gross features of the polarization of the τ's. The reason is that the polarization components are obtained as a ratio between linear combinations of nuclear structure functions and the RPA changes similarly numerator and denominator. In addition, one should bear in mind that RPA corrections take into account the absorption of the gauge boson, mediator of the interaction, by the nucleus as a whole instead of by an individual nucleon, and their importance decreases as the gauge boson wave-length becomes much shorter than the nuclear size. Thus, RPA effects on the polarization observables become little relevant, even for the total or partially integrated cross sections [79, 4], for a great part of the phase-space accessible in the CC reaction [36, 248].

This chapter, based on Ref. [250], is organized as follows. In Sec. 7.1 we introduce the formalism and the basic concepts: polarization vector, its longitudinal and transverse components. In Sec. 7.2, in the first place, we define the phase space to be explored in our analysis, and then perform a comparison of the results obtained using two realistic SF models and the more approximate GFG approach. In Appendix E we collect some kinematical relations for weak charged lepton production off nucleons.

7.1 Lepton polarized CC cross section

We will investigate CC (anti-)neutrino–nucleus reactions

$$\nu_\ell / \bar{\nu}_\ell(k) + A \to \ell^{\mp}(k') + X, \quad \ell = e, \mu, \tau \tag{7.1}$$

With the axis of quantization in the rest frame [$k'^\mu = (m_\ell, \vec{0}\,)$] of the outgoing $\ell^{\mp}$ specified by the unit vector $\hat{n}$, we define in this frame a unit space-like four-vector s^μ as

$$s^\mu = (0, \hat{n}). \tag{7.2}$$

From the invariance of scalar products, it follows that in any other frame,

$$s^\mu = \left(\frac{\vec{k}' \cdot \hat{n}}{m_\ell}, \hat{n} + \frac{\vec{k}'}{m_\ell} \frac{(\vec{k}' \cdot \hat{n})}{E_{k'} + m_\ell} \right), \qquad s^2 = -1, \qquad s \cdot k' = 0 \tag{7.3}$$

The spin-projection operators are then given by [251]

$$\Pi(s;h) = \frac{1}{2} \left(1 + h \gamma_5 \not{s} \right), \qquad h = \pm 1, \tag{7.4}$$

and commute with the energy projection operators $(\pm \not{k}' + m_\ell)/2m_\ell$.

The (anti)neutrino inclusive-differential cross section for a $(s;h)-$polarized outgoing lepton is given by (we follow the conventions of Ref. [3]):

$$\left. \frac{d^2\sigma^{(\nu_\ell, \bar{\nu}_\ell)}}{d\Omega_{k'} dE_{k'}} \right|_{s;h} = \left(\frac{G_F}{2\pi} \right)^2 \frac{|\vec{k}'|}{|\vec{k}|} L_{\mu\nu}^{(\nu_\ell, \bar{\nu}_\ell)}(s;h) W^{\mu\nu}_{(\nu_\ell, \bar{\nu}_\ell)} \tag{7.5}$$

in the laboratory (LAB) frame (nucleus at rest). $L_{\mu\nu}(s;h)$ is a polarized lepton tensor:

$$L^{(\nu_\ell,\bar{\nu}_\ell)}_{\mu\nu}(s;h) = \frac{1}{8}\mathrm{Tr}\left[\not{k}'\gamma^\mu \not{k}(1+\eta\gamma_5)\gamma^\nu\right] - \eta h\frac{m_\ell}{8}\mathrm{Tr}\left[\gamma^\mu \not{k}(1+\eta\gamma_5)\gamma^\nu \not{s}\right]$$

$$= \frac{L^{(\nu_\ell,\bar{\nu}_\ell)}_{\mu\nu}}{2} - \eta h\frac{m_\ell}{2}s^\alpha\left(k_\mu g_{\nu\alpha} + k_\nu g_{\mu\alpha} - k_\alpha g_{\mu\nu} + i\eta\varepsilon_{\mu\nu\alpha\beta}k^\beta\right), \tag{7.6}$$

where $\eta = \pm$ for the neutrino and antineutrino induced reactions, respectively, and $L_{\mu\nu}$ the unpolarized lepton tensor of Eq. (2.19).

From Eqs. (7.5) and (7.6), one readily finds,

$$\left.\frac{d^2\sigma^{(\nu_\ell,\bar{\nu}_\ell)}}{d\Omega_{k'}dE_{k'}}\right|_{s;h} = \frac{1}{2}\Sigma_0^{(\nu_\ell,\bar{\nu}_\ell)}\left(1 + h s_\alpha \mathscr{P}^\alpha_{(\ell^-,\ell^+)}\right) \tag{7.7}$$

$$\Sigma_0^{(\nu_\ell,\bar{\nu}_\ell)} = \frac{|\vec{k}'|\,G_F^2 M_i}{2\pi^2}F^{(\nu_\ell,\bar{\nu}_\ell)} \tag{7.8}$$

where Σ_0 is the LAB double differential cross section corresponding to unpolarized leptons and $\mathscr{P}^\mu$ is the polarization vector. The term F depends on the kinematics of the leptons and on five out of the six structure functions, W_i, that define the hadronic tensor, see Eq. (2.65), which are different for $\nu/\bar{\nu}$ case. The neutrino and antineutrino W_3 contributions to F have opposite signs, and besides of that, one should take into account that in the QE-regime, the knocked nucleon is a proton (neutron) in the case of the antineutrino (neutrino) reaction.

The polarization vector $\mathscr{P}^\alpha$ of the outgoing $\ell^\mp$ lepton is determined by the nuclear response,

$$\mathscr{P}^{(\ell^-,\ell^+)}_\alpha = -\eta m_\ell \frac{\left(k_\mu g_{\nu\alpha} + k_\nu g_{\mu\alpha} - k_\alpha g_{\mu\nu} + i\eta\varepsilon_{\mu\nu\alpha\beta}k^\beta\right)W^{\mu\nu}_{(\nu_\ell,\bar{\nu}_\ell)}}{\left[L_{\mu\nu}W^{\mu\nu}\right]_{(\nu_\ell,\bar{\nu}_\ell)}}, \tag{7.9}$$

which can be decomposed as follows

$$\mathscr{P}^\alpha_{(\ell^-,\ell^+)} = -\left(P_L n_l^\alpha + P_T n_t^\alpha + P_{TT} n_{tt}^\alpha\right)\big|_{(\ell^-,\ell^+)} \tag{7.10}$$

where the three four-vectors n_l, n_t and n_{tt} are given by

$$n_l^\alpha = \left(\frac{|\vec{k}'|}{m_\ell}, \frac{E_{k'}\vec{k}'}{m_\ell|\vec{k}'|}\right), \qquad n_t^\alpha = \left(0, \frac{(\vec{k}\times\vec{k}')\times\vec{k}'}{|(\vec{k}\times\vec{k}')\times\vec{k}'|}\right), \qquad n_{tt}^\alpha = \left(0, \frac{\vec{k}\times\vec{k}'}{|\vec{k}\times\vec{k}'|}\right) \tag{7.11}$$

We have ignored the projection of $\mathscr{P}^\alpha$ onto the direction of the four vector k'^α, because it is irrelevant for the $(s;h)-$polarized differential cross section since $s\cdot k' = 0$. In addition, $\mathscr{P}\cdot n_{tt} = 0$ and therefore $P_{TT} = 0$, which means that the polarization three-vector lies in the lepton-scattering plane (see Fig.1 of Ref. [248]). Note that under parity, $\mathscr{P}^\alpha$ transforms as

$$\mathscr{P}^\alpha \to \mathscr{P}_\alpha \tag{7.12}$$

which automatically requires $P_{TT} = 0$, since n_{tt}^α stays invariant under a parity transformation. (Time reversal invariance can be also used to show that $P_{TT} = 0$). In addition, it is obvious that $\mathscr{P}^2$, called the degree of polarization [247],

$$-\mathscr{P}^2_{(\ell^-,\ell^+)} = \left(P_L^2 + P_T^2\right)\big|_{(\ell^-,\ell^+)} \tag{7.13}$$

is a Lorentz scalar, as $P_{L,T}$ also are, since they can be computed taking scalar products, *i.e.*, $P_{L,T} = -(\mathscr{P}\cdot n_{l,t})$. From the polarized double differential cross section of Eq. (7.7), we obtain

these longitudinal and perpendicular components of the outgoing lepton polarization vector as follows

$$P_{L,T}^{(\ell^-,\ell^+)} = \frac{\frac{d^2\sigma^{(\nu_\ell,\bar{\nu}_\ell)}}{d\Omega_{k'}dE_{k'}}\Big|_{n_{l,t}}^{h=+} - \frac{d^2\sigma^{(\nu_\ell,\bar{\nu}_\ell)}}{d\Omega_{k'}dE_{k'}}\Big|_{n_{l,t}}^{h=-}}{\frac{d^2\sigma^{(\nu_\ell,\bar{\nu}_\ell)}}{d\Omega_{k'}dE_{k'}}\Big|_{n_{l,t}}^{h=+} + \frac{d^2\sigma^{(\nu_\ell,\bar{\nu}_\ell)}}{d\Omega_{k'}dE_{k'}}\Big|_{n_{l,t}}^{h=-}}$$

$$= \frac{1}{\Sigma_0^{(\nu_\ell,\bar{\nu}_\ell)}} \left\{ \frac{d^2\sigma^{(\nu_\ell,\bar{\nu}_\ell)}}{d\Omega_{k'}dE_{k'}}\Big|_{n_{l,t}}^{h=+} - \frac{d^2\sigma^{(\nu_\ell,\bar{\nu}_\ell)}}{d\Omega_{k'}dE_{k'}}\Big|_{n_{l,t}}^{h=-} \right\} \tag{7.14}$$

By construction, it follows that $|P_{L,T}| \leq 1$. Furthermore, $(P_L^2 + P_T^2) \leq 1$, because $|\mathscr{P}^2| \leq 1$. This can be easily deduced in the outgoing lepton rest frame, considering that in this system, $|\vec{\mathscr{P}} \cdot \hat{n}| \leq 1$ for any unit vector $\hat{n}$, since for both polarizations $h = \pm$, the double differential cross section $\frac{d^2\sigma^{(\nu_\ell,\bar{\nu}_\ell)}}{d\Omega_{k'}dE_{k'}}\Big|_{\hat{n};h} \geq 0$.

The $P_{L,T}$ components depend on the lepton kinematics and on the structure functions, W_i, introduced in Eq. (2.65). Explicit expressions for these observables in the LAB system are given in Eqs. (5) and (6) of Ref. [248], which were obtained from the findings of [247]. Besides masses, they depend on the scalars $(k \cdot P)$, $(k' \cdot P)$ and q^2, which define the neutrino and outgoing lepton energies and the angle, θ, between $\vec{k}$ and $\vec{k}'$ in the LAB system.

It can be seen that for $W_3 = 0$, ℓ^+ and ℓ^- have opposite polarizations, up to some effects due to the asymmetry of the role played by protons and neutrons in the nuclear system.

The operators $(1 \pm \gamma_5 \not{n}_l)/2$, with n_l^α obtained from s^α in Eq. (7.3) using $\vec{k}'/|\vec{k}'|$ as unit vector, are helicity projectors [251], and thus, the asymmetry proposed in Eq. (7.14) for the case of P_L turns out to be the outgoing lepton helicity asymmetry. Moreover, since at high energies helicity and chirality coincide, and the latter is conserved in CC reactions, we conclude

$$\lim_{(m_\ell/|\vec{k}'|)\to 0} P_L^{\ell^-} = -1\,, \qquad \lim_{(m_\ell/|\vec{k}'|)\to 0} P_L^{\ell^+} = 1\,, \tag{7.15}$$

which follows from the negative (positive) chirality of the neutrino (antineutrino) that is inherited by the outgoing $\ell^-(\ell^+)$ produced in the CC transition. In addition, in the $(m_\ell/|\vec{k}'|) \to 0$ limit, the transverse polarization $\mathscr{P}_T$ vanishes, for both neutrino and antineutrino processes. Indeed, it is proportional to the outgoing lepton mass and to $\sin\theta$ [248, 247]. (Note that for P_L, m_ℓ in the definition of $\mathscr{P}^\alpha$ in Eq. (7.9) cancels out with the $1/m_\ell$ common factor that contains n_l^α in Eq. (7.11)). In this ultra-relativistic energy regime the whole nontrivial behaviour of the polarization components, coming from the hadron tensor, cancels out in the ratio taken in Eq. (7.9).

In the case of electron and muon CC production the cross section depends mostly on W_1, W_2 and W_3, while the contribution of the other structure functions are suppressed by the small lepton mass. Therefore, P_T takes small values close to zero, while P_L is expected to differ little from the asymptotic ∓ 1 values for neutrino or antineutrino reactions, respectively, in most of the available phase space.

QE hadron tensor

When considering the interaction of a (anti-)neutrino with a single free nucleon the hadron dynamics is determined by the nucleon tensor $A^{\mu\sigma}$, see Eq. (2.79). Let us recall that for sufficiently large values of the momentum transfer ($|\vec{q}| \gtrsim 500$ MeV) the lepton-nucleus scattering can be safely treated within the Impulse Approximation (IA). In this framework the hadron tensor of Eq. (2.64) is obtained as a convolution of the spin averaged squared amplitude of the hadron

matrix element of Eq. (2.79) and the hole SF:

$$W^{\mu\nu}(q) = \frac{\cos^2\theta_C}{4M^2}\theta(q^0)\int\frac{d^3p}{(2\pi)^3}\int dE\bar{S}_h(E,\vec{p})\frac{M}{E_p}\frac{M}{E_{p+q}} \times \theta(|\vec{p}+\vec{q}|-p_F)\delta(q^0+M+E-E_{p+q})A^{\nu\mu}(p,q)\,. \quad (7.16)$$

In our analysis we will use the GFG model and spectral functions introduced in Secs. 3.2 and 3.3.1. For the GFG the hole SF is given in Eq. (3.1) with the relativistic energy of Eq. (3.5) (here normalized to the number of active nucleons). The effective Fermi momenta p_F are determined from the analysis of electron-scattering data of Ref. [147] for different nuclear species. In this chapter, we will show results for ^{16}O, for which we take $p_F = 225$ MeV and $B = 15(11)$ MeV for $\nu_\ell(\bar{\nu}_\ell)$ induced reactions.

In the case of $S_h^{\rm LDA}(E,\vec{p},\rho)$, an additional integration over nucleus volume has to be performed in Eq. (7.16) (the exact formula is given in Eq. (3.10)). Here we will set $p^0 = E+M$, and calculate $A^{\mu\nu}(p,q)$ for an off-shell nucleon, *i.e.* we take the energy and momentum distributions from the hole spectral function $S_h^{\rm LDA}(E,\vec{p})$, changing the dispersion relation of the initial nucleon. However, there exists a little inconsistency here, since the sums over nucleons' spins in Eq. (2.79) were carried out assuming free dispersion relations for the nucleons. As we will see below, this procedure is more accurate than setting $p^0 = E_p$ in Eq. (3.10). Nevertheless, the differences are relatively small and visible only for forward scattering.

The CBF SF results which we present in this chapter have been obtained replacing in the one-body current operator $j^\mu_{cc\pm}$ of Eq. (2.79), the four momentum $q^\mu = (q^0,\vec{q})$ by $\tilde{q}^\mu = (\tilde{q}^0,\vec{q})$, such that $\tilde{q}^0 = q^0 - (E_p - M - E)$, in analogy with the prescription adopted in the GFG case. The quadrispinors entering the evaluation of the hadron tensor are those of free nucleon states. Note that this approximation leads to a violation of current conservation for the electromagnetic case. Different procedures aimed at restoring the gauge invariance have been discussed in Refs. [252, 12]. In particular, the authors of Ref. [12] argue that the violation of gauge invariance in the IA scheme is expected to become less and less important in inclusive electron scattering at large momentum transfers.

7.2 Results

The analysis carried out in Ref. [247] clearly shows that for LAB energies of the $\nu_\tau/\bar{\nu}_\tau$ beam comprised between 3.5 and 10 GeV, the QE cross section is sizable. This study was done for a scattering on a single nucleon and neglecting multi-nucleon emission; their contribution, albeit nonvanishing, would be smaller than the former one. The breakdown of the total neutrino cross section into the QE, pion production, and DIS contributions is shown in Fig. 5 of Ref. [247]. The QE mechanism is found to be dominant up to $E_\nu \sim 6$ GeV and the same observation holds true for $\bar{\nu}_\tau$ reactions.

7.2.1 QE mechanism phase space

The large mass of the τ lepton greatly limits the phase space available for the single-nucleon knockout processes, being prohibited the large LAB dispersion angles, as discussed in Appendix E. In Fig. 7.1, we analyze the phase space for different values of the incoming neutrino energy, E_ν, and of the lepton scattering angle in the LAB system (θ). We show

$$|\vec{q}|_{[E_\nu,q^0,\theta]} = \left[E_\nu^2 + (E_\nu - q^0)^2 - m_\tau^2 - 2E_\nu\sqrt{(E_\nu-q^0)^2-m_\tau^2}\cos\theta\right]^{\frac{1}{2}} \quad (7.17)$$

as a function of the energy transfer q^0, together with the QE-peak curve $|\vec{q}|_{\rm QE} = \sqrt{2Mq^0 + (q^0)^2}$ (black solid line). The shaded areas in Fig. 7.1 have been obtained by varying the outgoing lepton scattering angle from 0° to 16°, 24°, 28° and 30° for E_ν= 4, 6, 8 and 10 GeV, respectively. All the angles chosen to evaluate the upper bands are greater than $\theta_{\rm max}(E_\nu)$, introduced in the Appendix E. It corresponds to the maximum allowed LAB $\tau-$scattering angle for the weak production off a free nucleon, and its dependence on the incoming neutrino energy is given in Eq. (E.6). This limiting angle takes the approximate values of 11.4°, 20.3°, 23.6° and 25.5° for E_ν =4 , 6, 8 and 10 GeV, respectively (see also the right panel of Fig. E.1 for further details). The range of q^0 values, $[q^0_{\rm min}, q^0_{\rm max}]$, for which there exist solutions (θ) of the QE condition $|\vec{q}|_{\rm QE} = |\vec{q}|_{[E_\nu, q^0, \theta]}$ grows rapidly with E_ν. Actually at threshold, $E_\nu = m_\tau + m_\tau^2/2M \sim 3.46$ GeV, $q^0_{\rm min} = q^0_{\rm max} \sim 0.58$ GeV, and when the neutrino energy gets bigger, $q^0_{\rm min}$ and $q^0_{\rm max}$ quickly decreases and increases, tending to zero and to $E_\nu - (m_\tau^2 + M^2)/2M$, respectively. The q^0-range is shown in the left panel of Fig. E.1 of the Appendix E, up to $E_\nu = 10$ GeV.

Additionally in each panel of Fig. 7.1, the yellow curve shows $|\vec{q}|_{[E_\nu, q^0, \theta]}$ for an intermediate angle among those accounted for in the band. We see that this curve, as well as the $(\theta = 0°)-$one, intercepts twice the $|\vec{q}|_{\rm QE}-$line. This is because for any LAB $\tau-$scattering angle $\theta \leq \theta_{\rm max}(E_\nu)$, there exist two different values of the LAB $\tau-$energy that satisfies the QE condition $|\vec{q}|_{\rm QE} = |\vec{q}|_{[E_\nu, q^0, \theta]}$. Thus, we might expect the existence of two QE peaks in the nuclear differential cross section, located at different values of q^0 for fixed E_ν and θ LAB variables. This never occurs for charged muon or electron productions, except for a extremely narrow range of neutrino energies. A detailed discussion can be found in Appendix E, and in particular this nonbiunivocal correspondence between $\tau-$lepton LAB scattering angle and energy is shown in the right panel of Fig E.1.

One should bear in mind that the nuclear QE cross section is strongly suppressed when $-q^2$ is above 1 GeV, and thus its size notably decreases with q^0, since at the QE-peak, $-q^2 \approx 2Mq^0$. We see that one could only expect to obtain sizable cross sections for forward scattering angles. For instance, at $E_\nu = 10$ GeV, the energy transfer at the QE peak ranges from very low $q^0 \sim 15$ MeV for $\theta = 0°$, up to 7 GeV for $\theta = \theta_{\rm max}(E_\nu = 10\ {\rm GeV}) \sim 25.5°$. Coming back to existence of two QE peaks, the higher one will be much more suppressed, and it might not be visible in the differential distribution. For example, at $E_\nu = 4$ GeV and in the forward direction, the two peaks occur for $q^2 = -0.36$ GeV^2 ($q^0 = 0.19$ GeV) and -2.88 GeV^2 ($q^0 = 1.53$ GeV), respectively. For larger neutrino energies the $|q^2|$ value of the second QE peak grows rapidly, and its impact in the cross sections should become less important. Moreover, the results should be more sensitive to nuclear effects for small values of the scattering angle where the QE cross section is high and peaks in the low q^0 region. Hence, we have studied the impact of using the different nuclear SFs to compute the $\nu_\tau/\bar{\nu}_\tau$ differential cross section and the τ polarizations in the region of small θ.

7.2.2 Differential cross sections and polarization observables

In Fig. 7.2, we analyze the double-differential cross section (panels in the first column), P_L and P_T (panels in the second and third column, respectively) for the $\nu_\tau + {}^{16}{\rm O} \to \tau^- + X$ process at $E_\nu = 4$ GeV, and $\theta = 0°, 2°, 4°$, and 16°. The dotted (blue) and the dashed (red) and dot-dashed (black) curves have been obtained using the GFG model and the LDA and the CBF hole SFs, respectively. Predictions for $E_\nu = 6$ GeV are shown in Fig. 7.3. The comparison of the three-different sets of results for the differential cross sections clearly reveals that the inclusion of nucleon-nucleon correlations in the hole SF leads to a significant quenching of the QE peak and a shift of its position towards higher energy transfers in the dashed (LDA SF IA) and dot-dashed (CBF SF) curves with respect to the dotted one (GFG). The distinctive SF tail at high-energy-transfers, that arises when short-range correlated pairs are included in the description of the

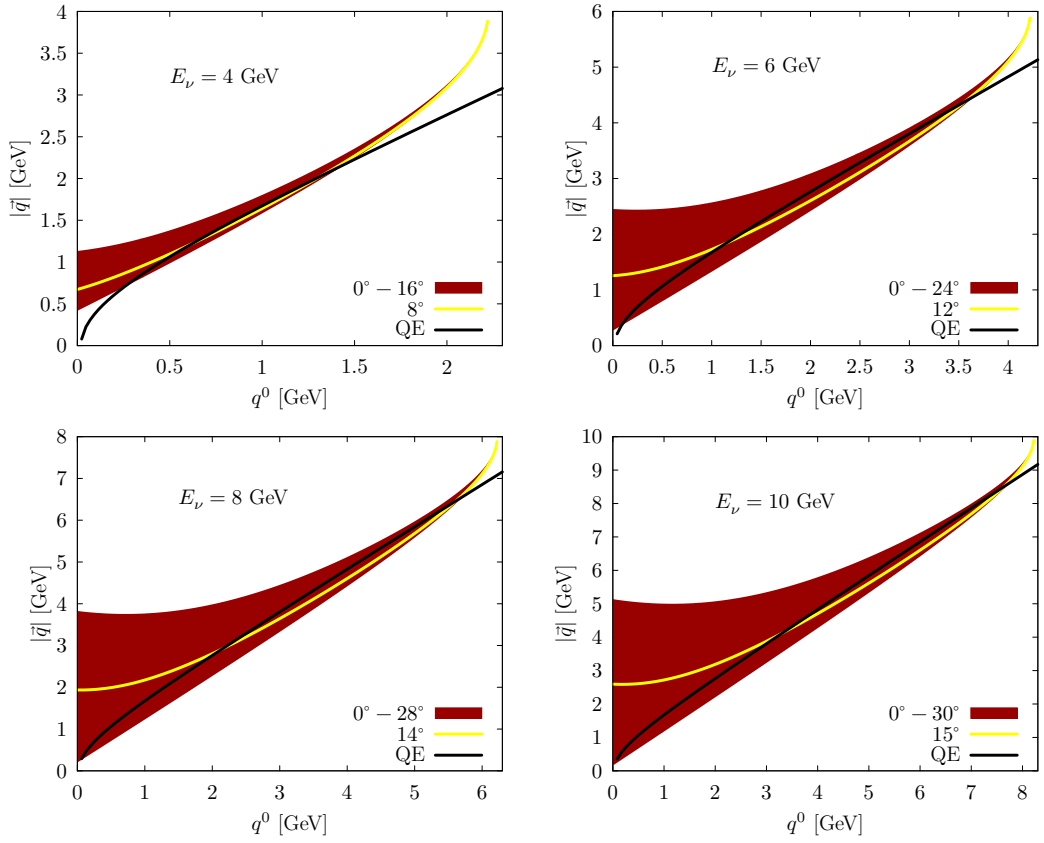

FIGURE 7.1: Some regions of the available phase space for CC $\tau-$ production for E_ν= 4, 6 8 and 10 GeV (panels from left to right). We display $|\vec{q}|_{[E_\nu,q^0,\theta]}$ (Eq. (7.17)) and also the approximated position of the QE peak ($|\vec{q}|_{\rm QE} = \sqrt{2Mq^0 + (q^0)^2}$), labeled as QE (black solid line). For each neutrino energy, the shaded area spans between $\tau-$scattering angle 0° (lower boundary) up to $16^\circ, 24^\circ, 28^\circ$ and 24° (upper boundary), respectively. In each panel, the yellow curve shows $|\vec{q}|_{[E_\nu,q^0,\theta]}$ for an intermediate angle among those accounted for in the band.

ground state, is only visible for $E_\nu = 6$ GeV. Unexpectedly for $E_\nu = 4$ GeV, the GFG model seems to provide a q^0 tail similar to those found in the LDA SF IA and CBF SF calculations. However, its origin in the former model should not be attributed to short range correlations, but rather it is produced by the kinematics of the QE CC $\tau-$production. If we come back to Fig. 7.1, we discussed that the $|\vec{q}|_{[E_\nu=4\,\text{GeV},q^0,\theta=0^\circ]}-$curve intersects the QE-one for two different values of $q^0 = 0.19$ and 1.53 GeV. These values correspond to forward and backward $\nu_\tau N \to \tau N$ scattering in the neutrino-nucleon CM system, respectively. The boost to the LAB system converts both CM kinematics into forward scattering in the LAB frame[1] (see Appendix E). In Fig. 7.4, we show the dependence of the imaginary part of Lindhard function, $\text{Im}U(q^0, |\vec{q}|_{[E_\nu,q^0,\theta]})$, on q^0 and q^2 for charged τ production for two different kinematics (dashed red curves). As discussed in Ref. [3], $\text{Im}U(q)$ essentially gives the single-nucleon knockout GFG nuclear response for a unit amplitude, at the nucleon level. For both kinematics, we clearly see two peaks, induced by the forward and backward $\nu_\tau N \to \tau N$ scattering in the neutrino-nucleon CM system, which lead to shapes different from those found for QE-processes involving massless leptons. These distributions should be affected by the nucleon form factors that produce sizable q^2-suppression in the differential cross sections. As an example, in Fig. 7.4 we also display the results modulated

[1]For massless charged leptons, however, the CM backward kinematics does not lead to forward scattering in the LAB frame, while the QE condition for $\theta = 0^\circ$ occurs for $q^0_{\rm QE}(m_\ell = 0) = 0$. As the dispersion angle grows, $q^0_{\rm QE}(m_\ell = 0)$ increases, but there is still a single value where the condition of the QE peak is satisfied (Eq. (E.5)).

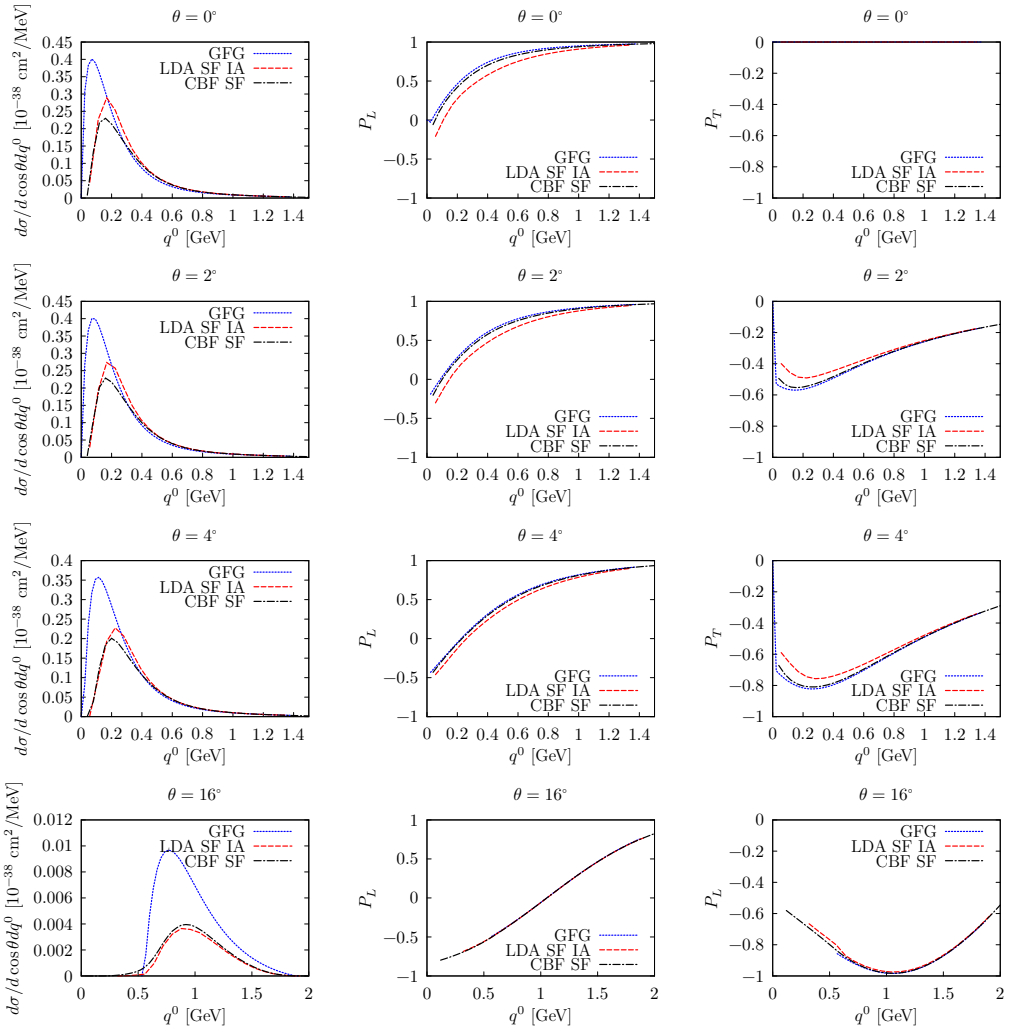

FIGURE 7.2: Double-differential cross section $d\sigma/(dq^0 d\cos\theta)$ and polarization components P_L, P_T for ν_τ scattering off ^{16}O for $E_\nu = 4$ GeV and scattering angles 0°, 2°, 4° and 16°.

by the square of a dipole nucleon form factor, with a cutoff of 1 GeV^2 (dotted blue curves). In these latter cases the second peak disappears, though its existence provides a longer high q^0-tail, what is qualitatively observed in the GFG predictions shown in Figs. 7.2 and 7.3.

Coming back to the discussion of these latter figures, we observe a very nice agreement between the CBF SF and LDA SF IA cross sections for both $E_\nu = 4$, and 6 GeV and $\theta = 16°$ as opposed to $\theta = 0°$, 2° and 4° cases, where some discrepancies appear. They are likely to be ascribed to the different approximations made to account for the off-shellness of the struck nucleon, as discussed in Subsec. 7.1. These approximations play a more important role in the limit of low momentum transfer and very forward angles. Let us notice that both SF approaches converge when we move to higher scattering angles, and for 16° the differences practically disappear. For the LDA SF IA model, the four-momentum p of the initial nucleon is taken from the SF energy–momentum distribution, thus within this scheme, the hole state is treated as an off-shell nucleon. However in the CBF SF approach, the energy transfer is modified to include the SF effects $\tilde{q}^0 \leftrightarrow q^0$, leaving the hole state on-shell (with the momentum taken from the SF and setting $E_p = \sqrt{M^2 + \vec{p}^2}$).

The production of the massive τ lepton is particularly interesting since it might present different polarization components. This fact has a direct implication on the angular distribution of the particles which are subsequently produced in the τ-decay. In the second and third rows on

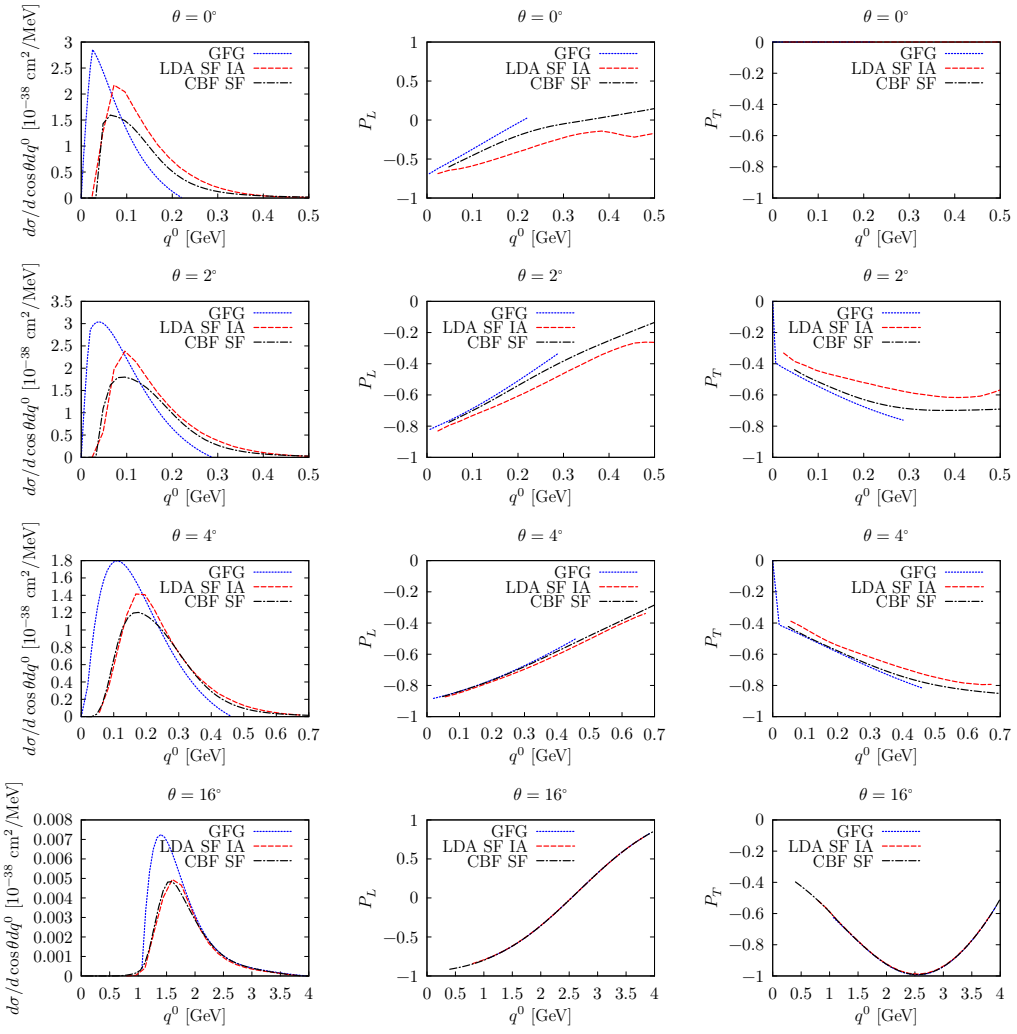

FIGURE 7.3: Same as Fig. 7.2 but for $E_\nu = 6$ GeV.

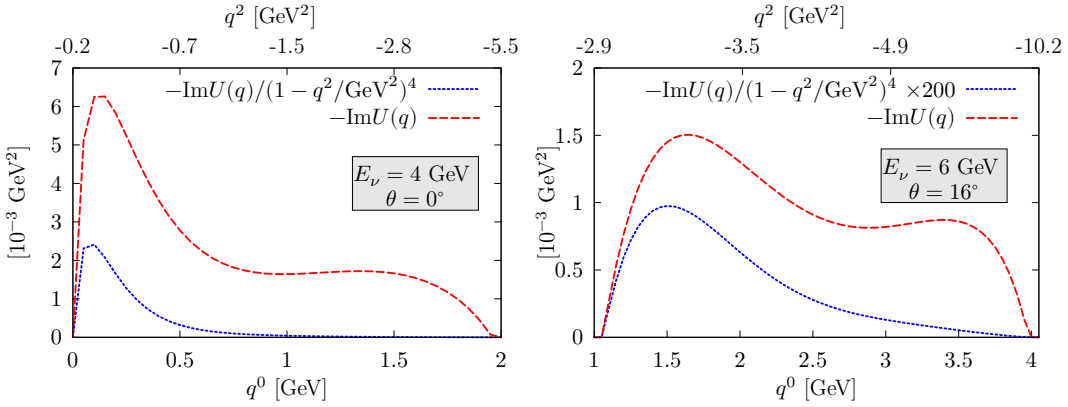

FIGURE 7.4: Imaginary part of the Linhard particle-hole propagator as a function of q^0 and q^2, with $|\vec{q}| = |\vec{q}|_{[E_\nu, q^0, \theta]}$ defined in Eq. (7.17). To evaluate $\mathrm{Im}U(q^0, |\vec{q}|)$ we have used Eq. (B2) of Ref. [3], with $\bar{p}_F = 0.225$ GeV for both neutron and proton Fermi momenta. The left and right panels correspond to ($E_\nu = 4$ GeV, $\theta = 0°$) and to ($E_\nu = 6$ GeV, $\theta = 16°$), respectively. In addition, we also show the expected q^2-reduction in the cross section provided by dipole weak nucleon form factors, with a mass scale of 1 GeV.

Figs. 7.2 and 7.3 we show the impact of nuclear effects on P_L and P_T for different kinematical setups. For increasing values of the scattering angle the transverse polarization, P_T, of the τ becomes more visible. This is not surprising because it is proportional to $m_\ell \sin\theta$ [248]. On the other hand, as the incoming neutrino energy grows, P_L takes values closer to -1 for low energy transfers, as expected for the conservation of chirality in CC processes. One can also observe that P_L and P_T obtained within the CBF SF and LDA SF IA approaches, in most of the cases, do not differ so much from the simplistic GFG predictions, in spite of leading to significantly distinct double differential cross sections. This should be ascribed to the cancellations that take place when the ratios of Eq. (7.14) are calculated.

Figs. 7.5 and 7.6 are the analogous of Figs. 7.2 and 7.3 but for the $\bar{\nu}_\tau + {}^{16}\mathrm{O} \to \tau^+ + X$ process. The results obtained for the double differential cross sections are qualitatively consistent with the observations we made for the ν_τ case. Nuclear effects are clearly visible in all the kinematical setups analyzed and the discrepancies between the CBF SF and LDA SF IA predictions are sizable also in this case up to $\theta = 4^\circ$, while for $\theta = 16^\circ$ the two set of results are almost coincident. It is worth noticing that the τ^+'s produced in the $\bar{\nu}_\tau$-nucleus scattering are more strongly longitudinally polarized ($P_L \sim 1$ and $P_T \sim 0$) than the τ^-'s. For $E_{\bar{\nu}} = 6$ GeV and scattering angles $0^\circ - 4^\circ$, P_L is rather constant through the whole range of available q^0 and very close to 1; it departs significantly from 1 only at $\theta = 16^\circ$, when P_T takes larger values (in modulus). For strictly forward scattering,

$$\begin{aligned} P_L^{(\tau^-,\tau^+)} &= \mp\left(1 - 2\frac{E_{k'} - |\vec{k}|}{F^{\nu_\tau,\bar{\nu}_\tau}(\theta = 0^\circ)}\left[2W_1 \pm \frac{|W_3|}{M_i}(E_{k'} - |\vec{k}|)\right]\right) \\ &= \mp\left(1 - 2\frac{E_{k'} - |\vec{k}|}{M_i F^{(\nu_\tau,\bar{\nu}_\tau)}(\theta = 0^\circ)}\left[W_{xx} \pm |W_{xy}|\right]\right) \end{aligned} \tag{7.18}$$

where the factor $F^{\nu,\bar{\nu}}$ can be found in Eq. (2) of Ref. [248], both for neutrino and antineutrino reactions, and $\vec{q}$ is taken in the positive $Z-$direction. There exists a large cancellation between the xx and xy spatial components of the hadron tensor that is responsible for the much smaller values of the antineutrino cross sections than the neutrino ones. This cancellation also leads to values of P_L closer to 1 in the case of τ^+ production, and because of the factor $(E_{k'} - |\vec{k}|)$, deviations from chirality should increase with the transferred energy q^0. Moreover, differences between nuclear corrections stemming from different approaches should be more visible for antineutrino distributions. Thus for instance within the LDA SF IA approach, if p^0 is fixed to E_p instead of to $E + M$ in Eq. (3.10), values of $P_L^{\tau^+} > 1$ are found in the case of forward antineutrino reactions, while $|P_L^{\tau^-}|$ still keeps smaller than one for neutrino processes. The consistent use of the energy and momentum distributions obtained from the hole spectral function $S_h^{\mathrm{LDA}}(E,\vec{p})$, changing the dispersion relation of the initial nucleon, leads to reasonable predictions for $P_L^{\tau^+}$ below one.

We observe that the inclusion of the CBF and LDA nuclear SFs significantly modifies also the $\bar{\nu}_\tau$-^{16}O differential cross section with respect to the GFG results, and leads to a significant quenching of the QE peak and a shift of its position towards higher energy transfers. The role played by nuclear effects in the determination of P_L and P_T is less systematic. The curves corresponding to the different SFs are found to differ for most of the kinematics considered in Figs. 7.2, 7.3 7.5 and 7.6. In particular, we find the GFG predictions for $P_L^{\tau^-}$ and $E_\nu = 6$ GeV lay in between the CBF SF and LDA SF IA ones. We interpret this behavior as a manifestation of the strong dependence of the polarization variables on the approximations made in the hadron tensor to treat the off-shell struck nucleon.

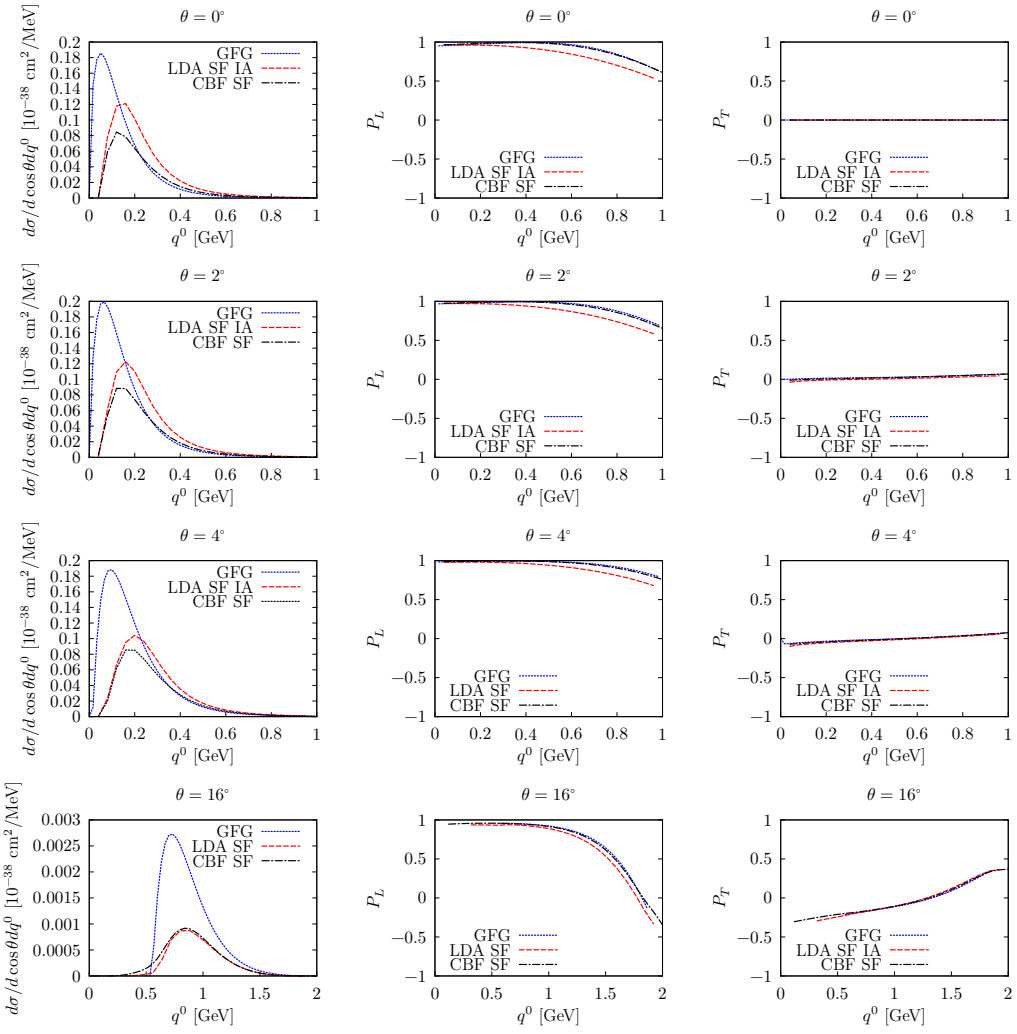

FIGURE 7.5: Double-differential cross section $d\sigma/(dq^0 d\cos\theta)$ and polarization components P_L, P_T for $\bar{\nu}_\tau$ scattering off ^{16}O for $E_{\bar{\nu}} = 4$ GeV and scattering angles 0°, 2°, 4° and 16°.

The mean value of the degree of polarization of the $\tau^{\mp}$ lepton is defined as

$$\langle \mathscr{P}^{(\tau^-,\tau^+)} \rangle = \frac{1}{\sigma^{(\nu_\tau,\bar{\nu}_\tau)}(E_\nu)} \int dE_\tau d\Omega_{k'} \Sigma_0^{(\nu_\tau,\bar{\nu}_\tau)}(E_\tau,\theta)\, \mathscr{P}^{(\tau^-,\tau^+)}(E_\tau,\theta) \tag{7.19}$$

with Σ_0 the LAB unpolarized double differential cross section of Eq. (7.8) and the Lorentz scalar degree of polarization for a given outgoing $\tau-$lepton kinematics given by

$$\mathscr{P}(E_\tau,\theta) = \sqrt{P_L^2(E_\tau,\theta) + P_T^2(E_\tau,\theta)} \tag{7.20}$$

The dependence of the mean value of the degree of polarization on the neutrino (antineutrino) energy is shown in Fig. 7.7. The small discrepancies between the curves are likely to originate from the different treatment of the nucleon off-shellness in the LDA SF IA and CBF SF results. However, a clear-cut identification of their source can not be easily achieved in this case. For the antineutrino, the degree of polarization reaches the asymptotic chiral value more rapidly than for the neutrino case, saturating already at about 5 GeV. Results are in qualitative agreement with those obtained with the simple models considered in Ref. [36].

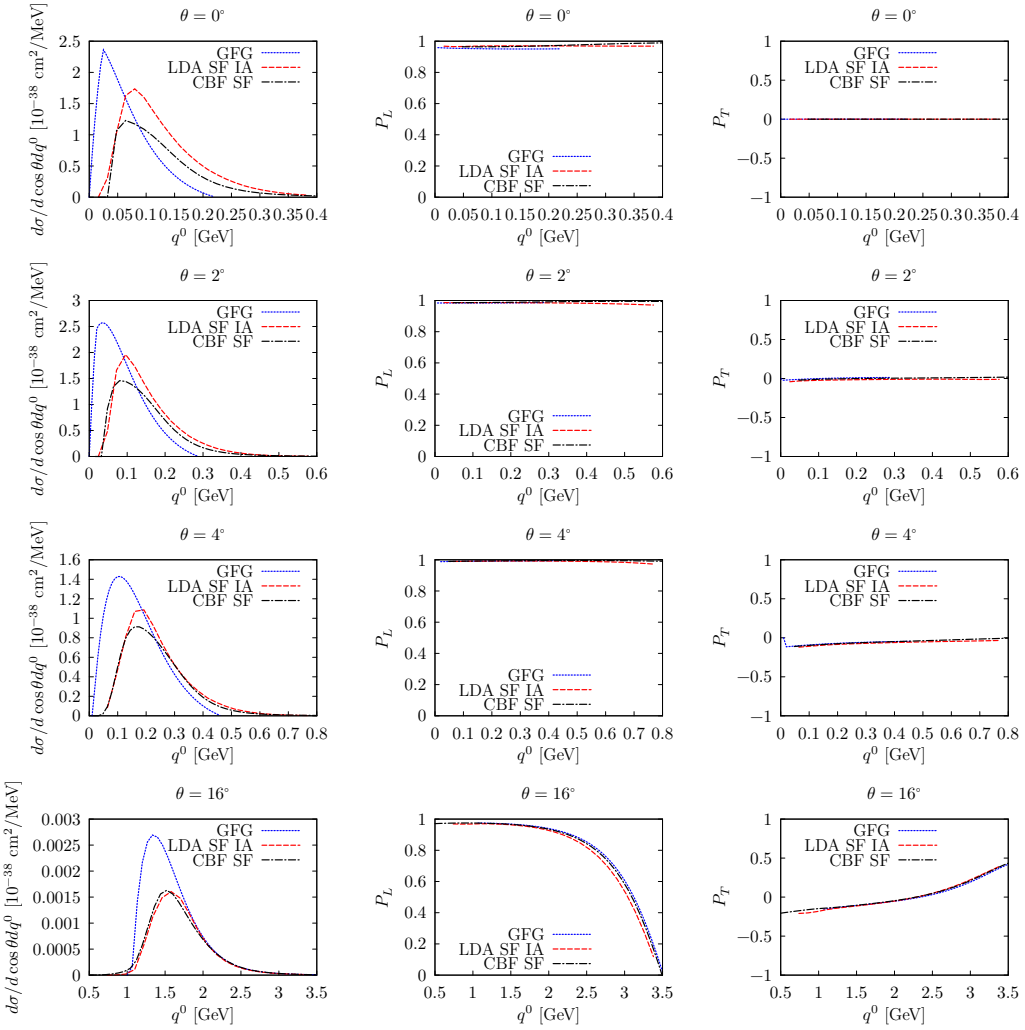

FIGURE 7.6: Same as Fig. 7.5 but for $E_{\bar{\nu}} = 6$ GeV.

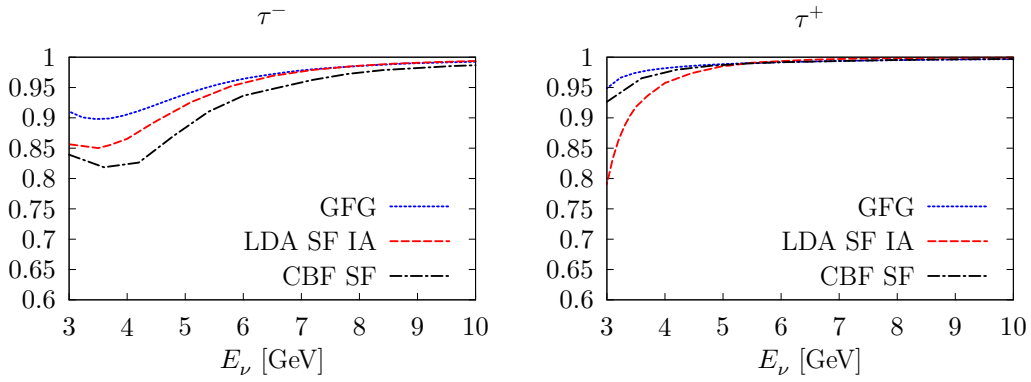

FIGURE 7.7: Mean value of the degree of polarization of τ^- (left) and τ^+ (right), defined in Eq. (7.19), as a function of the incoming neutrino energy. We show results for the GFG model (blue–dotted) and the LDA SF IA (red-dashed) and CBF SF (black dash-dotted) approaches.

Chapter 8

Conclusions

We have presented an exhaustive analysis of the role played by spectral functions in the description of the QE neutrino-nucleus interaction mechanism. The formalism used in the calculations presented in this Thesis was introduced in Ref. [3], and it is based on a semi-phenomenological model for the nucleon self-energy in a (symmetric) nuclear medium [2]. This approach has proved to describe various properties of the many-body system, important from the point of view of the neutrino oscillation experiments, where both a correct reconstruction of the neutrino energy and the value of the cross section on various nuclei are needed.

We have focused on four main topics:

1. A careful and detailed comparison of several neutrino-nucleus observables, governed by the QE mechanism, with the available data and with the results of other approaches, taking into account also RPA effects. We have further compared with inclusive electron scattering data which is much more precise than the neutrino measurements and puts constraints on the vector part of the interaction.

2. The investigation of the scaling properties of the nuclear system response described in terms of the hole and particle spectral functions. We analyzed with more profundity how various approximations (e.g. plane-wave impulse approximation, inclusion of the final state interactions/particle SF) influence the scaling.

3. The study of the role played by both initial-ground correlations and final state interactions in the QE hyperon production. Here, we investigated both inclusive and semi-exclusive (distributions of the outgoing hyperons) $\Delta S = 1$ processes. We have also studied final state interactions, modelled by means of an internuclear Monte Carlo cascade.

4. The analysis of the effects of the many-body description of the ground state on the polarization of the outgoing τ lepton in (anti)neutrino-nucleus CCQE reactions.

These topics cover a wide range of theoretical problems and provided a valuable insight into various aspects of the physical properties of the response of a many-body nuclear system interacting with an electroweak probe in the QE region.

Before entering into the details of each particular analysis, in Chpt. 2 we presented a wide introduction to the formalism used in this Thesis. We started from the Standard Model for fundamental interactions, focusing on how neutrinos interact with the quark sector. In the effective low-energy nuclear theory, the emerging degrees of freedom are baryons and mesons, bound states of quarks. The physical mechanisms we explored involved both nucleons and strange hyperons (we will later refer also to the production of charmed baryons). Their QE interaction with an electroweak probe can be parametrized (in general) in terms of six form factors. Moreover, the $N \to N'$ and $N \to Y$ form factors can be related under the assumption of unbroken SU(3) flavour symmetry.

Further, when considering interactions on nuclei, one should account for the nuclear effects. Solving the many-body problem is a difficult task where different nuclear effects may become

more or less relevant depending on the momentum transferred to the nucleus. The simplest approach, introduced in Subsec. 2.3.1 consists in taking into account only statistical correlations between nucleons. In a system of fermions at zero temperature due to the Pauli exclusion principle, particles occupy energy levels up to the Fermi level. The additional assumption of the LDA leads to the Local Fermi gas model.

The FG model has been used as a starting point to introduce the theoretical approach presented in this Thesis. We have briefly introduced some basic notions used to describe the properties of nucleons in the nuclear medium, in particular their Green's functions (and their modification when the self-energy is included) and the relation with the spectral functions. We have made also a detailed derivation of how the response of the nuclear system interacting with an electroweak probe for high enough momentum transfers can be expressed in terms of the spectral functions. In the last section of Chpt. 2 we addressed other effects like the RPA summation or the importance of implementing a correct energy balance.

Chpt. 3 has been focused on the description of different models for the spectral functions. Following the same scheme as in Chpt. 2, we have started our considerations from the Fermi gas model. Spectral functions in this case are simple step functions, which further lead to flat distributions for the nucleon momenta (the situation is slightly different in the case of a LFG for which the Fermi level depends on the nuclear density). Next, in Sec. 3.2 we have presented the semi-phenomenological model for the nucleon self-energy introduced in Ref. [2]. This approach has as an input NN scattering data, which is used to construct an effective NN interaction in the medium that accounts for both short and long (RPA) range nuclear correlations. The model has proved to work well when applied to various physical reactions [3, 4, 5, 6, 7, 8, 9, 10]. One of the virtues of this approach is the possibility to describe, within the same formalism, both the initial and final nucleons (*i.e.* states with energy below and above the Fermi level) and its easy implementation for different isospin symmetric nuclei. Although the calculation of Ref. [2] was performed in a nonrelativistic regime, it was then extended to the relativistic case in Ref. [5]. This could be done, since the input experimental NN cross section data by definition accounts for relativistic effects. Another idea of how to use this model in the relativistic regime, consists in neglecting nuclear corrections in the particle spectral function. This requires fitting an additional phenomenological parameter to obtain the experimental removing energy (using the Koltun sum rule of Ref. [11]).

In neutrino-nucleus interaction studies, there exist several theoretical models describing the QE mechanism. In Sec. 3.3 we have made a survey of those which are most widely used in the analyses of neutrino scattering experimental data and in Monte Carlo event generators. Thus, in Subsec. 3.3.1, we have focused our attention on the CBF approach based on the Impulse Approximation, successfully tested in electroweak-nuclear reactions [14, 15, 16, 17, 18, 19]. In Chpts. 5-7 we have performed various comparisons between the predictions obtained within this formalism and those found using the semi-phenomenological one described in Sec. 3.2. Within the CBF framework, the hole spectral function is expressed as the sum of two contributions. The dominating one comes from shell-model calculations, quenched by experimental spectroscopic factors. This MF description does not account for the high momentum-energy part of the nucleon wave function. This latter contribution is modelled within an ab initio Correlated Basis Function formalism for symmetric nuclear matter, and added assuming the LDA. To account for the final state interactions, yet another strategy is employed, based on the generalized Glauber theory. It takes as an input nuclear transparencies and the real part of an optical potential obtained from a fit of a Dirac phenomenological interaction to data.

We have also explored the predictions of other four theoretical schemes. The GiBUU [20] approach is also based on the LDA, applying a phenomenological potential (both density and momentum dependent) obtained from heavy-ion reactions studies. The framework is relativistic, allowing the description of both initial and final nucleons. SuSA (SuperScaling Approach) model [21] follows a different idea. Starting from the scaling properties of electron-nucleus

scattering cross section, a phenomenological scaling function is extracted from data, and used as an input to predict neutrino-nucleus QE cross sections. The Ghent group has developed a MF approach [22] with a Skyrme potential for which parameters were fixed against the low-energy excitations of spherical nuclei . The effect of long-range correlations (RPA) is included using the same residual interaction. Finally, the MECM model [23], developed initially by the Lyon group, accounts for the latter nuclear corrections using an effective Landau-Migdal interaction analogous to that used in our approach presented in Subsec. 2.5.2.

In Chpt. 4 we have presented a theoretical description of other QE processes – muon and radiative pion captures in nuclei – which were used to investigate the applicability of the nuclear model used in this Thesis. These reactions involve small energy and momentum transfers, and hence, test the model of Refs. [3, 2] in a kinematic regime where a more elaborated description of the initial and final nuclear states might be needed. We observe that SFs are responsible for the quenching of the QE peak, produce a spreading of the strength of the response functions to higher energy transfers and shift the peak position in the same direction. The overall result is a decrease of the integrated decay rates and a considerable change of the differential shapes. RPA effects in the integrated decay rates become significantly smaller when SF corrections are also taken into account, in sharp contrast to the case of a free LFG where they lead to large reductions, even of around 40%. This interesting result was mentioned already in [3], and it is mainly due to the change of the nucleon dispersion relation in the medium (effects of the real parts of the particle and hole nucleon self-energies). Moreover, this is also in agreement with the findings of Refs. [22, 24], from which one can conclude that RPA effects on top of the MF results are moderately small for sufficiently large values of Q^2, far from the giant-resonance regime.

The final results for low energy processes (including both RPA and full SF effects for the very first time), presented in Chpt. 4, although subject to some theoretical errors (originated from the RPA parameters uncertainty and the possible contribution of discrete states), describe the data with a good precision, and provide a clear improvement of the poor description obtained by only imposing Pauli blocking and the correct energy balance in the reactions. For radiative pion capture, we observe that the use of realistic SFs places the QE peak in a reasonable position and changes the shape of the differential decay width, making it definitely more accurate than that obtained with the RPA model. However, the description is obscured by a discrete spectrum of resonances not taken into account in the model. For muon capture, we only have at our disposal data of integrated widths; these rates are well recovered by our model for various symmetric nuclei. These results, along with the LSND, KARMEN and LAMPF neutrino cross sections on carbon near threshold, which also stay in agreement with LDA SF+RPA predictions, confirm the reliability of the model derived in [3, 4]. This also ensures the accuracy of the predictions obtained within this model for intermediate energy neutrino scattering cross sections of interest for oscillation experiments, which are also given, and that for the first time have been obtained considering full SFs for both particle and hole nucleons. We present results for (anti)neutrino integrated and differential cross sections, and discuss the magnitude of the RPA and SF effects. Moreover, we use MC techniques to estimate the uncertainties of our predictions. We also show that errors on the σ_μ / σ_e ratio are much smaller than 5%, and also much smaller than the LDA SF+RPA nuclear corrections, which produce significant effects, not only in the individual cross sections, but also in their ratio for neutrino energies below 400 MeV. These latter nuclear corrections, beyond Pauli blocking, turn out to be thus essential to perform a correct analysis of appearance neutrino oscillation events in long-baseline experiments.

We have also performed a detailed analysis and comparison of various theoretical models with electron-nucleus inclusive scattering data in the momentum-energy region important for the T2K experiment. All the considered theoretical models: LDA SF, CBF SF (with FSI included) and GiBUU are able to describe quite successfully the inclusive data in the QE peak region. One has to take into account, however, that for a fully meaningful comparison with data,

one should include other mechanisms which give some contribution to the cross section in that kinematical region. As was shown, for some kinematical setups, both 2p2h and Δ production overlap with the QE peak.

Chpt. 5 was devoted to studying the scaling properties of the nucleon-density response, a key quantity to understand the scaling of the electromagnetic longitudinal and transverse response functions [25]. We have calculated the nucleon-density response of ^{12}C in a kinematical region where collective excitations can be safely neglected. To that end, we employed particle and hole SFs obtained within two many-body methods, LDA SF and CBF SF, widely explored in this work.

We have shown that both approaches lead to compatible ^{12}C nucleon-density scaling functions, characterized by an asymmetric shape, although less pronounced than the one derived from the experimental data on the electromagnetic longitudinal response functions. Whilst the CBF SF provides a more accurate description of the ground-state of ^{12}C, presently it can only be applied to closed-shell nuclei. On the other hand, the LDA SF model can be readily extended to the ^{40}Ar nucleus, which will be employed in future neutrino-oscillation experiments [26].

Employing a simplified model of nuclear dynamics, which retains the main aspects of the many-body problem, we discussed the dynamical origin of the scaling of the first kind exhibited by the nucleon-density response function. We have argued that its asymmetric shape is mostly due to the $2h1p$ dynamics incorporated in the continuum component of the hole SF of Ref. [27], that in turn accounts for NN correlations. Within the semi-phenomenological model developed in Ref. [2], this effect is taken into account through the imaginary part of the nucleon hole self-energy, ImΣ. In this latter reference, an appreciable quenching of ImΣ, due to polarization effects, was found at low nucleon energies and momenta. However, we expect RPA (collective) corrections to produce small modifications in the high momentum components, which are responsible for the tail. On the other hand, we have shown that the asymmetry is only slightly enhanced by FSI effects. The latter lead to a shift of the peak position towards smaller values of ψ^{nr} (variable constructed out of q^0 and $|\vec{q}|$) and to a redistribution of the strength towards larger values of the scaling variable ψ^{nr}. According to the RMF study carried out in Ref. [28], the asymmetry of the scaling function has to be ascribed to the dynamical enhancement of the lower component of the Dirac spinors, which, in principle, is not present in the nonrelativistic nucleon-density response function. Analogously to the Green Function MC results of Ref. [25], the asymmetry is also observed within the nonrelativistic scheme of nuclear dynamics based on the particle and hole SFs. Our results do not necessarily invalidate the RMF picture of scaling since some of the nonrelativistic correlations might arise from the nonrelativistic reduction performed already at the MF level. Nevertheless, this intriguing hypothesis deserves further investigations.

Within the SF formalism, we found that, once the prefactors describing the single-nucleon interaction-vertices are divided out, the longitudinal and transverse electromagnetic response functions share a common kernel, intimately connected to the one of the nucleon-density response function. Consequently, the electromagnetic longitudinal and transverse scaling functions are very similar to the nucleon-density scaling function – the small differences being ascribable to discrepancies between GFG and SF prefactors. Therefore, besides two-body current and collective corrections effects, the breaking of zeroth and first kind scalings has to be attributed to deficiencies in the nuclear model used to estimate the single-nucleon electroweak matrix elements in nuclei.

In Chpt. 6 we have presented the weak production of Λ and Σ hyperons induced by $\bar{\nu}_\mu$ scattering off nuclei, carefully considering the effects of nuclear dynamics. To describe correlations in the initial nuclear target, we employed the two distinct models for the hole SFs examined in this Thesis. The propagation of the hyperons in the nuclear medium is tackled by a MCC algorithm, which treats the rescattering processes in a classical fashion. The MCC does not modify the inclusive $(\bar{\nu}_l, l^+ Y)$ cross sections, if the sum for $Y = \Lambda, \Sigma^0$ and $\Sigma^\pm$ is considered.

On the other hand, when more exclusive processes are analyzed, such as the production rates, the energies, and the angular distributions of the specific hyperons' species, the MCC plays a major role. For instance, although the Σ^+ hyperon is not produced in the weak interaction vertex, because of secondary collisions, its production rate in the scattering process does not vanish. Of course, when all the possible channels are summed, the inclusive cross section is recovered.

We find that our calculations carried out employing semi-phenomenological LDA SF [2] and the CBF SF [29, 27] nicely agree, providing robust estimates of the importance of dynamical correlations in the initial nuclear state, neglected in the pioneering work of Ref. [30], based on the LFG model. We show how the inclusive double-differential $d^2\sigma/(d\cos\theta dq^0)$ [θ is the scattering angle of the outgoing charged lepton] distributions are significantly affected, as the correlations encoded in the hole SFs bring about a reduction of the height of the QE peak and a redistribution of the strength to higher energy transfers regions. In the case of the differential cross section $d\sigma/dq^2$ and the total one, the effects of considering realistic hole SFs are not as important as in the $d^2\sigma/(d\cos\theta dq^0)$ distribution, and are less relevant than those produced by the FSI of the produced hyperon. The MCC strongly modifies the IA results for the exclusive processes, leading to a non-zero Σ^+ cross section, to a sizable enhancement of the Λ production and to drastic reductions of the Σ^0 and Σ^- distributions.

It has to be mentioned that the MCC effects we obtained here are much larger and more visible than those reported in Ref. [30]. This is due to an imprecise implementation of the Pauli blocking of the outgoing nucleons produced in secondary collisions in the latter work, that led to an important reduction of the number of collisions experienced by the hyperons during their path through the nucleus.

Motivated by the recent BESIII measurements of the branching ratios of $\Lambda_c \to \Lambda l^+ \nu_l$ ($l = e, \mu$) decays and by the CHORUS results for the ratio of the cross section for Λ_c production in neutrino-nucleon scattering, we computed the QE weak Λ_c production cross section on nuclei. We estimated the impact of the $n \to \Lambda_c$ matrix-element theoretical uncertainties. To this aim, we employed form factors computed within different approaches ranging from the LQCD calculations of Ref. [31] to the state-of-the-art nonrelativistic and relativistic quark models of Refs. [32, 33, 34, 35]. Note that, while for the $N \to \Lambda, \Sigma^0, \Sigma^-$ transitions the theoretical predictions are consistent with the available experimental data, in the Λ_c case, the main source of uncertainty is associated with the different theoretical parameterizations of the form factors. For this reason, we neglect nuclear effects beyond the Fermi gas model, as their inclusion would introduce additional theoretical errors (the behaviour of Λ_c in the nuclear medium is poorly known). We also expect them to provide significantly smaller corrections than the discrepancies produced by the use of different sets of form factors. Indeed, we find significant variations in the predictions from the different schemes adopted to compute the relevant form factors, despite the fact that all of them are constrained by the experimental $\Lambda_c \to \Lambda e^+ \nu_e$ decay width. This is a direct consequence of the unavoidable ambiguities induced by extrapolating the form factors from the q^2 region relevant for the Λ_c decay to the kinematics relevant to the Λ_c production. Nevertheless, the theoretical uncertainties are estimated to be below 30% for $E_\nu \lesssim 3.5$ GeV. For the neutrino energies corresponding to the peaks of the MINERvA and DUNE fluxes, we predict the cross sections – normalized to the number of neutrons – to be $\sigma(E_\nu = 3\,\text{GeV})/N = (0.9^{+0.2}_{-0.1}) \times 10^{-40}\text{cm}^2$ and $\sigma(E_\nu = 5\,\text{GeV})/N = (4.5^{+2.0}_{-0.9}) \times 10^{-40}\text{cm}^2$, respectively.

In Chpt. 7 we have performed an analysis of the cross sections and polarization components for the CC reaction in which a $\nu_\tau/\bar{\nu}_\tau$ scatters off ^{16}O, focusing on the QE region where the single nucleon knock-out is the dominant reaction mechanism. From the theoretical perspective, the ν_τ CC scattering gives a unique opportunity to further investigate the role played by the nuclear correlations of the ground state in the description of neutrino-nucleus interaction. The large mass of the $\tau^\pm$ lepton, with respect to those of the $\mu^\pm$ and $e^\pm$, enables a deeper insight into

the nuclear structure of the nucleus when interacting with an electroweak probe. From the total number of five structure functions which are in general needed to describe the hadron tensor of neutrino-nucleus scattering, ν_e and ν_μ reactions give access only to three of them, $W_{1,2,3}$, being the contribution of the others suppressed by the low e^- and μ^- masses.

The longitudinal and transverse polarization components of the outgoing τ are interesting observables, both from the experimental and theoretical points of view. They allow for further tests of the hadron tensor properties, since they are sensitive to different combinations of the structure functions. In order to provide a realistic description of the nuclear dynamics accounting for NN correlations, also in this context, we have used the LDA and CBF hole SFs derived in Refs. [2] and [29, 27], successful in modeling inclusive electro– and (anti)neutrino–nuclear QE responses. We should mention in this context that the SF approaches are substantially more realistic than those based on the use of an effective nucleon mass to describe the initial nuclear state, as done in the previous study of Ref. [36]. The implementation of a constant effective mass is just a crude approximation to account for the effects due to the change of the dispersion relation of a nucleon inside of a nuclear medium.

For each of the considered models, CBF SF and LDA SF, we used slightly different prescriptions of how the single nucleon matrix element is calculated in the nuclear medium. The ambiguity stems from the fact that the hit nucleon is off-shell, with its energy-momentum distribution determined by the SF. In the CBF approach the initial nucleon is taken to be on-shell with the momentum distribution taken from the SF. The energy distribution of the hole SF is taken into account as the modification of the energy transfer. The LDA treats the initial nucleon as an off-shell particle; however, the master equation for the matrix element at the nuclear level (where the sum over spins is performed) is obtained assuming on-shell nucleons. The results for very forward scattering angles turned out to be very sensitive to this choice, affecting both the cross sections and the polarization components. Nevertheless, the discrepancies become very small already for angles $\sim 4^\circ$. We have shown that the effect of SFs is sizable when the differential cross sections are considered, producing a quenching of the QE peak and a shift of its position towards higher energy transfers, as in the other cases studied in this work. However, nuclear effects are less pronounced for the polarization components, because they are obtained as ratios of terms proportional to the hadron tensor, where some cancellations of the nuclear corrections occur.

Outlook

The main motivation for this work has originated from the neutrino experimental studies. In the current and future oscillation measurements, in particular at DUNE and T2HK long baseline accelerator experiments, a precise knowledge of the cross sections and of the neutrino reconstructed energy are highly desired. We have focused our attention on the QE mechanism which is the dominant process in the energy range of T2K (and future T2HK) experiment, and one of the main contributions for DUNE.

Bearing in mind the status of neutrino experiments and various challenges which were presented in the Introduction, we discuss some possible improvements and further developments of the studies presented in this Thesis.

- Additional validation, tests of the model for the SFs can be done by performing comparisons with semi-exclusive data in which both the final lepton and the knocked-out proton are observed. The current experimental program, aiming at high-precision measurements of electron-nucleus scattering, in JLAB has made it possible for a wide range of kinematical setups and various nuclei. This test for the nuclear model would need an additional Monte Carlo cascade to propagate the final nucleon through the nucleus.

- One of the biggest challenges in neutrino detection is the fact that the beam is not monoenergetic and typically covers a wide range of energies from MeV to few GeV. Therefore, all kinematically allowed mechanisms (which usually include QE, multi-nucleon knock-out, pion production and DIS) compete and give contributions to the total rate of observed events. It becomes indispensable to have a theoretical framework where all these mechanisms could be included. The model developed by the Valencia group is able to address this problem. However, a full description of both CC and NC processes is yet to come. Thus, we are currently working in the evaluation of inclusive 2p2h and pion production cross sections driven by both CC and NC.

- It is widely known that the uncertainties of neutrino-nucleus cross sections affect the analysis of oscillation parameters. However, the estimation of these theoretical errors is a difficult task which has not been fully done within any nuclear model. Some attempts have been made (see for instance Refs. [13, 68]).This analysis can be done using our approach and certainly could be quite useful.

- To make the model available for a wider use in the experimental studies, it should be implemented in one of the Monte Carlo event generators. This is a nontrivial task from the point of view of numerical calculations. The shape of spectral function, particularly in the vicinity of Fermi level, is delta-like, making the integration over it potentially unstable.

- It might be interesting to perform further analyses for the relativistic extension of the SF obtained within the model description in Subsec. 3.2.4, and compare their predictions to the available electron scattering data. Besides the GiBUU phenomenological potential which is relativistic, our model is the only one in the field of neutrino-nucleus studies which allows for a consistent description of both the hole and particle states.

Appendix A

Constants and conventions

Notation

When we use nonrelativistic kinematics for nucleons, we choose the origin of energy in its mass.

notation	meaning
$k = (E_k, \vec{k})$	incoming lepton
$k' = (E_{k'}, \vec{k}')$	outgoing lepton
$p = (E_p, \vec{p})$	incoming nucleon
$p' = (E_{p'}, \vec{p}')$	outgoing nucleon
$q = k - k' = (q^0, \vec{q})$	momentum transfer
Y	hyperon

TABLE A.1: Notation used in this Thesis.

Constants

constant	symbol	value
Fermi constant	G_F	$1.1664 \times 10^{-5}\text{GeV}^{-2}$
fine structure constant	α	$(137.036)^{-1}$
muon mass	m_μ	105.66 MeV
tau mass	m_τ	1776.82 MeV
pion mass	m_π	139.6 MeV
nucleon mass	M	938 MeV
Λ mass	M_Λ	1115.7 MeV
Σ^+ mass	M_{Σ^+}	1189.3 MeV
Σ^- mass	M_{Σ^-}	1197.4 MeV
Σ^0 mass	M_{Σ^0}	1192.6 MeV
Λ_c mass	M_{Λ_c}	2455 MeV
Cabbibo angle	$\cos\theta_C$	0.974

TABLE A.2: Constants used in this Thesis.

Metric tensor

$$g^{\mu\nu} = g_{\mu\nu} = \begin{pmatrix} 1 & 0 & 0 & 0 \\ 0 & -1 & 0 & 0 \\ 0 & 0 & -1 & 0 \\ 0 & 0 & 0 & -1 \end{pmatrix} \tag{A.1}$$

Levi-Civita symbol

We use sign convention

$$\varepsilon_{0123} = \varepsilon^{0123} = +1 \tag{A.2}$$

Pauli matrices

$$\sigma^1 = \begin{pmatrix} 0 & 1 \\ 1 & 0 \end{pmatrix}, \quad \sigma^2 = \begin{pmatrix} 0 & -i \\ i & 0 \end{pmatrix}, \quad \sigma^3 = \begin{pmatrix} 1 & 0 \\ 0 & -1 \end{pmatrix} \tag{A.3}$$

Dirac matrices

Dirac matrices are defined by the anticommutation relation

$$\{\gamma^\mu, \gamma^\nu\} = 2g^{\mu\nu} I_{4\times 4} \tag{A.4}$$

In the Dirac basis:

$$\gamma^0 = \begin{pmatrix} I_{2\times 2} & 0 \\ 0 & -I_{2\times 2} \end{pmatrix}, \quad \gamma^k = \begin{pmatrix} 0 & \sigma^k \\ -\sigma^k & 0 \end{pmatrix}, \quad \gamma^5 = \gamma_5 = \begin{pmatrix} 0 & I_{2\times 2} \\ I_{2\times 2} & 0 \end{pmatrix} \tag{A.5}$$

We also define

$$\sigma^{\mu\nu} = \frac{i}{2}[\gamma^\mu, \gamma^\nu] \tag{A.6}$$

Spinor normalization

Traditionally we denote $u_s(p)$ to describe fermions with helicity s and momentum $\vec{p}$ while $v_s(p)$ corresponds to antiparticles. The adjoint solution is given by $\bar{u}_s(p) = u_s(p)^\dagger \gamma^0$ and similar for $v_s(p)$. Spinor normalization used in this Thesis (for a particle of mass M and $E_p = \sqrt{M^2 + \vec{p}^{\,2}}$):

$$\begin{aligned} \bar{u}(p,s)u(p,s') &= 2M\delta_{s,s'} \\ \bar{v}(p,s)v(p,s') &= -2M\delta_{s,s'} \\ v^\dagger(p,s)v(p,s') &= 2E_p\delta_{s,s'} \\ u^\dagger(p)u(p,s') &= 2E_p\delta_{s,s'} \\ \sum_s u(p,s)\bar{u}(p,s) &= \not{p} + M \\ \sum_s v(p,s)\bar{v}(p,s) &= \not{p} - M \end{aligned} \tag{A.7}$$

State normalization

One-particle state normalization is given by

$$\langle \vec{p} | \vec{p}\,' \rangle = (2\pi)^3 2E_p \delta^3(\vec{p} - \vec{p}\,') \tag{A.8}$$

More on normalization conventions can be found in Appendix D.

Gell-Mann matrices

Gell-Mann matrices which span the Lie algebra of the SU(3) group and define the adjoint representation are taken as

$$\begin{aligned}
\lambda_1 &= \begin{pmatrix} 0 & 1 & 0 \\ 1 & 0 & 0 \\ 0 & 0 & 0 \end{pmatrix}, \quad \lambda_2 = \begin{pmatrix} 0 & -i & 0 \\ i & 0 & 0 \\ 0 & 0 & 0 \end{pmatrix}, \quad \lambda_3 = \begin{pmatrix} 1 & 0 & 0 \\ 0 & -1 & 0 \\ 0 & 0 & 0 \end{pmatrix}, \\
\lambda_4 &= \begin{pmatrix} 0 & 0 & 1 \\ 0 & 0 & 0 \\ 1 & 0 & 0 \end{pmatrix}, \quad \lambda_5 = \begin{pmatrix} 0 & 0 & -i \\ 0 & 0 & 0 \\ i & 0 & 0 \end{pmatrix}, \quad \lambda_6 = \begin{pmatrix} 0 & 0 & 0 \\ 0 & 0 & 1 \\ 0 & 1 & 0 \end{pmatrix}, \\
\lambda_7 &= \begin{pmatrix} 0 & 0 & 0 \\ 0 & 0 & -i \\ 0 & i & 0 \end{pmatrix}, \quad \lambda_8 = \frac{1}{\sqrt{3}} \begin{pmatrix} 1 & 0 & 0 \\ 0 & 1 & 0 \\ 0 & 0 & -2 \end{pmatrix}
\end{aligned} \tag{A.9}$$

Appendix B

Constructing the $N \to N'$ vertex

The CC nucleon-nucleon transition matrix element for weak current has a general form:

$$\langle N'; p'|J^\mu|N; p\rangle = \bar{u}(p')\Gamma^\mu u(p) \tag{B.1}$$

where the Dirac matrix vertex Γ^μ has axial-vector structure $V^\mu - A^\mu$.

To construct the most general form of the vertex we have at disposal four-vectors p^μ, p'^μ and a set of 4×4 matrices which when put between two Dirac spinors give rise to an expression with definite transformations under the Lorentz group and the space inversion operation [253]:

$$\begin{array}{cccc} I_{4\times4}, & \gamma^\mu, & \sigma^{\mu\nu} = \frac{i}{2}[\gamma^\mu, \gamma^\nu] \\ & \gamma^\mu\gamma^5, & \gamma^5 \end{array} \tag{B.2}$$

The latter two operators containing γ_5 define pseudo-vector or pseudo-scalar objects, breaking parity conservation. In what follows we neglect the difference between proton and neutron masses and take $M_p \approx M_n \equiv M$.

Vector part

We consider first the vector part V^μ, which is invariant under parity. It can be built out of the first three matrices listed in Eq. (B.2). We can easily see that there exist five possibilities, each one can be multiplied by a scalar quantity, called form factor (FF), function of the available Lorentz scalars. Besides the masses, there is only one independent scalar, q^2, since $p^2 = p'^2 = M^2$ and $p\cdot p' = M^2 - q^2/2$, using that $q^\mu = p^\mu - p'^\mu$. Thus, in general, using only Lorentz symmetry and parity invariance:

$$\begin{aligned} V^\mu =& F_1(q^2)\gamma^\mu + F_2(q^2)(p^\mu - p'^\mu) + F_3(q^2)(p^\mu + p'^\mu) \\ &+ F_4(q^2)\sigma^{\mu\nu}(p_\nu - p'_\nu) + F_5(q^2)\sigma^{\mu\nu}(p_\nu + p'_\nu) \end{aligned} \tag{B.3}$$

Not all of the five terms above are independent. Using the Dirac equation one can show that:

$$\bar{u}(p')\sigma_{\mu\nu}(p+p')^\nu u(p) = i\bar{u}(p')(p'-p)_\mu u(p) \tag{B.4}$$

and therefore it is possible to omit the last term $F_5(q^2)$ since it is already included in $F_2(q^2)$. Thanks to the Gordon identity,

$$2M\bar{u}(p')\gamma^\mu u(p) = \bar{u}(p')\left[(p'^\mu + p^\mu) + i\sigma^{\mu\nu}(p_\nu - p'_\nu)\right]u(p) \tag{B.5}$$

we can eliminate also the term proportional to $F_3(q^2)$ and we are left with:

$$V^\mu = F_1(q^2)\gamma^\mu + F_2(q^2)(p^\mu - p'^\mu) + F_4(q^2)\sigma^{\mu\nu}(p_\nu - p'_\nu). \tag{B.6}$$

In the literature different sets of FFs are used. In this work we redefine them as

$$V^\mu = F_1(q^2)\gamma^\mu + F_2(q^2)\frac{i\sigma^{\mu\nu}q_\nu}{2M} + F_3(q^2)\frac{q^\mu}{M} \tag{B.7}$$

where are FFs are dimensionless.

Time reversal invariance of strong interactions implies that form factors F_j are all real (that is why the imaginary unit was put into the F_2 term). G-parity (a combination of charge conjugation and isospin rotation of an angle π along the Y axis) in turn leads to the conclusion that $F_3 = 0$. This is often referred to as absence of a "second class vector current". A detailed derivation can be found in [254].

Assuming isospin symmetry, the vector part of the weak charged current is a member of a triplet of currents which are supposed to be conserved (CVC - "conserved vector current" hypothesis). Another member of the triplet is the isovector part of the electromagnetic current. This allows to express the matrix elements of the vector part of the weak current in terms of electromagnetic FFs: isoscalar parts of the electromagnetic currents cancel out. For charge current transitions we obtain:

$$F_j^V = F_j^p - F_j^n, \tag{B.8}$$

where $F_j^{p/n}$ are the electromagnetic FFs introduced in the standard expressions for the electromagnetic current matrix elements:

$$\langle N; p'|J^\mu_{em}|N; p\rangle = \bar{u}(p')\Gamma^\mu_{N,em}u(p) \tag{B.9}$$

$$\Gamma^\mu_{N,em} = F_1^N(q^2)\gamma^\mu + F_2^N(q^2)\frac{i\sigma^{\mu\nu}q_\nu}{2M} \tag{B.10}$$

with N standing for either proton or neutron.

Axial part

We can follow the same initial steps to get the axial part of the vertex. This time, however, we make use of two latter terms from Eq. (B.2),

$$A^\mu = \quad G_A(q^2)\gamma^\mu\gamma_5 + \frac{G_P(q^2)}{M}q^\mu\gamma_5 + \frac{G_3(q^2)}{M}(p^\mu + p'^\mu)\gamma_5 \tag{B.11}$$

Invariance of strong interactions under time reversal implies that G_A, G_P, G_3 are real. G-parity leads to the constrain $G_3 = 0$, like in the case of vector current also referred to the absence of the "second class current".

The value of $G_A(0) \approx 1.26$ can be determined from β decay. On the other hand, G_A and G_P are related by means of PCAC – "partial conservation of axial current" hypothesis. It states that the axial current is conserved in the chiral limit, and that its divergence scales with the pion mass. Thus, in the soft pion limit, we have

$$\partial_\mu A^\mu_a = -f_\pi m_\pi^2 \phi_a \tag{B.12}$$

where f_π is the pion decay constant and ϕ_a is the pion field. This, together with the assumption of the "pion pole dominance", allows us to express G_P in terms of G_A.

The main steps of the derivation of the relation between G_P and G_A are as follows:

1. From Eq. (B.11), taking $G_3 = 0$, the divergence of the axial current is

$$q_\mu A^\mu = 2MG_A(q^2)\gamma_5 + q^2 \frac{G_P(q^2)}{M}\gamma_5 \tag{B.13}$$

   where we have made use of the Dirac equation of motion.

2. In the limit of vanishing pion mass the current is conserved so

$$G_P \underset{m_\pi \to 0}{=} -G_A \frac{2M^2}{q^2} \tag{B.14}$$

3. The appearance of q^2 in the denominator is interpreted as resulting from a pion propagator and we get

$$G_P = G_A \frac{2M^2}{m_\pi^2 - q^2} \tag{B.15}$$

4. An extra important additional relation comes from the assumption that G_P term comes from the Feynman diagram containing the NNπ vertex, the pion propagator and π decay vertex ("pion pole dominance"). The Lagrangian for the NNπ interaction:

$$\mathscr{L}_{\mathrm{NN}\pi} = -\frac{g_{\mathrm{NN}\pi}}{f_\pi} \bar{\psi}_N \gamma_\mu \gamma^5 \left(\partial^\mu \vec{\phi}\right) \vec{\sigma} \psi_N \tag{B.16}$$

   and the pion decay vertex for π^- reads:

$$\langle 0 | A_+^\mu | \pi^- \rangle = i\sqrt{2} f_\pi q^\mu \tag{B.17}$$

   where q is pion four-momentum and $\sqrt{2}$ is an isospin factor. Finally we get:

$$\frac{G_P}{M} q^\mu \bar{u}\gamma_5 u = \left(-\sqrt{2}\, 2M \frac{g_{\mathrm{NN}\pi}}{f_\pi} \bar{u}\gamma_5 u\right) \times \left(\frac{-i}{q^2 - m_\pi^2}\right) \times \left(i\sqrt{2} f_\pi q^\mu\right) \tag{B.18}$$

   which leads to:

$$G_P = -2 g_{\mathrm{NN}\pi} \frac{2M^2}{q^2 - m_\pi^2} \tag{B.19}$$

5. After imposing limit $m_\pi \to 0$ we obtain Goldberger-Treiman relation:

$$G_A = 2 g_{\mathrm{NN}\pi} \tag{B.20}$$

Thus we finally get

$$A^\mu = \gamma^\mu \gamma_5 G_A(q^2) + \frac{q^\mu}{M} G_A(q^2) \frac{2M^2}{m_\pi^2 - q^2} \gamma_5 \tag{B.21}$$

Appendix C

Generalized Lindhard function

We present an analytical expression for the generalized Lindhard function. In this case the particle and hole states have different masses, M_h and M_p, and the particle state is not Pauli blocked. This situation describes e.g. the weak hyperon production considered in Chpt. 6.

$$\bar{U}(q,p_F) = 2\int \frac{d^3p}{(2\pi)^3}\frac{M_h}{E_p}\frac{M_p}{E_{p+q}}\frac{\theta(p_F-|\vec{p}|)}{q^0+E_p-E_{p+q}+i\varepsilon} + (q\to -q) \tag{C.1}$$

We are interested in its imaginary part which corresponds to putting both particle and hole states on-shell. Only the direct part contributes for $q^0>0$

$$\mathrm{Im}\bar{U}(q,p_F) = -\int \frac{d^3p}{(2\pi)^2}\frac{M_h}{E_p}\frac{M_p}{E_{p+q}}\theta(q^0)\theta(p_F-|\vec{p}|)\delta(q^0+E_p-E_{p+q}) \tag{C.2}$$

The integral $\int d^3p = \int |\vec{p}|^2 d|\vec{p}| d\phi d\cos\theta$ can be done using (i) rotation symmetry to integrate over ϕ and (ii) the energy conserving delta function to select an angle formed by the $\vec{p}$ and $\vec{q}$ three-vectors.

Let us introduce:

$$f(\cos\theta) = q^0 + E_p - E_{p+q}(\cos\theta) \tag{C.3}$$

$$\frac{\partial f}{\partial\cos\theta} = \frac{|\vec{p}|\,|\vec{q}|}{E_{p+q}} \tag{C.4}$$

and the solution of $f(\cos\theta)=0$ (which depends on $|\vec{p}|$) we will denominate as $\cos\theta_0$. Then:

$$\begin{aligned}
\mathrm{Im}\bar{U}(q,p_F) &= -\int \frac{|\vec{p}|^2 d|\vec{p}|}{2\pi}\frac{M_h}{E_p}\frac{M_p}{E_{p+q}}\theta(q^0)\theta(p_F-|\vec{p}|)\theta(1-\cos^2\theta_0)/\frac{\partial f}{\partial\cos\theta}\bigg|_{\cos\theta} \\
&= -\int \frac{|\vec{p}|^2 d|\vec{p}|}{2\pi}\frac{M_h}{E_p}\frac{M_p}{E_{p+q}}\theta(q^0)\theta(p_F-|\vec{p}|)\theta(1-\cos^2\theta)\frac{E_{p+q}}{|\vec{p}|\,|\vec{q}|}\bigg|_{\cos\theta_0} \\
&= -\int \frac{|\vec{p}| d|\vec{p}|}{2\pi}\frac{M_h M_p}{|\vec{q}|\,E_p}\theta(q^0)\theta(p_F-|\vec{p}|)\theta(1-\cos^2\theta)\bigg|_{\cos\theta_0} \\
&= -\int \frac{dE_p}{2\pi}\frac{M_h M_p}{|\vec{q}|}\theta(q^0)\theta(E_F-E_p)\theta(1-\cos^2\theta)\bigg|_{\cos\theta_0}
\end{aligned} \tag{C.5}$$

where in the last step we used that $E_p dE_p = |\vec{p}|d|\vec{p}|$ and $E_F = \sqrt{M_h^2+|\vec{p}|^2}$.

Now we need to find limits of integration over E_p. The upper limit cannot be larger than E_F while the lower cannot be smaller than M_h. Further kinematical conditions can be read-off from

the step function $\theta(1-\cos^2\theta_0)$ that guarantees $-1 \leq \cos\theta_0 \leq 1$. This amounts to:

$$-1 \leq \frac{q^2 + 2q^0E_p + (M_h^2 - M_p^2)}{2|\vec{p}|\,|\vec{q}|} \leq 1 \tag{C.6}$$

We will introduce λ:

$$\lambda \equiv 1 + \frac{M_h^2 - M_p^2}{q^2} \tag{C.7}$$

which is equal to 1 in the case of $M_h = M_p$.

Condition (C.6) gives a quadratic equation for E_p:

$$0 \leq -4q^2E_p^2 - 4q^0\lambda^2q^2E_p - 4|\vec{q}|^2M_h^2 - \lambda^4(q^2)^2 \tag{C.8}$$

After a short calculation we get that:

$$E_{\mp} = \frac{-q^0\lambda \mp |\vec{q}|\sqrt{\lambda^2 - 4M_h^2/q^2}}{2} \tag{C.9}$$

Looking at Eq. (C.8), the condition is fulfilled for $E_p \leq E_-$ or $E_p \geq E_+$. The first solution is always negative and therefore not physical. The other one gives a lower boundary for E_p. Finally

$$\mathrm{Im}\bar{U}(q, p_F) = -\frac{M_hM_p}{2\pi|\vec{q}|}\theta(q^0)\theta(E_F - E_{\min})(E_F - E_{\min}) \tag{C.10}$$

with

$$E_{\min} = \max\left(M_h, \frac{1}{2}\left(-q^0\lambda + |\vec{q}|\sqrt{\lambda^2 - 4M_h^2/q^2}\right)\right)$$

.

Appendix D

Normalization conventions

In quantum field theory we have the freedom to choose the normalization of the fermion and boson fields. Following the discussion of Ref. [99], we will introduce the normalizations:

- spinors $u(p,s)$, $v(p,s)$ of momentum p and spin s:

$$u^\dagger(\vec{p},s)u(\vec{p},s') = N2E_p\delta_{ss'} \tag{D.1}$$

  Since we consider on-shell particles, $p^0 = E_p = \sqrt{M^2+\vec{p}^2}$.

- anti-commutator relation between creation and annihilation operators $a(p,s)$, $a^\dagger(p,s)$ (and for antiparticles b, $b^\dagger$):

$$\begin{aligned}\{a(\vec{p},s),a^\dagger(\vec{p'},s')\} &= F\delta_{ss'}\delta^3(\vec{p}-\vec{p}')\\ \{b(\vec{p},s),b^\dagger(\vec{p'},s')\} &= F\delta_{ss'}\delta^3(\vec{p}-\vec{p}')\end{aligned} \tag{D.2}$$

- integration measure in the definition of the Dirac field $\psi(x)$:

$$\psi(x) = \sum_s \int \frac{d^3p}{D}\left(a(\vec{p},s)u(\vec{p},s)e^{-ipx} + b^\dagger(\vec{p},s)v(\vec{p},s)e^{ipx}\right) \tag{D.3}$$

- one-particle states:

$$|\vec{p},s\rangle = Ga^\dagger(\vec{p},s)|0\rangle \tag{D.4}$$

All the normalization factors have an implicit dependence on p. The relations between N, F and D will be restricted when we set canonical anticommutation relations for $\psi(x)$. For given indices a, b and position x we have:[1]

$$\{\psi_\alpha(\vec{x},t),\psi^\dagger_\beta(0,t)\} = \delta_{\alpha\beta}\delta^3(\vec{x}) \tag{D.5}$$

[1] Here we set the position of one of the particles to 0 since the system is invariant under translations.

Using Eq. (D.3), we get:

$$
\begin{aligned}
&\{\psi_\alpha(\vec{x},t),\psi^\dagger_\beta(0,t)\} = \psi_\alpha(\vec{x},t)\psi^\dagger_\beta(0,t)+\psi^\dagger_\beta(0,t)\psi_\alpha(\vec{x},t) = \\
&= \int \frac{d^3p}{D}\frac{d^3p'}{D'}\sum_{s,s'}\Big(a(\vec{p},s)u_\alpha(\vec{p},s)e^{-ipx}+b^\dagger(\vec{p},s)v_\alpha(\vec{p},s)e^{ipx}\Big) \\
&\qquad\qquad \times\Big(a^\dagger(\vec{p}\,',s')u^\dagger_\beta(\vec{p}\,',s')e^{iE't}+b(\vec{p}\,',s')v^\dagger_\beta(\vec{p}\,',s')e^{-iE't}\Big) \\
&+\int \frac{d^3p}{D}\frac{d^3p'}{D'}\sum_{s,s'}\Big(a^\dagger(\vec{p},s)u^\dagger_\beta(\vec{p}\,',s')e^{iE't}+b(\vec{p}\,',s)v^\dagger_\beta(\vec{p}\,',s')e^{-iE't}\Big) \\
&\qquad\qquad \times\Big(a(\vec{p},s)u_\alpha(\vec{p},s)e^{-ipx}+b^\dagger(\vec{p},s)v_\alpha(\vec{p},s)e^{ipx}\Big) \\
&= \int \frac{d^3p}{D}\frac{d^3p'}{D}\sum_{s,s'}\Big(a(\vec{p},s)a^\dagger(\vec{p}\,',s')u_\alpha(\vec{p},s)u^\dagger_\beta(\vec{p}\,',s')e^{-ipx}e^{iE't} \\
&\qquad\qquad +b^\dagger(\vec{p},s)b(\vec{p}\,',s')v_\alpha(\vec{p},s)v^\dagger_\beta(\vec{p}\,',s')e^{ipx}e^{-iE't} \\
&\qquad\qquad +a^\dagger(\vec{p}\,',s')a(\vec{p},s)u^\dagger_\beta(\vec{p}\,',s')u_\alpha(\vec{p},s)e^{-ipx}e^{iE't} \\
&\qquad\qquad +b(\vec{p}\,',s)b^\dagger(\vec{p},s)v^\dagger_\beta(\vec{p}\,',s')v_\alpha(\vec{p},s)e^{ipx}e^{-iE't}\Big) \\
&= \int \frac{d^3p}{D}\frac{d^3p'}{D'}\sum_{s,s'}\Big(\{a(\vec{p},s),a^\dagger(\vec{p}\,',s')\}u_\alpha(\vec{p},s)u^\dagger_\beta(\vec{p}\,',s')e^{-ipx}e^{iE't} \\
&\qquad\qquad +\{b^\dagger(\vec{p},s),b(\vec{p}\,',s')\}v_\alpha(\vec{p},s)v^\dagger_\beta(\vec{p}\,',s')e^{ipx}e^{-iE't}\Big)
\end{aligned}
\tag{D.6}
$$

We make use of Eq. (D.2) and the fact that $u^\dagger(\vec{p},s)=\bar{u}(\vec{p},s)\gamma^0$,

$$
\begin{aligned}
&\int \frac{d^3p}{D}\frac{d^3p'}{D'}F\sum_s\Big(u_\alpha(\vec{p},s)u^\dagger_\beta(\vec{p}\,',s)e^{-ipx}e^{iE't}+v_\alpha(\vec{p},s)v^\dagger_\beta(\vec{p}\,',s)e^{-iE't}e^{ipx}\Big)\delta^3(\vec{p}-\vec{p}\,') \\
&= \int d^3p\frac{F}{D^2}\sum_s\Big(\big[u(\vec{p},s)u^\dagger(\vec{p},s)\big]_{\alpha\beta}e^{-ipx}e^{iEt}+\big[v(\vec{p},s)v^\dagger(\vec{p},s)\big]_{\alpha\beta}e^{-iEt}e^{ipx}\Big) \\
&= \int d^3p\frac{F}{D^2}\sum_s\Big(\big[u(\vec{p},s)\bar{u}(\vec{p},s)\gamma^0\big]_{\alpha\beta}e^{i\vec{p}\vec{x}}+\big[v(\vec{p},s)\bar{v}(\vec{p},s)\gamma^0\big]_{\alpha\beta}e^{-i\vec{p}\vec{x}}\Big) \\
&= \int d^3p\frac{NF}{D^2}\Big(\big[(E_p\gamma^0-\vec{p}\vec{\gamma}+M)\gamma^0\big]_{\alpha\beta}e^{i\vec{p}\vec{x}}+\big[(E_p\gamma^0-\vec{p}\vec{\gamma}-M)\gamma^0\big]_{\alpha\beta}e^{-i\vec{p}\vec{x}}\Big)
\end{aligned}
\tag{D.7}
$$

In the second integral we change $\vec{p}\to-\vec{p}$:

$$
\begin{aligned}
&\int d^3p\frac{NF}{D^2}\Big(\big[(E_p\gamma^0-\vec{p}\vec{\gamma}+M)\gamma^0\big]_{\alpha\beta}e^{i\vec{p}\vec{x}}+\big[(E_p\gamma^0+\vec{p}\vec{\gamma}-M)\gamma^0\big]_{\alpha\beta}e^{i\vec{p}\vec{x}}\Big) \\
&= \int d^3p\frac{NF}{D^2}\Big(\big[2E_p\gamma^0\gamma^0\big]_{\alpha\beta}e^{i\vec{p}\vec{x}}\Big)=\int d^3p\frac{2NFE_p}{D^2}e^{i\vec{p}\vec{x}}\delta_{\alpha\beta}
\end{aligned}
\tag{D.8}
$$

Finally we want Eq. (D.5), so:

$$\int d^3p \frac{2NFE_p}{D^2} e^{-i\vec{p}\vec{x}} \delta_{\alpha\beta} = \delta_{\alpha\beta}\delta^3(\vec{x}) \tag{D.9}$$

Now we can use the identity:

$$\int d^3p\, e^{i\vec{p}\vec{x}} = (2\pi)^3\delta^3(\vec{x}) \tag{D.10}$$

to obtain a relation between D, F and N:

$$\frac{FN}{D^2} = \frac{1}{(2\pi)^3 2E_p} \tag{D.11}$$

Next, let us express the probability density (since we deal with quantized fermionic fields, we will in fact consider a single-particle expectation value of this operator):

$$\rho = \langle p,s|\psi^\dagger(x)\psi(x)|p,s\rangle \tag{D.12}$$

After a short calculations we get:

$$\rho = \frac{FG^2}{(2\pi)^3}. \tag{D.13}$$

It has the same physical interpretation as in quantum mechanics. A free solution of Dirac equation is not properly normalized and to treat physical particles, one has to define wave packets which are normalized to a finite number (the most natural would be normalization to 1 if a field represents a single particle state). Here, for the sake of simplicity, we will use that the states are normalized in a finite volume V.

Phase space per particle can be read off using completeness relations:

$$\int \frac{d^3p}{X}|p,s\rangle\langle p,s| = 1 \quad \rightarrow \quad X = FG^2 = (2\pi)^3\rho \tag{D.14}$$

The relation between the scattering probability amplitude and the invariant matrix element $\mathscr{M}_{i\to f}$ depends on the chosen normalization:

$$\begin{aligned}\langle f|S-1|i\rangle &= -i(2\pi)^4\delta^4(p_A+p_B-\sum_i p_i)\prod_{i\in A,B,1,..n}\left(\frac{F_iG_i}{D_i}\right)\mathscr{M}_{i\to f}\\ &= -i(2\pi)^4\delta^4(p_A+p_B-\sum_i p_i)\prod_{i\in A,B,1,..n}\left(\frac{\rho_i}{2E_iN_i}\right)^{1/2}\mathscr{M}_{i\to f}\end{aligned} \tag{D.15}$$

where the initial and final scattering states have defined momentum.

The transition probability $i\to f$ per unit time and unit volume is:

$$|\langle f|S-1|i\rangle|^2 = \frac{P_{i\to f}}{dVdt} = (2\pi)^4\delta^4(p_A+p_B-\sum_i p_i)\prod_{i\in A,B,1,..n}\left(\frac{\rho_i}{2E_iN_i}\right)|\mathscr{M}_{i\to f}|^2 \tag{D.16}$$

Let us consider the cross section for the process $A+B\to 1+2+...+n$. The incident particles A and B move with velocities $\vec{v}_A$ and $\vec{v}_B$. In the rest frame of particles A, we have that the incident flux of B particles is given by $f = N_B/dSdt = N_B/dV\times dl/dt = \rho_B(\vec{v}_A-\vec{v}_B)$. The cross section is defined as the transition probability per target density $\rho_A\times$ incident flux of particles B, $\rho_B(v_A-v_B)$,

$$\sigma = \frac{1}{\rho_A\rho_B(v_A-v_B)}\int\left(\prod_{k=1}^n\frac{d^3p_k}{(2\pi)^3\rho_k}\right)\frac{P_{i\to f}}{dVdt} \tag{D.17}$$

The phase space per outgoing particle is taken from Eq. (D.14). We use that:

$$|\vec{v}_A - \vec{v}_B| = \frac{[(p_A \cdot p_B)^2 - m_A^2 m_B^2]^{1/2}}{E_A E_B} \tag{D.18}$$

And finally we get:

$$\begin{aligned}
\sigma &= \frac{E_A E_B}{\rho_A \rho_B [(p_A \cdot p_B)^2 - m_A^2 m_B^2]^{1/2}} \\
&\times \frac{\rho_A \rho_B}{4 E_A E_B N_A N_B} \int \left(\prod_{k=1}^{n} \frac{d^3 p_k}{2 E_k N_k} \right) (2\pi)^4 \delta^4 (p_A + p_B - \sum_k p_k) |\mathscr{M}_{i \to f}|^2 \\
&= \frac{1}{4 N_A N_B [(p_A \cdot p_B)^2 - m_A^2 m_B^2]^{1/2}} \int \left(\prod_{k=1}^{n} \frac{d^3 p_k}{2 E_k N_k} \right) (2\pi)^4 \delta^4 (p_A + p_B - \sum_k p_k) |\mathscr{M}_{i \to f}|^2
\end{aligned} \tag{D.19}$$

As could be predicted, the result does not depend on the chosen normalization except for N_i factors (spinor normalization), which also enter in the invariant matrix element $\mathscr{M}_{i \to f}$ and will cancel out.

Appendix E

Kinematics for τ production off nucleons

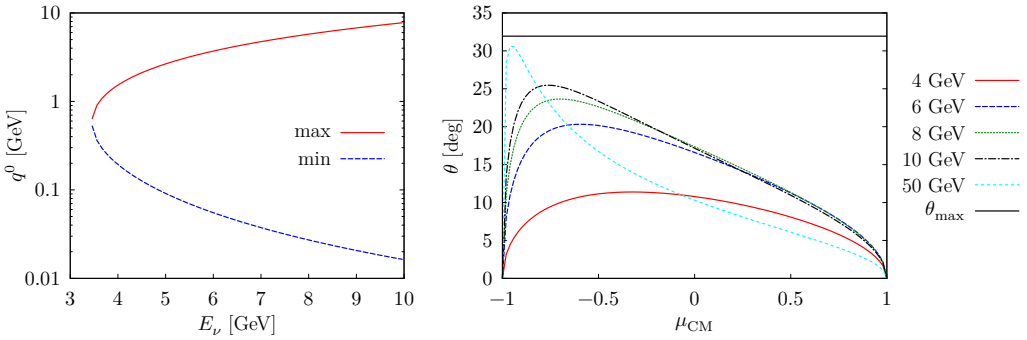

FIGURE E.1: Left: Maximum and minimum LAB lepton transferred energies ($q^0_{\rm max,min} = E_\nu - E_{k'}^{\rm min,max}$) as a function of the incoming neutrino energy for weak τ production off nucleons. Right: LAB $\tau-$lepton scattering angle (deg) as a function of $\mu_{\rm CM}$, or equivalently of the LAB outgoing tau energy, for several incoming neutrino LAB energies: $E_\nu = 4$ GeV (solid–red), 6 GeV (dashed–blue), 8 GeV (dotted–green), 10 GeV (dot-dashed–black) and 50 GeV (short-dashed–cyan). In addition, the horizontal black–solid line stands for the upper bound, $\theta_{\rm max} = \arcsin\left(M/m_\tau\right)$, that is reached in the $E_\nu \gg M, m_\tau$ limit.

We will collect here some kinematical relations for the two body reaction

$$\nu_\ell(E_\nu) N \to \ell(k') N' \,, \quad \ell = e, \mu, \tau \tag{E.1}$$

paying a special attention to the differences induced by the large mass of the τ, with respect to the $\mu-$ and $e-$lepton cases. The LAB threshold neutrino energy, $E^{\rm th}_{\nu_\ell} = m_\ell + m_\ell^2/2M$, is around 3.5 GeV ($\sim 2m_\tau$) for τ production, while the correction ($m_\ell^2/2M$) to m_ℓ is negligible for muons and electrons. Taking the incoming neutrino in the positive $Z-$axis, the lepton scattering angle, $\theta_{\rm CM}$, in the neutrino-nucleon center of mass (CM) frame is not limited and thus, $\mu_{\rm CM} = \cos\theta_{\rm CM}$ can take any value between -1 and 1. The lepton energy ($E_{k'}$) and scattering angle (θ) in the LAB system are obtained through

$$E_{k'} = \frac{(E_\nu + M) E^{\rm CM}_{k'} + \mu_{\rm CM} E_\nu |\vec{k}'|^{\rm CM}}{\sqrt{s}} \,, \quad s = 2ME_\nu + M^2 \,, \quad E^{\rm CM}_{k'} = \frac{s + m_\ell^2 - M^2}{2\sqrt{s}} \tag{E.2}$$

$$\tan\theta = \frac{\sqrt{s}}{E_\nu + M} \frac{\sqrt{1-\mu^2_{\rm CM}}}{\mu_{\rm CM} + a} \,, \qquad a = \frac{E_\nu}{E_\nu + M} \frac{E^{\rm CM}_{k'}}{|\vec{k}'|^{\rm CM}} \tag{E.3}$$

with $|\vec{k}'|^{\rm CM} = \sqrt{(E_{k'}^{\rm CM})^2 - m_\ell^2}$. The maximum and minimum LAB energies of the outgoing lepton correspond to $\mu_{\rm CM} = +1$ and -1, respectively, and they read

$$E_{k'}^{\rm max} = \frac{(E_\nu + M)E_{k'}^{\rm CM} + E_\nu |\vec{k}'|^{\rm CM}}{\sqrt{s}}, \qquad E_{k'}^{\rm min} = \frac{(E_\nu + M)E_{k'}^{\rm CM} - E_\nu |\vec{k}'|^{\rm CM}}{\sqrt{s}} \tag{E.4}$$

The range of transferred energies to the nucleon in the LAB system, and for $\tau-$lepton production, is shown in the left panel of Fig. E.1 as a function of E_ν, up to 10 GeV.

The parameter $a > 0$, introduced in Eq. (E.3), plays an important role to determine the LAB angular distribution. It diverges at threshold and it becomes 1 when $E_\nu \gg M, m_\ell$. For muon production $a < 1$, except for a very narrow region (~ 1 MeV) comprised between threshold and $E_\nu^{a=1} = m_\mu(M - m_\mu/2)/(M - m_\mu)$, with m_μ the muon mass[1]. The situation, conveniently rescaled, is similar for electron production. For τ production, however, a is a decreasing monotone function, being always greater than 1 and reaching this latter value only in the $E_\nu \to \infty$ limit. Thus, we have

- $a < 1$ (muon and electron production): The LAB lepton scattering angle θ can take any value between 0 and π, with $\theta > \pi/2$ ($\theta \leq \pi/2$) for $\mu_{\rm CM} < -a$ ($\mu_{\rm CM} \geq -a$). Furthermore, there is a biunivocal correspondence between $\mu_{\rm CM}$ and $\cos\theta$, and hence between the LAB variables $E_{k'}$ and $\cos\theta$. Namely, neglecting the muon or electron masses with respect to that of the nucleon or the neutrino energy, one finds

$$E_{k'} = \frac{ME_\nu}{M + E_\nu - E_\nu \cos\theta} \tag{E.5}$$

- $a > 1$ (tau production): We see that $\tan\theta$ is always greater than zero, and therefore $\theta < \pi/2$. Actually, $\tan\theta$, seen as a function of $\mu_{\rm CM}$ or equivalently of the LAB outgoing tau energy, has a maximum for $\mu_{\rm CM} = -1/a < 0$. We find that the maximum lepton scattering angle in the LAB frame, $\theta_{\rm max}$, is

$$\theta_{\rm max} = \arcsin\left(\frac{\sqrt{s}|\vec{k}'|^{\rm CM}}{E_\nu m_\tau}\right) < \arcsin\left(\frac{M}{m_\tau}\right) \sim 31.9^o \tag{E.6}$$

  where the upper bound is reached for $E_\nu \gg M, m_\tau$. The dependence of θ on $\mu_{\rm CM}$ is shown in the right panel of Fig. E.1 for different incoming neutrino LAB energies. We observe that any LAB $\tau-$scattering angle is obtained for two different values of $\mu_{\rm CM}$ (two different values of the LAB $\tau-$energy, $E_{k'}$, as inferred from Eq. (E.2)), and hence the $(\theta, \mu_{\rm CM})-$correspondence is not biunivocal in this case. One of the solutions (A) always corresponds to the $\tau-$lepton coming out backwards in the CM frame ($\mu_{\rm CM} < -1/a \leftrightarrow \theta_{\rm CM} > \pi/2$). For the second one (B) $\mu_{\rm CM} > -1/a$, which depending on the neutrino energy and on θ might also correspond to $\mu_{\rm CM} < 0$. The CM to LAB boost transforms both CM configurations into quite forward scattering in the LAB system ($\theta < 32^o$). The B–solution gives rise to a larger (smaller) outgoing LAB $\tau-$energy (transferred energy $q^0 = E_\nu - E_{k'}$) than the A one. The details of the $\theta(\mu_{\rm CM})$ distribution depends on the incoming neutrino energy, as can be seen in Fig. E.1, and its asymmetry becomes more pronounced as E_ν grows, with the the maximum position approaching to $\mu_{\rm CM} = -1$ and θ at the maximum to $\theta_{\rm max}$.

  This is the kinematics that always applies for $\tau-$production, while as mentioned for muon or electron weak production, the parameter a is greater than zero only for a very

[1] The parameter a takes the value of 1 for $E_\nu = E_\nu^{a=1}$, reaches a minimum above this energy and after, it begins to grow approaching the asymptotic value of 1 for large neutrino energies.

narrow range of LAB neutrino energies comprised between $m_\ell + m_\ell^2/2M$ and $m_\ell(M - m_\ell/2)/(M - m_\ell)$, with $\ell = e, \mu$.

List of Figures

List of Tables

Bibliography

[1] L. Alvarez-Ruso et al. “NuSTEC White Paper: Status and challenges of neutrino–nucleus scattering”. In: *Prog. Part. Nucl. Phys.* 100 (2018), pp. 1–68. DOI: 10.1016/j.ppnp.2018.01.006.

[2] P. Fernandez de Cordoba and E. Oset. “Semiphenomenological approach to nucleon properties in nuclear matter”. In: *Phys. Rev.* C46 (1992), pp. 1697–1709. DOI: 10.1103/PhysRevC.46.1697.

[3] J. Nieves, Jose Enrique Amaro, and M. Valverde. “Inclusive quasi-elastic neutrino reactions”. In: *Phys.Rev.* C70 (2004), p. 055503. DOI: 10.1103/PhysRevC.70.055503, 10.1103/PhysRevC.72.019902.

[4] Juan Nieves and Joanna Ewa Sobczyk. “In medium dispersion relation effects in nuclear inclusive reactions at intermediate and low energies”. In: *Annals Phys.* 383 (2017), pp. 455–496. DOI: 10.1016/j.aop.2017.06.002.

[5] E. Marco, E. Oset, and P. Fernandez de Cordoba. “Mesonic and binding contributions to the EMC effect in a relativistic many body approach”. In: *Nucl. Phys.* A611 (1996), pp. 484–513. DOI: 10.1016/S0375-9474(96)00289-8.

[6] A. Gil, J. Nieves, and E. Oset. “Many body approach to the inclusive (e, e-prime) reaction from the quasielastic to the Delta excitation region”. In: *Nucl.Phys.* A627 (1997), pp. 543–598. DOI: 10.1016/S0375-9474(97)00513-7.

[7] E. Oset et al. “A Review on mesonic decay of Lambda hypernuclei”. In: *Prog. Theor. Phys. Suppl.* 117 (1994), pp. 461–476. DOI: 10.1143/PTPS.117.461.

[8] E. Marco and E. Oset. “Mesonic and binding contributions to the nuclear Drell-Yan process”. In: *Nucl. Phys.* A645 (1999), pp. 303–313. DOI: 10.1016/S0375-9474(98)00607-1.

[9] M. Sajjad Athar, S. K. Singh, and M. J. Vicente Vacas. “Nuclear effects in F(3) structure function of nucleon”. In: *Phys. Lett.* B668 (2008), pp. 133–142. DOI: 10.1016/j.physletb.2008.08.019.

[10] M. Sajjad Athar, I. Ruiz Simo, and M. J. Vicente Vacas. “Nuclear medium modification of the F(2)(x,Q**2) structure function”. In: *Nucl. Phys.* A857 (2011), pp. 29–41. DOI: 10.1016/j.nuclphysa.2011.03.008.

[11] Daniel S. Koltun. “Theory of mean removal energies for single particles in nuclei”. In: *Phys. Rev.* C9 (1974), pp. 484–497. DOI: 10.1103/PhysRevC.9.484.

[12] Omar Benhar, Donal Day, and Ingo Sick. “Inclusive quasi-elastic electron-nucleus scattering”. In: *Rev. Mod. Phys.* 80 (2008), pp. 189–224. DOI: 10.1103/RevModPhys.80.189.

[13] Omar Benhar et al. “Neutrino-nucleus interactions and the determination of oscillation parameters”. In: *Phys. Rept.* 700 (2017), pp. 1–47. DOI: 10.1016/j.physrep.2017.07.004.

[14] Artur M. Ankowski, Omar Benhar, and Makoto Sakuda. “Improving the accuracy of neutrino energy reconstruction in charged-current quasielastic scattering off nuclear targets”. In: *Phys. Rev.* D91.3 (2015), p. 033005. DOI: 10.1103/PhysRevD.91.033005.

[15] Omar Benhar et al. “Electron- and neutrino-nucleus scattering in the impulse approximation regime”. In: *Phys.Rev.* D72 (2005), p. 053005. DOI: 10.1103/PhysRevD.72.053005.

[16] Omar Benhar and Davide Meloni. “Total neutrino and antineutrino nuclear cross-sections around 1-GeV”. In: *Nucl.Phys.* A789 (2007), pp. 379–402. DOI: 10.1016/j.nuclphysa.2007.02.015.

[17] Omar Benhar and Davide Meloni. “Impact of nuclear effects on the determination of the nucleon axial mass”. In: *Phys.Rev.* D80 (2009), p. 073003. DOI: 10.1103/PhysRevD.80.073003.

[18] Omar Benhar, Pietro Coletti, and Davide Meloni. “Electroweak nuclear response in quasi-elastic regime”. In: *Phys.Rev.Lett.* 105 (2010), p. 132301. DOI: 10.1103/PhysRevLett.105.132301.

[19] Erica Vagnoni, Omar Benhar, and Davide Meloni. “Inelastic Neutrino-Nucleus Interactions within the Spectral Function Formalism”. In: *Phys. Rev. Lett.* 118.14 (2017), p. 142502. DOI: 10.1103/PhysRevLett.118.142502.

[20] O. Buss et al. “Transport-theoretical Description of Nuclear Reactions”. In: *Phys.Rept.* 512 (2012), pp. 1–124. DOI: 10.1016/j.physrep.2011.12.001.

[21] Jose Enrique Amaro et al. “Using electron scattering superscaling to predict charge-changing neutrino cross sections in nuclei”. In: *Phys.Rev.* C71 (2005), p. 015501. DOI: 10.1103/PhysRevC.71.015501.

[22] V. Pandey et al. “Low-energy excitations and quasielastic contribution to electron-nucleus and neutrino-nucleus scattering in the continuum random-phase approximation”. In: *Phys. Rev.* C92.2 (2015), p. 024606. DOI: 10.1103/PhysRevC.92.024606.

[23] M. Martini et al. “Neutrino and antineutrino quasielastic interactions with nuclei”. In: *Phys.Rev.* C81 (2010), p. 045502. DOI: 10.1103/PhysRevC.81.045502.

[24] V. Pandey et al. “Impact of low-energy nuclear excitations on neutrino-nucleus scattering at MiniBooNE and T2K kinematics”. In: *Phys. Rev.* C94.5 (2016), p. 054609. DOI: 10.1103/PhysRevC.94.054609.

[25] N. Rocco et al. “Electromagnetic scaling functions within the Green’s Function Monte Carlo approach”. In: *Phys. Rev.* C96 (2017), p. 015504. DOI: 10.1103/PhysRevC.96.015504.

[26] http://www.dunescience.org.

[27] O. Benhar et al. “Spectral function of finite nuclei and scattering of GeV electrons”. In: *Nucl. Phys.* A579 (1994), pp. 493–517. DOI: 10.1016/0375-9474(94)90920-2.

[28] J. A. Caballero et al. “Scaling and isospin effects in quasielastic lepton-nucleus scattering in the Relativistic Mean Field Approach”. In: *Phys. Lett.* B653 (2007), pp. 366–372. DOI: 10.1016/j.physletb.2007.08.018.

[29] O. Benhar, A. Fabrocini, and S. Fantoni. “The Nucleon Spectral Function in Nuclear Matter”. In: *Nucl. Phys.* A505 (1989), pp. 267–299. DOI: 10.1016/0375-9474(89)90374-6.

[30] S. K. Singh and M. J. Vicente Vacas. “Weak quasi-elastic production of hyperons”. In: *Phys. Rev.* D74 (2006), p. 053009. DOI: 10.1103/PhysRevD.74.053009.

[31] Stefan Meinel. “$\Lambda_c \to N$ form factors from lattice QCD and phenomenology of $\Lambda_c \to n\ell^+\nu_\ell$ and $\Lambda_c \to p\mu^+\mu^-$ decays”. In: *Phys. Rev.* D97.3 (2018), p. 034511. DOI: 10.1103/PhysRevD.97.034511.

[32] R. Perez-Marcial et al. "Predictions for Semileptonic Decays of Charm Baryons. 2. Nonrelativistic and MIT Bag Quark Models". In: *Phys. Rev.* D40 (1989). [Erratum: Phys. Rev.D44,2203(1991)], p. 2955. DOI: 10.1103/PhysRevD.44.2203,10.1103/PhysRevD.40.2955.

[33] Thomas Gutsche et al. "Heavy-to-light semileptonic decays of Λ_b and Λ_c baryons in the covariant confined quark model". In: *Phys. Rev.* D90.11 (2014). [Erratum: Phys. Rev.D94,no.5,059902(2016)], p. 114033. DOI: 10.1103/PhysRevD.90.114033,10.1103/PhysRevD.94.059902.

[34] Thomas Gutsche et al. "Semileptonic decays $\Lambda_c^+ \to \Lambda \ell^+ \nu_\ell$ $(\ell = e, \mu)$ in the covariant quark model and comparison with the new absolute branching fraction measurements of Belle and BESIII". In: *Phys. Rev.* D93.3 (2016), p. 034008. DOI: 10.1103/PhysRevD.93.034008.

[35] Md Mozammel Hussain and Winston Roberts. "Λ_c Semileptonic Decays in a Quark Model". In: *Phys. Rev.* D95.5 (2017). [Addendum: Phys. Rev.D95,no.9,099901(2017)], p. 053005. DOI: 10.1103/PhysRevD.95.099901,10.1103/PhysRevD.95.053005.

[36] Krzysztof M. Graczyk. "Tau polarization in quasielastic charge-current neutrino (antineutrino) -nucleus scattering". In: *Nucl.Phys.* A748 (2005), pp. 313–330. DOI: 10.1016/j.nuclphysa.2004.10.029.

[37] H. Bethe and R. Peierls. "The 'neutrino'". In: *Nature* 133 (1934), p. 532. DOI: 10.1038/133532a0.

[38] Murray Gell-Mann and A. Pais. "Behavior of neutral particles under charge conjugation". In: *Phys. Rev.* 97 (1955), pp. 1387–1389. DOI: 10.1103/PhysRev.97.1387.

[39] G. Danby et al. "Observation of High-Energy Neutrino Reactions and the Existence of Two Kinds of Neutrinos". In: *Phys. Rev. Lett.* 9 (1962), pp. 36–44. DOI: 10.1103/PhysRevLett.9.36.

[40] B. Pontecorvo. "Neutrino Experiments and the question of lepton charge conservation". In: *Zh. Eksp. Teor. Fiz.* 53 (1967). [Zh. Eksp. Teor. Fiz.53: 1717-25(Nov. 1967), pp. 1717–25.

[41] Christian Spiering. "Towards High-Energy Neutrino Astronomy. A Historical Review". In: *Eur. Phys. J.* H37 (2012), pp. 515–565. DOI: 10.1140/epjh/e2012-30014-2.

[42] R. Davis. "Solar neutrinos. II: Experimental". In: *Phys. Rev. Lett.* 12 (1964). [,107(1964)], pp. 303–305. DOI: 10.1103/PhysRevLett.12.303.

[43] Y. Fukuda et al. "Measurements of the solar neutrino flux from Super-Kamiokande's first 300 days". In: *Phys. Rev. Lett.* 81 (1998). [Erratum: Phys. Rev. Lett.81,4279(1998)], pp. 1158–1162. DOI: 10.1103/PhysRevLett.81.1158,10.1103/PhysRevLett.81.4279. arXiv: hep-ex/9805021 [hep-ex].

[44] P. Anselmann et al. "Solar neutrinos observed by GALLEX at Gran Sasso." In: *Phys. Lett.* B285 (1992), pp. 376–389. DOI: 10.1016/0370-2693(92)91521-A.

[45] W. Hampel et al. "GALLEX solar neutrino observations: Results for GALLEX IV". In: *Phys. Lett.* B447 (1999), pp. 127–133. DOI: 10.1016/S0370-2693(98)01579-2.

[46] J. N. Abdurashitov et al. "Measurement of the solar neutrino capture rate with gallium metal". In: *Phys. Rev.* C60 (1999), p. 055801. DOI: 10.1103/PhysRevC.60.055801. arXiv: astro-ph/9907113 [astro-ph].

[47] Q. R. Ahmad et al. "Measurement of the rate of $\nu_e + d \to p + p + e^-$ interactions produced by ^8B solar neutrinos at the Sudbury Neutrino Observatory". In: *Phys. Rev. Lett.* 87 (2001), p. 071301. DOI: 10.1103/PhysRevLett.87.071301. arXiv: nucl-ex/0106015 [nucl-ex].

[48] K. Eguchi et al. “First results from KamLAND: Evidence for reactor anti-neutrino disappearance”. In: *Phys. Rev. Lett.* 90 (2003), p. 021802. DOI: 10.1103/PhysRevLett.90.021802. arXiv: hep-ex/0212021 [hep-ex].

[49] Y. Fukuda et al. “Evidence for oscillation of atmospheric neutrinos”. In: *Phys. Rev. Lett.* 81 (1998), pp. 1562–1567. DOI: 10.1103/PhysRevLett.81.1562. arXiv: hep-ex/9807003 [hep-ex].

[50] D. G. Michael et al. “Observation of muon neutrino disappearance with the MINOS detectors and the NuMI neutrino beam”. In: *Phys. Rev. Lett.* 97 (2006), p. 191801. DOI: 10.1103/PhysRevLett.97.191801. arXiv: hep-ex/0607088 [hep-ex].

[51] K. Abe et al. “Precise Measurement of the Neutrino Mixing Parameter θ_{23} from Muon Neutrino Disappearance in an Off-Axis Beam”. In: *Phys. Rev. Lett.* 112.18 (2014), p. 181801. DOI: 10.1103/PhysRevLett.112.181801. arXiv: 1403.1532 [hep-ex].

[52] M. G. Aartsen et al. “PINGU: A Vision for Neutrino and Particle Physics at the South Pole”. In: *J. Phys.* G44.5 (2017), p. 054006. DOI: 10.1088/1361-6471/44/5/054006. arXiv: 1607.02671 [hep-ex].

[53] S. Adrian-Martinez et al. “Letter of intent for KM3NeT 2.0”. In: *J. Phys.* G43.8 (2016), p. 084001. DOI: 10.1088/0954-3899/43/8/084001. arXiv: 1601.07459 [astro-ph.IM].

[54] K. Abe et al. “Letter of Intent: The Hyper-Kamiokande Experiment — Detector Design and Physics Potential —”. In: (2011). arXiv: 1109.3262 [hep-ex].

[55] Xinheng Guo et al. “A Precision measurement of the neutrino mixing angle θ_{13} using reactor antineutrinos at Daya-Bay”. In: (2007). arXiv: hep-ex/0701029 [hep-ex].

[56] Y. Abe et al. “Improved measurements of the neutrino mixing angle θ_{13} with the Double Chooz detector”. In: *JHEP* 10 (2014). [Erratum: JHEP02,074(2015)], p. 086. DOI: 10.1007/JHEP02(2015)074, 10.1007/JHEP10(2014)086. arXiv: 1406.7763 [hep-ex].

[57] J. K. Ahn et al. “Observation of Reactor Electron Antineutrino Disappearance in the RENO Experiment”. In: *Phys. Rev. Lett.* 108 (2012), p. 191802. DOI: 10.1103/PhysRevLett.108.191802. arXiv: 1204.0626 [hep-ex].

[58] R. Acciarri et al. “Long-Baseline Neutrino Facility (LBNF) and Deep Underground Neutrino Experiment (DUNE)”. In: (2015). arXiv: 1512.06148 [physics.ins-det].

[59] K. Abe et al. “A Long Baseline Neutrino Oscillation Experiment Using J-PARC Neutrino Beam and Hyper-Kamiokande”. In: 2014. arXiv: 1412.4673 [physics.ins-det].

[60] Cristina Volpe. “Neutrino Astrophysics”. In: *Acta Phys. Polon. Supp.* 9 (2016), p. 769. DOI: 10.5506/APhysPolBSupp.9.769.

[61] Andrea Meucci and Carlotta Giusti. “Relativistic Green’s function model in charged-current quasielastic neutrino and antineutrino scattering at MINERvA kinematics”. In: *Phys. Rev.* D89.11 (2014), p. 117301. DOI: 10.1103/PhysRevD.89.117301.

[62] Andrea Meucci and Carlotta Giusti. “Relativistic Green’s function model and charged-current inclusive neutrino-nucleus scattering at T2K kinematics”. In: *Phys. Rev.* D91.9 (2015), p. 093004. DOI: 10.1103/PhysRevD.91.093004.

[63] Noemi Rocco, Alessandro Lovato, and Omar Benhar. “Unified description of electron-nucleus scattering within the spectral function formalism”. In: *Phys. Rev. Lett.* 116.19 (2016), p. 192501. DOI: 10.1103/PhysRevLett.116.192501.

[64] K. Gallmeister, U. Mosel, and J. Weil. “Neutrino-Induced Reactions on Nuclei”. In: *Phys. Rev.* C94.3 (2016), p. 035502. DOI: 10.1103/PhysRevC.94.035502.

[65] M. Martini et al. "Electron-neutrino scattering off nuclei from two different theoretical perspectives". In: *Phys. Rev.* C94.1 (2016), p. 015501. DOI: 10.1103/PhysRevC.94.015501.

[66] G. D. Megias et al. "Charged-current neutrino-nucleus reactions within the SuSAv2-MEC approach". In: *Phys. Rev.* D94.9 (2016), p. 093004. DOI: 10.1103/PhysRevD.94.093004.

[67] S. X. Nakamura et al. "Towards a Unified Model of Neutrino-Nucleus Reactions for Neutrino Oscillation Experiments". In: *Rept. Prog. Phys.* 80.5 (2017), p. 056301. DOI: 10.1088/1361-6633/aa5e6c. arXiv: 1610.01464 [nucl-th].

[68] Artur M Ankowski and Camillo Mariani. "Systematic uncertainties in long-baseline neutrino-oscillation experiments". In: *J. Phys.* G44.5 (2017), p. 054001. DOI: 10.1088/1361-6471/aa61b2. arXiv: 1609.00258 [hep-ph].

[69] Jorge G. Morfin, Juan Nieves, and Jan T. Sobczyk. "Recent Developments in Neutrino/Antineutrino - Nucleus Interactions". In: *Adv.High Energy Phys.* 2012 (2012), p. 934597. DOI: 10.1155/2012/934597.

[70] L. Alvarez-Ruso, Y. Hayato, and J. Nieves. "Progress and open questions in the physics of neutrino cross sections at intermediate energies". In: *New J.Phys.* 16 (2014), p. 075015. DOI: 10.1088/1367-2630/16/7/075015.

[71] Teppei Katori and Marco Martini. "Neutrino–nucleus cross sections for oscillation experiments". In: *J. Phys.* G45.1 (2018), p. 013001. DOI: 10.1088/1361-6471/aa8bf7. arXiv: 1611.07770 [hep-ph].

[72] M. Martini et al. "A Unified approach for nucleon knock-out, coherent and incoherent pion production in neutrino interactions with nuclei". In: *Phys.Rev.* C80 (2009), p. 065501. DOI: 10.1103/PhysRevC.80.065501.

[73] J. Nieves, I. Ruiz Simo, and M.J. Vicente Vacas. "Inclusive Charged–Current Neutrino–Nucleus Reactions". In: *Phys.Rev.* C83 (2011), p. 045501. DOI: 10.1103/PhysRevC.83.045501.

[74] J. Nieves, I. Ruiz Simo, and M.J. Vicente Vacas. "The nucleon axial mass and the MiniBooNE Quasielastic Neutrino-Nucleus Scattering problem". In: *Phys.Lett.* B707 (2012), pp. 72–75. DOI: 10.1016/j.physletb.2011.11.061.

[75] M. Martini, M. Ericson, and G. Chanfray. "Neutrino quasielastic interaction and nuclear dynamics". In: *Phys.Rev.* C84 (2011), p. 055502. DOI: 10.1103/PhysRevC.84.055502.

[76] J. Nieves et al. "Neutrino Energy Reconstruction and the Shape of the CCQE-like Total Cross Section". In: *Phys.Rev.* D85 (2012), p. 113008. DOI: 10.1103/PhysRevD.85.113008.

[77] J. Nieves, I. Ruiz Simo, and M.J. Vicente Vacas. "Two Particle-Hole Excitations in Charged Current Quasielastic Antineutrino–Nucleus Scattering". In: *Phys.Lett.* B721 (2013), pp. 90–93. DOI: 10.1016/j.physletb.2013.03.002.

[78] M. Martini and M. Ericson. "Quasielastic and multinucleon excitations in antineutrino-nucleus interactions". In: *Phys.Rev.* C87 (2013), p. 065501. DOI: 10.1103/PhysRevC.87.065501.

[79] R. Gran et al. "Neutrino-nucleus quasi-elastic and 2p2h interactions up to 10 GeV". In: *Phys.Rev.* D88 (2013), p. 113007. DOI: 10.1103/PhysRevD.88.113007.

[80] J.E. Amaro et al. "Meson-exchange currents and quasielastic antineutrino cross sections in the SuperScaling Approximation". In: *Phys.Rev.Lett.* 108 (2012), p. 152501. DOI: 10.1103/PhysRevLett.108.152501.

[81] I. Ruiz Simo et al. “Angular distribution in two-particle emission induced by neutrinos and electrons”. In: *Phys. Rev.* D90.5 (2014), p. 053010. DOI: 10.1103/PhysRevD.90.053010.

[82] G. D. Megias et al. “Meson-exchange currents and quasielastic predictions for charged-current neutrino-^{12}C scattering in the superscaling approach”. In: *Phys. Rev.* D91.7 (2015), p. 073004. DOI: 10.1103/PhysRevD.91.073004.

[83] I. Ruiz Simo et al. “Emission of neutron-proton and proton-proton pairs in neutrino scattering”. In: *Phys. Lett.* B762 (2016), pp. 124–130. DOI: 10.1016/j.physletb.2016.09.021.

[84] Omar Benhar. “Confronting Electron- and Neutrino-Nucleus Scattering”. In: (2011). [J. Phys. Conf. Ser.408,012042(2013)]. DOI: 10.1088/1742-6596/408/1/012042.

[85] J. Nieves et al. “Neutrino-nucleus CCQE-like scattering”. In: *Nucl. Part. Phys. Proc.* 273-275 (2016), pp. 1830–1835. DOI: 10.1016/j.nuclphysbps.2015.09.295.

[86] R. Machleidt and I. Slaus. “The Nucleon-nucleon interaction: Topical review”. In: *J. Phys.* G27 (2001), R69–R108. DOI: 10.1088/0954-3899/27/5/201.

[87] R. Machleidt, K. Holinde, and C. Elster. “The Bonn Meson Exchange Model for the Nucleon Nucleon Interaction”. In: *Phys. Rept.* 149 (1987), pp. 1–89. DOI: 10.1016/S0370-1573(87)80002-9.

[88] V. G. J. Stoks et al. “Construction of high quality N N potential models”. In: *Phys. Rev.* C49 (1994), pp. 2950–2962. DOI: 10.1103/PhysRevC.49.2950.

[89] R. Machleidt. “The High precision, charge dependent Bonn nucleon-nucleon potential (CD-Bonn)”. In: *Phys. Rev.* C63 (2001), p. 024001. DOI: 10.1103/PhysRevC.63.024001.

[90] Robert B. Wiringa, V. G. J. Stoks, and R. Schiavilla. “An Accurate nucleon-nucleon potential with charge independence breaking”. In: *Phys. Rev.* C51 (1995), pp. 38–51. DOI: 10.1103/PhysRevC.51.38.

[91] R. Machleidt and D. R. Entem. “Chiral effective field theory and nuclear forces”. In: *Phys. Rept.* 503 (2011), pp. 1–75. DOI: 10.1016/j.physrep.2011.02.001.

[92] Steven Weinberg. “Nuclear forces from chiral Lagrangians”. In: *Phys. Lett.* B251 (1990), pp. 288–292. DOI: 10.1016/0370-2693(90)90938-3.

[93] Steven Weinberg. “Effective chiral Lagrangians for nucleon - pion interactions and nuclear forces”. In: *Nucl. Phys.* B363 (1991), pp. 3–18. DOI: 10.1016/0550-3213(91)90231-L.

[94] Steven Weinberg. “Three body interactions among nucleons and pions”. In: *Phys. Lett.* B295 (1992), pp. 114–121. DOI: 10.1016/0370-2693(92)90099-P.

[95] S. L. Glashow. “Partial Symmetries of Weak Interactions”. In: *Nucl. Phys.* 22 (1961), pp. 579–588. DOI: 10.1016/0029-5582(61)90469-2.

[96] Abdus Salam. “Weak and Electromagnetic Interactions”. In: *Conf. Proc.* C680519 (1968), pp. 367–377.

[97] Steven Weinberg. “A Model of Leptons”. In: *Phys. Rev. Lett.* 19 (1967), pp. 1264–1266. DOI: 10.1103/PhysRevLett.19.1264.

[98] Chen-Ning Yang and Robert L. Mills. “Conservation of Isotopic Spin and Isotopic Gauge Invariance”. In: *Phys. Rev.* 96 (1954). [,150(1954)], pp. 191–195. DOI: 10.1103/PhysRev.96.191.

[99] John F. Donoghue, Eugene Golowich, and Barry R. Holstein. *Dynamics of the Standard Model*. Cambridge University Press, 1996. ISBN: 0-521-36288-1.

[100] Paolo Lipari, Maurizio Lusignoli, and Francesca Sartogo. "The Neutrino cross-section and upward going muons". In: *Phys. Rev. Lett.* 74 (1995), pp. 4384–4387. DOI: 10.1103/PhysRevLett.74.4384.

[101] S. Galster et al. "Elastic electron-deuteron scattering and the electric neutron form factor at four-momentum transfers 5fm$^{-2} < q^2 <$ 14fm^{-2}". In: *Nucl. Phys.* B32 (1971), pp. 221–237. DOI: 10.1016/0550-3213(71)90068-X.

[102] V. A. Andreev et al. "Measurement of Muon Capture on the Proton to 1% Precision and Determination of the Pseudoscalar Coupling g_P". In: *Phys. Rev. Lett.* 110.1 (2013), p. 012504. DOI: 10.1103/PhysRevLett.110.012504.

[103] Luis Alvarez-Ruso, Krzysztof M. Graczyk, and Eduardo Saul-Sala. "Nucleon axial form factor from a Bayesian neural-network analysis of neutrino-scattering data". In: *Phys. Rev.* C99.2 (2019), p. 025204. DOI: 10.1103/PhysRevC.99.025204. arXiv: 1805.00905 [hep-ph].

[104] Andreas S. Kronfeld et al. "Lattice QCD and Neutrino-Nucleus Scattering". In: (2019). arXiv: 1904.09931 [hep-lat].

[105] Alexander L. Fetter and John Dirk Walecka. *Quantum Theory of Many-particle Systems*. Dover, 2003. ISBN: 0-486-42827-3.

[106] R. C. Carrasco and E. Oset. "Interaction of Real Photons With Nuclei From 100-MeV to 500-MeV". In: *Nucl. Phys.* A536 (1992), pp. 445–508. DOI: 10.1016/0375-9474(92)90109-W.

[107] R. B. Firestone and V. S. Shirley. *Table of Isotopes*. 8 edition. New York: John Wiley & Sons, 1996.

[108] C. W. de Jager, H. de Vries, and C. de Vries. "Nuclear charge and magnetization density distribution parameters from elastic electron scattering". In: *Atom. Data Nucl. Data Tabl.* 14 (1974), pp. 479–508.

[109] C. W. de Jager, H. de Vries, and C. de Vries. "Nuclear charge and magnetization density distribution parameters from elastic electron scattering". In: *Atom. Data Nucl. Data Tabl.* 36 (1987), pp. 495–536.

[110] C. Garcia-Recio, J. Nieves, and E. Oset. "Neutron distribution from pionic atoms". In: *Nucl. Phys. A* 547.473-487 (1992).

[111] Willem H. Dickhoff and Dimitri Van Neck. *Many-Body Theory Exposed!* World Scientific, 2005. ISBN: 981-256-294-X.

[112] J. Nieves. "Neutrinos in Nuclear Physics: RPA, MEC, 2p2h (Pionic Modes of Excitation in Nuclei)". In: *Springer Proc. Phys.* 182 (2016), pp. 3–54. DOI: 10.1007/978-3-319-21191-6_1.

[113] J. Nieves, M. Valverde, and M. J. Vicente Vacas. "Inclusive nucleon emission induced by quasi-elastic neutrino-nucleus interactions". In: *Phys. Rev.* C73 (2006), p. 025504. DOI: 10.1103/PhysRevC.73.025504.

[114] S.K. Singh and E. Oset. "Quasielastic neutrino (anti-neutrino) reactions in nuclei and the axial vector form-factor of the nucleon". In: *Nucl.Phys.* A542 (1992), pp. 587–615. DOI: 10.1016/0375-9474(92)90259-M.

[115] T.S. Kosmas and E. Oset. "Charged current neutrino nucleus reaction cross-sections at intermediate-energies". In: *Phys.Rev.* C53 (1996), pp. 1409–1415. DOI: 10.1103/PhysRevC.53.1409.

[116] S.K. Singh, Nimai C. Mukhopadhyay, and E. Oset. "Inclusive neutrino scattering in C-12: Implications for muon-neutrino to electron-neutrino oscillations". In: *Phys.Rev.* C57 (1998), pp. 2687–2692. DOI: 10.1103/PhysRevC.57.2687.

[117] J. Speth et al. “The influence of the π and ρ exchange potential on magnetic properties of nuclei”. In: *Nucl.Phys.* A343 (1980), pp. 382–416. DOI: 10.1016/0375-9474(80)90660-0.

[118] J Speth, E Werner, and W Wild. “Theory of infinite Fermi systems and application to the lead region”. In: *Phys. Rept.* 33 (1977), pp. 127–208.

[119] E. Oset, H. Toki, and W. Weise. “Pionic modes of excitation in nuclei”. In: *Phys. Rept.* 83 (1982), pp. 281–380. DOI: 10.1016/0370-1573(82)90123-5.

[120] M. B. Barbaro, R. Cenni, and M. R. Quaglia. “The generalised relativistic Lindhard functions”. In: *Eur. Phys. J.* A25 (2005), pp. 299–318. DOI: 10.1140/epja/i2005-10105-4.

[121] J. Nieves, E. Oset, and C. Garcia-Recio. “A Theoretical approach to pionic atoms and the problem of anomalies”. In: *Nucl. Phys.* A554 (1993), pp. 509–553. DOI: 10.1016/0375-9474(93)90245-S.

[122] M. Valverde, Jose Enrique Amaro, and J. Nieves. “Theoretical uncertainties on quasielastic charged-current neutrino-nucleus cross sections”. In: *Phys. Lett.* B638 (2006), pp. 325–332. DOI: 10.1016/j.physletb.2006.05.053.

[123] P. Fernandez de Cordoba et al. “Deep inelastic lepton scattering in nuclei at x > 1 and the nucleon spectral function”. In: *Nucl. Phys.* A611 (1996), pp. 514–538. DOI: 10.1016/S0375-9474(96)00249-7.

[124] P. Fernandez de Cordoba and E. Oset. “A mesonic decay in nuclei and the occupation number”. In: *Nucl. Phys.* A528 (1991), pp. 736–744. DOI: 10.1016/0375-9474(91)90259-9.

[125] S. Fantoni, B. L. Friman, and V. R. Pandharipande. “Correlated basis theory of nucleon optical potential in nuclear matter”. In: *Nucl. Phys.* A399 (1983), pp. 51–65. DOI: 10.1016/0375-9474(83)90593-6.

[126] S. Fantoni and V. R. Pandharipande. “Momentum distribution of nucleons in nuclear matter”. In: *Nucl. Phys.* A427 (1984), pp. 473–492. DOI: 10.1016/0375-9474(84)90226-4.

[127] A. Ramos, A. Polls, and W. H. Dickhoff. “Single-particle properties and short-range correlations in nuclear matter”. In: *Nucl. Phys.* A503 (1989), pp. 1–52. DOI: 10.1016/0375-9474(89)90252-2.

[128] H. Muther, G. Knehr, and A. Polls. “Momentum distribution in nuclear matter and finite nuclei”. In: *Phys. Rev.* C52 (1995), pp. 2955–2968. DOI: 10.1103/PhysRevC.52.2955.

[129] C. Mahaux et al. “Dynamics of the shell model”. In: *Phys. Rept.* 120 (1985), pp. 1–274. DOI: 10.1016/0370-1573(85)90100-0.

[130] Teppei Katori. “Meson Exchange Current (MEC) Models in Neutrino Interaction Generators”. In: *AIP Conf. Proc.* 1663 (2015), p. 030001. DOI: 10.1063/1.4919465.

[131] Omar Benhar, Alessandro Lovato, and Noemi Rocco. “Contribution of two-particle two-hole final states to the nuclear response”. In: *Phys. Rev.* C92.2 (2015), p. 024602. DOI: 10.1103/PhysRevC.92.024602.

[132] M. B. Barbaro et al. “The role of meson exchange currents in charged current (anti)neutrino -nucleus scattering”. In: *35th International Workshop on Nuclear Theory (IWNT 2016) Rila Mountains, Bulgaria., June 26-July 2, 2016*. 2016. URL: http://inspirehep.net/record/1490921/files/arXiv:1610.02924.pdf.

[133] S. Pastore et al. "Quantum Monte Carlo calculations of electromagnetic moments and transitions in A $\leq$ 9 nuclei with meson-exchange currents derived from chiral effective field theory". In: *Phys. Rev.* C87.3 (2013), p. 035503. DOI: 10.1103/PhysRevC.87.035503.

[134] E. D. Cooper et al. "Global Dirac phenomenology for proton nucleus elastic scattering". In: *Phys. Rev.* C47 (1993), pp. 297–311. DOI: 10.1103/PhysRevC.47.297.

[135] R. J. Woo et al. "Measurement of the Induced Proton Polarization Pn in the C-12 (e, e-prime p –>) Reaction". In: *Phys. Rev. Lett.* 80 (1998), pp. 456–459. DOI: 10.1103/PhysRevLett.80.456.

[136] Stefano Fantoni and Adelchi Fabrocini. "Correlated basis function theory for fermion systems". In: *Microscopic Quantum Many-Body Theories and Their Applications*. Ed. by Jesús Navarro and Artur Polls. Berlin, Heidelberg: Springer Berlin Heidelberg, 1998. ISBN: 978-3-540-69787-9.

[137] J. Mougey et al. "Quasifree (e, e' p) Scattering on C-12, Si-28, Ca-40 and Ni-58". In: *Nucl. Phys.* A262 (1976), pp. 461–492. DOI: 10.1016/0375-9474(76)90510-8.

[138] D. Dutta et al. "A Study of the quasielastic (e,e-prime p) reaction on C-12, Fe-56 and Au-97". In: *Phys. Rev.* C68 (2003), p. 064603. DOI: 10.1103/PhysRevC.68.064603.

[139] B. S. Pudliner et al. "Quantum Monte Carlo calculations of nuclei with A <= 7". In: *Phys. Rev.* C56 (1997), pp. 1720–1750. DOI: 10.1103/PhysRevC.56.1720.

[140] Steven C. Pieper et al. "Realistic models of pion exchange three nucleon interactions". In: *Phys. Rev.* C64 (2001), p. 014001. DOI: 10.1103/PhysRevC.64.014001.

[141] S. Fantoni and V. R. Pandharipande. "Orthogonalization of correlated states". In: *Phys. Rev.* C37 (1988), pp. 1697–1707. DOI: 10.1103/PhysRevC.37.1697.

[142] Omar Benhar, Adelchi Fabrocini, and Stefano Fantoni. "Occupation probabilities and hole-state strengths in nuclear matter". In: *Phys. Rev.* C41 (1990), R24–R27. DOI: 10.1103/PhysRevC.41.R24.

[143] O. Benhar et al. "Scattering of GeV electrons by nuclear matter". In: *Phys. Rev.* C44 (1991), pp. 2328–2342. DOI: 10.1103/PhysRevC.44.2328.

[144] Omar Benhar. "Final state interactions in the nuclear response at large momentum transfer". In: *Phys. Rev.* C87.2 (2013), p. 024606. DOI: 10.1103/PhysRevC.87.024606.

[145] T. Leitner et al. "Electron- and neutrino-nucleus scattering from the quasielastic to the resonance region". In: *Phys.Rev.* C79 (2009), p. 034601. DOI: 10.1103/PhysRevC.79.034601.

[146] J. Lehr et al. "Nuclear matter spectral functions by transport theory". In: *Nucl. Phys.* A703 (2002), pp. 393–408. DOI: 10.1016/S0375-9474(01)01534-2. arXiv: nucl-th/0108008 [nucl-th].

[147] C. Maieron, T. W. Donnelly, and Ingo Sick. "Extended superscaling of electron scattering from nuclei". In: *Phys. Rev.* C65 (2002), p. 025502. DOI: 10.1103/PhysRevC.65.025502.

[148] R. Gonzaléz-Jiménez et al. "Extensions of Superscaling from Relativistic Mean Field Theory: the SuSAv2 Model". In: *Phys. Rev.* C90.3 (2014), p. 035501. DOI: 10.1103/PhysRevC.90.035501.

[149] J. Marteau. "Effects of the nuclear correlations on the neutrino oxygen interactions". In: *Eur. Phys. J.* A5 (1999), pp. 183–190. DOI: 10.1007/s100500050274. arXiv: hep-ph/9902210 [hep-ph].

[150] Joanna Ewa Sobczyk. "Intercomparison of the lepton-nucleus scattering models in the quasielastic region". In: *Phys. Rev.* C96.4 (2017), p. 045501. DOI: 10.1103/PhysRevC.96.045501.

[151] B. E. Bodmann et al. "Neutrino interactions with carbon: Recent measurements and a new test of electron-neutrino, anti-muon-neutrino universality". In: *Phys. Lett.* B332 (1994), pp. 251–257. DOI: 10.1016/0370-2693(94)91250-5.

[152] C. Athanassopoulos et al. "Measurements of the reactions C-12 (electron-neutrino, e-) N-12 (g.s.) and C-12 (electron-neutrino, e-) N*-12". In: *Phys. Rev.* C55 (1997), pp. 2078–2091. DOI: 10.1103/PhysRevC.55.2078.

[153] D. A. Krakauer et al. "Experimental study of neutrino absorption on carbon". In: *Phys. Rev.* C45 (1992), pp. 2450–2463. DOI: 10.1103/PhysRevC.45.2450.

[154] H. C. Chiang et al. "Inclusive Radiative Pion Capture in Nuclei". In: *Nucl. Phys.* A510 (1990). [Erratum: Nucl. Phys.A514,749(1990)], p. 573. DOI: 10.1016/0375-9474(90)90349-Q.

[155] J. A. Bistirlich et al. "Photon spectra from radiative absorption of pions in nuclei". In: *Phys. Rev.* C5 (1972), pp. 1867–1883. DOI: 10.1103/PhysRevC.5.1867.

[156] Jose Enrique Amaro, A. M. Lallena, and J. Nieves. "Radiative pion capture in nuclei: A Continuum shell model approach". In: *Nucl. Phys.* A623 (1997), pp. 529–547. DOI: 10.1016/S0375-9474(97)00187-5.

[157] S. Kamerdzhiev, J. Speth, and G. Tertychny. "Extended theory of finite Fermi systems: Collective vibrations in closed shell nuclei". In: *Phys. Rept.* 393 (2004), pp. 1–86. DOI: 10.1016/j.physrep.2003.11.001.

[158] Antonio Botrugno and Giampaolo Co'. "Excitation of nuclear giant resonances in neutrino scattering off nuclei". In: *Nucl. Phys.* A761 (2005), pp. 200–231. DOI: 10.1016/j.nuclphysa.2005.07.010.

[159] T. Suzuki, David F. Measday, and J. P. Roalsvig. "Total Nuclear Capture Rates for Negative Muons". In: *Phys. Rev.* C35 (1987), p. 2212. DOI: 10.1103/PhysRevC.35.2212.

[160] M. Albert et al. "Measurement of the reaction C-12 (muon-neutrino, mu-) X near threshold". In: *Phys. Rev.* C51 (1995), pp. 1065–1069. DOI: 10.1103/PhysRevC.51.1065.

[161] A. C. Hayes and I. S. Towner. "Shell model calculations of neutrino scattering from C-12". In: *Phys. Rev.* C61 (2000), p. 044603. DOI: 10.1103/PhysRevC.61.044603.

[162] C. Volpe et al. "Microscopic theories of neutrino C-12 reactions". In: *Phys.Rev.* C62 (2000), p. 015501. DOI: 10.1103/PhysRevC.62.015501.

[163] E. Kolbe et al. "Neutrino nucleus reactions and nuclear structure". In: *J. Phys.* G29 (2003), pp. 2569–2596. DOI: 10.1088/0954-3899/29/11/010.

[164] C. Athanassopoulos et al. "Measurements of the reactions C-12 (muon-neutrino, mu-) N-12 (g.s.) and C-12 (muon-neutrino, mu-) X". In: *Phys. Rev.* C56 (1997), pp. 2806–2819. DOI: 10.1103/PhysRevC.56.2806.

[165] L. B. Auerbach et al. "Measurements of charged current reactions of muon neutrinos on C-12". In: *Phys. Rev.* C66 (2002), p. 015501. DOI: 10.1103/PhysRevC.66.015501.

[166] A.A. Aguilar-Arevalo et al. "First Measurement of the Muon Neutrino Charged Current Quasielastic Double Differential Cross Section". In: *Phys. Rev.* D81 (2010), p. 092005. DOI: 10.1103/PhysRevD.81.092005.

[167] A.A. Aguilar-Arevalo et al. "The Neutrino Flux prediction at MiniBooNE". In: *Phys. Rev.* D79 (2009), p. 072002. DOI: 10.1103/PhysRevD.79.072002.

[168] M. Waroquier et al. “Rearrangement Effects in Shell Model Calculations Using Density Dependent Interactions”. In: *Phys. Rept.* 148 (1987), p. 249. DOI: 10.1016/0370-1573(87)90066-4.

[169] Jose Enrique Amaro et al. “Superscaling and neutral current quasielastic neutrino-nucleus scattering”. In: *Phys. Rev.* C73 (2006), p. 035503. DOI: 10.1103/PhysRevC.73.035503.

[170] J.E. Amaro et al. “Meson-exchange currents and quasielastic neutrino cross sections in the SuperScaling Approximation model”. In: *Phys.Lett.* B696 (2011), pp. 151–155. DOI: 10.1016/j.physletb.2010.12.007.

[171] J.E. Amaro et al. “Relativistic analyses of quasielastic neutrino cross sections at MiniBooNE kinematics”. In: *Phys.Rev.* D84 (2011), p. 033004. DOI: 10.1103/PhysRevD.84.033004.

[172] R. Gonzalez-Jimenez et al. “Neutral current (anti)neutrino scattering: relativistic mean field and superscaling predictions”. In: *Phys.Lett.* B718 (2013), pp. 1471–1474. DOI: 10.1016/j.physletb.2012.11.065.

[173] E. Oset et al. “Decay Modes of Σ and Λ Hypernuclei”. In: *Phys. Rept.* 188 (1990), p. 79. DOI: 10.1016/0370-1573(90)90091-F.

[174] P. Fernandez de Cordoba and E. Oset. “Projectile and target delta excitation in the (He-3, t) and (He-3, He-3) reactions”. In: *Nucl. Phys.* A544 (1992), pp. 793–810. DOI: 10.1016/0375-9474(92)90541-Q.

[175] J. Nieves, E. Oset, and C. Garcia-Recio. “Many body approach to low-energy pion nucleus scattering”. In: *Nucl.Phys.* A554 (1993), pp. 554–579. DOI: 10.1016/0375-9474(93)90246-T.

[176] P. Fernandez de Cordoba et al. “Coherent pion production in the (He-3, t) reaction in nuclei”. In: *Phys.Lett.* B319 (1993), pp. 416–420. DOI: 10.1016/0370-2693(93)91744-8.

[177] J. Nieves and E. Oset. “Pionic decay of Lambda hypernuclei”. In: *Phys. Rev.* C47 (1993), pp. 1478–1488. DOI: 10.1103/PhysRevC.47.1478.

[178] S. Hirenzaki et al. “Coherent pi0 electroproduction”. In: *Phys.Lett.* B304 (1993), pp. 198–202. DOI: 10.1016/0370-2693(93)90282-M.

[179] R. C. Carrasco, M. J. Vicente Vacas, and E. Oset. “Inclusive (gamma, N), (gamma, N N) and (gamma, N pi) reactions in nuclei at intermediate-energies”. In: *Nucl. Phys.* A570 (1994), pp. 701–721. DOI: 10.1016/0375-9474(94)90080-9.

[180] P. Fernandez de Cordoba et al. “Projectile delta excitation in alpha - proton scattering”. In: *Nucl. Phys.* A586 (1995), pp. 586–606. DOI: 10.1016/0375-9474(94)00815-5.

[181] C. Garcia-Recio, J. Nieves, and E. Oset. “Pion cloud contribution to K+ nucleus scattering”. In: *Phys. Rev.* C51 (1995), pp. 237–251. DOI: 10.1103/PhysRevC.51.237.

[182] S. Hirenzaki, P. Fernandez de Cordoba, and E. Oset. “Roper excitation in alpha - proton scattering”. In: *Phys. Rev.* C53 (1996), pp. 277–284. DOI: 10.1103/PhysRevC.53.277.

[183] A. Gil, J. Nieves, and E. Oset. “Inclusive (e, e-prime N), (e, e-prime N N), (e, e-prime pi): Reactions in nuclei”. In: *Nucl.Phys.* A627 (1997), pp. 599–619. DOI: 10.1016/S0375-9474(97)00515-0.

[184] C. Albertus, Jose Enrique Amaro, and J. Nieves. “What does free space Lambda-Lambda interaction predict for Lambda-Lambda hypernuclei?” In: *Phys. Rev. Lett.* 89 (2002), p. 032501. DOI: 10.1103/PhysRevLett.89.032501.

[185] C. Albertus, Jose Enrique Amaro, and J. Nieves. "Pionic decay of Lambda hypernuclei in a continuum shell model". In: *Phys. Rev.* C67 (2003), p. 034604. DOI: 10.1103/PhysRevC.67.034604.

[186] P. E. Bosted and V. Mamyan. "Empirical Fit to electron-nucleus scattering". In: (2012). arXiv: 1203.2262 [nucl-th].

[187] Omar Benhar, Donal Day, and Ingo Sick. "An Archive for quasi-elastic electron-nucleus scattering data". In: (2006). arXiv: nucl-ex/0603032 [nucl-ex].

[188] J. E. Sobczyk et al. "Scaling within the Spectral Function approach". In: *Phys. Rev.* C97 (2018), p. 035506. DOI: 10.1103/PhysRevC.97.035506.

[189] W. M. Alberico et al. "Scaling in electron scattering from a relativistic Fermi gas". In: *Phys. Rev.* C38 (1988), pp. 1801–1810. DOI: 10.1103/PhysRevC.38.1801.

[190] M. B. Barbaro et al. "Relativistic y - scaling and the Coulomb sum rule in nuclei". In: *Nucl. Phys.* A643 (1998), pp. 137–160. DOI: 10.1016/S0375-9474(98)00443-6.

[191] T.W. Donnelly and Ingo Sick. "Superscaling of inclusive electron scattering from nuclei". In: *Phys.Rev.* C60 (1999), p. 065502. DOI: 10.1103/PhysRevC.60.065502.

[192] P. Barreau et al. "Deep Inelastic electron Scattering from Carbon". In: *Nucl. Phys.* A402 (1983), pp. 515–540. DOI: 10.1016/0375-9474(83)90217-8.

[193] D. T. Baran et al. "Δ Electroproduction and Inelastic Charge Scattering From Carbon and Iron". In: *Phys. Rev. Lett.* 61 (1988), pp. 400–403. DOI: 10.1103/PhysRevLett.61.400.

[194] R. R. Whitney et al. "Quasielastic electron Scattering". In: *Phys. Rev.* C9 (1974), p. 2230. DOI: 10.1103/PhysRevC.9.2230.

[195] U. Mosel. "Talk (April 18, 2017) given at IPPP/NuSTEC topical meeting on neutrino-nucleus scattering (Durham, UK). " In: (). URL: https://conference.ippp.dur.ac.uk/event/583/.

[196] K. Abe et al. "T2K neutrino flux prediction". In: *Phys. Rev.* D87.1 (2013). [Addendum: Phys. Rev.D87,no.1,019902(2013)], p. 012001. DOI: 10.1103/PhysRevD.87.012001,10.1103/PhysRevD.87.019902. arXiv: 1211.0469 [hep-ex].

[197] G. D. Megias et al. "Inclusive electron scattering within the SuSAv2 meson-exchange current approach". In: *Phys. Rev.* D94 (2016), p. 013012. DOI: 10.1103/PhysRevD.94.013012. arXiv: 1603.08396 [nucl-th].

[198] J. D. Bjorken. "Asymptotic Sum Rules at Infinite Momentum". In: *Phys. Rev.* 179 (1969), pp. 1547–1553. DOI: 10.1103/PhysRev.179.1547.

[199] Geoffrey B. West. "Electron Scattering from Atoms, Nuclei and Nucleons". In: *Phys. Rept.* 18 (1975), pp. 263–323. DOI: 10.1016/0370-1573(75)90035-6.

[200] R. Rosenfelder. "Quasielastic electron scattering from nuclei". In: *Annals Phys.* 128 (1980), pp. 188–240. DOI: 10.1016/0003-4916(80)90059-7.

[201] D. B. Day et al. "Y Scaling in Electron Nucleus Scattering". In: *Phys. Rev. Lett.* 59 (1987), pp. 427–430. DOI: 10.1103/PhysRevLett.59.427.

[202] T. W. Donnelly and Ingo Sick. "Superscaling in inclusive electron - nucleus scattering". In: *Phys. Rev. Lett.* 82 (1999), pp. 3212–3215. DOI: 10.1103/PhysRevLett.82.3212.

[203] E. Pace and G. Salme. "Nuclear Scaling Function and Quasielastic Electron Scattering by Nuclei". In: *Phys. Lett.* 110B (1982), p. 411. DOI: 10.1016/0370-2693(82)91283-7.

[204] R. Cenni, Claudio Ciofi degli Atti, and G. Salme. "A Y Scaling Analysis of the Electromagnetic Longitudinal and Transverse Response Functions". In: *Phys. Rev.* C39 (1989), pp. 1425–1437. DOI: 10.1103/PhysRevC.39.1425.

[205] J. A. Caballero et al. "Superscaling in charged current neutrino quasielastic scattering in the relativistic impulse approximation". In: *Phys. Rev. Lett.* 95 (2005), p. 252502. DOI: 10.1103/PhysRevLett.95.252502.

[206] A. N. Antonov et al. "Scaling Function, Spectral Function and Nucleon Momentum Distribution in Nuclei". In: *Phys. Rev.* C83 (2011), p. 045504. DOI: 10.1103/PhysRevC.83.045504.

[207] Jose Enrique Amaro et al. "Quasielastic Charged Current Neutrino-nucleus Scattering". In: *Phys. Rev. Lett.* 98 (2007), p. 242501. DOI: 10.1103/PhysRevLett.98.242501.

[208] J. Carlson et al. "Quantum Monte Carlo methods for nuclear physics". In: *Rev. Mod. Phys.* 87 (2015), p. 1067. DOI: 10.1103/RevModPhys.87.1067.

[209] R. B. Wiringa et al. "Nucleon and nucleon-pair momentum distributions in $A \leq 12$ nuclei". In: *Phys. Rev.* C89.2 (2014), p. 024305. DOI: 10.1103/PhysRevC.89.024305.

[210] Robert B. Wiringa. "Single-particle potential in dense nuclear matter". In: *Phys. Rev.* C38 (1988), pp. 2967–2970. DOI: 10.1103/PhysRevC.38.2967.

[211] Omar Benhar and Alessandro Lovato. "Perturbation Theory of Nuclear Matter with a Microscopic Effective Interaction". In: *Phys. Rev.* C96.5 (2017), p. 054301. DOI: 10.1103/PhysRevC.96.054301. arXiv: 1706.00760 [nucl-th].

[212] A. Lovato et al. "Charge Form Factor and Sum Rules of Electromagnetic Response Functions in ^{12}C". In: *Phys.Rev.Lett.* 111.9 (2013), p. 092501. DOI: 10.1103/PhysRevLett.111.092501.

[213] A. Lovato et al. "Electromagnetic and neutral-weak response functions of ^{4}He and ^{12}C". In: *Phys. Rev.* C91.6 (2015), p. 062501. DOI: 10.1103/PhysRevC.91.062501.

[214] A. Lovato et al. "Electromagnetic response of ^{12}C: A first-principles calculation". In: *Phys. Rev. Lett.* 117.8 (2016), p. 082501. DOI: 10.1103/PhysRevLett.117.082501.

[215] https://www-sciboone.fnal.gov/.

[216] https://microboone.fnal.gov/.

[217] https://minerva.fnal.gov/.

[218] http://t962.fnal.gov/.

[219] M. Ablikim et al. "Measurement of the absolute branching fraction for $\Lambda_c^+ \to \Lambda e^+ \nu_e$". In: *Phys. Rev. Lett.* 115.22 (2015), p. 221805. DOI: 10.1103/PhysRevLett.115.221805.

[220] Medina Ablikim et al. "Measurement of the absolute branching fraction for $\Lambda_c^+ \to \Lambda \mu^+ \nu_\mu$". In: *Phys. Lett.* B767 (2017), pp. 42–47. DOI: 10.1016/j.physletb.2017.01.047.

[221] R. N. Faustov and V. O. Galkin. "Semileptonic decays of Λ_c baryons in the relativistic quark model". In: *Eur. Phys. J.* C76.11 (2016), p. 628. DOI: 10.1140/epjc/s10052-016-4492-z.

[222] Stefan Meinel. "$\Lambda_c \to \Lambda l^+ \nu_l$ form factors and decay rates from lattice QCD with physical quark masses". In: *Phys. Rev. Lett.* 118.8 (2017), p. 082001. DOI: 10.1103/PhysRevLett.118.082001.

[223] J. E. Sobczyk et al. "Weak production of strange and charmed ground-state baryons in nuclei". In: *Phys. Rev.* C99.6 (2019), p. 065503. DOI: 10.1103/PhysRevC.99.065503. arXiv: 1901.10192 [nucl-th].

[224] A. Kayis-Topaksu et al. “Measurement of Lambda/c+ production in neutrino charged-current interactions”. In: *Phys. Lett.* B555 (2003), pp. 156–166. DOI: 10.1016/S0370-2693(03)00045-5.

[225] Giovanni De Lellis, Pasquale Migliozzi, and Pietro Santorelli. “Charm physics with neutrinos”. In: *Phys. Rept.* 399 (2004). [Erratum: Phys. Rept.411,323(2005)], pp. 227–320. DOI: 10.1016/j.physrep.2005.02.001.

[226] W. Roberts and Muslema Pervin. “Heavy baryons in a quark model”. In: *Int. J. Mod. Phys.* A23 (2008), pp. 2817–2860. DOI: 10.1142/S0217751X08041219.

[227] Mikhail A. Ivanov et al. “Heavy baryon transitions in a relativistic three quark model”. In: *Phys. Rev.* D56 (1997), pp. 348–364. DOI: 10.1103/PhysRevD.56.348.

[228] Tanja Branz et al. “Relativistic constituent quark model with infrared confinement”. In: *Phys. Rev.* D81 (2010), p. 034010. DOI: 10.1103/PhysRevD.81.034010.

[229] Thomas Gutsche et al. “Rare baryon decays $\Lambda_b \to \Lambda l^+ l^- (l = e, \mu, \tau)$ and $\Lambda_b \to \Lambda\gamma$: differential and total rates, lepton- and hadron-side forward-backward asymmetries”. In: *Phys. Rev.* D87 (2013), p. 074031. DOI: 10.1103/PhysRevD.87.074031.

[230] M. Avila-Aoki et al. “Predictions for Semileptonic Decays of Charm Baryons. 1. SU(4) Symmetry Limit”. In: *Phys. Rev.* D40 (1989), p. 2944. DOI: 10.1103/PhysRevD.40.2944.

[231] A. Chodos et al. “A New Extended Model of Hadrons”. In: *Phys. Rev.* D9 (1974), pp. 3471–3495. DOI: 10.1103/PhysRevD.9.3471.

[232] A. Chodos et al. “Baryon Structure in the Bag Theory”. In: *Phys. Rev.* D10 (1974), p. 2599. DOI: 10.1103/PhysRevD.10.2599.

[233] J.J.J. Kokkedee. *Quark Model*. New York, W.A. Benjamin, 1969.

[234] K. A. Olive et al. “Review of Particle Physics”. In: *Chin. Phys.* C38 (2014), p. 090001. DOI: 10.1088/1674-1137/38/9/090001.

[235] A. Zupanc et al. “Measurement of the Branching Fraction $\mathscr{B}(\Lambda_c^+ \to pK^-\pi^+)$”. In: *Phys. Rev. Lett.* 113.4 (2014), p. 042002. DOI: 10.1103/PhysRevLett.113.042002.

[236] Y. Aoki et al. “Continuum Limit Physics from 2+1 Flavor Domain Wall QCD”. In: *Phys. Rev.* D83 (2011), p. 074508. DOI: 10.1103/PhysRevD.83.074508.

[237] T. Blum et al. “Domain wall QCD with physical quark masses”. In: *Phys. Rev.* D93.7 (2016), p. 074505. DOI: 10.1103/PhysRevD.93.074505.

[238] Claude Bourrely, Irinel Caprini, and Laurent Lellouch. “Model-independent description of B —> pi l nu decays and a determination of |V(ub)|”. In: *Phys. Rev.* D79 (2009). [Erratum: Phys. Rev.D82,099902(2010)], p. 013008. DOI: 10.1103/PhysRevD.82.099902,10.1103/PhysRevD.79.013008.

[239] A. Bouyssy. “Strangeness exchange reactions and hypernuclear spectroscopy”. In: *Phys. Lett.* 84B (1979), pp. 41–45. DOI: 10.1016/0370-2693(79)90644-0.

[240] Y. Hayato. “NEUT”. In: *Nucl. Phys. Proc. Suppl.* 112 (2002). [,171(2002)], pp. 171–176. DOI: 10.1016/S0920-5632(02)01759-0.

[241] Cezary Juszczak, Jaroslaw A. Nowak, and Jan T. Sobczyk. “Simulations from a new neutrino event generator”. In: *Nucl. Phys. Proc. Suppl.* 159 (2006). [,211(2005)], pp. 211–216. DOI: 10.1016/j.nuclphysbps.2006.08.069.

[242] C. Andreopoulos et al. “The GENIE Neutrino Monte Carlo Generator”. In: *Nucl. Instrum. Meth.* A614 (2010), pp. 87–104. DOI: 10.1016/j.nima.2009.12.009.

[243] D. Drakoulakos et al. "Proposal to perform a high-statistics neutrino scattering experiment using a fine-grained detector in the NuMI beam". In: (2004). arXiv: hep-ex/0405002 [hep-ex].

[244] N. Agafonova et al. "Evidence for $\nu_\mu \to \nu_\tau$ appearance in the CNGS neutrino beam with the OPERA experiment". In: *Phys. Rev.* D89.5 (2014), p. 051102. DOI: 10.1103/PhysRevD.89.051102.

[245] K. Kodama et al. "Final tau-neutrino results from the DONuT experiment". In: *Phys. Rev.* D78 (2008), p. 052002. DOI: 10.1103/PhysRevD.78.052002.

[246] Walter M. Bonivento. "The SHiP experiment at CERN". In: *EPJ Web Conf.* 182 (2018), p. 02016. DOI: 10.1051/epjconf/201818202016.

[247] Kaoru Hagiwara, Kentarou Mawatari, and Hiroshi Yokoya. "Tau polarization in tau neutrino nucleon scattering". In: *Nucl. Phys.* B668 (2003). [Erratum: Nucl. Phys. B701, 405(2004)], pp. 364–384. DOI: 10.1016/S0550-3213(03)00575-3.

[248] M. Valverde et al. "Nuclear effects on lepton polarization in charged-current quasielastic neutrino scattering". In: *Phys. Lett.* B642 (2006), pp. 218–226. DOI: 10.1016/j.physletb.2006.08.087.

[249] S. Fantoni and V. R. Pandharipande. "Correlated basis theory of nuclear matter response functions". In: *Nucl. Phys.* A473 (1987), pp. 234–266. DOI: 10.1016/0375-9474(87)90144-8.

[250] J. E. Sobczyk, N. Rocco, and J. Nieves. "Polarization of Tau in Quasielastic (Anti)Neutrino Scattering: The Role of Spectral Functions". In: *Phys. Rev.* C100.3 (2019), p. 035501. DOI: 10.1103/PhysRevC.100.035501. arXiv: 1906.05656 [nucl-th].

[251] Franz Mandl and Graham Shaw. *Quantum Field Theory*. 1985. URL: http://eu.wiley.com/WileyCDA/WileyTitle/productCd-0471496839.html.

[252] T. De Forest. "Off-Shell electron Nucleon Cross-Sections. The Impulse Approximation". In: *Nucl. Phys.* A392 (1983), pp. 232–248. DOI: 10.1016/0375-9474(83)90124-0.

[253] Michael E. Peskin and Daniel V. Schroeder. *An Introduction to Quantum Field Theory*. Perseus Books, 1995. ISBN: 0-201-50397-2.

[254] Carlo Giunti and Chung W. Kim. *Fundamentals of Neutrino Physics and Astrophysics*. 2007. ISBN: 9780198508717.